

# **DIELECTRIC SPECTROSCOPY OF VERY LOW LOSS MODEL POWER CABLES**

**Thesis submitted for the degree of**

**Doctor of Philosophy**

**at the University of Leicester**

**by**

**Tong Liu, MSc, BSc**

**Department of Engineering**

**University of Leicester**

**February 2010**

# **DIELECTRIC SPECTROSCOPY OF VERY LOW LOSS MODEL POWER CABLES**

**by**

**Tong Liu**

## **Abstract**

This research study focuses on the dielectric response of XLPE model power cables that have combinations of homo- and co-polymer insulation with furnace and acetylene carbon black semicon shields. Three dielectric spectroscopy techniques, which are frequency response analyzer and transformer ratio bridge in both frequency domain, and charging/discharging current system in time domain, were jointly used to measure the low loss XLPE cables in the frequency range from  $10^{-4}$ Hz to  $10^4$ Hz at temperatures from 20°C to 80°C. Degassing effects and thermal ageing effects have also been studied with the spectroscopy techniques. Thermal-electric behaviour and maximum voltages for thermal breakdown have been theoretically simulated for the model cables.

Three loss origins of the XLPE cables have been found with different loss mechanisms. Conduction loss due to thermally activated electron/hole hopping dominates the lower frequency range from  $10^{-4}$ Hz to 1Hz; Semicon loss due to its in series resistance with the insulation layer in cable equivalent circuit dominates the higher frequency range from  $10^2$ Hz to  $10^4$ Hz; intrinsic polarization loss of the XLPE insulation has dominant flat loss spectra in the mid-frequency range from 1Hz to  $10^2$ Hz. Degassing was found to decrease the conductivity of the model cables, while thermal ageing greatly increased the conductivity. Thermal-electric simulation results with FEMLAB have shown that the position of maximum field changes from inner to outer insulation boundary under higher applied voltages. A loss mechanism model with mathematical expression for dielectric loss spectrum calculation is finally proposed to explain the total dielectric loss of polymer power cables.

## **Acknowledgements**

I am greatly thankful to my supervisor, Professor John Fothergill, for his helps, inspirations and encouragement on my study and life. His broad knowledge, hard-working attitude, optimistic character, generous mind and kind heart towards all the other people have impressed and moved me. He has fundamentally changed me during my three years in Leicester. I feel lucky to be a student of such a great person.

I also sincerely thank my co-supervisor, Dr Stephen Dodd, for his excellent guidance. His expertise always helped me to choose the best solution for lots of problems in my study. He is extremely serious and passionate to scientific research, which makes me feel hungry for knowledge. I would not have done a good research if not him.

I wish to thank Dr Mingli Fu for all his enormous supports and kind helps on both my study and my life all along the way. He is my benefactor.

I would like to thank Dr Paul Lefley for his precious advice on my first year and second year report which formed a good basis for my PhD thesis.

Besides, Professor Len Dissado, Andy Willby, Alan Wales, Nikola Chalashkanov, Abdelghaffar Abdelmalik and Antonios Tzimas all gave me many helps. They are the ones of many people I would like to thank in the Engineering Department.

Especially, this is also a chance to express my thanks to Borealis AB for its sponsorship and Mr Ulf Nilsson for all his kind helps on my research.

Finally, I must thank my family. My parents gave me unconditional support on my PhD study. My wife sacrificed herself to support me while taking care of our daughter. I will try my best to give my family happy life.

## Contents

1	Introduction.....	1
2	Literature review.....	7
2.1	Background knowledge .....	7
2.2	Dielectric properties of insulation materials.....	12
2.2.1	Polarization of dielectric materials .....	12
2.2.2	Dielectric loss and conduction in dielectrics .....	18
2.2.3	The Debye model of dielectric relaxation and its modifications .....	21
2.2.4	Equivalent circuit analysis .....	25
2.3	Cable insulation materials.....	30
2.3.1	Materials of cable insulation layer.....	30
2.3.2	Materials of semiconducting layer.....	33
2.3.3	Degradation and breakdown of XLPE cable insulation.....	35
2.4	Electrical conduction in polymeric materials .....	39
2.4.1	Conduction mechanisms of bulk insulation.....	40
2.4.2	Conduction mechanisms due to electrode charge injection.....	43
2.5	Dielectric spectroscopy techniques .....	45
2.5.1	Time domain dielectric spectroscopy .....	46
2.5.2	Bridge techniques .....	50
2.5.3	Frequency response analyzer technique .....	53
3	Characterizing the dielectric response of power cables.....	56
3.1	Sample preparation of model power cables.....	56
3.1.1	Introduction to model power cables.....	56
3.1.2	Sample preparation .....	58
3.2	Choice and development of techniques for low loss measurement .....	61
3.2.1	Frequency response analyzer in the range from $10^{-4}$ Hz to 1Hz.....	61
3.2.2	Transformer ratio bridge in the range from 300Hz to 10kHz.....	75
3.2.3	Time domain charging/discharging current technique in the range from 1Hz to 250Hz.....	81
3.3	Experimental procedures .....	105
3.3.1	Degassing and ageing of the model cables .....	105
3.3.2	Experimental plan on different XLPE model cables .....	107
3.4	Conclusions.....	109
4	Dielectric response analysis of model power cables .....	111
4.1	Dielectric response at low frequencies of from $10^{-4}$ Hz to 1Hz.....	111
4.1.1	Thermal expansion calibration.....	111
4.1.2	Temperature dependent dielectric loss .....	115
4.1.3	Comparison of different model cables.....	118
4.2	Dielectric loss in the higher frequency range of from 300Hz to 10kHz.....	120
4.2.1	Loss tangent measurement results on different model cables.....	120
4.2.2	The loss origins due to semicon shields.....	123
4.2.3	MATLAB modelling of dielectric response of the power cables .....	126
4.3	Dielectric response with discharging current measurement .....	133
4.3.1	Temperature dependent discharging current of different cables .....	133
4.3.2	Transformation of discharging current into frequency spectra.....	137
4.4	Master curve in the frequency range from $10^{-4}$ Hz to $10^4$ Hz.....	144
4.4.1	Data combination of different techniques.....	144

4.4.2	Loss tangent master curves .....	153
4.5	Effect of degassing by conduction current measurement .....	156
4.5.1	Time delay for conduction measurement.....	156
4.5.2	Results of non-degassed, air degassed and vacuum degassed cables .....	157
4.6	Conclusions.....	162
5	Thermal ageing effects on model power cables.....	163
5.1	Dielectric response of aged model power cables using FRA .....	164
5.1.1	Ageing effect on homo-polymer model power cables.....	164
5.1.2	Ageing effect on co-polymer model power cables .....	166
5.2	Discharging current of aged model power cables.....	169
5.3	The loss tangent spectra from $10^{-4}$ Hz to $10^2$ Hz .....	173
5.4	Ageing effects on conductivity of model power cables.....	176
5.4.1	Influence of thermal ageing on conductivity of model power cables.....	176
5.4.2	Activation energy change after thermal ageing .....	178
5.5	Dielectric loss measurement using Schering bridge .....	181
5.5.1	Measurement system and sample preparation .....	181
5.5.2	Measurement results .....	184
5.6	Conclusions.....	188
6	Thermal breakdown simulation on model power cables .....	189
6.1	Introduction.....	189
6.2	Mathematical model of thermal-electric behaviour for power cables .....	191
6.3	Thermal breakdown simulation setup in FEMLAB .....	198
6.4	Simulation results of model power cables .....	205
6.4.1	MTV without load current at different ambient temperatures .....	205
6.4.2	MTV with heat injection due to load current.....	215
6.5	Conclusions.....	219
7	Discussion .....	220
7.1	Summary of experimental results on the model power cables .....	220
7.2	Conduction loss of cable insulation .....	222
7.3	Resistive loss of semicon layers .....	227
7.4	Polarization loss of XLPE insulation.....	232
7.5	Dielectric loss model for XLPE power cables.....	236
8	Conclusions and Further Work .....	242
9	References.....	247
	Appendix A: Meetings and publications .....	262

## 1 Introduction

A power cable is an assembly used for transmission of electrical power. In power systems, power cables are used all through the network in power plants, substations, high voltage transmission lines, and mains lines. They are installed everywhere as permanent wiring within buildings, buried in the ground, run overhead, or exposed. Like blood vessels of human bodies, power cables are critical components of power systems. The research, development and application of power cables are important for the performance and reliability of power transmission. High voltages carried by power cables are insulated by dielectric materials. Nowadays the insulation systems of power cables need to withstand extra high voltages with reliable long-term operation and insulation thickness as thin as possible. Any insulation defects of power cables can cause power failure, which subsequently result in economic loss including power cut cost, compensation cost, replacement cost and health/safety cost. Therefore, the study on the insulation system of power cables has great benefit to the cable manufacturing industry.

The oil-paper insulated power cable was invented by Ferranti in 1891 [1] and used for a long time without fundamental changes in the basic cable insulation system until the early 1960s, when polymeric insulation, predominantly polyethylene (PE), cross-linked polyethylene (XLPE) and ethylene propylene rubber (EPR), was introduced [2]. There has been enormous technical improvement based on the research of high voltage engineering and insulation dielectrics to minimise defects, such as voids and conducting impurities.

Because of the intrinsic breakdown strength of up to 800kV/mm and enhanced operating temperature from 75°C to 90°C after cross linking [3], XLPE cables are the best choice and dominating in power industry nowadays. The typical structure of XLPE cables is shown in Figure 1.1. The conductor is insulated by the XLPE insulation layer, which is sandwiched by two semiconductive screen layers. This comprises the basis of a power cable. Metallic shielding and outer covering layers are used for further protection. Over the past 30 years XLPE cable system failure rates have dramatically decreased even though the voltage stress per millimeter of insulation has continuously increased. 500kV power cables have been already developed for more than 10 years with an insulation thickness of 27mm [4] [5]. However, with more and more demanding requirements for the insulation systems of power cables, XLPE cables are still subject to further improvements. It has problems such as dielectric energy loss due to polarization/relaxation and ionic conduction, appearance of water and/or electrical trees, which are normally found after long term operating.

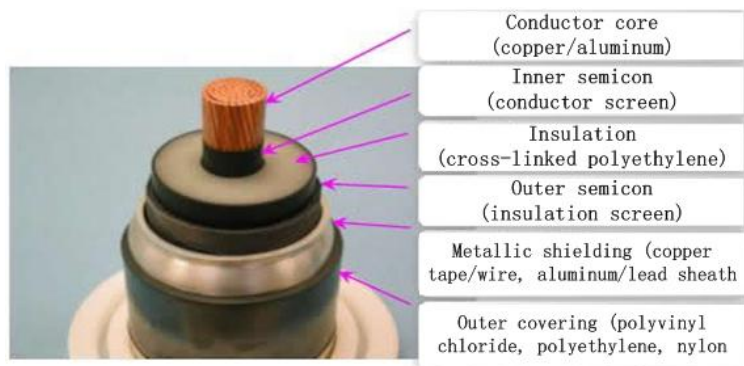


Figure 1.1 Typical structure of XLPE power cables

As a consequence, insulation ageing and failure have been widely studied for the reliable operation and safety of power equipment for many years. As one of the most popular and powerful research techniques, dielectric spectroscopy is playing a main role

in both ageing and fault detection for insulation systems including power cables. Dielectric spectroscopy is a technique to study the interaction of a material and the applied electric field. In particular, dielectric loss mechanisms which lead to energy dissipation and ageing of the insulation material are studied under variable frequency AC conditions and stepped DC conditions. Although there are various techniques for dielectric spectroscopy studies, including frequency and time domain measurements, the dielectric loss measurement of XLPE cables is beyond the abilities of many commercial instruments due to the following facts:

1. XLPE theoretically contains only very weak polar molecular groups and is without a net permanent dipole. As a consequence, XLPE has a very low dielectric constant and very low energy dissipation factor.
2. Commercial XLPE and subsequent thermal conditioning results in a material with low levels of impurities and additives which can contribute to electrical conductivity and dielectric loss.
3. XLPE cables have much thicker insulation than typical film samples used for dielectric spectroscopy. For a given value of applied voltage, the higher electric field that will exist within film samples make their dielectric properties easier to measure.

Film samples cannot represent the insulation system of power cables, although they will make more sensitive measurements of the dielectric properties. It is not possible to study the loss mechanisms of power cables with measurement on film samples due to the following reasons:

1. The formation of crystalline structures, which are known as lamella, are influenced by thermal history and manufacturing methods. This makes the morphological characteristics of thin films different from the bulk insulation layer of XLPE cables.
2. Unlike film samples, the insulation system of power cables includes semiconducting layers, which are carbon black filled polymers and used to smooth the electric field between central/outer conductors and insulation layer. The semiconducting layers have relatively smaller resistance with unique dielectric properties and may contribute to dielectric loss of power cables.
3. The cross linking by-products and impurities greatly influence the dielectric properties of XLPE material. The concentration and distribution of these insulation defects inside power cables which are produced by extrusion manufacturing process is different from film samples.

In order to study the dielectric properties of power cables more accurately, model cables with the same composition and manufacturing process can be used. The model cables should have extrusion production as actual cables comprising of inner conductor, inner semiconducting layer, polymer insulation and outer semiconducting layer. They should also have thinner insulation layer enabling higher electric fields to be applied. The investigation on these model cables can provide more useful and accurate information on the dielectric properties and loss mechanisms, which are important for studying the ageing and breakdown of power cables.

The purpose of this research project is to study the origins of dielectric loss in XLPE power cables using XLPE model cables manufactured by Borealis AB. These model

cables are extruded cables with a central conductor surrounded by an inner semiconducting layer, primary XLPE insulation and an outer semiconducting layer. The base materials for both semiconducting layers and primary insulation can be altered to assess the influence of the dielectric loss mechanisms by different materials and combinations. The model cables are studied by means of both frequency dielectric spectroscopy (FDDS) and time domain dielectric spectroscopy (TDDS), in order to determine the loss mechanisms of the power cables with broad dielectric spectra. As XLPE has very low dielectric loss, different techniques and measurement instruments are surveyed in order to resolve the dielectric loss over a wide range of frequency from  $10^{-4}$ Hz to  $10^4$ Hz. Different spectroscopy techniques such as frequency response analyzer, transformer ratio bridges and electrometers have different capabilities and sensitivities over a fixed range of frequencies and applied voltage. Hence, dielectric spectroscopy techniques that are capable of resolving the very low loss XLPE cables must be identified and developed. In addition, sensitive measurements of current are also required to measure the low level of electrical conductivity of the insulation as this will also contribute to electrical power loss within the cable. With these novel techniques, different types of XLPE model cables, which have different insulation layer and semiconducting layer materials, will be measured for comparison and identification of the loss mechanisms that could lead to ageing of the cable and subsequent failure. The results of this work will, therefore, provide cable manufacturers relevance in reducing power dissipation within high voltage cables and improve the reliability of cable designs. Equivalent circuit simulations of XLPE cables incorporating the various loss mechanisms, modelling of thermal runaway and microscopic investigation of the cable insulation will be complementary activities in order to aid interpretation of the

dielectric response and provide predictive models for cable ageing that can be scaled up to production cables.

In this thesis, chapter 2 contains the research background information from literature survey and introduction of relevant theories, knowledge and techniques that are important and fundamental for this research study. Chapter 3 introduces the exploration of appropriate spectroscopy techniques for low loss power cable measurement in both time and frequency domains. Chapter 4 discusses the dielectric loss spectra of three different techniques and the master curves in a wide frequency range from  $10^{-4}$ Hz to  $10^4$ Hz. The degassing effects of the model XLPE cables are also studied in this chapter. Chapter 5 includes the thermal ageing effects of the model power cables. The field dependent measurement on both aged and unaged cable samples using Schering bridge at 50Hz is shown in this chapter. In chapter 6, the thermal-electric behaviour and maximum voltage for thermal breakdown of the model cables is studied, based on the previous conductivity measurement results. Chapter 7 discusses the dielectric origins and possible loss mechanisms of the XLPE power cables. Conclusions and proposed further work are in the last chapter 8.

## 2 Literature review

### 2.1 Background knowledge

A dielectric or insulation material is a non-conducting substance, i.e. an insulator. The term was coined by Whewell [6] in response to a request from Faraday. Dielectric materials can be solids, liquids, or gases and have a variety of applications in power industry. The use of electrical insulation is as old as the science and technology of electrical phenomena, and systematic investigations of dielectric properties may also be traced back to 1870's. After Debye's theory on ideally non-interactive molecular dipole model of dielectrics, numerous monographs have been done by scientists from different aspects of view to understand dielectric materials. Theory of Dielectrics [7] provides an insight into the mathematical origins of dielectric behaviours. After long history of evolution, more practical and recent studies by A. K. Jonscher [8] [9] are emphasizing on the solid dielectrics and trying to establish a universal law based on all the experimental works so far. Other scientists, i.e. Daniel [10] and Hill et al.. [11], also contributed greatly to the understanding of dielectric theories with many approaches. As far as the polymeric insulation materials are concerned, L.A. Dissado and J.C. Fothergill have intensively investigated the mechanisms of degradation and breakdown of polymers, based on decades of research work on polymer insulation materials [12].

Since the application of polymeric cables came into use, the insulation systems of power cables have been studied worldwide, mainly on XLPE cables, in order to improve their reliability and performance. The dielectric loss mechanism study on power cables are mainly experimental investigation, with the dielectric science theoretical foundations. While it is a cross linked scientific area of electrical engineering

and material science, many practical techniques play a role in the study, typically dielectric spectroscopy of this research, space charge measurement popularly by PEA method, thermally stimulated depolarisation current (TSDC) measurement and scanning electron microscopy (SEM). John Densley[13] proposed an overview on multi-factor ageing mechanisms and list of diagnostic techniques for power cables including paper-insulated lead covered cables (PILC), self-contained fluid-filled (SCFF) cables, XLPE and ethylene propylene rubber (EPR) cables. John Fothergill [14] has led the European “HVDC” project to explore diagnostic techniques for HV XLPE cables based on electrical, micro-structural, physical and chemical characterization with lots of cooperated experimental work in UK, France and Italy. Space charge accumulation and behaviour in the cable insulation have been investigated recent years, especially on HVDC cables. Fabiani and Montanari et al. [15] [16] [17] have published series feature articles on polymeric cable design and space charge accumulation, following the enormous work by other people’s previous studies on XLPE power cables [18] [19] [20] [21] [22]. Recently, the semiconducting shields and their interfaces with the insulation layers of power cables raised focus while it was found that the defects of power cables are generally in these areas. Kegerise in Okonite company and Person in Dow Chemical company have studied the influence of cable semiconducting shields on cable dielectric losses and proposed dome manufacturing and performance criteria [23] [24]. The degradation of XLPE cables due to the semiconducting protrusion during production will initiate electrical trees by lightning and switching surges, as Bamji has found [25]. Tanaka [26] studied the facilitation of oriented lamellar growth at the interface by addition of special ingredients to the semiconducting layer, in order to improve the interfaces between shields and insulation. The role of degassing in XLPE power cables was studied and reviewed in joined effort of international companies by people of T.

Andrews (NEETRAC, Georgia Tech, USA), A. Smedberg (Borealis AB, Sweden), V. Waschk (NKT Cables, Germany) and W. Weissenberg (Brugg Cables, Switzerland) [27]. They concluded that degassing contributes greatly to the quality of power cables by improving the certainty in electrical testing and improving the dielectric properties. As the most important factor for XLPE cable failures, water trees have been studied by measuring the cable's relative permittivity and conduction with equivalent circuit under different voltages [28]. Thermal ageing effects of XLPE cables were also studied by Boubakeur [29], while thermo-luminescence in XLPE cable insulation was measured by Bamji and Bulinski [30]. Besides lots of research work on XLPE cables, a comparison of thermal and mechanical properties of EPR and XLPE cable compounds was introduced by Xiaoguang Qi [31].

Dielectric spectroscopy has a long history application on the research of dielectric materials, but not until recent years has it been used for the study and diagnostics of power equipment. Primary use of dielectric spectrometer includes some dielectric organic materials which were measured to study their polarization behaviour [32] or find out the property change due to ageing phenomenon [33]. Later on, more and more applications on power equipment test helped the development of novel insulation materials [34] [35] [36]. Time domain dielectric spectroscopy, which includes DC conduction measurement, also has lots of global application on various practical materials such as LDPE, HDPE, XLPE [37] [38] [39], epoxy [40], polyimide-Teflon [41], polyethyleneterephthalate [42] and holmium oxide [43]. Together with space charge and TSDC measurement, the charging/discharging current can provide polarization details inside the materials and frequency spectra by Fourier transform or Hammon approximation. In addition to the basic theories of solid dielectrics, Walter S. Zaengl has summarized the basic theoretical features of dielectric spectroscopy in both

time and frequency domain for HV power equipment [44] and introduced several applications on power transformers and different types of power cables in his following feature article [2]. New spectroscopic measurement techniques have also been improved to be more sensitive, precise and automatic for low loss dielectric materials [45] [46] [47].

Research on dielectric spectroscopy of XLPE power cables does not have a long history, though studies on various engineering materials including polymers began as early as the application of these kinds of materials. Dielectric spectroscopy can be classified into frequency domain techniques and time domain techniques. As far as the dielectric loss of power cables is concerned, frequency dependent spectroscopy is commonly used and particularly favoured by industrial research, probably because of the commercial availability of frequency response analyzers by GE, Novocontrol and Solartron [48] and other bridge-based high sensitivity instruments for power frequency test such as Schering Bridge. The research group at the Royal Institute of Technology in Sweden, cooperating with ABB Corporate Research, spent several years developing an impedance analyzer based on high voltage dielectric spectroscopy system for XLPE power cables [49] [50] and some direct experimental results up to 100Hz were obtained [51] [52] [53] [54]. General Electric Company is also concerned with the dielectric spectroscopy as a condition assessment for XLPE and PILC (paper insulated lead covered) cables by their frequency domain measuring equipment IDA 200 [55]. Together with SINTEF Energy Research in Norway, ABB Corporate Research finished a joint project on condition assessment of 12kV and 24kV XLPE cables using frequency response analyzer and found that a correlation between the voltage level and breakdown voltage of the cable [56]. Although the frequency range of frequency domain dielectric spectroscopy on XLPE cables and other power equipment is generally below 1kHz,

high frequency range spectroscopy using Fourier transform infrared spectroscopy has also been done by KIM Chonung from 70kHz~10MHz [57]. Because of the nonlinearity of polyethylene material under different levels of AC voltages, which is explained by Jean Crine [58], the frequency domain method has difficulty to detect nonlinear phenomenon, although it is the most popular and widely used technique. Due to the limitation of frequency domain dielectric spectroscopy of linear assumption and indirect DC conduction measurement, time domain dielectric spectroscopy, specifically polarization/depolarization or charging/discharging current measurement technique and return voltage measurement method, is complementary and can provide the same information on the materials [2] [44] [59]. While there exist no commercial instrument of time domain technique due to difficulties in low level measurement precision and proper explanation of acquired information, especially for the low loss polymeric XLPE cables, charging/discharging current measurement has been used as a laboratory research tool. The transient current measurement for water tree detecting in polymeric cables has been studied by Li et al. [60]. The influence of time window size on frequency spectra was theoretically analyzed and charging/discharging currents of LDPE samples are measured. The temperature, pressure and field dependence of anomalous discharging currents in XLPE films have been investigated by Malec et al. [61]. They concluded that the blocking by electrodes and mobility of both charge carriers play an important role in the discharging behaviour of XLPE samples, and the conclusion support the suggestion that the time domain discharging current in polyethylene are caused by the movement of space charge built up during charging time. As time domain dielectric spectroscopy techniques are becoming mature, proposal work of online diagnostic application on XLPE power cables has been done by National Research Council of Canada using depolarization current measurement [62] [63].

Following the continuous efforts of commercialization for time domain spectroscopy, very recently an instrument, AVO Megger S1-5010 with up to 5kV 2% accuracy and 0.1nA detection limit, was used for condition assessment of XLPE cables by polarization/depolarization current with 1s interval [64].

Individual dielectric spectroscopy technique in either frequency or time domain is no longer sufficient to reveal the status of cable insulation, hence more and more researchers in recent years are studying both time and frequency domain spectroscopy [59] [65]. Correlations and combination of the different techniques on critical materials such as polyethylene and epoxy or insulation systems such as transformers' oil-paper insulation and rotating machine's stator bars have already yielded valuable knowledge on condition assessment, diagnostics and development of power equipments [66] [67] [68] [69] [70] [71], among which XLPE cables attract many researchers [72] [73] [74]. Thanks to the persistent efforts of all dielectric scientists, the measurement techniques on power equipment are being improved and understanding of solid polymeric materials of practical importance is gradually being gained, although there are still difficulties and challenges, especially for very low loss materials and insulation systems of typically XLPE cables.

## 2.2 Dielectric properties of insulation materials

### 2.2.1 Polarization of dielectric materials

When a uniform static electric field  $E$  is applied on a plate capacitor with vacuum medium between the electrodes, according to Coulomb's law,

$$Q = \epsilon_0 E \quad \text{Equation 2-1}$$

where  $\epsilon_0$  is the free space permittivity with the value  $8.85 \times 10^{-12}$  F/m. The capacitance of the vacuum plate capacitor

$$C_0 = \frac{Q}{V} \quad \text{Equation 2-2}$$

If a dielectric material is inserted between the electrodes, as shown in Figure 2.1 with solid line connection of DC voltage application, the material will respond to the applied electric field by redistributing its component charges to some extent. Positive charges will be attracted towards the negative electrode and vice versa. This effect is called polarization of the material [75].

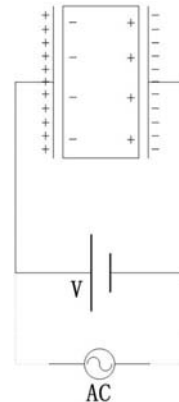


Figure 2.1 Polarization of dielectric material between plate electrodes

If the material is isotropic, certain amount of dipoles will be produced, aligning in the field direction inside the material. Thus, the polarization  $P$  is defined as a vector quantity of the magnitude and direction of the electric moment per unit volume in the material by the applied field. The polarization with bound charges makes more charge stored on the electrodes and, therefore, the capacitance after inserting the dielectric medium is increased. The ratio of the increased capacitance  $C$  to the vacuum

capacitance  $C_0$  used to be called dielectric constant and now is more scientifically named as real part relative permittivity  $\epsilon'$ ,

$$\epsilon' = \frac{C}{C_0} = \frac{Q+P}{Q} = \frac{\epsilon_0 E + P}{\epsilon_0 E} = 1 + \frac{P}{\epsilon_0 E} = 1 + \chi \quad \text{Equation 2-3}$$

where  $\chi$  is the susceptibility of the material.  $\epsilon'$  describes the ability of polarization that occurs in the material and is an important property of dielectric materials, depending on the frequency of the field applied, humidity, temperature.

In electromagnetism, the electric displacement field  $D$  represents how an electric field  $E$  influences the organization of electrical charges in a given medium, including charge migration and electric dipole reorientation. With the above Equation 2-3 the electric displacement  $D$  in the material can be rearranged as

$$D = \epsilon_0 \epsilon' E = \epsilon_0 E + P \quad \text{Equation 2-4}$$

This is the fundamental electric field equation that applies at any point in an isotropic medium.

The maximum polarization, corresponding to the highest observable relative permittivity, will be realised only when sufficient time is allowed after the application of an electric field. The observed permittivity is static permittivity (dielectric constant)  $\epsilon_s$ , if ample time is allowed. On the other hand, if the polarization is measured immediately after the field is applied, allowing no time for dipole orientation, the instantaneous relative permittivity  $\epsilon_\infty$  will be observed. Between these two extremes of time scale there is a dispersion, which could be examined by applying an alternating electric field  $E$  with magnitude  $E_0$  and angular frequency  $\omega$ , across a dielectric

material  $E = E_0 \cos \omega t$ . This will produce polarization, which alternates in direction, and if the frequency is high enough, the orientation of any dipoles will inevitably lag behind the applied field. As shown in Figure 2.2, the lag of polarization can be expressed as a phase lag  $\delta$  in the electric displacement:

$$\begin{aligned} D &= D_0 \cos(\omega t - \delta) \\ &= D_0 \cos(\omega t) \cos \delta + D_0 \sin(\omega t) \sin \delta \end{aligned} \quad \text{Equation 2-5}$$

which leads to the definition of two relative permittivities

$$\varepsilon' = \frac{D_0 \cos \delta}{\varepsilon_0 E_0} \text{ and } \varepsilon'' = \frac{D_0 \sin \delta}{\varepsilon_0 E_0} \quad \text{Equation 2-6}$$

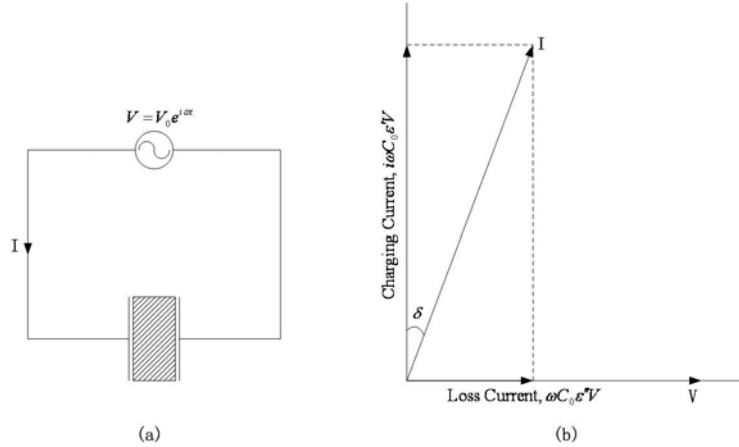


Figure 2.2 AC losses in a dielectric: (a) circuit diagram, (b) Argand diagram of complex current-voltage relationship.

At different frequencies, these two quantities are dependent on the lag angle  $\delta$ , which represents the molecular behaviour for different dielectrics. They are combined into a complex relative permittivity  $\varepsilon^*(\omega)$  for dielectric spectroscopy studies.

$$\varepsilon^*(\omega) = \varepsilon'(\omega) - j\varepsilon''(\omega) \quad \text{Equation 2-7}$$

There are a number of different dielectric polarization mechanisms at the molecular or microscopic level, connected to the way a studied medium reacts to the applied field. Each dielectric mechanism is centred around its characteristic frequency, which is the reciprocal of the characteristic time of the process. In general, dielectric polarization mechanisms can be divided into relaxation and resonance processes. Dielectric relaxation is the momentary delay in the dielectric constant of a material. This is usually caused by the delay in molecular polarization with respect to a changing electric field in a dielectric medium. Dielectric relaxation in changing electric fields could be considered analogous to hysteresis in changing magnetic fields. Relaxation in general is a delay or lag in the response of a linear system, and therefore dielectric relaxation is measured relative to the expected linear steady state (equilibrium) dielectric values.

The most common mechanisms, starting from high frequencies, can be divided into three main categories (shown in Figure 2.3):

- a. Electronic polarization: An electric field will cause a slight displacement of the electrons of any atom with respect to the positive nucleus. The shift is quite small because the applied field is usually quite weak relative to the intra-atomic field at an electron due to the nucleus. Electronic polarization can react to very high frequencies and is responsible for the refraction of light.
- b. Atomic polarization: An electric field can also distort the arrangement of atomic nuclei in a molecule or lattice. The movement of heavy nuclei is more sluggish than that of electrons, so that polarization cannot occur at such high frequencies as electronic polarization, and it is not observed above infra-red frequencies. The magnitude of atomic polarization is quite small, often only one-tenth of that of

electronic polarization, although there are exceptions where a particular mode of bending produces relatively large departure from the normally symmetric arrangements of positive and negative centres within the molecule. In ionic compounds the effect can sometimes be very large.

- c. Orientational polarization: Molecules with permanent dipole moments tend to be aligned by the applied field to give a net polarization in that direction. The rate of dipolar orientation is highly dependent on molecule-molecule interaction. Orientation of molecular dipoles can make a contribution which is large but may be slow to develop to the total polarization of a material in an applied field.

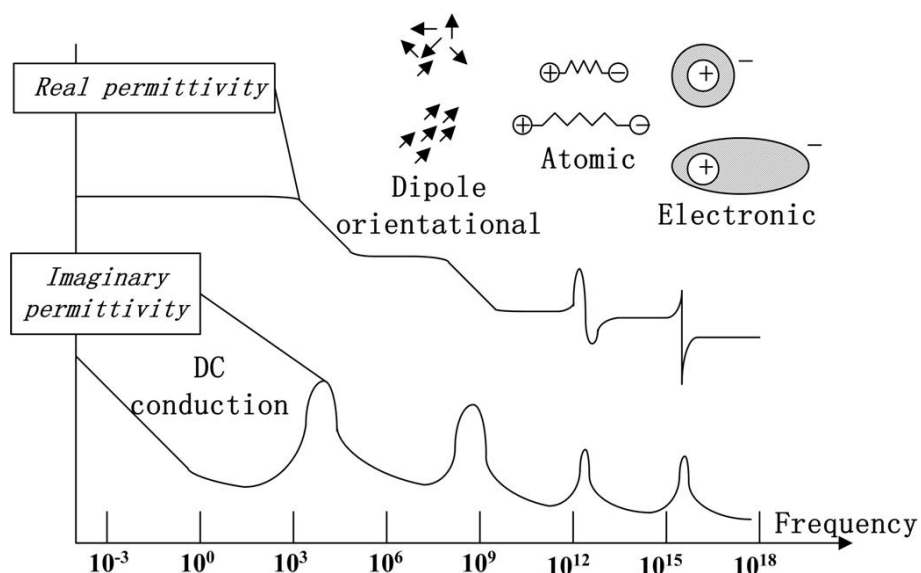


Figure 2.3 Dielectric permittivity spectrum over a wide range of frequencies

- d. Low frequency dispersion: In the low frequency range, multiple dielectric loss behaviour might be present. Conduction mechanism will result in a slope of -1 for the imaginary permittivity, while the real part remains constant when the polarizability of the material is not changed. This is the most common behaviour of dielectric material because any dielectrics have certain amount of

conductivity. If the real and imaginary part permittivities have the same slopes between -1 and 0, quasi-DC mechanism is present representing partially mobile charge carriers gradually moving or hopping to the opposite electrode when the frequency is lower. In this frequency region, Maxwell-Wagner polarization, which is the interfacial effect of different materials, is also observable when the real permittivity has a slope of -2 while the imaginary part has slope of -1.

### 2.2.2 Dielectric loss and conduction in dielectrics

Materials can be classified according to their permittivity and conductivity. Materials with a large amount of loss inhibit the propagation of electromagnetic waves. In this case, generally when  $\frac{\sigma}{\omega\epsilon'} \gg 1$ , we consider the material to be a good conductor.

Dielectrics are associated with lossless or low-loss materials, where  $\frac{\sigma}{\omega\epsilon'} \ll 1$  [76].

Those that do not fall under either limit are considered to be general media. A perfect dielectric is a material that has no conductivity, thus exhibiting only a displacement current. Therefore, it stores and returns electrical energy as if it were an ideal capacitor. In the case of lossy medium, a practical parameter to quantify the loss of a dielectric material is the dielectric loss tangent defined by the ratio of imaginary permittivity and real permittivity,

$$\tan \delta = \frac{\epsilon''}{\epsilon'} \quad \text{Equation 2-8}$$

As shown in Figure 2.2, the current  $I$  which flows in the external circuit after application of an alternating voltage  $V$  can be divided into a capacitive component,

$$I_C = i\omega C_0 \epsilon' V \quad \text{Equation 2-9}$$

which leads the voltage by  $90^\circ$ , and a resistive component,

$$I_R = \omega C_0 \epsilon'' V \quad \text{Equation 2-10}$$

which is in phase with the voltage. Work can only be done by the latter component, and the physical meaning of the  $\tan \delta$  is defined by:

$$\tan \delta = \frac{\epsilon''}{\epsilon'} \propto \frac{\text{energy dissipated/cycle}}{\text{energy/cycle}}. \quad \text{Equation 2-11}$$

$\epsilon''$  here can be called the dielectric loss factor and the dielectric loss tangent  $\tan \delta$  is usually called dissipation factor.

From the above deduction, the energy loss of an ideal capacitor results from the AC conductivity, whose difference to DC conduction should be emphasised. The AC conductivity signifies the movement of fixed charges between specific sites and actually by various types of polarization behaviour in molecular explanation. DC conductivity, however, involves the movement of free charges at a steady velocity and is due to any freely moving charge carriers such as free electrons or ions. It is not possible for any instrument to distinguish between these two types of conductivity, and in order to do this task interpretive skills are required during data analysis. When a DC conductance is present within a dielectric system, the DC response will be seen in addition to the AC conductivity. DC conductance is frequency independent, as it is equivalent to a resistor being present in parallel to the dielectric, with the results that the loss slope will be -1 as shown in Figure 2.3. Thus the measured dielectric loss tangent should be practically:

$$\tan \delta = \frac{\epsilon'' + \frac{\sigma_{DC}}{\omega \epsilon_0}}{\epsilon'} \quad \text{Equation 2-12}$$

including both polarization loss under AC field and direct current conduction existing at any frequencies.

Besides these two distinct types of conduction, another typical two types of dielectric phenomenon are also common, especially in polymeric solid materials, which are the primary interests of this research study. The charge hopping mechanism described by Dissado-Hill [77] [78] and Jonscher [9] [79] will also contribute to the measured conductivity in a dielectric system. This charge hopping conduction, either called low frequency dispersion (LFD) or quasi-DC (QDC), originates from the presence of partially mobile charge carriers in the material. It is comparatively easy to distinguish this response from the above two, as charge hopping is characterised by a corresponding increase in the real part capacitance as introduced previously. Another interfacial effect of the dielectric materials that have discontinuity has also been found and studied, firstly by Maxwell and Wagner. The two phase dielectric system has a different frequency response, which will be discussed in details later, contributing to the system energy loss with space charge build-up in the specimen. The Maxwell-Wagner polarisation is expected at the low frequency range and can shift to quite low frequencies, if the permittivity of the additive is reduced [80].

This can be concluded as three main types:

- a. The polarization current characterises the adjustment of the polarizing species to a step function field and it must go to zero at infinitely long times. No charges may leave the dielectric system or enter it from the outside as a result of this process.

- b. The steady conduction current, or direct current arises from continuous movement of free charges across the dielectric material from one electrode to the other. This current does not change the bonded charge distribution in the system.
- c. At low frequencies, QDC of restricted charge carrier conduction and Maxwell-Wagner mechanism of interfacial polarization will contribute to the dielectric loss and conduction in polymeric materials which have complex composition of different molecular species and combination of different molecules.

### 2.2.3 The Debye model of dielectric relaxation and its modifications

For a unitary substance, there are several empirical equations to describe the dielectric relaxation behaviour, based on solid fundamental work by Debye who pioneered the basic theory of dielectric relaxation behaviour, beginning of a macroscopic treatment of frequency dependence. This treatment rests on two essential premises: exponential approach to equilibrium and the applicability of the superposition principle. Debye relaxation is the dielectric relaxation response of an ideal, non-interacting population of dipoles to an alternating external electric field. It is usually expressed in the complex permittivity  $\epsilon^*$  of a medium as a function of the field's frequency  $\omega$  [81] [82]:

$$\epsilon^*(\omega) = \epsilon_\infty + \frac{\Delta\epsilon}{1 + i\omega\tau} \quad \text{Equation 2-13}$$

where  $\epsilon_\infty$  is the permittivity at the high frequency limit,  $\Delta\epsilon = \epsilon_s - \epsilon_\infty$  where  $\epsilon_s$  is the static, low frequency permittivity, and  $\tau$  is the characteristic relaxation time of the medium.

Havriliak-Negami relaxation is an empirical modification of the Debye relaxation model, accounting for the asymmetry and broadness of the dielectric dispersion curve. The model was first used to describe the dielectric relaxation of some polymers, by adding two exponential parameters to the Debye equation [83] [84]:

$$\varepsilon^*(\omega) = \varepsilon_\infty + \frac{\Delta\varepsilon}{(1 + (i\omega\tau)^\alpha)^\beta} \quad \text{Equation 2-14}$$

The exponents  $\alpha$  and  $\beta$  describe the asymmetry and broadness of the corresponding spectra. Illustration and comparison of different dielectric relaxation models is shown in Figure 2.4.

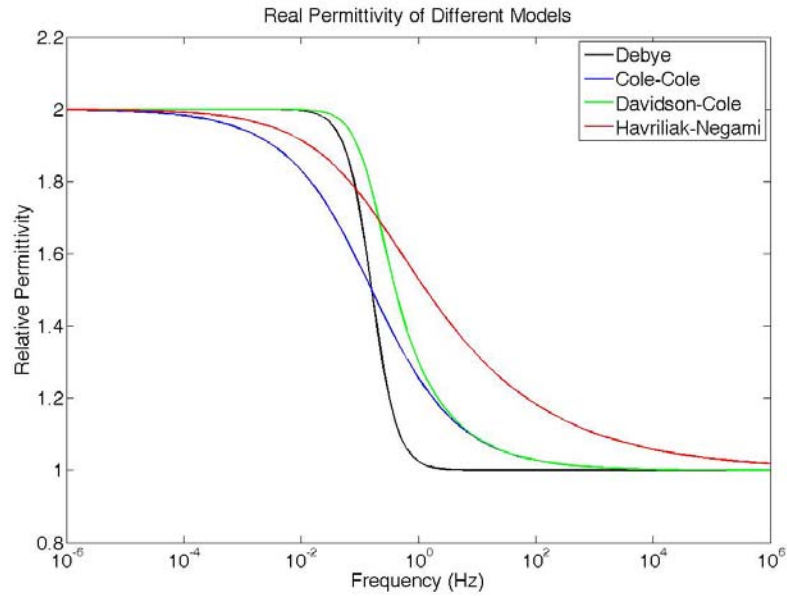
The Cole-Cole equation is a dielectric relaxation model that constitutes a special case of Havriliak-Negami relaxation when the symmetry parameter ( $\beta$ ) is equal to 1 - that is, when the relaxation peaks are symmetric [85]:

$$\varepsilon^*(\omega) = \varepsilon_\infty + \frac{\Delta\varepsilon}{1 + (i\omega\tau)^\alpha} \quad \text{Equation 2-15}$$

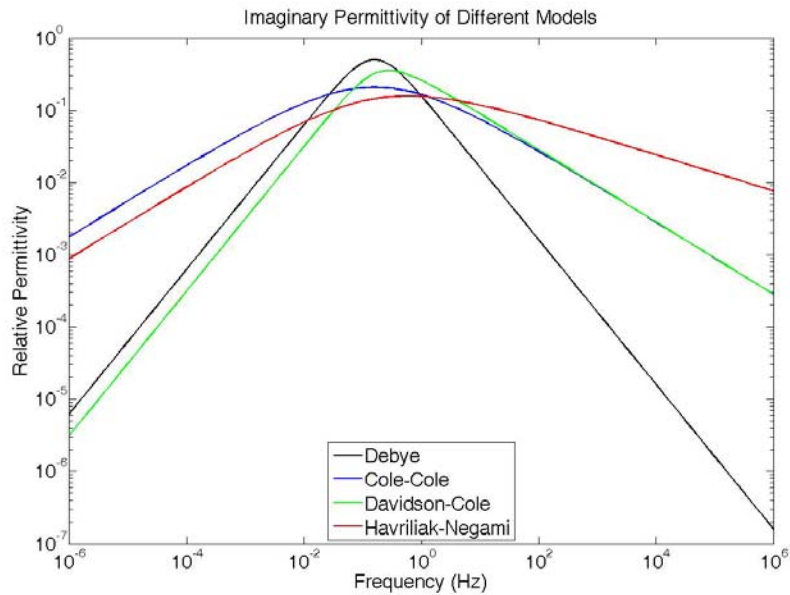
Most polymers show dielectric relaxation patterns that can be accurately modeled by this equation.

Davidson-Cole model is another model that is a special case of Havriliak-Negami relaxation, where the broadness parameter  $\alpha=1$ . It improved the fit with experiment by using a slightly different semi-empirical equation [86]:

$$\varepsilon^*(\omega) = \varepsilon_\infty + \frac{\Delta\varepsilon}{(1 + i\omega\tau)^\beta} \quad \text{Equation 2-16}$$



(a) Real permittivity of different models



(a) Imaginary permittivity of different models

Figure 2.4 Illustration of complex permittivity for different models

$$(\varepsilon_{\infty} = \Delta\varepsilon = \tau = 1, \alpha = \beta = 0.5)$$

This equation corresponds to a skewed distribution of relaxation times about  $\tau$ , but still has no particular theoretical foundation apart from the improved agreement with experiment for certain materials.

For the relaxation models of multiple dielectric materials, such as impurity effect or interfacial effect between the electrode and the dielectrics, more consideration and modifications may be needed. While the mathematical models can present the relaxation spectra fairly well, consideration of interfacial polarisation is also very important to be aware of because this can give totally misleading results if they are not recognised or avoided. In practice, a material is always likely to have regions of non-uniformity, and impurities may be present as a second phase. Effects on dielectric properties attributable to material discontinuities are usually called Maxwell-Wagner effects. Based on the work of Maxwell and Wagner, taking the model where the impurity (relative permittivity  $\epsilon_2'$ , conductivity  $\sigma_2$ ) exists as a sparse distribution of small spheres (volume fraction  $f$ ) in the dielectric matrix (relative permittivity  $\epsilon_1'$ , negligible conductivity), the equations of the complex relative permittivity of the composite are [75]:

$$\epsilon' = \epsilon_\infty' \left(1 + \frac{k}{1 + \omega^2 \tau^2}\right) \text{ and } \epsilon'' = \frac{\epsilon_\infty' k \omega \tau}{1 + \omega^2 \tau^2} \quad \text{Equation 2-17}$$

$$\text{where } \epsilon_\infty' = \epsilon_1' \left[1 + \frac{3f(\epsilon_2' - \epsilon_1')}{2\epsilon_1' + \epsilon_2'}\right], \quad k = \frac{9f\epsilon_1'}{2\epsilon_1' + \epsilon_2'}, \quad \text{and } \tau = \frac{\epsilon_0(2\epsilon_1' + \epsilon_2')}{\sigma_2}$$

Complications also often arise at electrode where contact with the specimen may be incomplete and where entities like discharged ions may form spurious boundary layers. For a purely capacitive impedance  $C_e$  at the electrode, in series with the specimen

proper (geometrical capacitance  $C_0$ ), Johnson and Cole showed that the apparent relative permittivity takes the approximate form [75]:

$$\epsilon_{app}' = \epsilon' + \frac{\sigma^2 C_0}{\omega^2 \epsilon_0^2 C_e}, \quad \text{Equation 2-18}$$

where  $\epsilon'$  and  $\sigma$  are the true (frequency-independent) relative permittivity and conductivity of the material of the specimen.

#### 2.2.4 Equivalent circuit analysis

Dielectric materials can be treated as lossy capacitances. Therefore an equivalent circuit can be used to study the spectroscopy of dielectrics. The simplest equivalent circuit for a dielectric material are series or parallel RC circuits, as shown in cases (a) and (b) of Table 2.1. The complex permittivity, which is proportional to the complex capacitance by the factor of the geometric capacitance, can be calculated from the relationship

$$Y^* = \frac{1}{Z^*} = j\omega C^* = j\omega C_0 \epsilon^* \quad \text{Equation 2-19}$$

where  $Y^*$  and  $Z^*$  are the admittance and impedance of the whole circuit;  $C^*$  is the complex capacitance and is proportional to  $\epsilon^*$  by the geometric capacitance  $C_0$ .

Case (a) represents a “leaky” capacitive material with finite resistance. This resistance will induce dielectric loss that is reciprocal to frequency with slope of -1 in logarithm plot, while the real permittivity remains constant. The real and imaginary permittivity can be calculated as

$$\epsilon' = \frac{C}{C_0} \quad \text{and} \quad \epsilon'' = \frac{G}{\omega C_0} \quad \text{Equation 2-20}$$

where G is the conductance. The dimensionless dielectric property loss tangent

$$\tan \delta = \frac{G}{\omega C} = \frac{1}{\omega RC} \quad \text{Equation 2-21}$$

Case (b) can represent a pure Debye peak as in a dielectric material. It can also describe a system where a barrier region is present and adjacent to a bulk conducting or semiconducting layer. There is a loss peak in this case at the frequency  $f_p$  that can be calculated from the circuit components by equation

$$\tau = RC = 2\pi f_p \quad \text{Equation 2-22}$$

where  $\tau$  is the time constant of the RC circuit. The real and imaginary permittivity can be calculated as

$$\epsilon' = \frac{1}{1 + \omega^2 R^2 C^2} \quad \text{Equation 2-23}$$

$$\epsilon'' = \frac{\omega RC}{1 + \omega^2 R^2 C^2} \quad \text{Equation 2-24}$$

where G is the conductance. The loss tangent in this case

$$\tan \delta = \omega RC \quad \text{Equation 2-25}$$

More complicated circuit combinations can better help study the dielectric response of real materials, which have multiple relaxation processes. Combinations of series and parallel circuit have the significance of phenomenological interpretation for the physical response of individual processes. In case (c), the parallel frequency-independent capacitance  $C_{\text{inf}}$  or  $C_{\infty}$ , corresponds to any physical process without dispersion in the frequency range of interest. This may be the free space capacitance with instant

polarization at extremely high frequencies. In the graph of complex permittivity, the imaginary part is exactly the same as series RC circuit because  $C_\infty$  does not affect the loss arising from the Debye peak combination. On the other hand, the real permittivity has an offset which is due to  $C_\infty$  at higher frequencies. This circuit model can exactly represent the Debye relaxation response of dielectric materials. The complex admittance

$$Y^* = j\omega C_\infty + \frac{1}{R + \frac{1}{j\omega C}} \quad \text{Equation 2-26}$$

Combined with Equation 2-19,

$$\epsilon' = \epsilon_\infty + \frac{\epsilon_s - \epsilon_\infty}{1 + \omega^2 R^2 C^2} \quad \text{Equation 2-27}$$

$$\epsilon'' = \frac{\epsilon_s - \epsilon_\infty}{1 + \omega^2 R^2 C^2} \cdot \omega RC \quad \text{Equation 2-28}$$

where  $\epsilon_\infty = \frac{C_\infty}{C_0}$  and  $\epsilon_s - \epsilon_\infty = \Delta\epsilon = \frac{C}{C_0}$ . When the dielectric relaxation time is equal to

the RC circuit time constant  $\tau = RC$ , the above equations are the same as Debye equation:

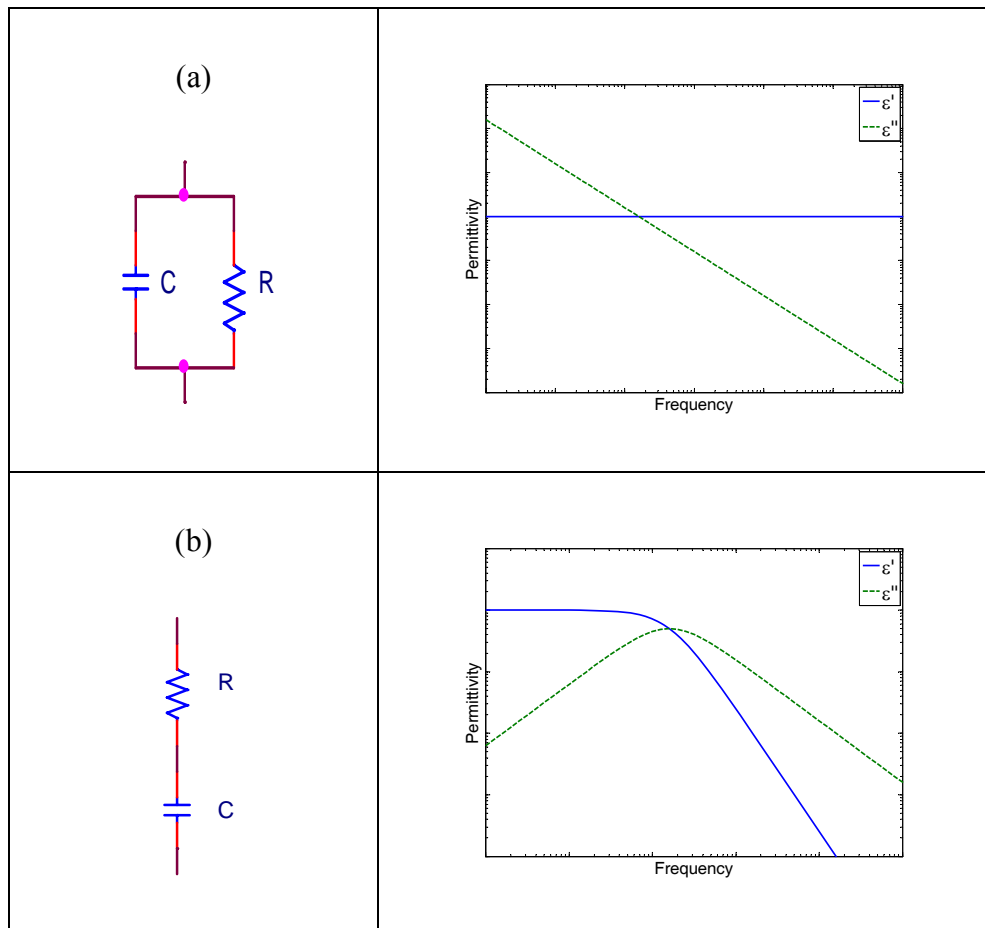
$$\epsilon' = \epsilon_\infty + \frac{\epsilon_s - \epsilon_\infty}{1 + \omega^2 \tau^2} \quad \text{and} \quad \epsilon'' = \frac{\epsilon_s - \epsilon_\infty}{1 + \omega^2 \tau^2} \cdot \omega \tau \quad \text{Equation 2-29}$$

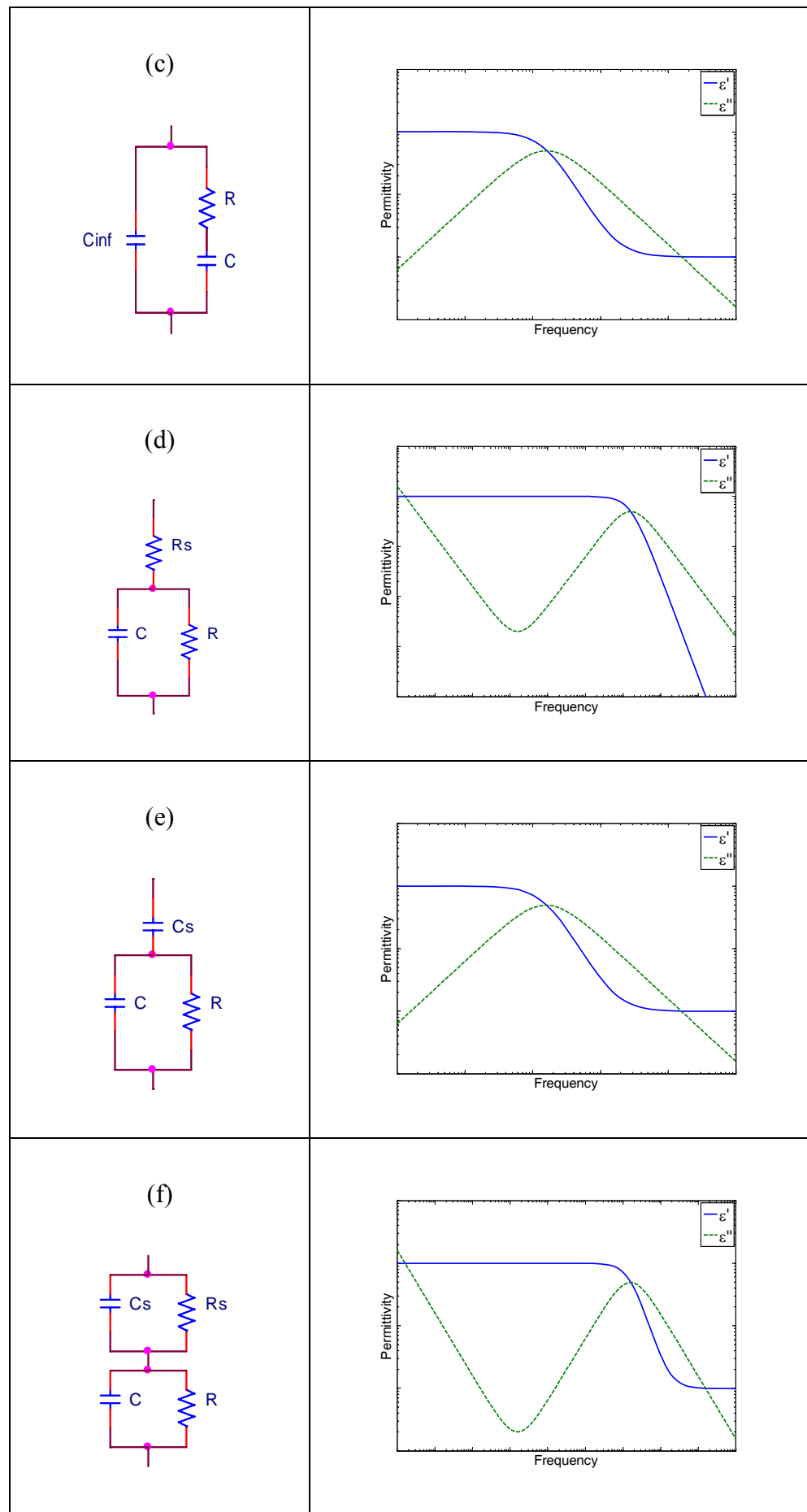
Therefore a Debye relaxation can be well represented by this equivalent circuit.

In Table 2.1, case (d) is a very common situation in which an insulation with some conductance across it is placed in series with a bulk conducting region of resistance  $R_s$ ; case (e) represents another physically often occurring situation in which the bulk region characterized by the parallel DC conductance and capacitance is bordered by a “barrier”

region in which the dominant element is the capacitance  $C_s$ ; case (f) is a generalization of the circuit to cover the possible existence of two different regions, each characterized by a DC conductance and a capacitance. Lumped circuits are well suited to represent a wide range of physical situations and their understanding is basic to the interpretation of most dielectric data. However, in some cases, distributed circuit networks are also widely used to study more complex cases by more precisely describing the structure of the tested dielectric materials. With modern technology, it is possible to simulate the distributed circuit networks.

Table 2.1 Schematic representations of complex permittivity for different equivalent circuits (data replicated in courtesy of Jonscher [8])





## 2.3 Cable insulation materials

### 2.3.1 Materials of cable insulation layer

As critical power equipment, polymeric cables have been in intensive interest for researchers all over the world for more than a century. The most commonly used polymer cable insulation materials are cross-linked polyethylene (XLPE) and ethylene propylene rubber (EPR).

Polyethylene is a thermoplastic polymeric materials. It is heavily used in consumer products and over 60 million tons of the materials are produced worldwide every year. Polyethylene is produced from ethylene gas. The polymerization of polyethylene is progressing when the double C=C bond is opened and form saturated bonds with other ethylene groups (shown in Figure 2.5). Polyethylene became very popular as power cable insulation when it was firstly introduced in 1960s, thanks to its low cost, better electrical properties compared to paper-oil insulation, processability, moisture and chemical resistance, and low temperature flexibility [27]. There are several types of PE, usually classified according to their density into low (LDPE), medium (MDPE), and high-density (HDPE) PE. LDPE is most commonly used in power cables, because it has a low relative permittivity of about 2.3 and very low dielectric loss tangent due to the absence of any permanent dipolar groups. The operating temperature of LDPE is restricted to 70°C because of its thermoplastic nature and it starts to soften at 80-90°C and melts at 110-115°C [87]. However, the operating temperature can be increased by cross-linking LDPE into a thermosetting polymer – XLPE.

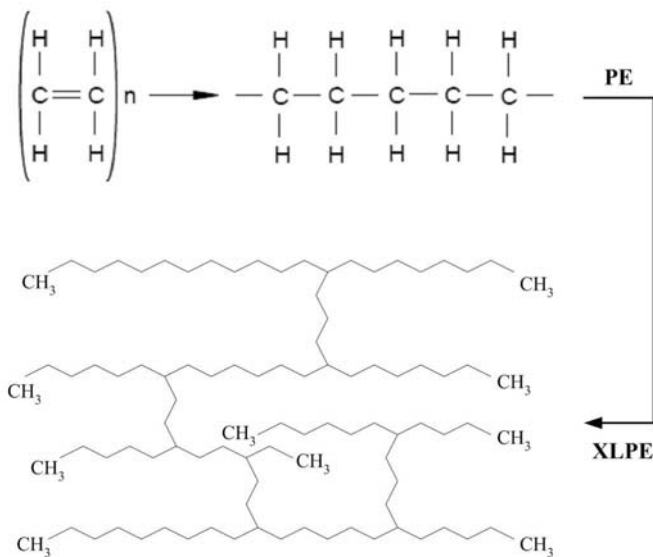


Figure 2.5 Polymerization of polyethylene and cross-linking of XLPE

By cross-linking PE process, the mechanical and thermal properties are improved, reaching a rated maximum conductor temperature of 90°C and a short circuit rating of 250°C, while the electrical properties remain more or less unchanged. There are several methods for the cross-linking of PE. Peroxide and silane cross-linking are used for power cable applications with the peroxide method being the most common. The cross-linking of LDPE with DiCumylPeroxide (DCP) to form XLPE was first accomplished by Gilbert and Precopio in 1955 at the GE Research Laboratory located in Niskayuna, NY [88]. In the peroxide method, curing agent DCP is added to the polymer compound and is activated right after the extrusion in a special curing tube at high temperature and high pressure. The long chain molecules become linked during the curing or vulcanizing process, as shown in Figure 2.5. Steam was previously used for achieving both pressure and heat, and therefore often referred to as “steam curing”. However “dry-curing” method became more popular when it has been shown that the use of steam causes high water concentrations and void formation in the product. In the “dry-curing” method, the insulation is pressurised by nitrogen gas and heated by radiation from the electrically-

heated curing tube. The cooling process in the dry-curing method is normally performed by using water [89].

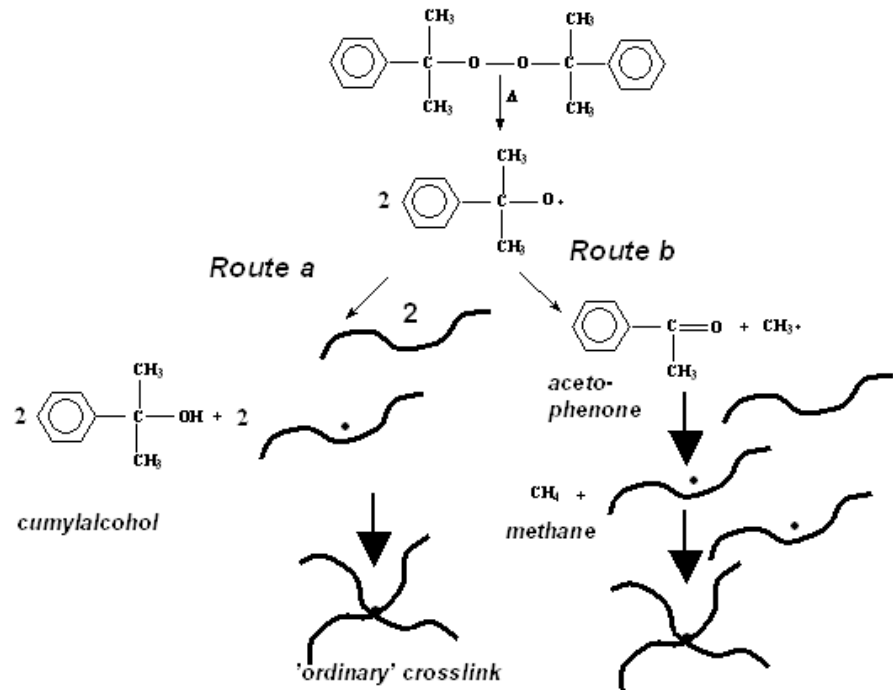
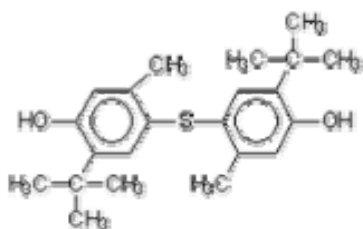


Figure 2.6 Peroxide initiated cross-linking of PE

When peroxide is used as a cross-linking agent for XLPE production, polar by-products are produced during the cross-linking process. The schematic explanation of DCP decomposition during the crosslink reaction is explained in Figure 2.6. During the cross-linking process, one -O-O- bond (generally one per peroxide molecule) can create one chemical crosslink in the chain network. Whether it provides a crosslink or not, there are two routes for every decomposed molecule of peroxide, giving out a multitude of by-product molecules [90], especially cumylalcohol, acetophenone and methane. These volatile by-products are contained within the structure and would form potentially harmful voids [27]. More importantly, the dielectric loss may be greatly increased due to the -OH or =O polar groups under alternating field in operation. The

exact proportion of the by-products will depend upon the exact proportions of different routes in Figure 2.6 and the time and temperature control in this procedure is of vital importance. Degassing of the cables is normally carried out in order to reduce the methane that might cause problems during cable installation and operation. Degassing effects on dielectric loss of XLPE power cables will be investigated in this research study. The insulation of the model power cables in this work are crosslinked with DCP. Santonox R type antioxidant, as shown below, is also added into the cable insulation.

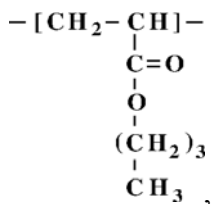


### 2.3.2 Materials of semiconducting layer

Research on semicon cable shields has been playing an important role in the development of electric power cables. In power cables nowadays, semiconducting materials have been an essential part of cable production, because they are used for:

- a. preventing partial discharge at the interfaces between the insulation and conductor and between the insulation and external shielding layer;
- b. moderating the electrical stress in the insulation layer by providing a uniform electric field around the cable insulation with reduced potential gradient;
- c. providing protection during short-circuit against damages caused by the heating of the conductor.

In power cables, conducting carbon black (CB)-filled ethylene copolymers, such as ethylene-butyl acrylate, ethylene vinyl acetate and ethylene ethyl acrylate, are commonly used as a semiconducting layer [3]. Different kinds of cables should have different suitable shields. Shields that are designed for use with XLPE dielectric are often not suitable for use with EPR dielectric, and vice versa. Likewise, the appropriate shield also depends on the configuration of the extrusion line on which the cable is manufactured [23]. In this research project specifically the semiconductor screen used is an ethylene-butyl acrylate copolymer



containing carbon black, antioxidant for protection against thermo-oxidative degradation and a peroxide for crosslinking. The antioxidant in semicon layer is different from that in insulation layer and gives good protection against degradation due to heat and oxygen [91]. The ethylene-butyl acrylate is also used for co-polymer insulation layer fillers in the form of micro size islands. Factors such as CB content, mixing quality and temperature that affects CB network development, affect the properties of CB filled semiconductors. Based on previous research studies, increasing CB loading and process temperature can decrease the volume resistivity, which usually vary between 10 and 100  $\Omega \text{ cm}$  and should not exceed  $10^4 \Omega \text{cm}$  [92] [93].

The dielectric strength of the insulation depends on the volume resistivity of the semicon material, which plays important role in smoothing the electric field distribution of insulation-semicon boundaries. As other factors—such as polarity, type, and amount

of cross-linking of semicon material—have a combined effect on the dielectric strength. Impurities in the semicon layers can cause partial discharge and greatly increase the possibility of water treeing. Therefore, the dielectric loss of XLPE power cables should include the contribution of semicon materials, as mentioned in former context that Dow Company has already realized this source of dielectric loss with some loss tangent test [24]. The conductivity of semicon materials and their charge injection into insulation layer may increase the bulk conductivity of cable insulation system, while the semicon layer in series with the insulation may greatly increase the dielectric loss of cables at higher frequencies. The studying of electrical properties on XLPE cables must include the influence of semicon shields, because they are main part of the insulation system.

### 2.3.3 Degradation and breakdown of XLPE cable insulation

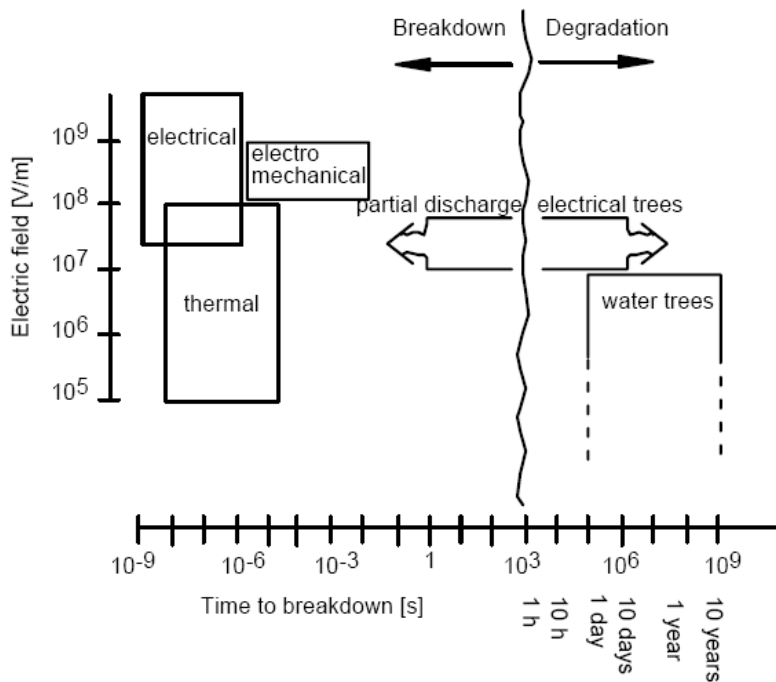


Figure 2.7 Various breakdown mechanisms with the times and electric fields [12]

Degradation and breakdown phenomena in polymerised insulating materials are closely related to the loss mechanism studying but have been extensively studied for several

years. Many empirical correlations have been found in these phenomena, but the basic understanding of the various physical phenomena involved is still the subject of ongoing research. There is not a clear distinction between breakdown and degradation, as illustrated in Figure 2.7. Especially degradation by partial discharges and electric-tree growth could also be referred to breakdown phenomena.

Degradation mechanisms in PE can be divided into physical ageing, chemical ageing, electrical ageing, and combined mechanical and electrical ageing mechanisms. Physical ageing (structural relaxation) means those physical changes occurring in the material over time, which lower entropy or free volume. Other types of physical degradation include for example the diffusion of additives or absorption of foreign solvents causing swelling. The rate of these processes increases with increasing temperature. Chemical ageing usually proceeds via the formation of polymeric free radicals. Free radicals are very reactive chemically and lead to propagating chain scission or cross-linking network formation via chain reactions. For XLPE, the chain scission sequence is random in space with free-radical transfer between chains. The initiation step leading to this ageing may be internal-thermal or oxidative factors, or UV absorption, ionising radiation or mechanical factors. Internal-thermal factors include chemical reactions taking place within the material without interaction with the surroundings. Both cross-linking and depolymerisation can occur when energy in the form of for instance heat or radiation is put in. Depolymerisation is essentially the reverse of chain polymerisation, breaking chemical bonds causing scissions. Oxidation caused by heat and oxygen is one of the most important forms of chemical degradation. The oxidation process involves free radical chain formation, and several ways of forming peroxide radicals are possible. The peroxide radicals then attack the C-H bonds, causing bond scissions. Thermal oxidation is autocatalytic (a self-accelerating process) causing large changes in mechanical and

electrical properties. The autoxidation will continue until some termination reaction occurs. Additives in the form of antioxidants are normally used to break this accelerating process. PE is sensitive to ultraviolet light and radiation that can cause both chain scission and cross-linking [12]. Electrical ageing requires an electrical field. The most common processes are water-tree ageing, electrical-tree ageing and partial-discharge ageing. Water trees are a chemical degradation of polymeric insulation such as XLPE or EPR that only occurs in the presence of water and electrical stress. They can grow throughout the entire insulation thickness without causing instantaneous failure but they weaken the cable electrically and lead to premature failure. Electrical tree inception (initiation) at a region of high electrical stress is followed by the growth of fine channels or small voids driven by partial discharge activity within the defects. Failure of the insulator eventually occurs once the tree channels have grown sufficiently to bridge the electrodes [94].

Table 2.2 Ageing Mechanisms for Power Cables [13]

Ageing Factor	Ageing Mechanisms	Effects
<b>Thermal</b>		
High temperature Temperature cycling	<ul style="list-style-type: none"> <li>-Chemical reaction</li> <li>-Incompatibility of materials</li> <li>-Thermal expansion (radial and axial)</li> <li>-Diffusion</li> <li>-Anneal locked-in mechanical stresses</li> <li>-Melting/low of insulation</li> </ul>	<ul style="list-style-type: none"> <li>-Hardening, softening, loss of mechanical strength, embrittlement</li> <li>-Increase tan delta</li> <li>-Shrinkage, loss of adhesion, separation, delamination at interfaces</li> <li>-Swelling</li> <li>-Loss of liquids, gases</li> <li>-Conductor penetration</li> <li>-Rotation of cable</li> <li>-Formation of soft spots, wrinkles</li> <li>-Increase migration of components</li> </ul>
Low temperature	<ul style="list-style-type: none"> <li>-Cracking</li> <li>-Thermal contraction</li> </ul>	<ul style="list-style-type: none"> <li>-Shrinkage, loss of adhesion, separation, delamination at interfaces</li> <li>-Loss/ingress of liquids, gases</li> <li>-Movement of joints, terminations</li> </ul>

Electrical		
Voltage: ac, dc Impulse	-Partial discharges (PD) -Electrical treeing (ET) -Water treeing (WT) -Dielectric loss and capacitance -Charge injection -Intrinsic breakdown	-Erosion of insulation → ET -PD -Increased losses and ET -Increased temperature, thermal ageing, thermal runaway -Immediate failure
Current	-Overheating	-Increased temperature, thermal ageing, thermal runaway
Mechanical		
Tensile, compressive, shear stresses Fatigue, cyclic bending, vibration	-Yielding of materials -Cracking -Rupture	-Mechanical rupture -Loss of adhesion, separation, delamination at interfaces -Loss/ingress of liquids, gases
Environmental		
Water/humidity Liquids/gases Contamination	-Dielectric losses and capacitance -Electrical tracking -Water treeing -Corrosion	-Increased temperature, thermal ageing, thermal runaway -Increased losses and ET -Flashover
Radiation	-Increase chemical reaction rate	Hardening, softening, loss of mechanical strength, embrittlement
The failure mechanism is usually electrical, e.g., by PD, ET or tracking		

The ageing factors such as impulse voltage, transient current and mechanical tension can cause irreversible changes in the properties of materials in an insulation system. This type of ageing is referred to as intrinsic ageing [95] and may affect a large volume of the insulation. External ageing factors include contaminants, defects, protrusions, or voids (CDPVs) in the materials or at interfaces to cause degradation. While The increased chemical reaction rate at high temperature, often referred to as thermal ageing, is the main ageing mechanism of fluid-filled cable systems [96], The main ageing factor of extruded cable systems is electrical, which include PD, electrical treeing, water treeing and charge injection, occurring at contaminants, defects, protrusions, and voids (CDPV), and thus tend to be localized. Possible ageing mechanisms for power cables are summarized in Table 2.2.

The breakdown mechanisms in PE can be divided into electric, thermal, electromechanical and partial discharge mechanisms. Electric or intrinsic breakdown can occur at very high electrical field strengths (approximately 500 kV/mm for PE). A free electron, accelerated by the field, initiates an electrode avalanche that causes the breakdown. In practice, the high field required for an intrinsic breakdown is never reached. Instead, the breakdown level is determined by imperfections. Thermal breakdown occurs when heat losses in the insulation cannot be balanced by heat transport in the material, usually in some localised area. The heat produced increases the electrical conductivity. Maintaining the electrical stress increases the current density in the area of higher temperature. This leads to further heating and increment in conductivity, and will ultimately cause thermal runaway (thermally-caused breakdown). Electromechanical breakdown can occur due to electrostatic forces attracting the electrodes and thereby decreasing the thickness of the insulation. The decrease in insulation thickness will increase the attraction if the electrical stress is maintained. The situation is made worse by heating and consequently softening of the insulation. However, this breakdown mechanism is unlikely to occur in reality since polymers are seldom used above their softening temperature. Partial discharges occurring in gas-filled voids degrade the insulation, and under certain circumstances can initiate electrical trees. The electrical trees can continue propagating through the insulation by continued discharges and finally give rise to breakdown [12].

## 2.4 Electrical conduction in polymeric materials

There are several conduction mechanisms that can be classified as bulk insulation and electrode injection processes. The theories for pure crystals have been well developed but cannot be directly applied on polymeric materials due to the complexity of the

material parameters such as crystallinity, crosslinking method, and additives [97]. Charge injection from electrodes into the polymer, traps and volumetric conduction, tunnelling and hopping conduction were found to play an important role in conduction and charge transport in polymers. Band theory and quantum mechanics for crystals are popularly transplanted into the explanation of electrical conduction in polymers, with the absence of good foundation for conduction mechanisms of insulators. Hence, the picture of the conducting/insulating properties of PE has to be painted with an increasingly complex palette [98]. Different classical theoretical models are introduced in this section, which would help explain the dielectric loss in later chapters.

#### 2.4.1 Conduction mechanisms of bulk insulation

There has been experimental evidence that the voltage-current relation of some polymers may follow Ohmic law under low fields [99] [12]. This is usually explained in the way that charge carriers including electrons and ions acquire an average velocity proportional to the field. The electrical conductivity, which is dependent on charge concentration and carrier mobility, will therefore have a linear relationship to the electric field  $E$ :

$$J = \sigma E = ne\mu E \quad \text{Equation 2-30}$$

where  $n$  and  $\mu$  are respectively the charge carrier concentration and mobility;  $e$  is the absolute value of electron charge ( $-1.6 \times 10^{-19} \text{ C}$ ). In this simple conduction model, because the average velocity of the charge carriers may be limited by collisions with the lattice at higher temperatures, the conductivity has a negative temperature coefficient. This trap-free Ohmic model was found to be fitted for doped semiconductors but difficult to represent good polymeric insulators. Therefore, another trap-limited Ohmic

conduction model was proposed. Traps in the forbidden band gap can hold activated carriers thereby decreasing their concentration and effectively lowering their mobility.

Except the classic simple Ohmic model, under higher electric field, Space Charge Limited Conduction (SCLC) and the Poole-Frenkel mechanisms are two main conduction mechanisms that may better account for the bulk conduction process in polymers [12]. The theory of SCLC between plane parallel electrodes was first given by Mott and Gurney (1940) and has been extended by several authors including Lampert (1956). The original theory is based on assuming the absence of any trapping effects the current density by the Mott-Gurney Law. The ratio of electrons in the conduction band and in traps  $\theta$  is considered to give a better expression of current density  $J$

$$J = \frac{9}{8} \mu \epsilon_r \epsilon_0 \frac{V^2}{d^3} \theta \quad \text{Equation 2-31}$$

where  $\mu$  is the mobility,  $V$  is the applied voltage and  $d$  is the thickness of the insulator. This equation has been well established by experiments in many substances [100]. Since SCLC is limited by space charge injected from electrodes, the current flowing between the electrodes will then depend on the charge concentration, the type of charge and the mobility of the charge carriers, together with the trapping ability. Figure 2.8 can be used to explain the classical conduction mechanisms. The high electric field conduction is based on the SCLC model with a single trap level. For semi-crystalline insulation materials, curved experimental results (solid curve in Figure 2.8) may be obtained instead of the low field Ohmic conduction. Under very high field when traps are filled, the steep slopes are practically from 3 to 10 rather than infinite.

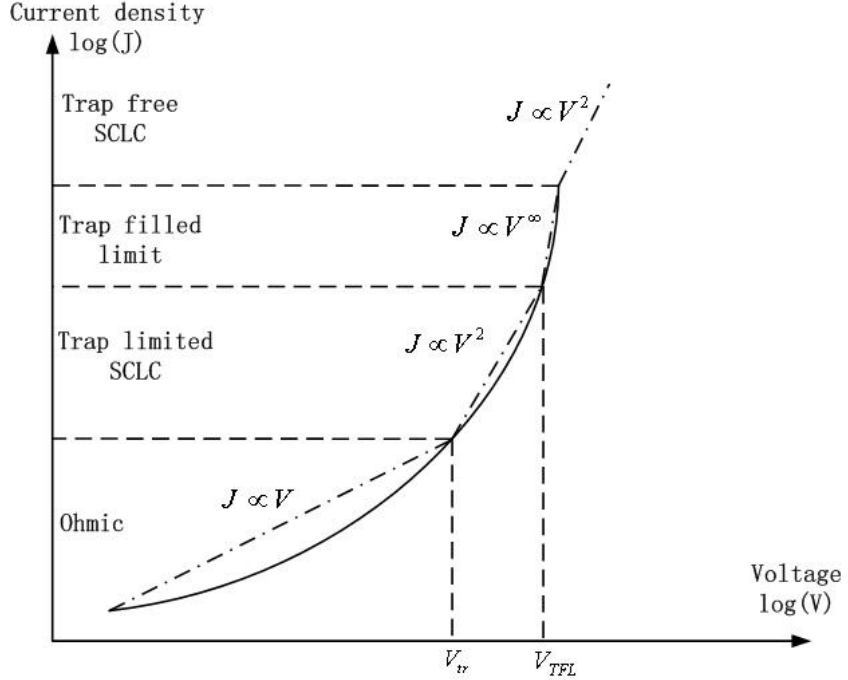


Figure 2.8 Voltage-current density relation based on space charge limited current model [12]. Solid lines are experimental data without obvious transition for different conduction processes

Poole-Frenkel [101] is the bulk equivalent to the Schottky effect and arises from field dependent thermionic emission from traps in the bulk of the insulator. An electron trapped in a donor state is normally surrounded by a potential barrier with height  $\varphi$ . If a donor state is ionised, the Coulombic force between the electron and the donor will modify this energy barrier. With an applied field, the reduction of the barrier becomes proportional to the square root of the applied field. The conduction current strongly depends on the expression of the energy band of the material. The standard quantitative expression of current density  $J$  for the Poole–Frenkel effect is [102]

$$J \propto E \exp\left(\frac{-q(\varphi - \sqrt{qE/\pi\varepsilon})}{k_B T}\right) \quad \text{Equation 2-32}$$

where  $E$  is electric field;  $k_B$  is Boltzmann's constant;  $T$  is temperature;  $\varepsilon$  is permittivity;  $q$  is elementary charge. It can be seen that the Poole-Frenkel effect is strongly related with temperature  $T$ .

Ionic conduction in polymeric dielectrics may also occur with ionized molecules in amorphous regions. It is generally defined as the movement of ions or vacancies through an ionic crystal and considers both the concentration of charge carriers and their mobility as function of temperature. Arrhenius-type relationship is a typical characteristic of ionic conduction and has been frequently observed in polymers. This model also includes the field dependence as [103]

$$J \propto \frac{E}{T} \exp(-E_a/kT) \quad \text{Equation 2-33}$$

where  $E$  is applied field and  $E_a$  is activation energy.

#### 2.4.2 Conduction mechanisms due to electrode charge injection

The electrode-insulator interface is important for controlling the current when charge carriers are injected into insulator. The interface is critical for the injection process, which is complicated by surface roughness, imperfect contact, and chemical impurities such as metal oxide layer. Two electron injection mechanisms form the basis of understanding this problem – Schottky effect and Fowler-Nordheim injection.

The Schottky injection mechanism arises from field assisted thermionic injection of electrons in conduction band from the electrode surface to the bulk insulation and describes how electrons are transferred from electrodes into a dielectric material [97] [102] [104] [105]. At an electrode-insulator interface, electrons overcome the potential barrier, leave the metal electrode and move to the adjacent insulation material. The

barrier is assumed to be abrupt between the metal and the insulator. In Schottky injection, the barrier is modified by the electrostatic attraction between the positively charged electrodes, since it has lost an electron. This electrostatic attraction leads to a change in the barrier due to the electron potential energy. The current density,  $J$ , can be obtained by the following equation,

$$J = AT^2 \exp\left(-\frac{E_a - \beta_s \sqrt{E}}{kT}\right) \quad (\beta_s = \sqrt{\frac{e^3}{4\pi\epsilon_0\epsilon_r}}) \quad \text{Equation 2-34}$$

where  $A$  is the Richard-Dushman constant ( $A = 1.2 \times 10^6 \text{ A}/(\text{m}^2\text{K})$ ),  $E_a$  is activation energy and  $E$  is the applied electrical field at the electrode interface.

Fowler-Nordheim injection is also called quantum tunnel injection, when charge carriers are injected between an electric conductor and a thin layer of an electric insulator [106] [107] [108]. At high fields and short distances the potential barrier becomes very thin and no classical mechanisms come into existence. Classical physics is no longer valid in this situation. Particles exhibit particle-wave duality and the principle of uncertainty comes into play. This will lead to electrons tunnelling through a potential energy barrier despite not having enough energy to hop over them. Also electrons will have a finite probability of existing at two different localised states. Fowler-Nordheim injection usually occurs at the contact barrier. It is noted Fowler-Nordheim injection is unlikely to occur through a polymer film or even a cable's insulation layer in this study. The insulator would probably have to be less than 40 nm thick. It may occur at a film-electrode boundary under high enough fields, through an oxide layer on a metal electrode, or perhaps even at the surface of a nano-particle [109].

## 2.5 Dielectric spectroscopy techniques

Dielectric spectroscopy measures the dielectric properties of a medium as a function of frequency. It is based on the interaction of an external field with the electric dipole moment of the sample, often expressed by permittivity [12]. Various dielectric spectroscopy techniques have been developed and improved to meet the more and more critical measurement requirement, such as dielectric loss measurement on low loss polymeric materials. According to their principles, dielectric spectroscopy techniques can be classified into frequency domain techniques and time domain techniques. Combination of various techniques in both domains is often utilized to study the whole frequency range of interest with their most accurate capabilities. The summary of dielectric spectroscopy techniques in their most accurate frequency range is shown in Figure 2.9. While time domain spectrometer is specialized in lowest frequency range, AC bridges and frequency response analyzers are complementary at relatively higher frequencies. The other techniques in green are techniques high frequency that are beyond the frequency range of interest in this research study on solid polymer materials and will not be discussed here.

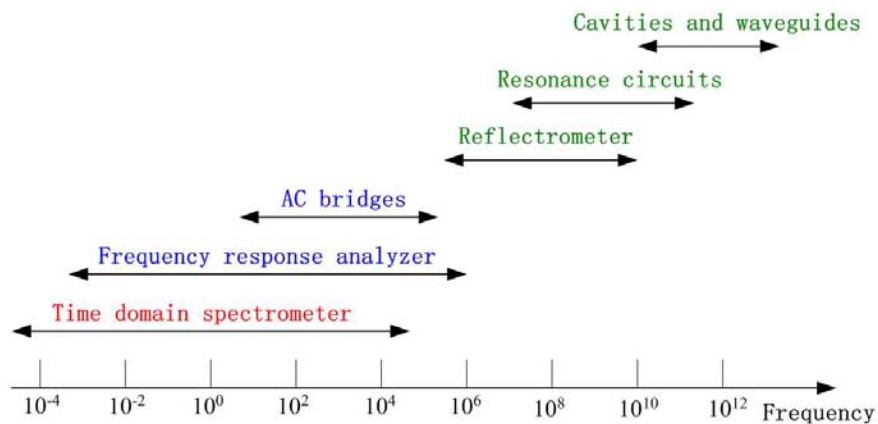


Figure 2.9 Summary of dielectric spectroscopy techniques

### 2.5.1 Time domain dielectric spectroscopy

The dielectric response in a static electric field provides the basic knowledge and represents very limited facet. Much more important experimentally, technologically and theoretically, is the time-dependent response to time-varying electric fields [8]. The most obvious physical reason for the time domain dielectric spectroscopy is the inevitable “inertia” for all physical process. Whether this inertia is due to mechanical inertia of the masses that have to be transferred from one position of orientation to another, or whether it is the outcome of more general rate processes, the net result is that the time dependent polarisation  $P(t)$  is not the same function as the time dependent driving field  $E(t)$ . The resulting current flowing in the system after application of a step DC voltage is therefore:

$$\begin{aligned} i_c(t) &= dD(t)/dt + \sigma_0 E_0 \\ &= \epsilon_0 dE_0 / dt + dP(t) / dt + \sigma_0 E_0 \\ &= \epsilon_0 E_0 \{\delta(t) + f(t)\} + \sigma_0 E_0 \end{aligned} \quad \text{Equation 2-35}$$

where  $\delta(t)$  is the delta function,  $f(t)$  is artificially defined as dielectric response function in order to study time dependence response on a mathematical basis and to characterise different material properties under different electrical excitations. The delta function in Equation 2-35 is due to the instantaneous response of the part of the total charge which is due to the step function electric field itself, in other words, it represents the free space response contained in the volume of the dielectric material. The polarisation  $P(t)$ , by contrast, arises from the response of the material medium, and it cannot follow the step field. The time domain response function of the dielectric material under investigation is  $f(t)$  which could be seen as the time dependent

polarising current. The term  $\sigma_0 E_0$  represents any direct current conductivity  $\sigma_0$  of the system [8].

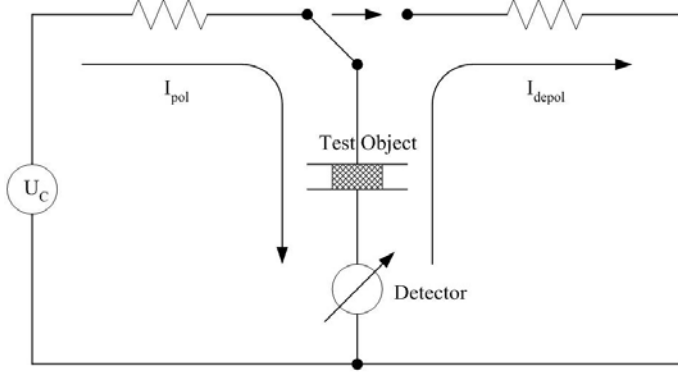


Figure 2.10 Circuit diagram of charging/discharging current technique [75]

Time domain dielectric spectroscopy techniques are normally preferred on the low frequency side of the dielectric spectrum ( $<10\text{Hz}$ ) but lots of research work has been done to increase the upper frequency limit recently. Charging/discharging or polarization/depolarization current measurement method is the most widely used technique for time domain dielectric spectroscopy, because both of polarization/depolarization and conduction phenomenon can be recorded with this technique while sudden application of a steady voltage across a dielectric material will produce a transient charging current whose form depends on the rate at which equilibrium polarization is attained in the dielectric. Figure 2.10 shows the circuit diagram of a typical charging/discharging current measurement system. When the switch is connected to the power supply, the voltage will be suddenly applied on the test object and the charging/polarization current recorded by a current detector. After the sample is charged for some time, generally 10 times of the discharging time, the switch can be used to make the sample grounded when the inverted discharging/depolarization

current can be measured. Two protective resistors are usually used to protect the current detector and power supply if breakdown occurs in the sample, but they will bring influence since a low-pass filter is effectively formed to make the voltage mainly drop on the protective resistors.

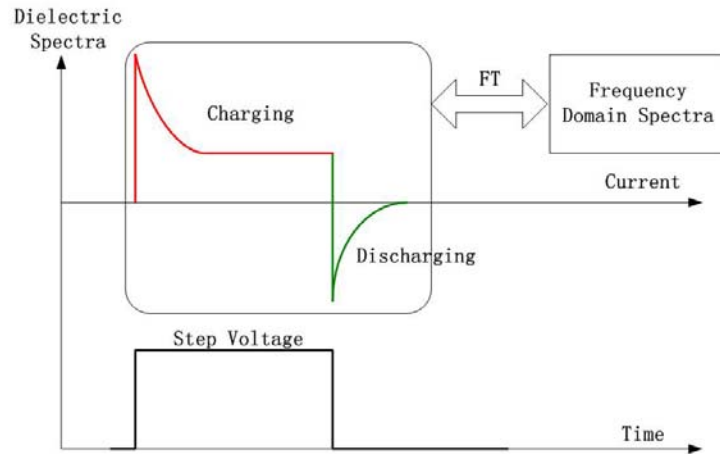


Figure 2.11 Principle of charging/discharging current measurement technique

Figure 2.11 shows the principle of charging/discharging time domain spectroscopy technique. For charging/discharging (polarization/depolarization) current measurement, the step field should be reduced abruptly to zero after the steady state polarization is reached in practically sufficient long time, and the discharging current can be observed. The difference between charging/polarization current and discharging/depolarization current is that the discharging current is given by the negative polarization current, including the negative delta function, but without the direct current. Therefore, it is more convenient to obtain the dielectric response function than the charging current.

As illustrated in Figure 2.11, the equivalent frequency domain behaviour of the dielectric can be obtained from this time dependent response by a Fourier integral

transformation which extracts all the separate relaxation components from the single transient signal in the time domain. For a linear dielectric material subjected to a step voltage  $V_0$  at time  $t = 0$ , the complex relative permittivity is given by [75]

$$\epsilon^*(\omega) = \epsilon_\infty + \frac{1}{C_0 V_0} \int_0^\infty I(t) e^{-j\omega t} dt - j \frac{G}{\omega C_0} \quad \text{Equation 2-36}$$

where  $\epsilon_\infty$  represents the atomic and electronic polarization which are effectively instantaneous.  $C_0$  is the geometric vacuum capacitance of the dielectric material and  $I(t)$  is the transient charging current at time  $t$ . The last imaginary part is the conductive contribution to the dielectric loss, if the dielectric has conductance  $G$ .

Because the Fourier transform of the transient current data needs very extensive numerical computation, Hamon approximation is sometimes used alternatively as

$$\epsilon^*(\omega) = \frac{I(t)t}{0.63 C_0 V_0} \quad \text{Equation 2-37}$$

and is based on the assumption that the current transient conforms to the equation

$$I(t) = At^{-n} \quad (0.5 < n < 1) \quad \text{Equation 2-38}$$

This assumption has been found efficient to fit the experimental data over a limited portion of the transient current curves for typical Debye-like relaxation processes in polymers [34] [110] [111].

Unlike frequency domain techniques or experimental systems that are commercially available nowadays, time domain dielectric spectroscopy system has to be specially built according to the desired experiment and frequency range. All the components are

not as simple as they are shown in Figure 2.10 because they should all have very demanding qualities to exclude extra influence. There are still lots of technical issues which are to be solved before the time domain dielectric spectrometer comes to fore.

### 2.5.2 Bridge techniques

As a frequency domain dielectric spectroscopy technique, bridge methods are the most popular techniques especially for high precision measurement. The most widely used way of determining the equivalent capacitance and resistance of a specimen is to use a type of Wheatstone bridge network to compare the unknown with standard components. The most popular technique for power frequency loss tangent detection is the Schering Bridge, which may also be used over the audio frequency range 10 to  $10^5$ Hz [75]. The basic circuit for a practical form of the bridge is shown in Figure 2.12. The circuit can be balanced with a null indicated by the detector, when the adjustable capacitance  $C_1$  and resistance  $R_1$  are tapped to have the same equivalent circuit as the unknown dielectrics -  $C_x$  and  $R_x$ . The balanced impedances will have the relation of

$$\frac{Z_1}{Z_2} = \frac{Z_3}{Z_x} \quad \text{Equation 2-39}$$

Based on this equation,  $C_x$  and  $R_x$  can be calculated by

$$C_x = \frac{R_1 \times C_2}{R_3} \quad \text{and} \quad R_x = \frac{C_1 \times R_3}{C_2} \quad \text{Equation 2-40}$$

where  $C_2$  and  $R_3$  are fixed-value standard capacitor and resistor. When the angular frequency  $\omega$  is determined, the loss tangent of the dielectric sample can be obtained by

$$\tan \delta = \frac{1}{\omega R_x C_x} \quad \text{Equation 2-41}$$

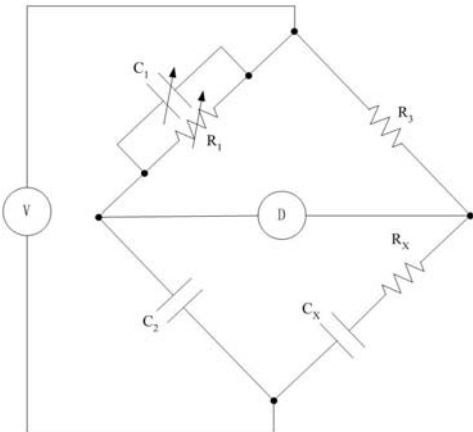


Figure 2.12 Circuit diagram of Schering Bridge [75]

The precision of Schering Bridge depends on the influence of stray impedances which couple various current sources of the bridge with unknown amount. The component settings and the position of operator can even deviate the balance of the detector. In order to solve this problem, extra electric components are used to form Wagner earth circuit, where the same earth potential can be obtained at some critical points with two relevant bridges balanced at the same time [112]. Earth screens are used around all bridge components and guard electrode in the sample cell in this situation. Wagner earth can be used to improve the precision of high frequency measurement, but the influence of stray impedances cannot be totally eliminated and, therefore, the application of Schering Bridge is limited.

Transformer Ratio Bridge is another spectroscopy technique for higher precision measurement on low loss dielectric materials. As shown in Figure 2.13, the bridge uses inductive ratio arms to compare directly the unknown impedance of the measured dielectric material  $Z_u$  with a variety of standard components  $Z_s$ . The voltage transformer is energized by a function generator connected to the primary winding and

develops on voltage  $V_2$  between the unknown impedance  $Z_U$  and the neutral line which is practically earthed. The other voltage  $V_1$ , which is  $180^\circ$  out of phase with  $V_2$ , is applied across the standard  $Z_S$ . The currents  $I_1$  and  $I_2$  flowing through  $Z_S$  and  $Z_U$  are respectively  $V_1/Z_S$  and  $V_2/Z_U$ . When the currents are equal in magnitude,

$$\frac{V_1}{Z_S} = \frac{V_2}{Z_U} \quad \text{Equation 2-42}$$

they will combine to produce zero core flux in the current transformer in the neutral line with a null indicator, because of their opposite phases.

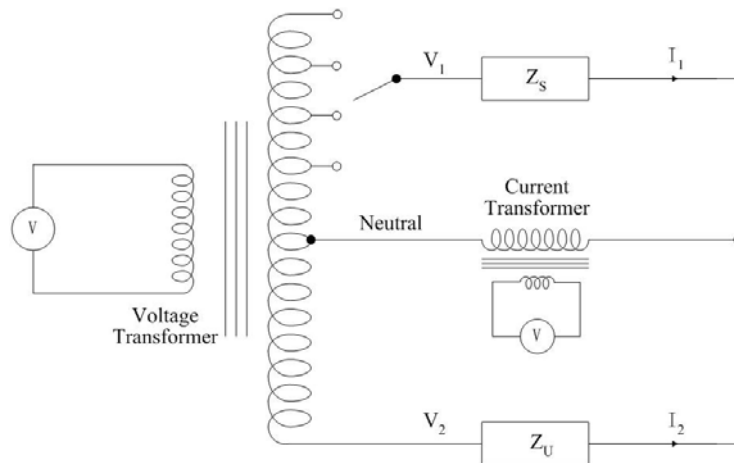


Figure 2.13 Principle circuit diagram of a Transformer Ratio-arm Bridge [75]

Transformer Ratio Bridge have two main advantages over Schering Bridge:

- a. Impedances between the unknown and earth do not affect the bridge balance so that long screened leads and guarded electrodes can be used.
- b. The voltage transformer can be tapped accurately to obtain decade ratios so that only a few standards are required.

With a very accurate measurement, a relatively smaller frequency range is a drawback of this frequency domain dielectric spectroscopy technique.

### 2.5.3 Frequency response analyzer technique

The frequency response analyzer, also called impedance analyzer, is an instrument for studying the frequency response of all kinds of materials. A schematic of frequency response analyzer technique is shown in Figure 2.14. The sinusoidal voltage  $U_1(\omega)$  is applied to the sample by the generator covering the frequency range from  $10^{-4}$  to  $10^7$  Hz. The resistor R converts the sample current  $I_s(\omega)$  into a voltage  $U_2(\omega)$ . The amplitude and the phases of the voltage  $U_1(\omega)$  and  $U_2(\omega)$  are measured by the use of two phase sensitive voltmeters. The complex sample impedance  $Z_s(\omega)$  can be calculated from the measured data by the basic equation

$$Z_s(\omega) = \frac{U_s(\omega)}{I_s(\omega)} = R \left( \frac{U_1(\omega)}{U_2(\omega)} - 1 \right) \quad \text{Equation 2-43}$$

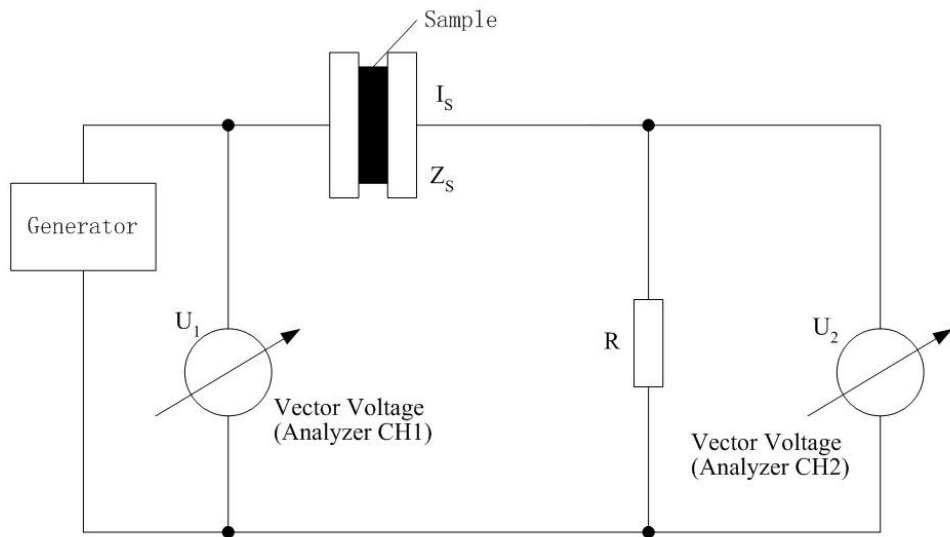


Figure 2.14 Schematic of frequency response analyzer

The complex relative permittivity can be then calculated by

$$\epsilon^* = \frac{1}{i\omega Z_s(\omega)C_0} \quad \text{Equation 2-44}$$

provided the geometric capacitance of the dielectric sample is known [113].

Based on the basic circuit diagram, commercial frequency response analyzers for dielectric spectroscopy have been improved with either digital lock-in amplifiers (e.g., Stanford SR 850, SR 830, and SR 810) or gain-phase analyzers (e.g., Solartron SI 1260 or SI 1255 and TA Instruments DEA2970) [113]. For higher sensitivity and accuracy an active interface has to be used (e.g., Chelsea Dielectric Interface, Novocontrol BDC) [114]. The schematic of frequency response analyzer with active interface and variable reference capacitor is shown in Figure 2.15, after the resistor R in Figure 2.14 is replaced by a current-to-voltage converter with variety of gains. In the circuit, if  $Z_x$  is a variable impedance that can be changed in resistance and capacitance, the sample impedance  $Z_s$  of a direct measurement is given by

$$Z_s = \frac{U_1}{I_s} = -\frac{U_1}{U_2} Z_x \quad \text{Equation 2-45}$$

Further improvement on the low loss dielectric measurement can be realized by a comparison of the sample capacitor with a variable reference capacitor, but the difference between the sample and the reference impedance must be minimized to reduce systematic errors otherwise nonlinear deviation will occur if the sample impedance differs more than 10% from the reference capacitor's value. Using this technique with commercial instrument, conductivity from  $10^7$  to  $10^{-16}\text{S/m}$  can be measured and loss tangent of  $10^{-4}$  may be achieved, if proper sample geometry is chosen.

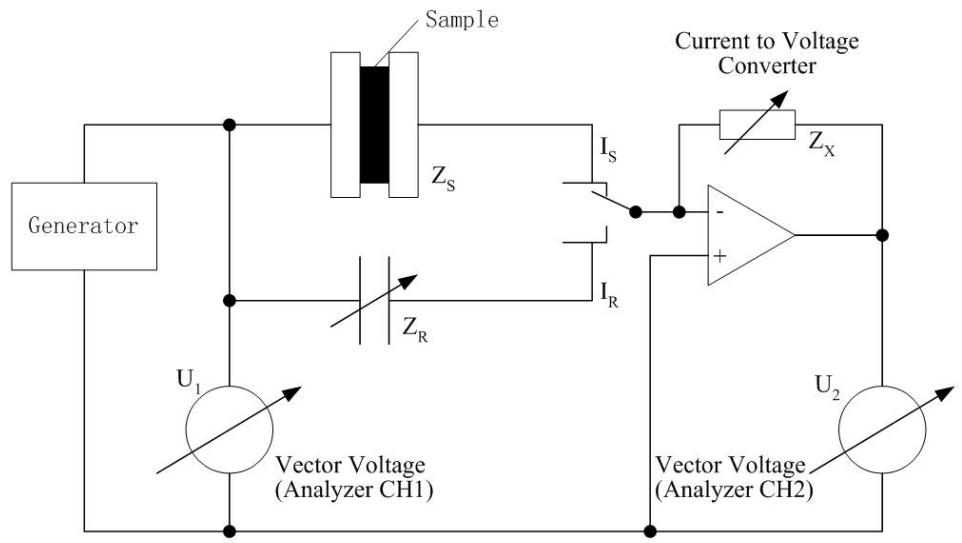


Figure 2.15 Schematic of frequency response analyzer with active interface  
and variable reference capacitor [113]

### 3 Characterizing the dielectric response of power cables

#### 3.1 Sample preparation of model power cables

##### 3.1.1 Introduction to model power cables

With the same extrusion manufacturing procedure as real full-size power cables, model cables are produced in Borealis AB in Sweden, in order to study the electric response of the whole cable insulation system, not just polymeric films. The advantages using the model cables have been stated in chapter 1 and in [115]. Three-layer model cables with insulation thickness 1.5 mm were extruded and dry-cured on a 1+2 pilot cable line, which has single extrusion (for inner semicon layer) and followed by double extrusion (for outer semicon layer and insulation layer) [116]. The dimensions are shown in Figure 3.1. The solid central copper conductor is 1.4 mm in diameter. Three layers are extruded around the conductor. The inner semicon layer is 0.7 mm thick and the outer semicon layer is 0.15 mm thick. The insulation layer is 1.5mm thick.

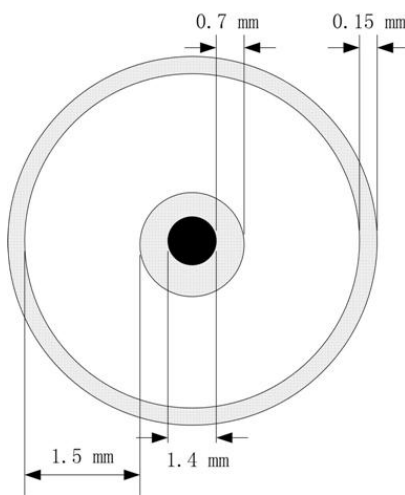


Figure 3.1 Dimension of the model power cables

Four different types of the model power cables, made of different combinations as listed in Table 3.1, are studied in this project. For the convenience of experiment, the cables are coded according to their different semicon and insulation materials, which are described in more details in Table 3.2.

Table 3.1 Codes for model power cables [117]

Cable code	Inner semicon	Insulation	Outer semicon
AAA	SC-A	INS-A	SC-A
ABA	SC-A	INS-B	SC-A
ACA	SC-A	INS-C	SC-A
BAB	SC-B	INS-A	SC-B

Table 3.2 Different materials of the model power cables [117]

Code	Description
INS-A	Homopolymer insulation (LDPE + antioxidant + peroxide).
INS-B	Homopolymer insulation (LDPE + antioxidant + peroxide). Different LDPE base resin compared to INS-A.
INS-C	Colpolymer insulation: $\mu$ m-size EBA (ethylene-butyl-acrylate) islands in a LDPE matrix
SC-A	Standard semicon (EBA + furnace carbon black + antioxidant + peroxide).
SC-B	Supersmooth semicon (EBA + acetylene carbon black + antioxidant + peroxide)

Three insulation materials are used as the insulation layer. The INS-A homo-polymer XLPE insulation is extruded from low density polyethylene (LDPE), with the additive of antioxidant and the cross-linking agent peroxide. The INS-B is still homo-polymer insulation but contains a different base resin. The INS-C is co-polymer insulation with micron-size ethylene-butyl-acrylate (EBA) islands, which can be used to improve the water treeing resistance. Semicon layers are produced with two carbon filled polymer

materials. The super-smooth semicon has acetylene carbon black, rather than furnace carbon black in standard semicon. These different combinations give the power cables different electrical properties that are studied in this project.

### 3.1.2 Sample preparation

There are no sample preparation standards for dielectric spectroscopy of power cables. Hence, limited publications can be referenced for this research project. As a convention for film samples that are mostly studied as test specimens, the cable insulation layer has been thought the only concern of dielectric measurement, while the inner semicon embracing the central conductor and the outer semicon shield should be the two electrodes. The influence of semicon layers had been ignored because their resistance is much less than that of the cable insulation.

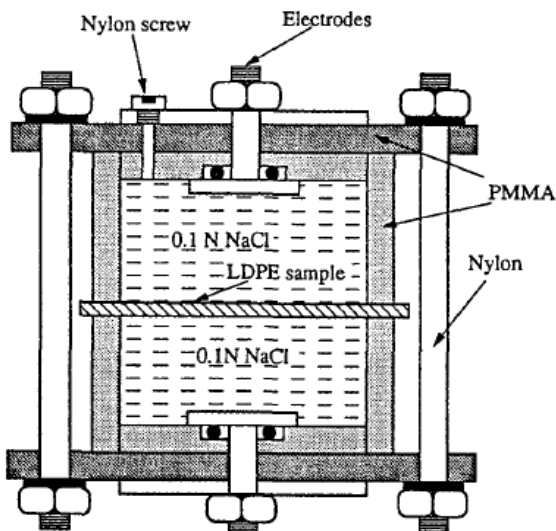


Figure 3.2 Steel tank with NaCl water as measuring electrode for XLPE cable spectroscopy, used by Scarpa et al [71]

In [71], the cable samples were placed in a steel tank, shown in Figure 3.2, filled with local tap water, which played as measurement electrode together with the outer semicon

layer. In paper [54] and [89], the semicon layer was treated as measuring electrode in the air, as shown in Figure 3.3. Therefore, the inner and outer semicon layers' resistance were neglected for the sample preparation referenced the methods in [54] [71] and [89], because they have smaller DC resistances than the insulation layer.

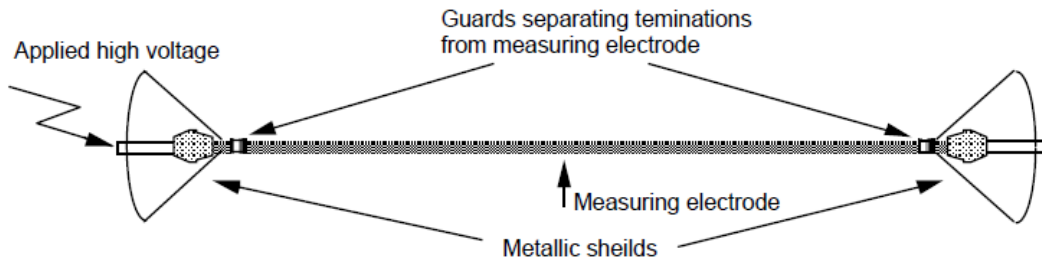


Figure 3.3 Cable sample preparation for dielectric spectroscopy [89]

However, based on recent research, it has been found that the semicon shields give rise to a significant dielectric loss in power cables [118] [119] [120]. The outer semicon should be considered as part of the whole insulation system of power cables. This thesis has studied the effect of semicon shields contribution to loss tangent and used copper tapes to avoid additional loss introduced by semicon layer's axial resistance, which is much bigger than its radial resistance. Two different sample preparation methods studied in experiments are shown in Figure 3.4, with the main purpose of eliminating the influence brought by the outer semicon layer's axial resistance. The first method is to use aluminium tape and heat-shrink tube to wrap the cable sample. Substantial improvement has been made but the contact was found not good enough at higher frequencies. There are still voids between the outer semicon layer and the aluminium. Further improvement was made using conductive adhesive copper tape. Better contact can be made through tight conductive adhesive. Therefore, the measured dielectric loss

only contains the radial resistance of semicon shields, without that due to axial resistance.



Figure 3.4 Comparison of two different sample preparation methods

The capacitance and conductance of a cable sample can be calculated by:

$$C = \frac{2\pi\epsilon_0\epsilon'L}{\ln(r_o/r_i)} \quad \text{Equation 3-1}$$

$$G = \frac{2\pi\sigma L}{\ln(r_o/r_i)} \quad \text{Equation 3-2}$$

When the geometry, real permittivity and conductivity are known for the cable insulation, the length of the sample is proportional to the sample's capacitance and conductance. Based on tests for different lengths, considering different techniques, the cable sample's conductance are measurable at 5m effective length while the capacitance is still in the instrument's accuracy range. This sample length should have  $4.29 \times 10^{-15} \text{ S}$  conductance if the conductivity of the cable insulation is  $10^{-16} \text{ S/m}$ . When 3V is applied for the measurement, about 13fA can be generated through the insulation. For example, the FRA has the ability to measure 1fA. Therefore it could precisely measure the dielectric response of cable insulation with the conductivity of  $10^{-16} \text{ S/m}$ .

## 3.2 Choice and development of techniques for low loss measurement

In order to measure the dielectric response of the model power cables, the measurement technique needs to be able to measure the loss tangent even smaller than  $10^{-4}$  [54][71]. It has been found necessary to combine three dielectric spectroscopy techniques, which are frequency response analyzer (FRA) and transformer ratio bridge (TRB) in frequency domain, and charging/discharging or polarization/depolarization current (PDC) technique in time domain, to measure the dielectric loss of the cables.

### 3.2.1 Frequency response analyzer in the range from $10^{-4}$ Hz to 1Hz

#### ***3.2.1.1 Accurate frequency range for measurement on the XLPE model cables***

A frequency response analyzer generally has a wide frequency range from  $10^{-5}$ Hz to  $10^7$ Hz. It is able to measure the dielectric's real permittivity over the frequency range according to the Figure 3.5, which shows the determination of typical accuracy frequency range for different resistances and capacitances of the test sample. In this study, the cable sample's real capacitance is 800pF and, therefore, has the optimum accuracy range from  $10\mu$ Hz to 1MHz, as shown in the blue area in Figure 3.5. Since the resistance of the model power cable insulation is at least  $100G\Omega$ , the maximum measurement accuracy is then restricted in the range below 1Hz, as shown in the red area. As for the imaginary capacitance that represents the dielectric loss, there is no available data in the specifications of FRA. An estimated minimum loss tangent value about  $10^{-4}$  is generally provided without specifying a frequency range. Because the power cables have very low loss insulation with their loss is even smaller than  $10^{-4}$ , the measurement results may be influenced or even dominated by the background noise.

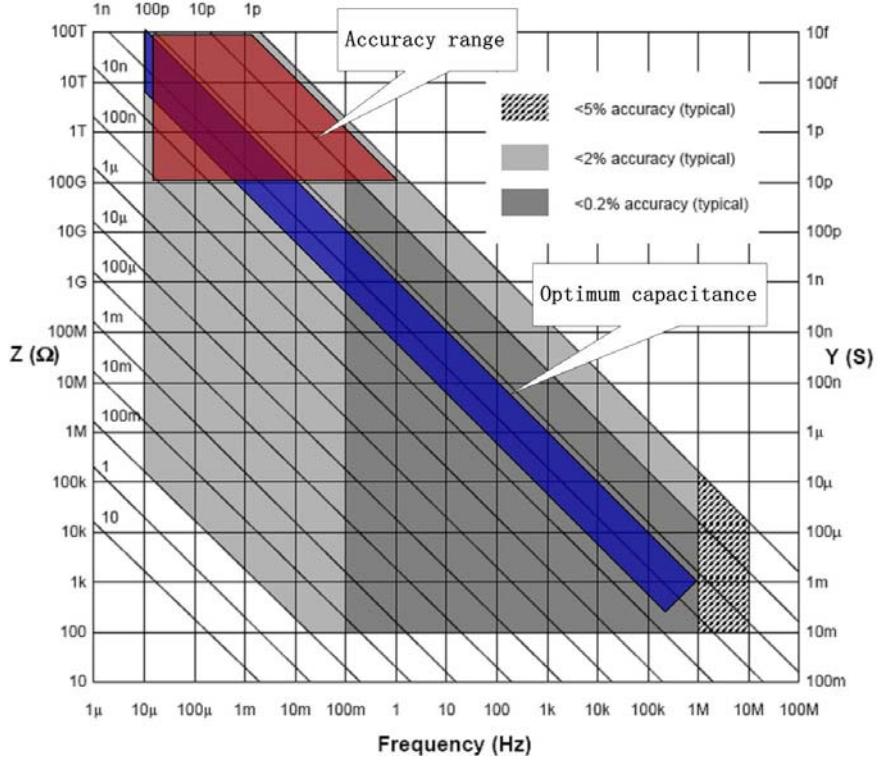


Figure 3.5 Accuracy frequency range of FRA on real capacitance measurement [121]

In order to find out the measurement limit of the FRA system, a standard 10pF reference capacitor with the same cylindrical geometry as the model cables was designed, as shown in Figure 3.6. This standard capacitor can be used in any measurement system to determine the limit on dielectric loss measurement. According to the calculation of empty cell capacitance

$$C_0 = \frac{2\pi\varepsilon_0 L}{\ln(r_o / r_i)} \quad \text{Equation 3-3}$$

when the radius ratio of the “air cable” is the same as all the model power cables in this study, the length is 0.2m. The inner radius is 8mm so that it could also withstand high voltage test up to 21kV, considering the breakdown voltage of air as 3kV/mm. A three electrode system is used to avoid surface leakage current. A plug-in connector in the central conductor is used to apply the high voltage energisation. A BNC cable connector

on the metal tube is used as measurement electrode while the small measured signal can be protected by the coaxial cable shield. This “air cable” is made of copper for central conductor, measuring electrode and guard electrode. PTFE is used to separate guard electrode and as skeleton to keep the correct distance between two electrodes.

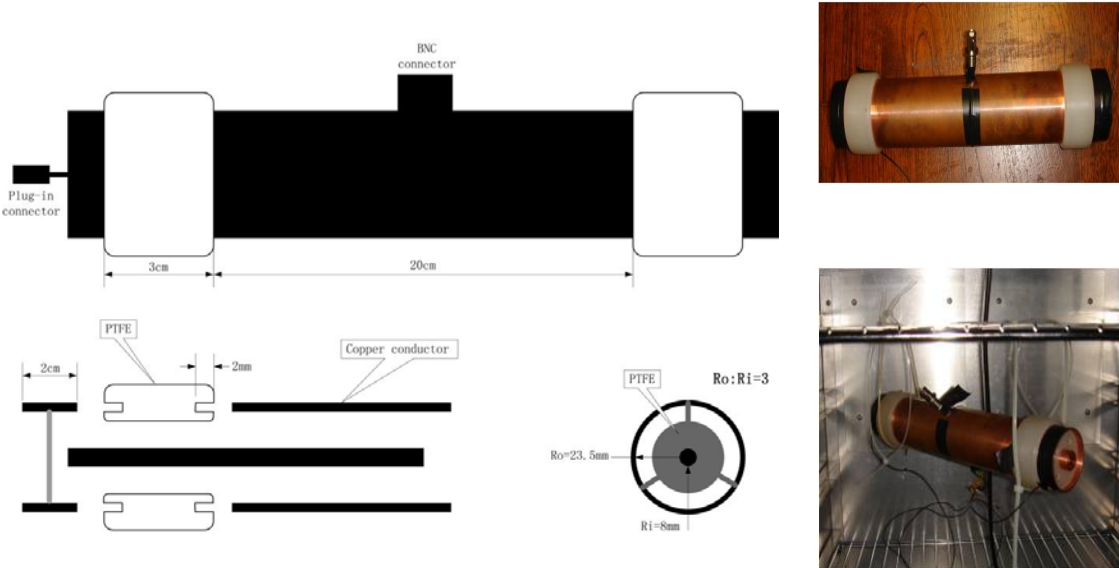


Figure 3.6 Reference capacitor design and photos

With the help of the “air cable”, the FRA system limit can be determined. Because the air is practically considered loss free and independent of frequency, the loss tangent measurement result on the “air cable” is the noise floor of the experimental system. Figure 3.7 shows the measurement results made by the FRA on a homo-polymer model cable sample at different temperatures and on the “air cable”. In the frequency range from  $10^{-4}$ Hz to  $10^6$ Hz, the loss tangent of this homo-polymer model cable sample was found noisy and increasing at higher frequencies above 1Hz (Figure 3.7). At higher frequencies, firstly, there is no change of the loss tangent at different temperatures. Secondly, the loss tangent is in fact the same as that of the “air cable”. Therefore, the effective accuracy frequency range for FRA technique can be determined as below 1Hz,

above which the instrument measures the noise floor. This experiment results agree with the analyzed accuracy range in Figure 3.5. The frequency range for accurate FRA measurement on the model power cables was finally determined as from  $10^{-4}$ Hz to 1Hz. It was found that no single dielectric spectroscopy technique can be used over the broad frequency range from  $10^{-4}$ Hz to  $10^6$ Hz. Therefore, a combination of three techniques is used in this study.

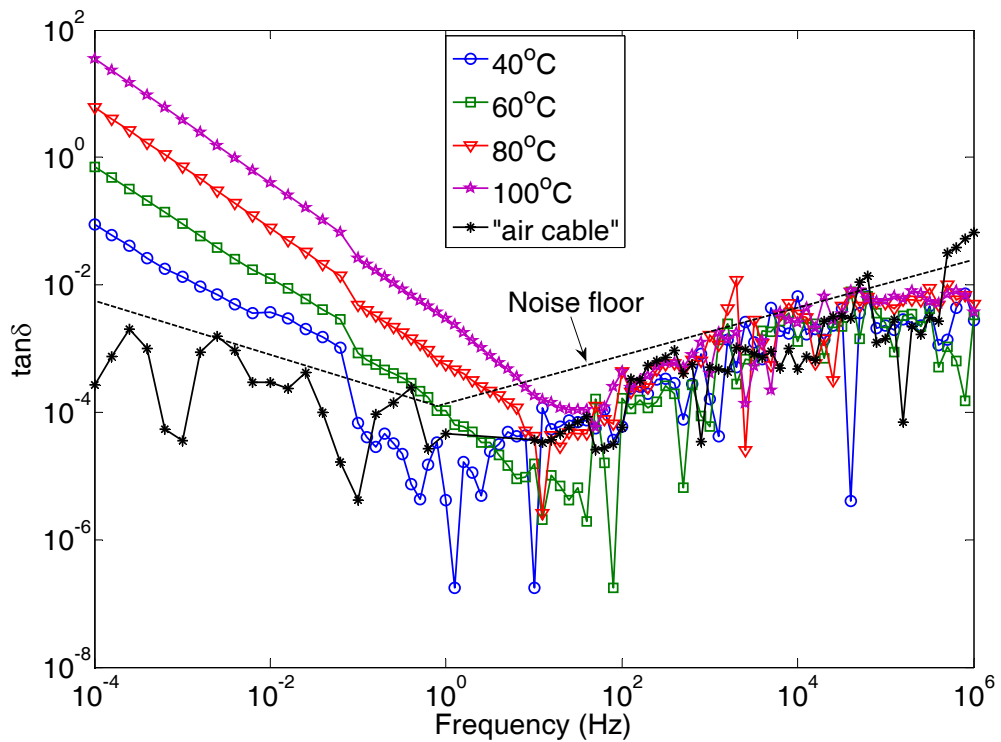


Figure 3.7 Loss tangent measurement using FRA on homo-polymer cable and the “air cable” demonstrating the measurement limitation below 1Hz

### 3.2.1.2 Measurement accuracy of different modes

In order to maximize the FRA’s accuracy over this frequency range on the power cable measurement, three different test methods – normal mode, internal reference mode and external reference mode – have been studied. A reference capacitor is commonly used

to increase the measurement sensitivity. In the FRA, the principle of reference measurement mode is explained in Figure 3.8. The reference capacitor, which is required to have comparable capacitance and negligible dielectric loss, is measured after the test sample. The calculated parameters are compared with the standard values of the reference capacitor, to determine the system errors for correction on the sample's measurement data. The measurement circuit stray parameters, such as the protective resistance, the lead capacitance and inductance, the electrode contact capacitance, can be effectively avoided with the reference mode particularly at higher frequencies.

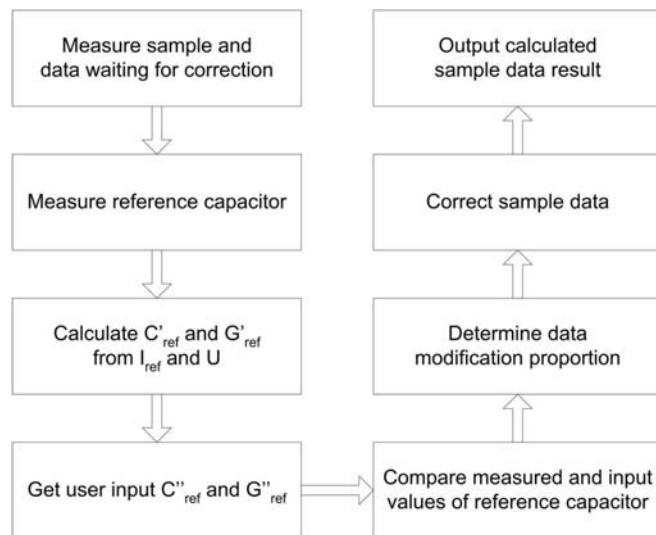


Figure 3.8 Circuit diagram and principle of reference measurement method

External and internal reference capacitors were both tried in reference mode to measure the model power cables. The internal reference mode was found better than the external reference mode, because the external reference capacitor easily coupled noise from the environment into the measurement channel of FRA and made it difficult to complete a stable measurement. The internal reference mode uses a reference capacitor that is shielded in the dielectric interface. The reference capacitor is automatically selected by the instrument comparable to the sample capacitance. Figure 3.9 shows the

measurement results on a homo-polymer cable sample with normal and internal reference mode in the frequency range from  $10^{-3}$ Hz to 10Hz. The real permittivity  $\epsilon'$  can be well measured in both modes and does not have a big difference. However, the imaginary permittivity  $\epsilon''$  in internal reference mode has negative values at lower frequencies and false results might be incorrectly displayed with absolute values in FRA software (SMaRT Version 2.8.0). The negative values are due to the low loss characteristic of the test cable sample and are produced by the calculation in reference mode. Although the reference capacitors are very low loss standard components with stable response in the frequency range, the model power cables have lower loss than the reference capacitor.

Therefore, the frequency response analyzer technique can be used to measure the low frequency dielectric response of the model power cables in the range from  $10^{-4}$ Hz to 1Hz. The dielectric loss due to DC conductivity has a slope of -1 in imaginary part as explained in chapter 2 and makes the measurement easier. At the other frequencies, up to 1MHz, the dielectric loss is smaller than that due to noise background. This frequency range is not a fixed region for accurate measurement and depends on the insulation materials and measuring conditions such as temperature. For example, the homo-polymer XLPE model cable AAA has no detectable loss until 80°C. Normal mode was found to be the best method with direct measurement of the cable sample, because the standard reference capacitors are too lossy to help improve the sensitivity. The direct measurement will give the most reliable results, despite the small ripple due to FRA's instrumental rearranging of the amplifiers.

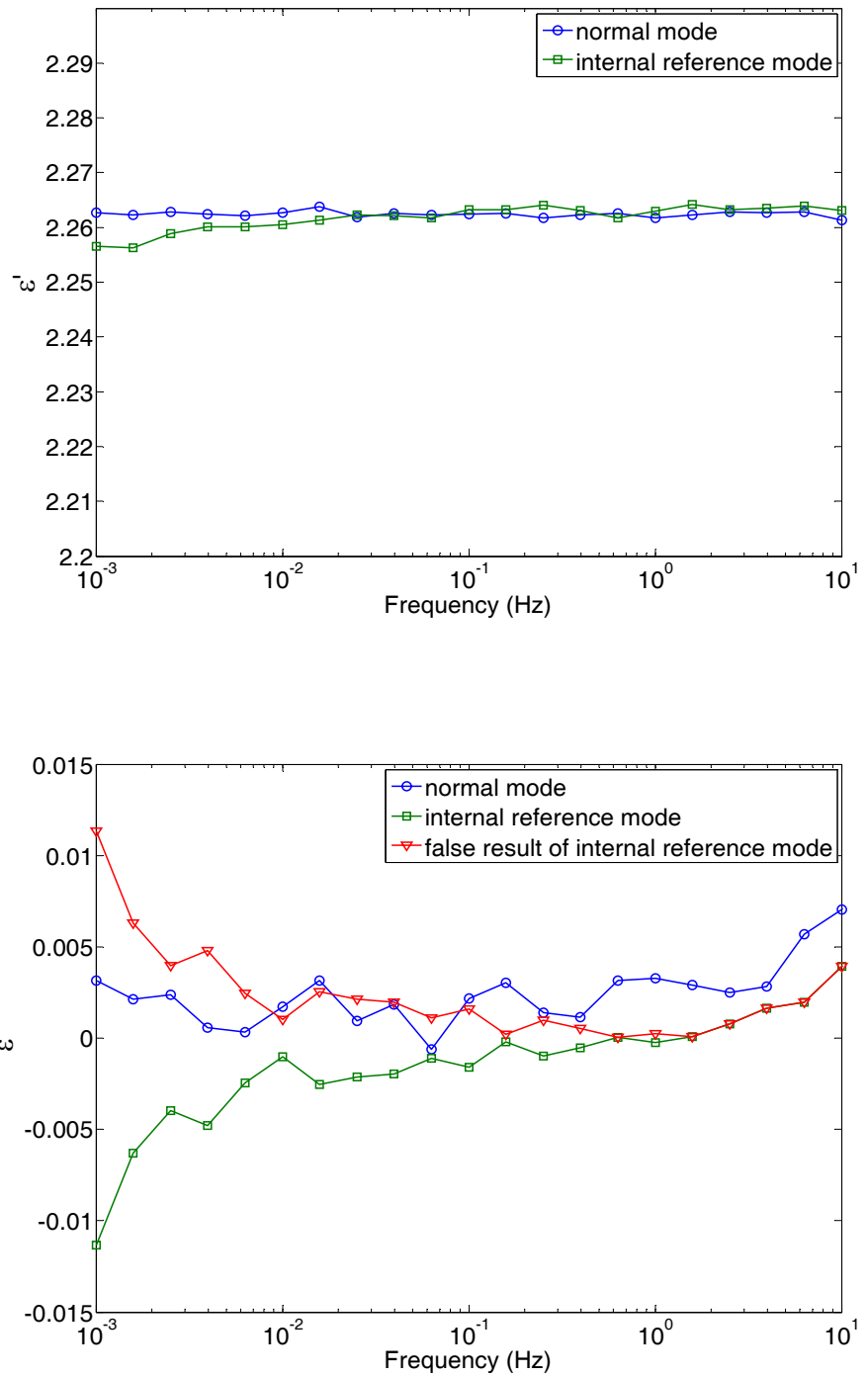


Figure 3.9 FRA test of normal and internal reference modes on the complex permittivity

### 3.2.1.3 High voltage dielectric spectroscopy

The possibility of integrating high voltage amplifier with the FRA system has been investigated. The circuit diagram of the HV system is shown in Figure 3.10 (a). The low

output voltage is amplified through the HV amplifier. The monitoring voltage of FRA is obtained via an internal potential divider in the HV amplifier. There is a 60pF internal capacitance that could influence the maximum output frequency in the equation

$$i = (C_{load} + 60\text{pF})2\pi f U_{peak}$$

Equation 3-4

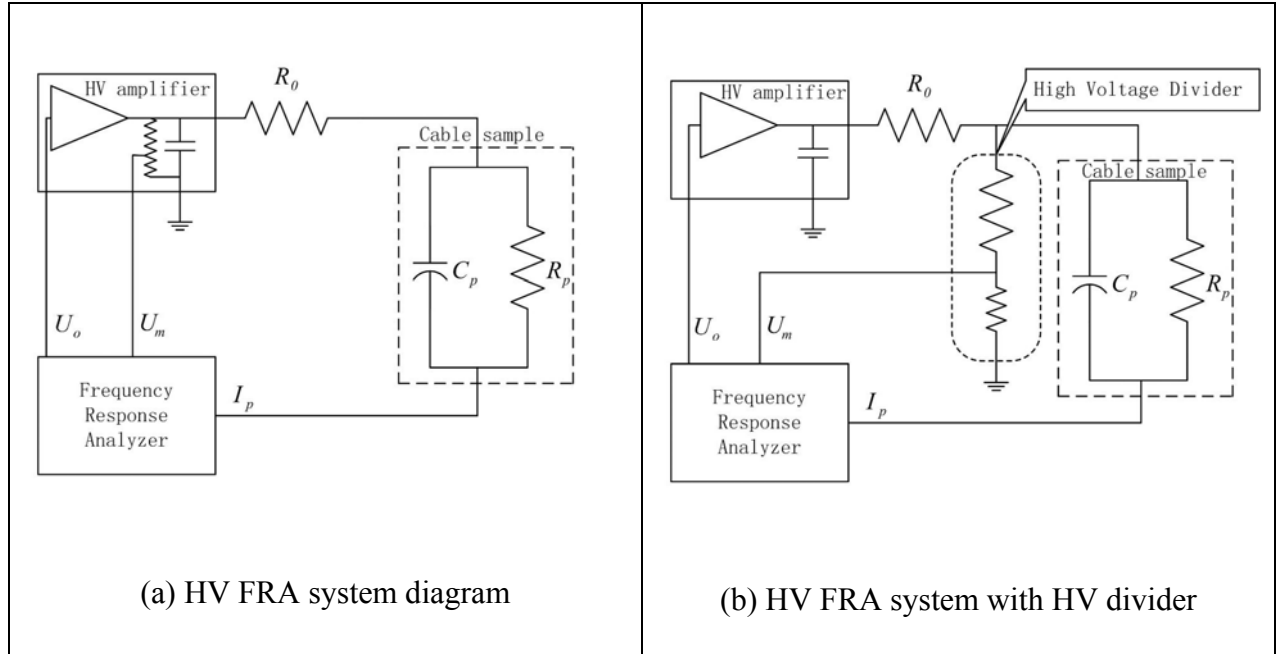


Figure 3.10 Circuit diagram for analysis of HV FRA measurement

For high voltage experiment with sensitive small current detector in FRA, a protective resistor has to be installed in series with the test sample. In the worst case of breakdown, the protective resistor should be big enough to restrict the current within 20mA, which is the maximum input current of the FRA, under the maximum voltage of the high voltage amplifier (20kV Trek 20/20B).

$$\text{minimum protective resistor} = \frac{\text{maximum output voltage of HV amplifier}}{\text{maximum input current of FRA}} = \frac{20\text{kV}}{20\text{mA}} = 1M\Omega$$

The cable sample is represented with its parallel equivalent circuit for the convenience of mathematic modelling. This equivalent circuit will be used all through the study.

With  $5\text{M}\Omega$  and  $10\text{M}\Omega$  protective resistors and different applied voltages from  $1\text{kVrms}$  to  $4\text{kVrms}$ , the measurement results are shown in Figure 3.11. The loss tangent was measured in the range from  $10^{-2}\text{Hz}$  to  $10^3\text{Hz}$ . With the same  $5\text{M}\Omega$  protective resistor, there is very little difference at all test voltage levels. After the resistance was changed to  $10\text{M}\Omega$ , an apparent increase can be observed. The most impressive characteristic of the measurement results is that the loss tangent increases with a slope close to 1 at higher frequencies. Cable samples with polymeric insulation cannot have such Debye-like loss phenomenon [8]. The loss tangent is more than 0.1 at  $50\text{Hz}$  and a higher protective resistor causes a bigger loss tangent. It is much higher than the reported results in [54] [71] [73]. With the same protective resistor, there is no difference at different voltages, especially at higher frequencies. However, when the resistor was changed to  $10\text{M}\Omega$ , the loss tangent has parallel increasing slopes at  $1\text{kV}$ . The abnormally high loss tangent and dependence on protective resistor imply that instrumental or system errors play the dominant part in the results.

In order to find out the effects of protective resistors, equivalent circuit modelling was studied in MATLAB. An equivalent circuit refers to the simplest form that retains all of the electrical characteristics of the original (and more complex) circuit or system. The equivalent circuit method has been widely used in the study of electric machines and power transformers. Its modelling theory of dielectric materials has already been summarized [122] and effectively applied in research studies on XLPE cables [123][28]. A commonly used parallel equivalent circuit for polymer cable insulation is shown in Figure 3.12 (a). The capacitance and resistance, namely  $C_p$  and  $R_p$ , are basic parameters for the dielectric spectroscopy modelling. The  $C_p$  and  $R_p$  could be

calculated by  $C = \frac{2\pi\epsilon_0\epsilon'L}{\ln(r_o/r_i)}$  and  $G = \frac{2\pi\sigma L}{\ln(r_o/r_i)}$ , where the inner radius  $r_i$ , the outer radius

$r_o$ , the length of cable  $L$  and the conductivity  $\sigma$  should be known. In this modelling study, the sample's length ( $d = 13\text{cm}$ ), static dielectric constant ( $\epsilon_r = 2.3$ ) and resistance ( $R_p = 10^{15}\Omega$ ) are used.

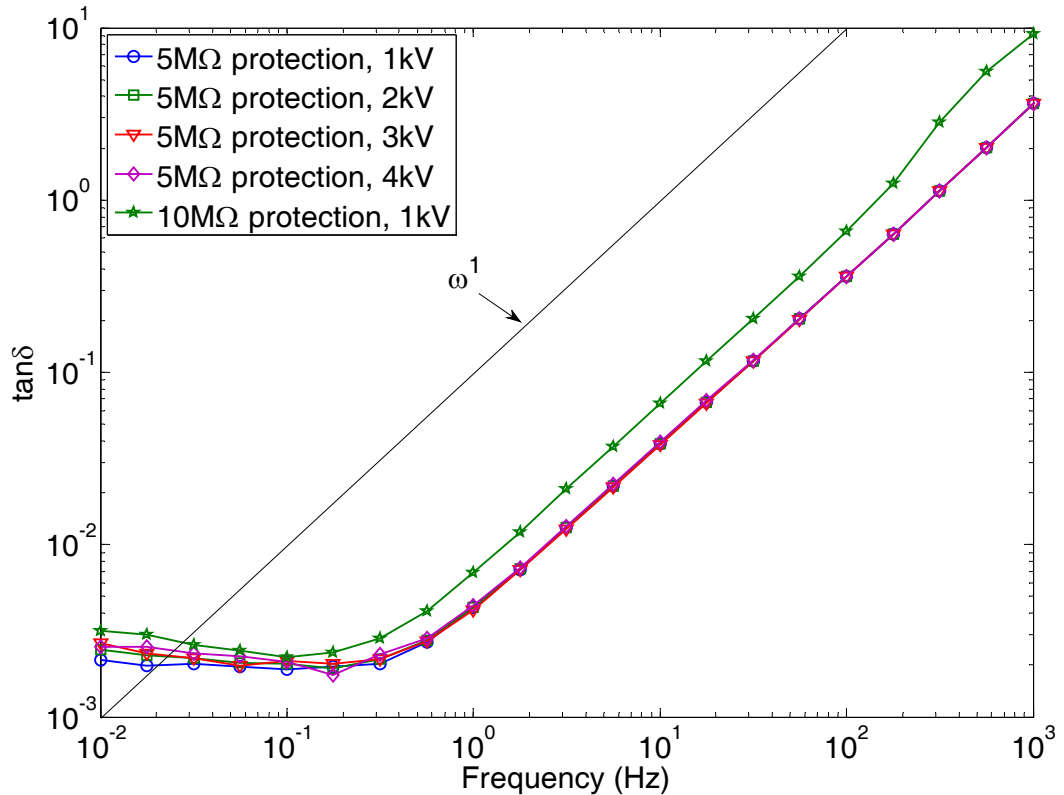


Figure 3.11 High voltage FRA measurement on XLPE model cable with different protective resistors

Figure 3.12 shows the comparison of loss tangent with different equivalent circuits. Without protection resistor, the blue curve shows the ideal dielectric response of the cable insulation. The loss tangent can be calculated as

$$\tan \delta = \frac{1}{\omega C_p R_p} = \frac{\epsilon''(\omega)}{\epsilon'(\omega)} \quad \text{Equation 3-5}$$

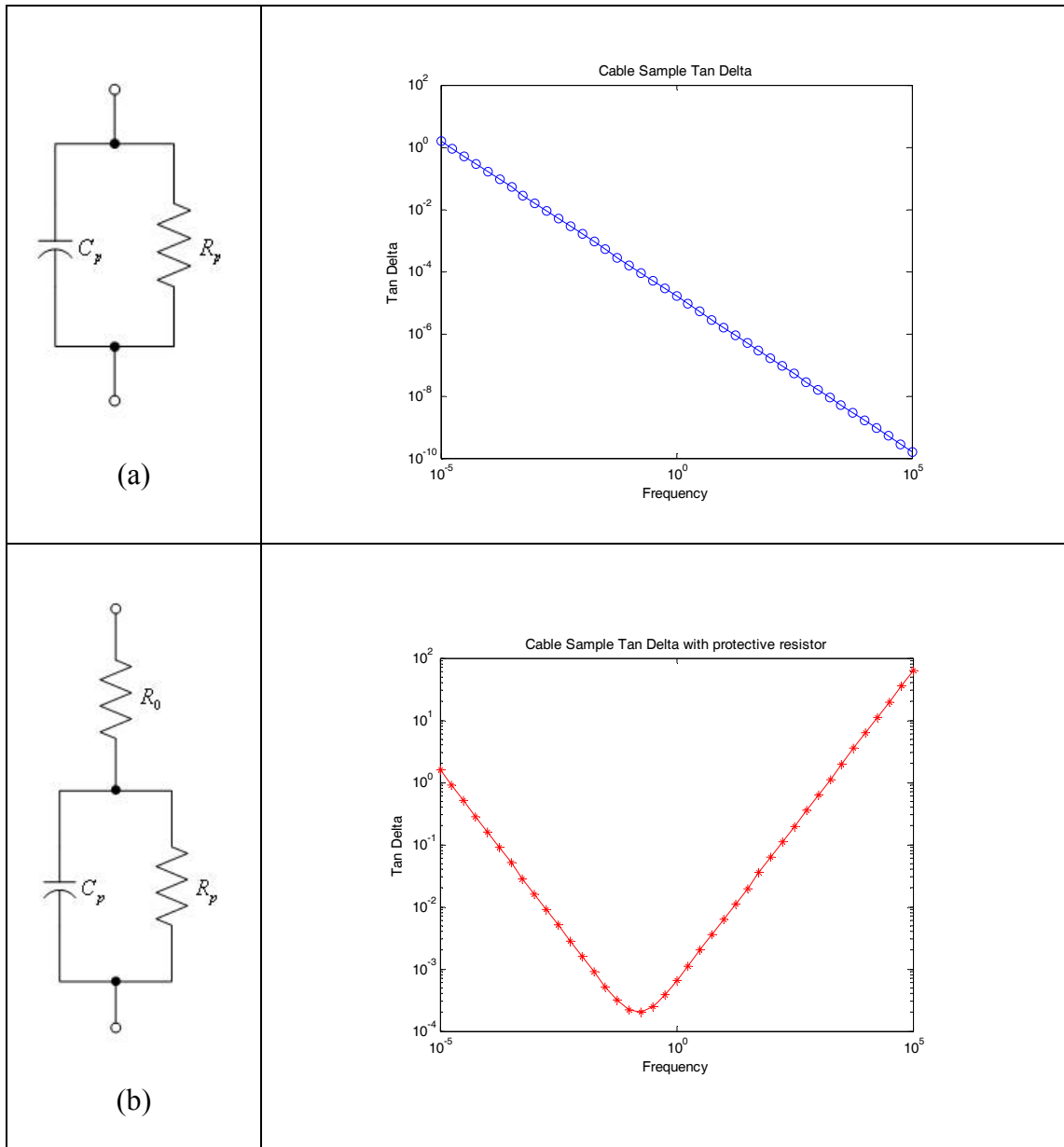


Figure 3.12 Equivalent circuit modelling on the effect of protective resistor

From the equation, it can be seen that the loss tangent is proportional to the reciprocal of frequency. After installing a  $10M\Omega$  protection resistor, the equivalent circuit and modelling result is shown in Figure 3.12 (b). It can be seen that the loss tangent increases at higher frequencies. The increasing loss is due to the protective resistor in series with the cable insulation based on the formula

$$\tan \delta = \frac{R_p + R_0(1 + \omega^2 C_p^2 R_p^2)}{\omega C_p R_p^2} = \frac{\epsilon''(\omega)}{\epsilon'(\omega)} \quad \text{Equation 3-6}$$

At lower frequencies when  $\omega R_p C_p \ll 1$ , the dielectric loss is mainly due to the bulk conduction of the insulation,  $\tan \delta \approx \omega C_p R_p \propto f^{-1}$ . At higher frequencies, when  $\omega R_p C_p \gg 1$ , the sample capacitance tends to short its parallel resistance. In this situation,  $\tan \delta \approx \omega C_p R_0 \propto f$ . The characteristic frequency can be calculated as

$$f = \frac{1}{2\pi R_0 C_p}.$$

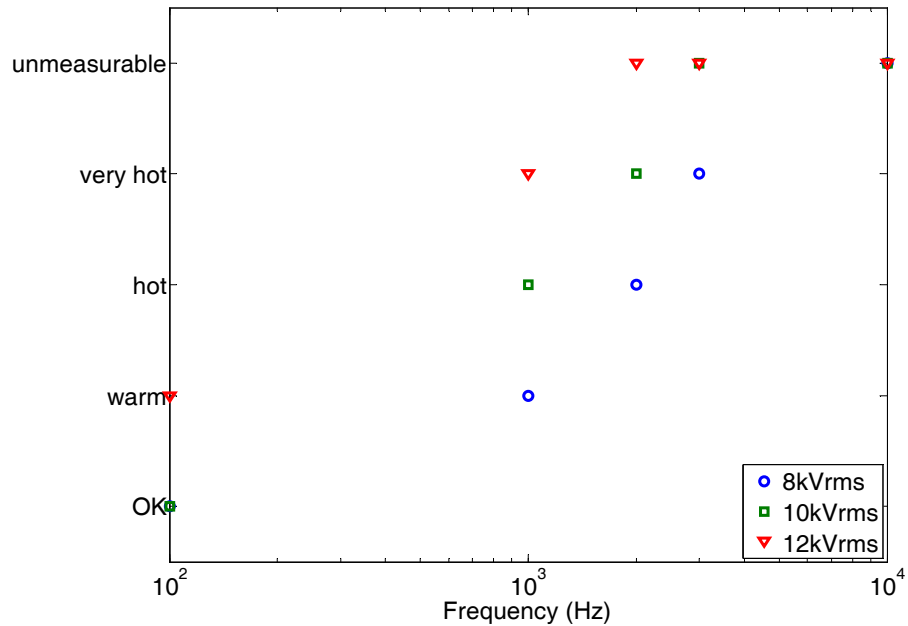


Figure 3.13 Resistive heating of the protective resistor at different voltages

The increasing loss tangent has also been experimentally proved to be due to the protective resistor, as shown in Figure 3.13. With  $5M\Omega$  protective resistor, high voltage spectroscopy using the FRA and Trek amplifier 20/20B was measured. The frequency

started at 100Hz and ended at 10kHz. Three different test voltages were used from 8kVrms to 12kVrms. Five  $1\text{M}\Omega$  0.6W carbon film resistors were used as protection. Temperature level was sensed by hand and recorded right after 1 minute measurement. It can be seen that at 8kVrms, the temperature of the protective resistors was normal at 100Hz but became hotter when the frequency increased. At 10kHz, it was not possible to measure current, since it exceeded 10mA, the set maximum set, in the amplifier for the safety of the FRA. This indicates that more power was consumed in the protective resistors at higher frequencies because more voltage was applied across them. At higher voltages, the same situation happened, and more resistive heating occurred at lower frequencies.

Since the protective resistor should not be removed for the safety of FRA, another possibility, as shown in Figure 3.10 (b), is to use a HV divider after the protection with the same ratio arms – 2000:1 – as the HV amplifier, and provide monitoring voltage from it. This method would exclude all the influence before the voltage is applied to the test sample. In this case, the potential divider sends a feedback voltage to the FRA that should be an exact proportion of the instantaneous sample voltage. However, a new problem would emerge by the HV divider. Every HV divider is originally designed with electrical component such as resistors and capacitors, it can be perfect only at fixed frequency and normally has very limited bandwidth. There may be small phase shift in its working frequency range and the phase change can be comparable or even bigger than that due to the actual dielectric loss of the cable samples. For example, a  $\tan\delta$  of  $10^{-4}$  equals a phase angle of  $5.73 \times 10^{-3}$ , which is a typical loss tangent angle of XLPE cables. Artefacts caused by the series resistor or the potential divider can be so much larger than the cable loss and it is not possible to account for their effects by numerical correction. Therefore, direct measurement, i.e. without any series resistor and potential

divider, provides the most reliable data. HV FRA system can be made with HV divider to shield the influence of protective resistor, but extra influence would be induced by the divider itself. Since very low dielectric loss model cables are the measurement objects in this study, the HV system is not appropriate. Only low voltage experiments with direct measurements have been carried out.

### ***3.2.1.4 The measurement system setup and specifications***

The FRA experiment system in this study is shown in Figure 3.14. The FRA generates a sinusoidal voltage of desired frequencies into the dielectric interface with “Gen” channel. Channel V1 sends back the original voltage directly to FRA as “norm” voltage. “Hi” outputs the voltage to the cable sample through a BNC connection. The current through the cable sample is measured by “V2” at “Lo”. The voltage of V1 and current at V2 are used to calculate the complex impedance  $Z^*$  and, therefore, the complex capacitance  $C^*$ . The FRA, Dielectric Interface and the oven are all controlled by a computer program (Solartron SMaRT 2.8.0) though GPIB and Modbus connections.

The specifications of the FRA system are:

- frequency range: from  $10^{-4}$ Hz to 1Hz (above 1Hz the dielectric loss below the noise floor of the FRA technique)
- applied voltage: from 0 to 3Vrms
- current measurement: from 1fA to 100mA
- Tan Delta Range: from  $10^{-3}$  to  $10^3$  in “normal” mode

- Capacitance Range: from 1pF to 0.1F (the optimum capacitance should be in the range from 100pF to 1nF)
- temperature range: from 20°C to 120°C (from 293 to 393K) (limited by the cable materials below any phase change or glass transition)

In conclusion, the Solartron FRA system was used for measuring at low voltages and at frequencies below 1Hz.

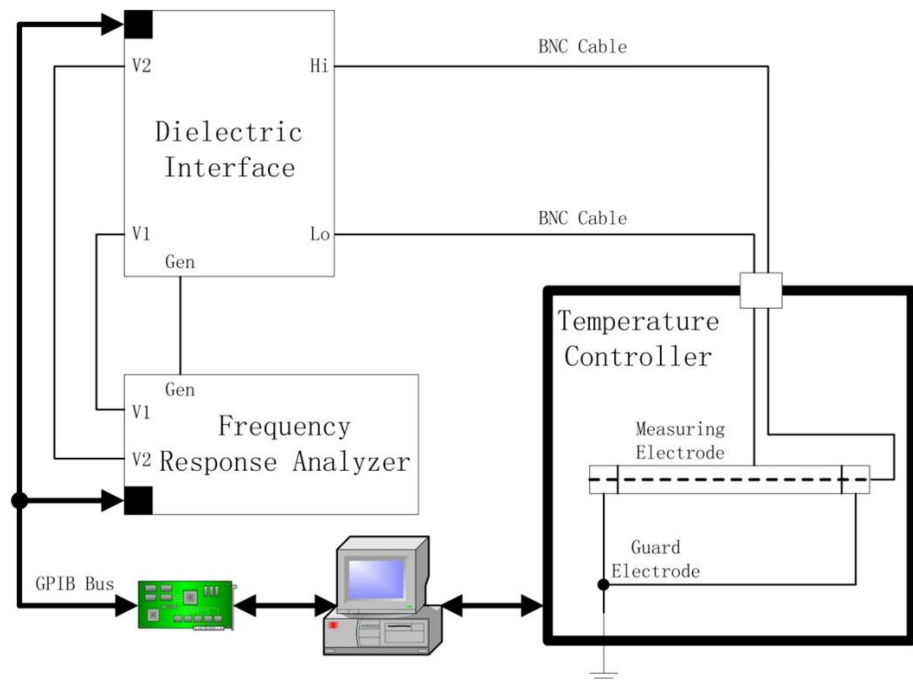


Figure 3.14 FRA experiment system on power cable measurement

### 3.2.2 Transformer ratio bridge in the range from 300Hz to 10kHz

In order to measure higher frequency dielectric loss of the model power cables, other techniques are needed. Having the advantages over the Schering bridge that have been introduced in chapter 2, the transformer ratio bridge was selected as the dielectric spectroscopy technique. A universal inductive bridge can be integrated with an external

function generator to extend the originally designed frequency range. The transformer coils become inefficient when below 100 Hz. Above 10 kHz, the balance detector cannot reach a null. Hence, the frequency range is from 100Hz to 10kHz. However, it has been found that noise greatly influenced the accuracy and efforts have been made to extend the frequency range while maintaining accurate measurement for the low loss model cables.

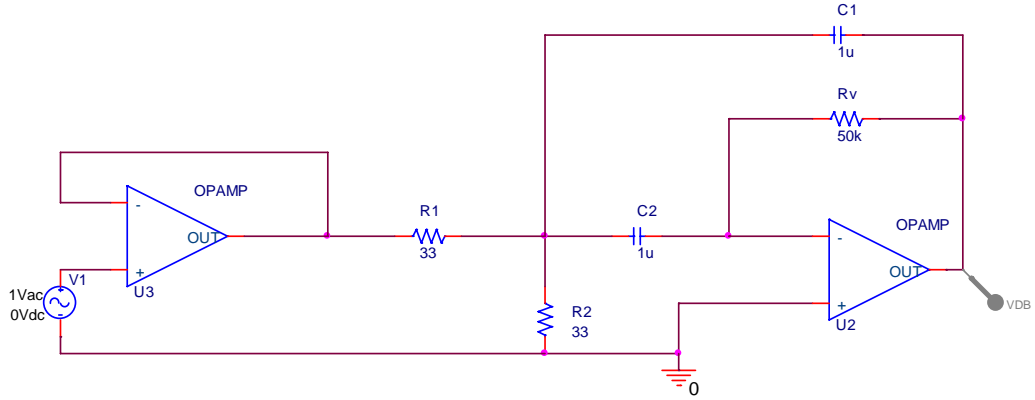
### ***3.2.2.1 Improvement on measurement accuracy***

Because the XLPE cables have extremely low dielectric loss and the measurement could be easily influenced by background noise and interference such as harmonics, these issues are the most important and the most difficult thing for precise measurement on the cable samples. A tuned amplifier has been designed to filter any signal of frequencies other than the frequency under measurement and finally enlarge the bandwidth [124]. The circuit of the tuned amplifier is shown in Figure 3.15 (a). A multiple-feedback analogue filter with resistors and capacitors works to amplify a specific frequency signal. The desired signal at that specific frequency can be amplified. Any signal other than the desired frequency is attenuated. In the circuit diagram,  $R_V$  is a logarithmic variable resistor used to modulate the “peak” frequency, based on Equation 3-7 [125]

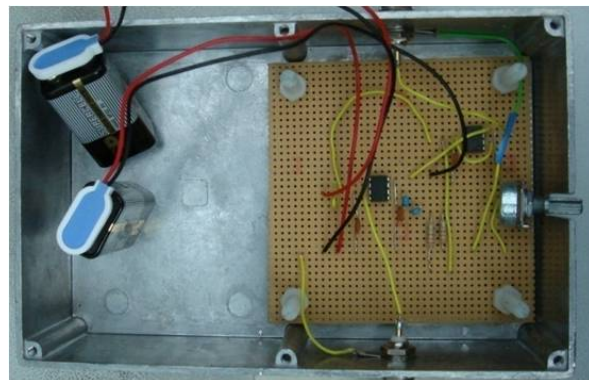
$$f_0 = \frac{1}{2\pi\sqrt{(R_1\|R_2)R_V C_1 C_2}} \quad \text{Equation 3-7}$$

where the  $f_0$  is the frequency to be amplified. In this study,  $R_1 = R_2 = 33\Omega$  and  $C_1 = C_2 = 1\mu F$ ,  $R_V$  was determined as  $50k\Omega$  covering the frequency range from 175Hz

to 39kHz. In order to prevent excessive current flowing into the circuit, a unity gain amplifier was placed before the filter.



(a) circuit diagram for simulation in PSpice



(b) photo of real circuit in a shielded box

Figure 3.15 Design of tuned amplifier for transformer ratio bridge system

The circuit was simulated on a computer with OrCAD PSpice. A frequency domain simulation with 1V AC voltage source was done in the frequency range from 100Hz to 10kHz. The output voltage in dB was obtained as shown in Figure 3.16, where the attenuation in dB is against frequency range from 100Hz to 10kHz. From the results, the specific signal of the applied frequency is amplified and the other frequencies are

attenuated greatly so that the high frequency environmental noise will be much smaller and will not influence the balance detector of the transformer ratio bridge. The real circuit of tuned amplifier has been built in a shielded box (Figure 3.15(b)). Two 9V batteries are used to drive the op-amps and a screwed logarithmic potentiometer is fixed near the wall of the shielding box so that it could be tapped outside when the shielding box is sealed.

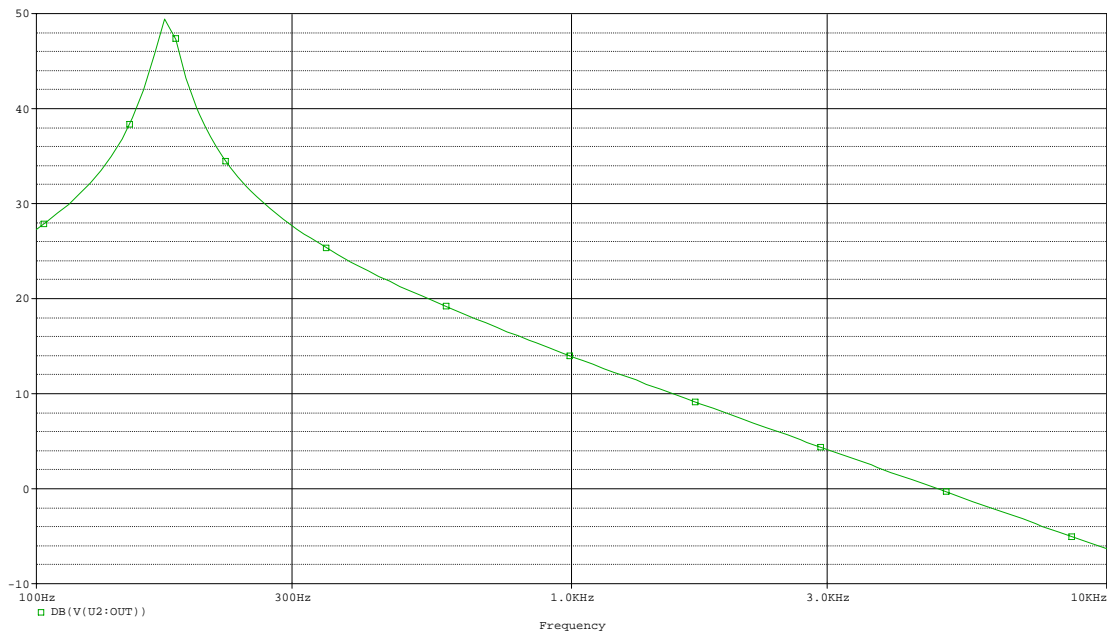


Figure 3.16 PSpice simulation result of the tuned amplifier

The system has been further improved against noise from mains power supply. The bridge circuits were originally designed to be driven by transforming and converting the mains supply. It was found with the samples and the tuned amplifier circuit being shielded, extremely small interference from the harmonics of the mains power can also make it difficult for the bridge to reach perfect balance. Therefore, a DC battery was used to replace the mains power supply. The battery is directly connected to the circuit of balance detector and is driving it without bringing any harmonics. It was found even higher precision was obtained by this means.

### 3.2.2.2 Experimental system setup

The transformer ratio bridge experiment system for low loss power cable measurement is shown in Figure 3.17. The system has been integrated with Wayne Kerr universal bridge B221 [126], function generator, tuned amplifier specially designed for improving system sensitivity, oscilloscope and temperature control oven to accommodate cable samples.

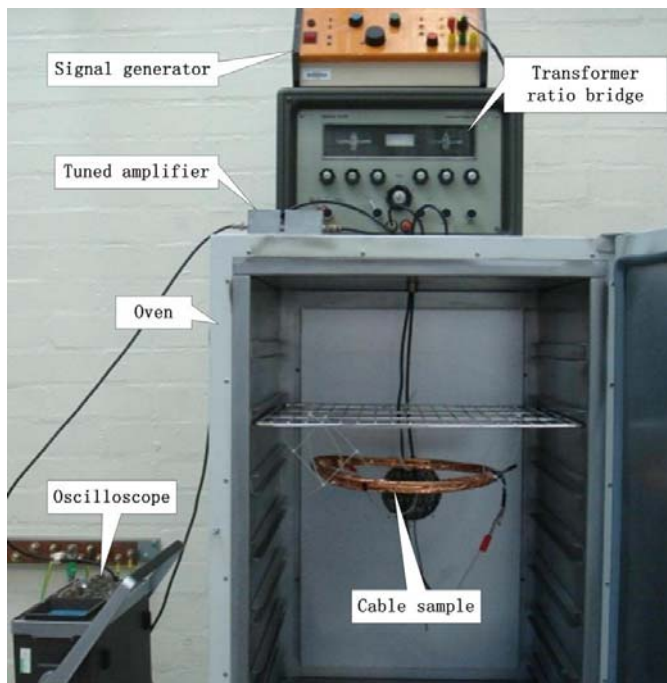


Figure 3.17 Transformer ratio bridge measurement system setup

The function generator is used as an external voltage source for the inductive bridge. The sinusoidal voltage is applied from the secondary windings of the bridge on the cable sample in the oven. According to the principles introduced in chapter 2, anti-phase voltage is therefore applied on the standard variable impedance inside the bridge. By adjusting the capacitance and conductance taps, the currents from the two halves of the bridge will be neutralized only when the impedance is the same as that of the cable

sample, which is hung in the oven for temperature control. The balance detector on the bridge shows null when the bridge is balanced. For higher resolution, the balance can be more sensitively monitored by the oscilloscope, which is connected to externally monitor the bridge. With the help of a tuned amplifier, the balance can be detected below 1kHz and the system frequency range has been extended down to 300Hz. Before measurement, the system can be calibrated with null buttons to cancel out the lead effect and background noises. For the transformer bridge system, the output voltage is limited below 2Vrms. A higher output voltage may cause the output voltage waveform to be distorted, because a higher current would be required for the secondary windings and this could saturate the winding coils.

The specifications of the transformer ratio bridge system are:

- frequency range: from 300Hz to 10kHz
- applied voltage: from 0 to 2Vrms
- capacitance range: from 1 to 999pF
- conductance Range: from  $10^{-9}$ S to  $10^{-6}$ S
- $\tan\delta$  range:  $>10^{-5}$
- temperature range: from 20°C to 120°C (from 293K to 393K)

### 3.2.3 Time domain charging/discharging current technique in the range from 1Hz to 250Hz

Because of the sensitivity limit of frequency domain techniques, time domain dielectric spectroscopy was used in this study to fill the gap between the other two frequency domain techniques in this study, as shown in Figure 3.18.

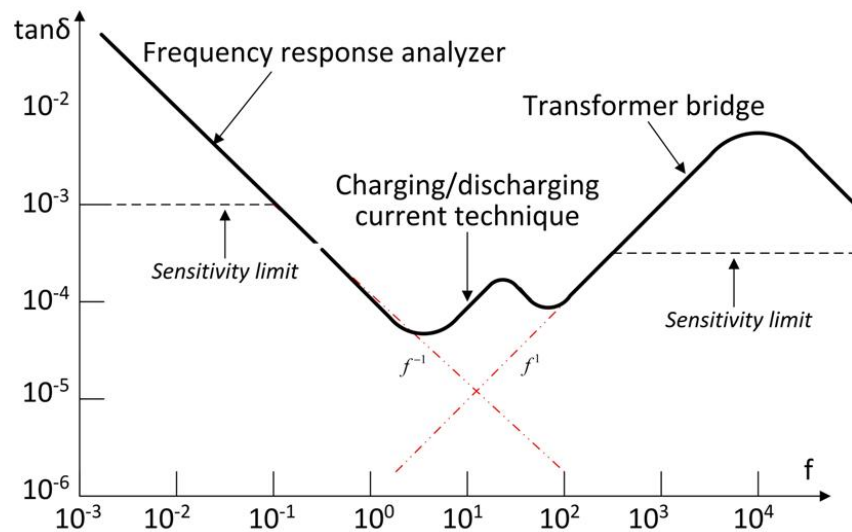


Figure 3.18 Combination of three dielectric spectroscopy techniques

The charging/discharging or polarization/depolarization current measurement system has been designed and developed to meet the requirement of very low loss power cable measurement. As introduced in chapter 2, the charging/discharging system measures charging and/or discharging currents versus time. The time domain data can be transformed into frequency domain to obtain frequency spectra of permittivity and loss tangent. For low loss measurement of power cables, the current sensitivity and anti-noise methods are important for accurate measurement. In this research study, the experiment system was developed with two different designs. Based on the problems that were found in the original designed system, a novel system has been finally

developed with the ability to measure the loss tangent of the model power cables in the frequency range from 1Hz to 250Hz.

### ***3.2.3.1 The original experiment system design***

The original charging/discharging experiment system was designed with a commercially available HVDC supply (Glassman Ltd), self made high voltage switch, Keithley picoammeter model 6485 and protection circuit, as shown in Figure 3.19. When measuring the cable sample in the test unit, the switch-on of the power supply starts the charging current measurement and the high voltage switch controls the commencing of discharging current measurement. The current is measured by the picoammeter that is connected to the computer and driven by LabVIEW program. The switch-off action for starting discharging measurement can tell the computer program via parallel port so that the data storage can be synchronized with the switch action.

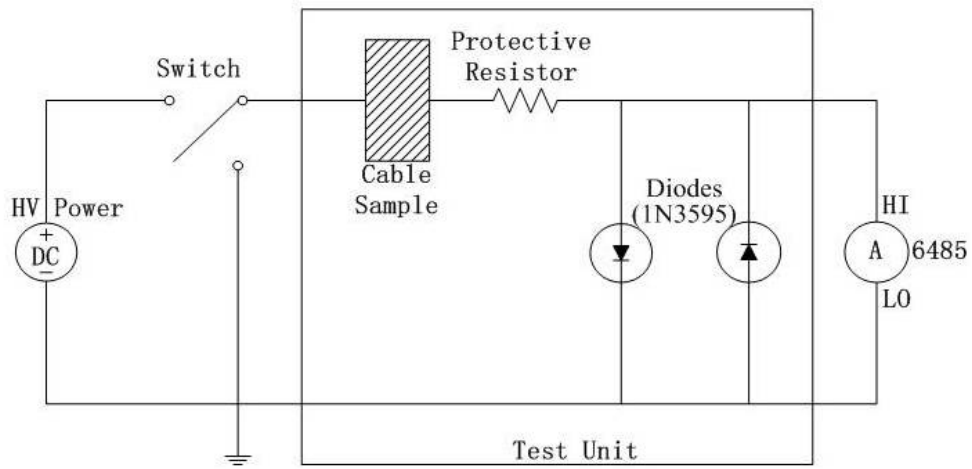


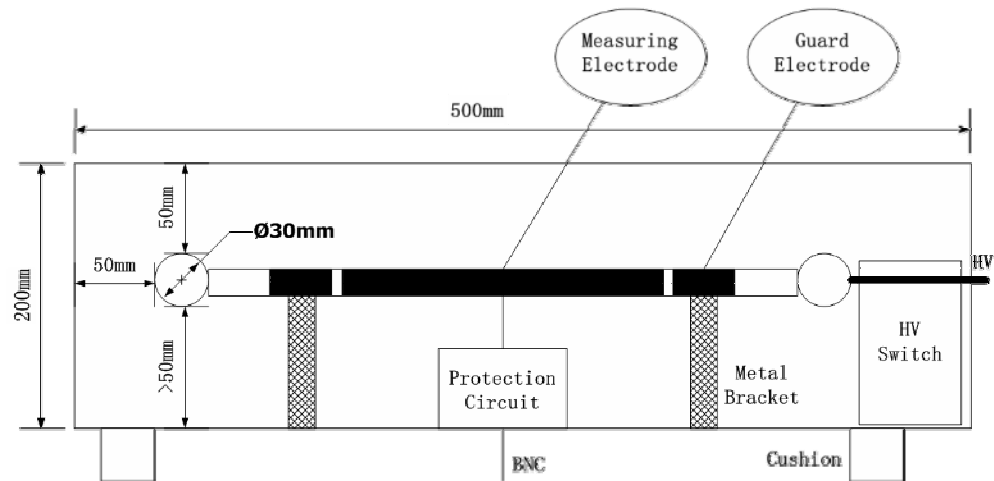
Figure 3.19 Basic design of charging/discharging experiment system

The test unit is originally designed as shown in Figure 3.20(a). It is made of an aluminium box with a copper chassis to reduce electromagnetic noise while the copper

chassis could maintain a good contact to ground. A three electrode system is used here. Conductor balls at both two ends of the cable sample have a diameter of 30mm which is enough to prevent corona. The gap from the balls to the metal walls is at least 50mm which could stop the danger of breakdown up to 50kV, according to the engineering consideration of 1kV/mm breakdown strength in the air. Metal brackets are used for holding the cable samples and provide a channel through which the guard electrode could be connected to the copper chassis. A high voltage switch is incorporated inside the test unit and will be discussed later. Another small aluminium shielding box is placed inside the test unit box to accommodate a protection circuit. The picoammeter incorporates protection circuitry against nominal overload conditions. However, a voltage higher than the maximum voltage (220V Peak) value for the selected current range, and the resultant current surge could damage the input circuitry [127]. Adding a resistor and two diodes (1N3595) provides considerable protection. The resistor must be large enough to limit the current through the diodes to 20mA or less, and be large enough to withstand the supply voltage. A  $5M\Omega$  carbon film resistor is enough to limit the current to 10mA when the voltage is 50kV. The two diodes prevent voltages of more than about 0.6V appearing across the input of the picoammeter even when the voltage polarity changes. They are put inside the light-tight conductive shield because their light sensitive property would cause noise when exposed to varying light intensity. A photo of the test unit is shown in Figure 3.20(b).

The high voltage switch plays an important role to switch charging current measurement to discharging current measurement. A high voltage switch was designed as shown in Figure 3.21. The main part (Figure 3.21(a)) is made of nylon and its dimensions are designed so that it will just fit into the test unit with good insulation. A switch bar (Figure 3.21(b)) with metal body and nylon handle is used to change the

measurement from charging to discharging. Through the metal balls and domes high voltage can be applied to the cable sample for charging current measurement. When discharging measurement should start, the switch bar is pressed to the end of the nylon box as quickly as possible in order to save as much high frequency information as possible.

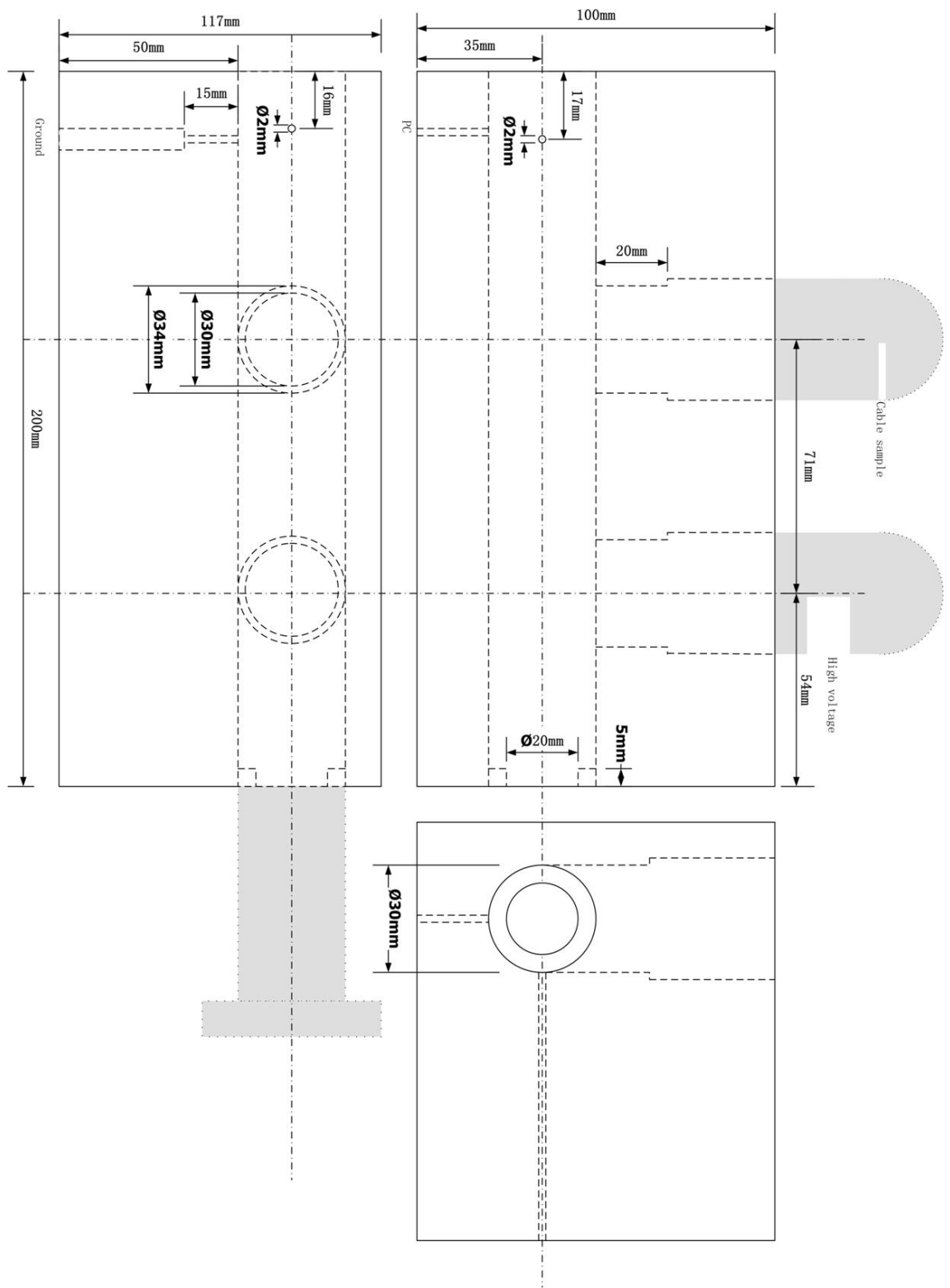


(a) the high voltage cable sample test unit design

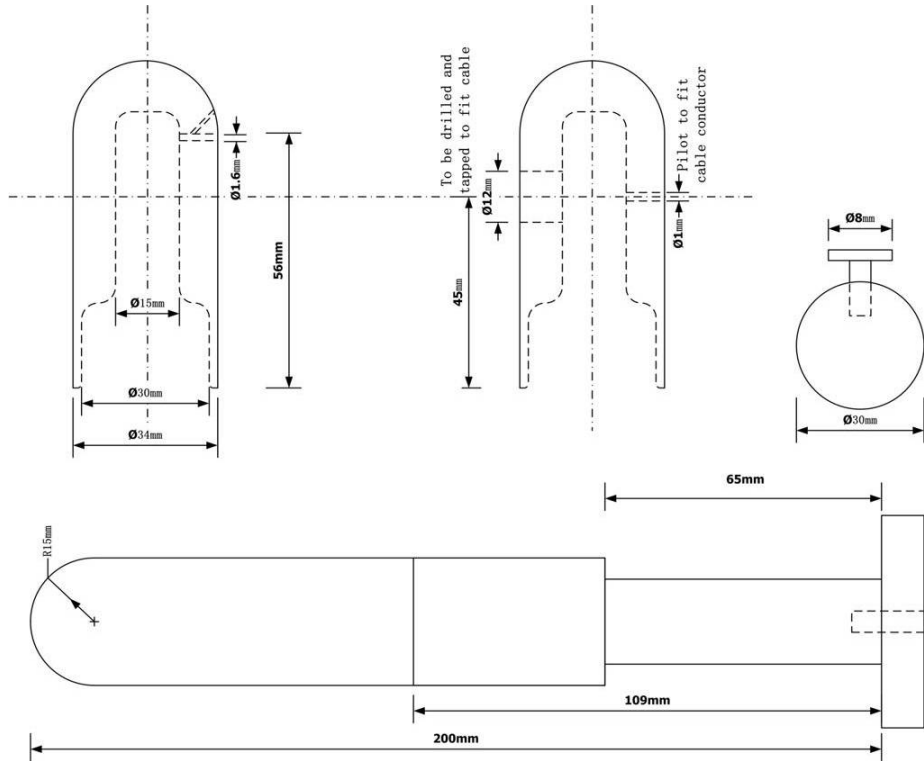


(b) photo of the test unit containing high voltage switch and a cable sample

Figure 3.20 High voltage test unit for the charging/discharging experiment system



(a) 3-view chart of the main part



(b) fittings of metal contacts

Figure 3.21 The high voltage switch design for charging/discharging experiment

There are two spring loaded contacts in the switch, one of which is connected to the copper chassis as ground connection. The other one is connected to the computer's parallel port through a communication circuit, as shown in Figure 3.22. When the charging current is measured, the spring loaded contact will float and 5V DC power will drag the port to logical "1" through a  $1k\Omega$  resistor. Pin 1 of parallel port (Strobe) provides logical "1" to pin 10 (Ack), which tells LabVIEW program that charging current is being measured. When the high voltage switch is pressed, the discharging current measurement starts. At this starting point, the spring loaded contact will be grounded and make pin 10 logical "0". This design can tell the computer software to

change accordingly when discharging begins. A 5.1V breakdown diode is also in the circuit to protect the input port in case there is too much residual charge from the high voltage switch.

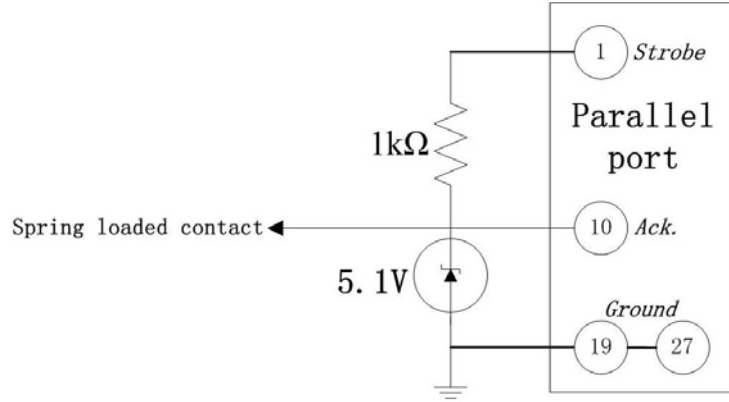


Figure 3.22 Parallel port control for discharging current measurement

LabVIEW 8.0 (Laboratory Virtual Instrumentation Engineering Workbench) was originally chosen as a program platform for the charging/discharging system. LabVIEW is a platform and development environment for a visual programming language from National Instruments. It is commonly used for data acquisition, instrument control, and industrial automation on a variety of platforms including Microsoft Windows, various flavors of UNIX, Linux, and Mac OS [128] [129]. In order to measure precisely the extremely small current, a Keithley picoammeter 6485 is used. A picoammeter is an ammeter built along the lines of the ammeter function of an electrometer [130]. LabVIEW also has a support for the Keithley picoammeter 6485 so the instrument driver could be programmed using the function toolbox.

The program was designed to have the function of measuring charging and discharging currents separately. The main software flowchart is shown in Figure 3.23. Before running the program, it is important to leave the picoammeter or electrometer power on

for at least 1 hour. This warming up period makes sure the instrument has the most accurate performance, especially for low level measurements. Background noise from the earth or Johnson noise from electric components should also be measured, stored and subtracted in the end. In the main program, some basic parameters, which include acquisition interval and measurement points, can be defined before measurement starts and some other initialization for the program interface will also finish firstly. Following the initialization, background noise data is loaded for correction of measurement data. Then the program will wait for the start button to be pressed when the high voltage is applied, after which the charging current is measured until the input port changes to logical “0” which means the high voltage switch is pressed to the discharging position. Then, discharging current will be measured according to the set points in the program. Charging and discharging currents are shown in real time in the program with both linear and logarithmic scales. All measurement data is saved for further analysis.

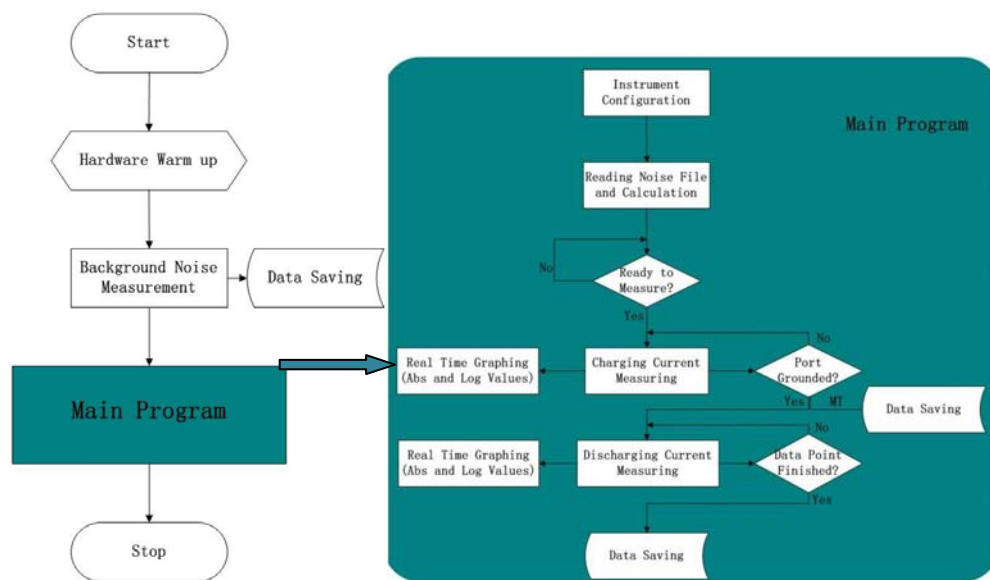


Figure 3.23 LabVIEW program flowchart for charging/discharging experiment system

### **3.2.3.2 Problems with the original experimental system**

A photo of the original charging/discharging system is shown in Figure 3.24. A Glassman high voltage DC power supply is used to supply up to 15kV on the 13cm cable sample inside the test unit in a fridge which is used as a temperature controller. High voltage cable glands are used to prevent leakage current and breakdown. Charging and discharging currents can be measured through a BNC coaxial cable that connects the protection circuit of the test unit to the input of the picoammeter. A GPIB card is used for instrument control and data acquisition by the LabVIEW program. When the high voltage DC power supply is switch on, the program should be clicked to run at the same time. When the high voltage switch in the temperature-controlled cabinet is pressed, the sample starts discharging and the status change is automatically detected by the program via a computer parallel port.



Figure 3.24 Charging/discharging experiment system with picoammeter

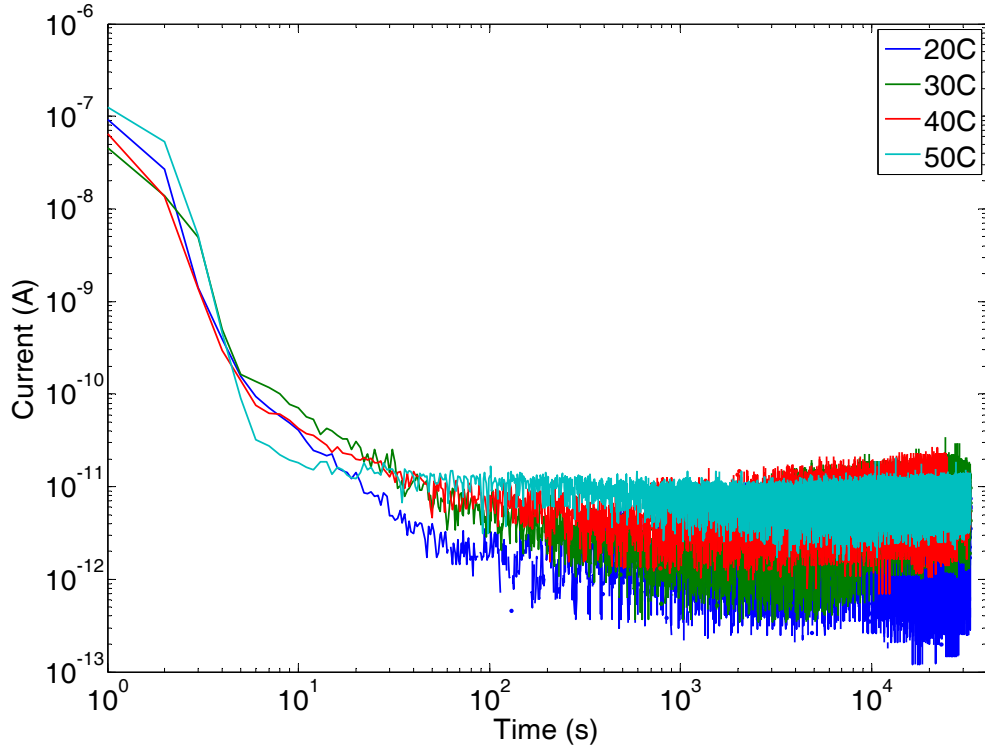


Figure 3.25 Charging current measurement on cable AAA

Typical charging current measurement results on a homo-polymer cable (AAA) is shown in Figure 3.25. The measurement was taken from 1s to  $3 \times 10^4$ s (9 hours) at different temperatures. The current decayed from about  $10^{-7}$ A to  $10^{-12}$ A in the first 100s. Afterwards, the current was in the noise floor and it cannot be correctly measured. The problem is caused by two reasons:

- The cable sample is too short to allow detectable current flowing through the insulation. According to  $G = \frac{2\pi\sigma L}{\ln(r_o/r_i)}$ , the conductance of the cable sample is proportional to the sample length, provided the conductivity is constant. Therefore, increasing the cable sample length can increase the current at the same applied voltage. When the current is much bigger than the noise floor, the charging and discharging process can be precisely measured. Based on tests for

all dielectric spectroscopy techniques, the minimum cable sample length has been determined as 5m.

- The noise from the power supply is another important issue for charging/discharging current measurement. The noisy measurement results, shown in Figure 3.25, was found to be at the level of  $\pm 5\text{pA}$ , which is difficult to tell the actual conduction of cable sample even using long time averaging method. The reason is that the commercial supply converts mains frequency voltage with power electronics converter and there are small high frequency fluctuations at the output. This voltage fluctuation is not negligible for the low current measurement on XLPE cables, according to equation

$$i = \frac{V}{R} + C \frac{dV}{dt} \quad \text{Equation 3-8}$$

where  $i$  is the total measured current,  $V$  is the applied DC voltage,  $R$  is the cable insulation resistance and  $C$  is the cable capacitance. Because the DC conduction part is very small around pA, the small voltage fluctuation will cause big influence in the total detectable current through the sample. More details can be found in [131].

The charging/discharging current in the first second is important in this study because the frequency range gap between the frequency response analyzer and the transformer ratio bridge can be covered within this time duration. In order to measure the dielectric response over the range from 1Hz to 200Hz, for example, the sampling rate should be at least 400 sample/second. From the measurement results in Figure 3.25, the sampling rate is 1 sample/second. It is difficult to increase the sampling rate further because the

instrument has a response time of about 16ms and there is no precise synchronization at the starting point. The problem was found to originate mainly from the electrometer but also due to the limited speed of the LabVIEW program. The internal circuit structure of a typical electrometer, including Keithley picoammeter 6485, is shown in Figure 3.26. The input signal is magnified by preamp according to a different function/range. The output of the preamp amplifies the original signal. The pre-amplified signal is sampled by a micro-processor, which determines the further ranging amplifier for final output. The final output is the signal after multiple amplifications, and this process needs hundreds of milliseconds typically. The sampling rate is greatly reduced using such commercial picoammeter or electrometer. Besides, LabVIEW program with GPIB has still about 20ms software delay at the beginning of the measurement. This will result in incorrect measurement data because the charging/discharging current is actually recorded 20ms after the voltage application.

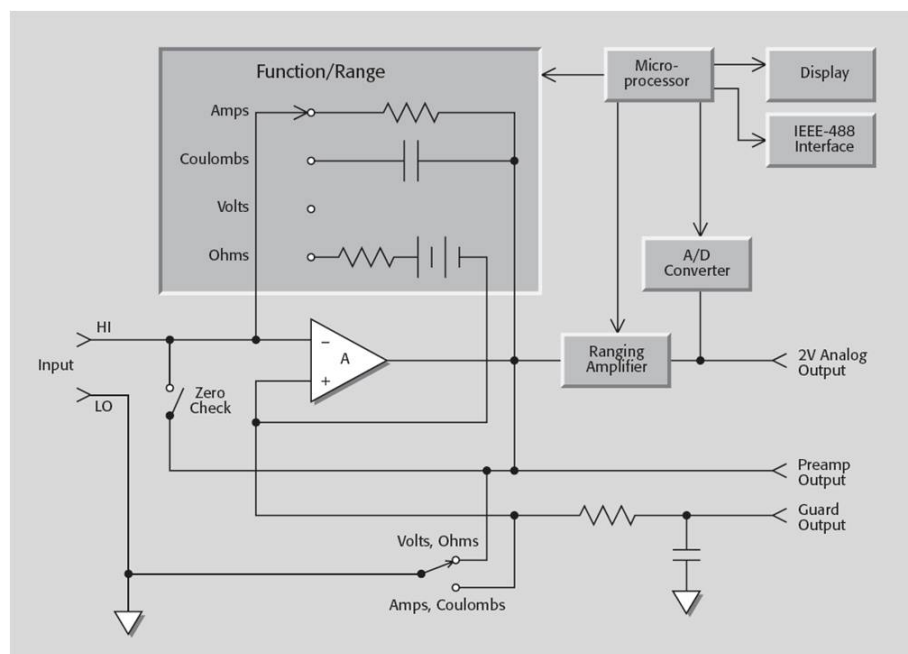


Figure 3.26 Internal circuit diagram of electrometers [130]

The principle of the charging/discharging current measurement requires that a step voltage be applied to the sample. In practice, there is always a rising/falling time for the voltage application. In order not to bring negative effect into the measurement results, the rise/fall time should be small enough for specific requirements. The commercial high voltage DC power supply in the original design was tested with a falling time of about 800ms, as shown in Figure 3.27. This substantially influences the discharging current measurement because the applied voltage cannot drop down to zero when the discharging current measurement has already started.

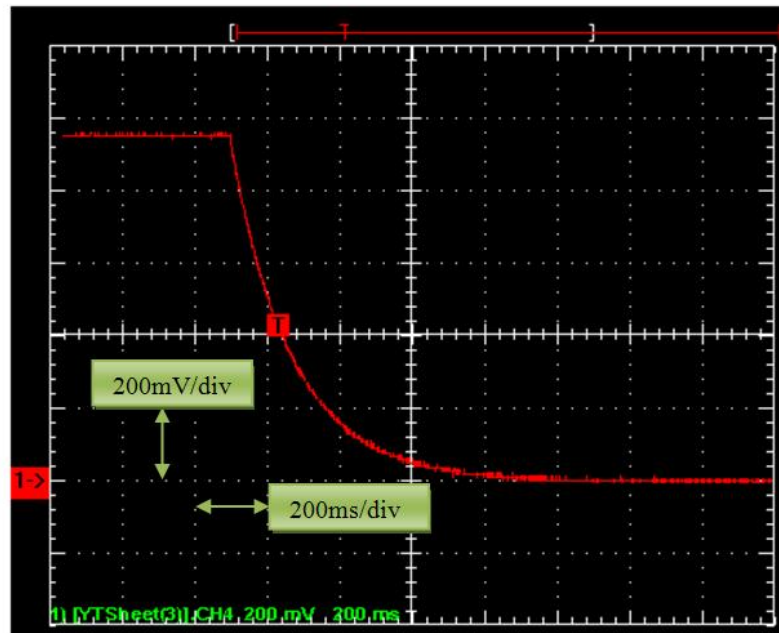


Figure 3.27 Switching time of commercial high voltage DC power supply

### ***3.2.3.3 Development of novel charging/discharging experiment system***

Based on the knowledge gained from the original charging/discharging experimental system, a novel measurement system has been developed, as shown in Figure 3.28. The new system incorporates a 1kV battery supply, high voltage toggle switches, a potential

divider as voltage monitor, a current-voltage converter and a storage oscilloscope. The commercial high voltage DC power supply was replaced by a hand-made battery supply with a very low ripple output voltage so that the conduction current of cable insulation can be accurately measured. High voltage toggle switches are used to make faster switching actions. As required from the other two measurement techniques, the switch should ideally have falling (switch-off) time less than 1ms, in order to include a frequency response up to 500Hz by Nyquist law. A resistive potential divider can be used to monitor the response. The charging/discharging current is converted by a fast converting electrometer. The voltage tolerance of the current-voltage converter is also considered because the transient current may exceed the maximum input voltage and damage the circuit. The oscilloscope is a digitizer of data with different channels working at the same input signal to overcome the digitizing problem. In this study, a four channel storage oscilloscope is used. One channel is connected to the potential divider as a voltage monitor and measurement trigger; the other three channels are in different resolutions from 1mV/div to 2V/div. By using several channels on the oscilloscope at different gains, the problems associated with changing ranges on the electrometer are obviated. This allows the current to be measured as it decays quickly over several decades without the necessity to change ranges on the oscilloscope. The data from different channels can be merged together.

The structural design of the DC battery supply, consisting of a high voltage toggle switches and resistive potential divider, is shown in Figure 3.29. One hundred and twenty 9V batteries are connected in series to get approximate 1kV voltage. The double-pole toggle switch can provide both positive and negative polarities. Another single-pole switch is used to earth the sample for discharging current measurement. A

high voltage capacitor is used together with the resistance potential divider to help hold the high voltage during the switching transient.

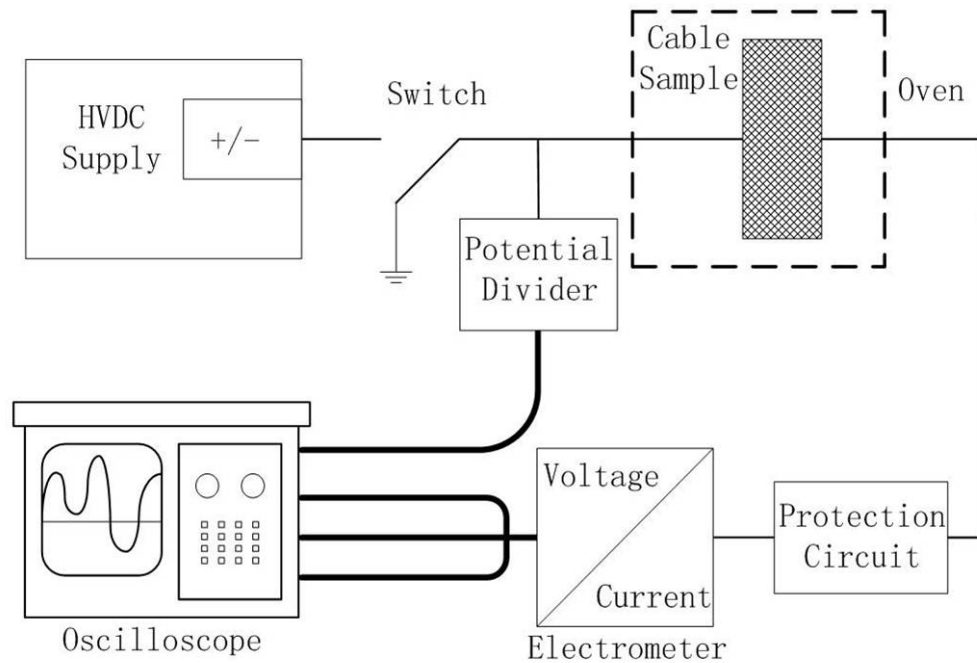


Figure 3.28 Discharging current measurement system setup

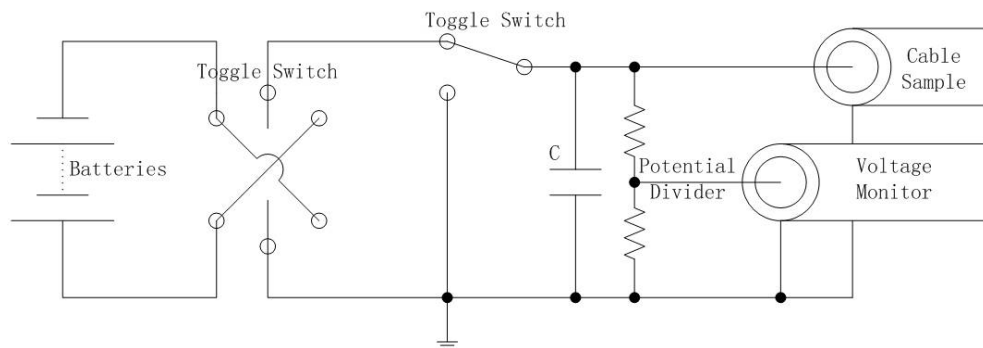


Figure 3.29 High voltage battery supply design diagram

Photographs of the actual high voltage battery supply are shown in Figure 3.30. The left photo shows the inside view; 30 batteries of the top layer are inter-connected in series while the other three layers are below the top one. A shielding box is used to prevent

environmental noise and provide a solid container for the batteries. Plastic foams and wooden plates are used to separate different layers and prevent any contact with the shielding box. The final output is wired into a plastic box on top of the aluminium shielding box, as shown in the right photo with a top view. A high voltage BNC connector is used to output the high voltage and another common BNC connector is the monitor output. Polarity switch and charging/discharging switch can be controlled from the top of the plastic box.



Figure 3.30 Photos of high voltage battery supply

The response time of the supply was checked by an oscilloscope through the monitor connector. The response time can be found in Figure 3.31 and a comparison between the battery supply (blue curve) and the former commercial one (red curve) can be made (note that the two curves have different time scales). From the results, the battery supply has a falling time of about  $500\mu\text{s}$ , while the commercial one has a falling time of about 1s. Therefore, the new battery supply can provide more than 1000 times faster response time and guarantee the switch action will not have influence on discharging current measurement.

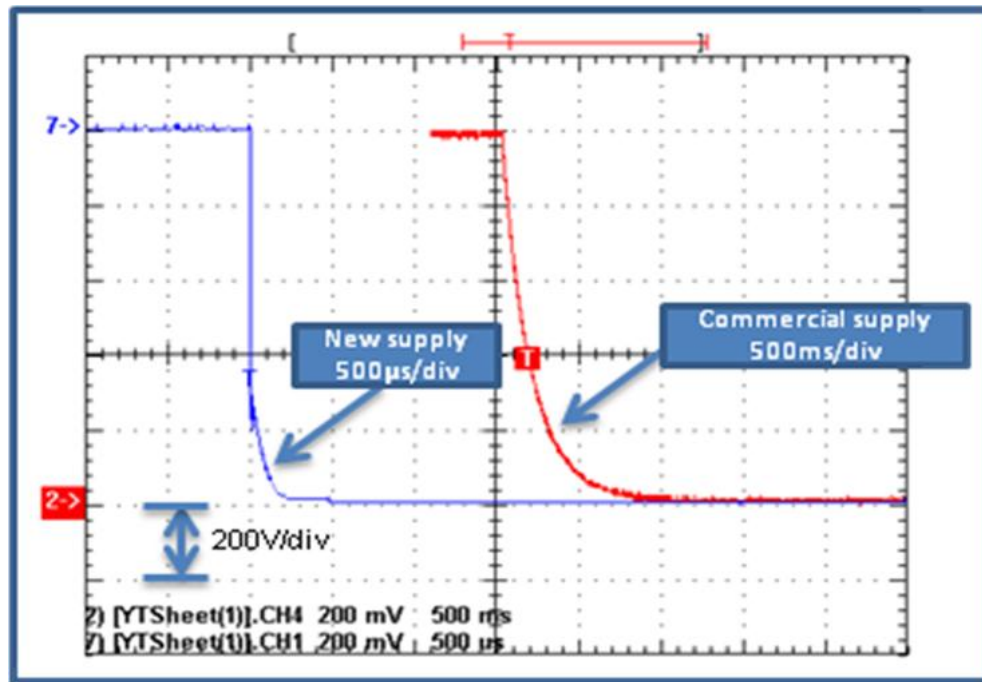


Figure 3.31 Comparison of response time between commercial supply (red) and the battery supply (blue)

Because the new supply is made of DC batteries, there are no high frequency harmonics or ripple on the output voltage. The only source of voltage fluctuation might be from the environment temperature, which influences the chemical reaction rate inside the alkaline battery. In order to make sure this will not cause a problem to the conduction current measurement, two batteries in series are measured under different temperatures from 10°C to 50°C. The result is shown in Figure 3.32, indicating a 0.3V/50°C variation that is equal to 18V/50°C or 0.36V/°C for 120 batteries. With a 5m cable sample in our study, the cable's capacitance can be calculated as about 800pF. Assuming 1pA current would be damageable to the results measured from this sample, according to equation

$$i = C \frac{dV}{dt} \quad \text{Equation 3-9}$$

the maximum voltage variation is

$$\frac{dV}{dt} = \frac{10^{-12}}{800 \times 10^{-12}} = 0.00125V / s$$
Equation 3-10

Therefore, the maximum temperature variation in this case is

$$\frac{0.00125V / s}{0.36V / C} = 0.0035^{\circ}C / s = 0.2^{\circ}C / minute = 12.5^{\circ}C / hour$$

This temperature variation is not likely to happen in the laboratory environment, so the voltage variation due to temperature will not influence the conduction measurement of XLPE cables.

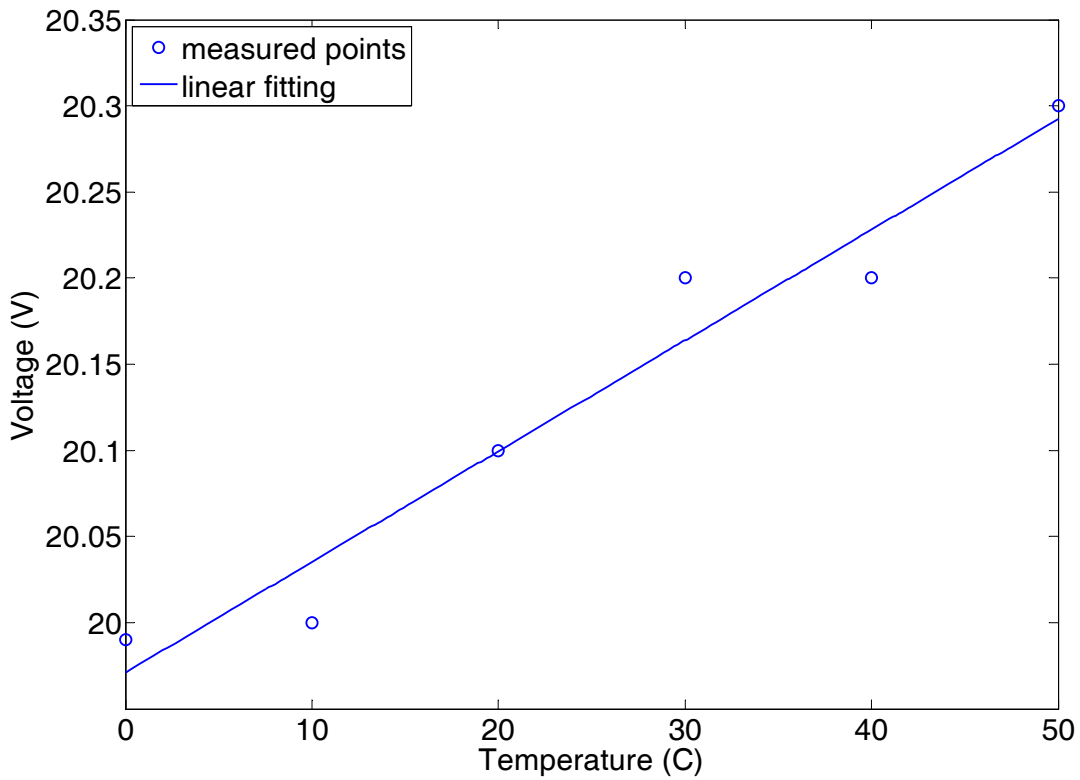


Figure 3.32 Temperature variation of two batteries in series

The commercial electrometer was replaced in this design by a bespoke current to voltage converter. The current to voltage converter is required to have reliable amplification in the frequency range for discharging current measurements. The current to voltage converter has different ranges. Ideally, the higher amplification range should be used, but the -3dB bandwidth becomes smaller as the gain is increased. The ranges with  $10^{-8}$ A/V (range 2) and  $10^{-7}$ A/V (range 3) have been tested. A function generator was used to generate signals of different frequencies from 10Hz to 1000Hz. Bode plots of the measurement results have shown that the -3dB frequency of Range 2 is at 30Hz above which the attenuation cannot be accepted for the measurement. Range 3 has improved -3dB amplitude attenuation frequency at about 280Hz (Figure 3.33) and has been chosen to convert the current in this measurement. Range 2 can still be used to increase the current sensitivity, but only the current at longer time than 1s is not affected by the bandwidth limitation.

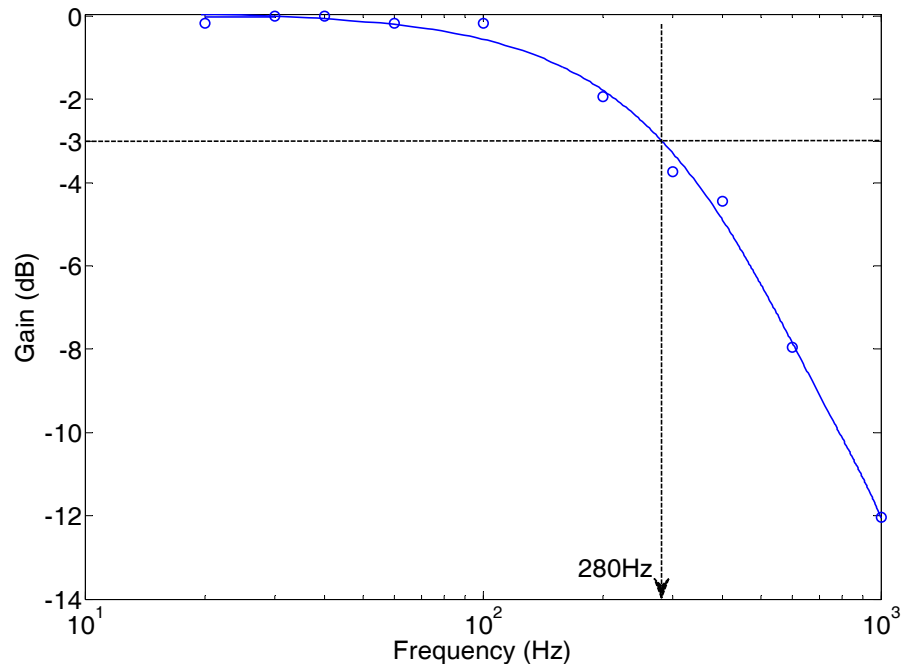


Figure 3.33 Bode plots of current-voltage converter

The frequency range from 1Hz to 250Hz requires the measurement to start within the first 1/500<sup>th</sup> of a second with a subsequent sampling rate of 500 samples/second and to finish at 1s. Since the digitizing speed of the oscilloscope can provide up to GHz sampling rate, measuring the discharging current of the cable samples correctly and accurately in the first 1 second needs several considerations about the influence of protective resistor and the current to voltage converter bandwidth. As shown in Figure 3.34, equivalent circuits were built to study the effects of system components on the measurement accuracy of the model cable samples. Similar to the values of the cable samples, C1, C2 and R2 simulate their equivalent circuit with a loss peak, which can vary with different R2 values. C1 and C2 are fixed capacitance of 1nF and 200pF. R2 has up to five different values from 50MΩ to 500MΩ.

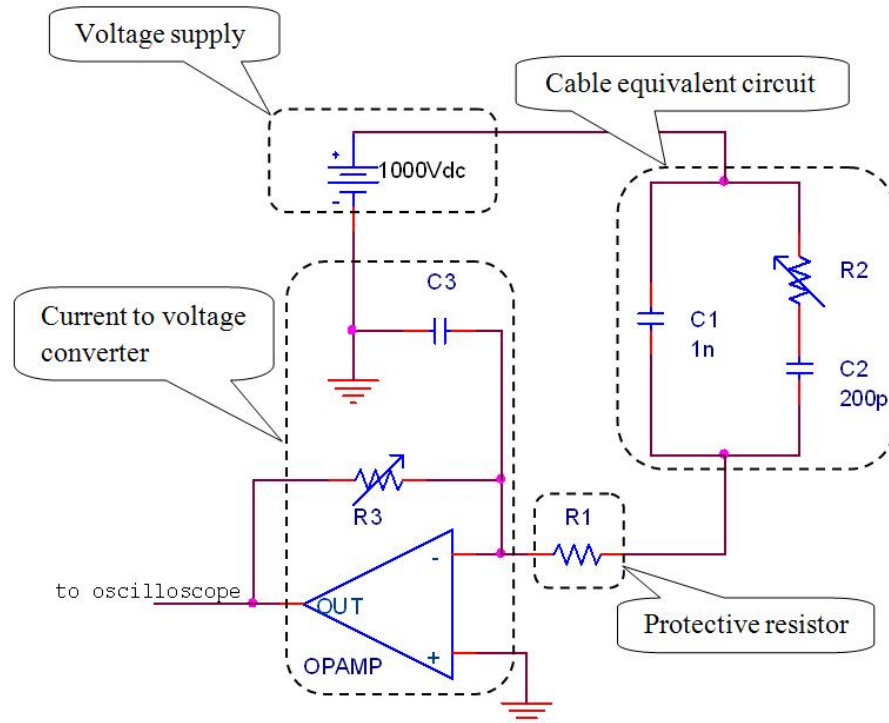


Figure 3.34 Equivalent circuit of charging/discharging current measurement system

With the protective resistor  $R1=2M\Omega$  and the current to voltage converter in range 3 (250Hz bandwidth), the discharging current measurement results are shown in Figure 3.35. There are five results for different  $R2$  values. The sampling rate is 10k sample/second and the measurement duration is 0.5s. Two different processes can be identified. In the very beginning with 2ms, the current for all cases decayed fast down to  $10^{-6}A$ . Then, the second process started to dominate with different decaying currents, which are due to different  $R2$  values. Therefore, the second process or long-term discharging currents represent the relaxation of the test object, while the beginning decaying currents are just the response of the protective resistor in series with the test sample. The time constant of the circuit due to protective resistor

$$\tau = R1 \times C1 = 2M\Omega \times 1nF = 2ms$$

Therefore, in frequency domain, there should be a peak at the frequency that can be calculated by

$$\omega\tau = 2\pi f\tau = 1 \quad \text{Equation 3-11}$$

The peak frequency

$$f = \frac{1}{2\pi\tau} = \frac{1}{2\pi \times 2 \times 10^{-3}} = 79.6Hz$$

This loss peak at 79.6Hz brought by the protective resistor can be found in Figure 3.36. The discharging currents in Figure 3.35 were transformed into frequency domain using Discrete Fourier Transform (DFT), which is introduced in details in section 4.3.2, and the loss part – imaginary permittivity was obtained. For different  $R2$  values, the loss peaks were calculated by Equation 3-11. There is generally coherence between the

transformed result of the measurement data and the calculated result of the loss peak frequencies, although disagreement is found due to the resolution of the measurement system. However, there is a much bigger loss peak, regardless of R2 value, at about 80Hz. This further proved that the protective resistor can bring big influence to the discharging current measurement of the model cable samples. Correct results cannot be measured if this loss peak is not removed from the frequency range from 1Hz to 250Hz.

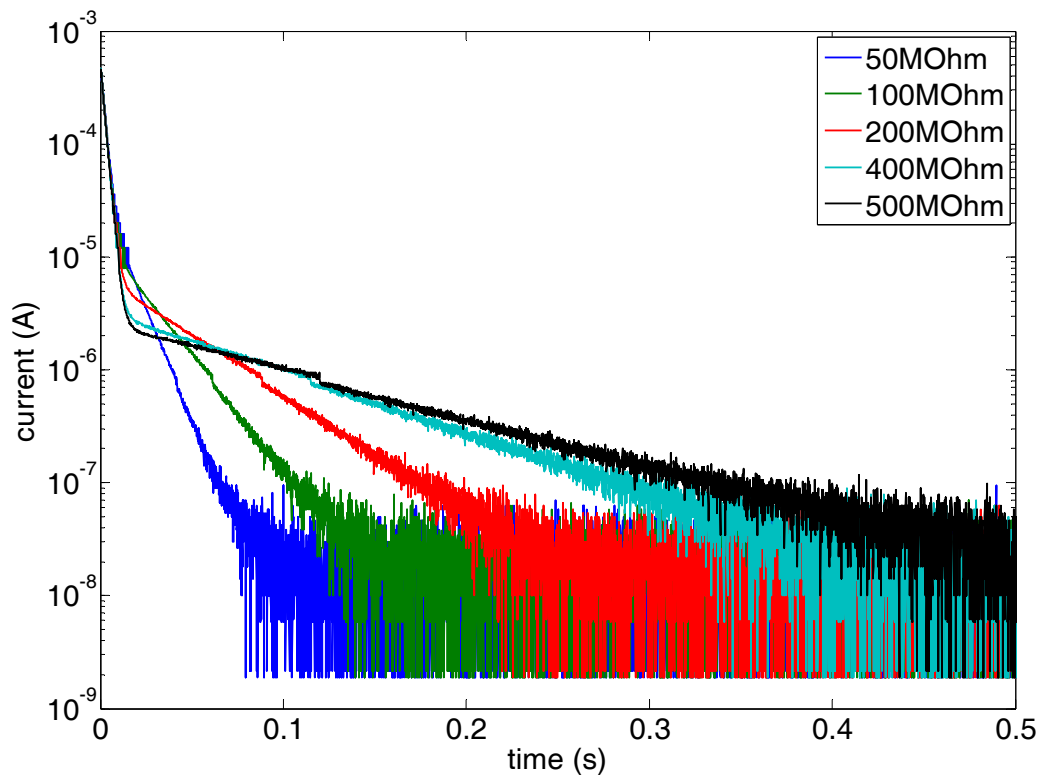


Figure 3.35 Discharging current of system equivalent circuits

Efforts have been made to remove the influence of the protective resistor while keeping the current to voltage converter safe from breakdown due to overload current, which is typically several milli-amps for an operational amplifier. In order to protect the current to voltage converter and keep it operate with high precision, input current less than 10mA should be guaranteed. Hence, 100k $\Omega$  protection was chosen as optimum value.

The equivalent circuit measurement result with  $100\text{k}\Omega$  is shown in Figure 3.37. This resistance is 20 times smaller than the result in Figure 3.36. After transforming the discharging current into frequency spectra, the induced loss peak can be shifted to 20 times higher frequency at 1492Hz, which is 6 times higher than 250Hz – the maximum frequency for this technique. As a result, the response of test sample can be correctly measured and the influence of the protective resistor has been reduced to minimum. For all the discharging current measurement in this study, this  $100\text{k}\Omega$  protective resistor is jointly used with two back-to-back diodes in a shielding box between the cable sample and the current to voltage converter input.

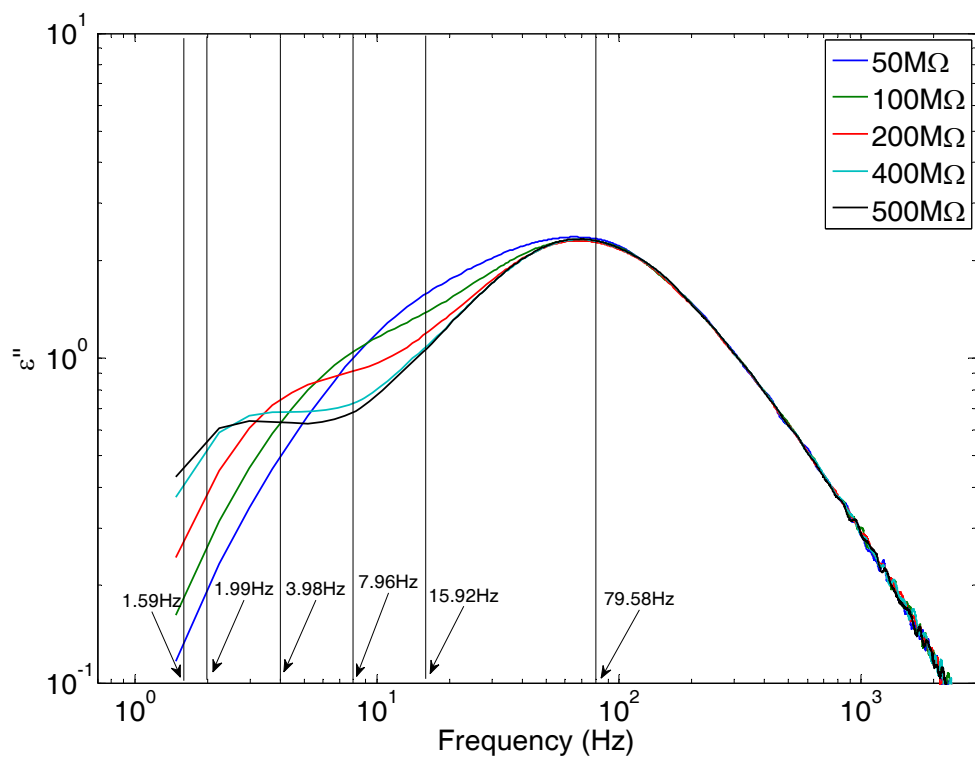


Figure 3.36 Frequency spectra (imaginary permittivity) of the discharging currents measured on the system equivalent circuits with  $2\text{M}\Omega$  protection

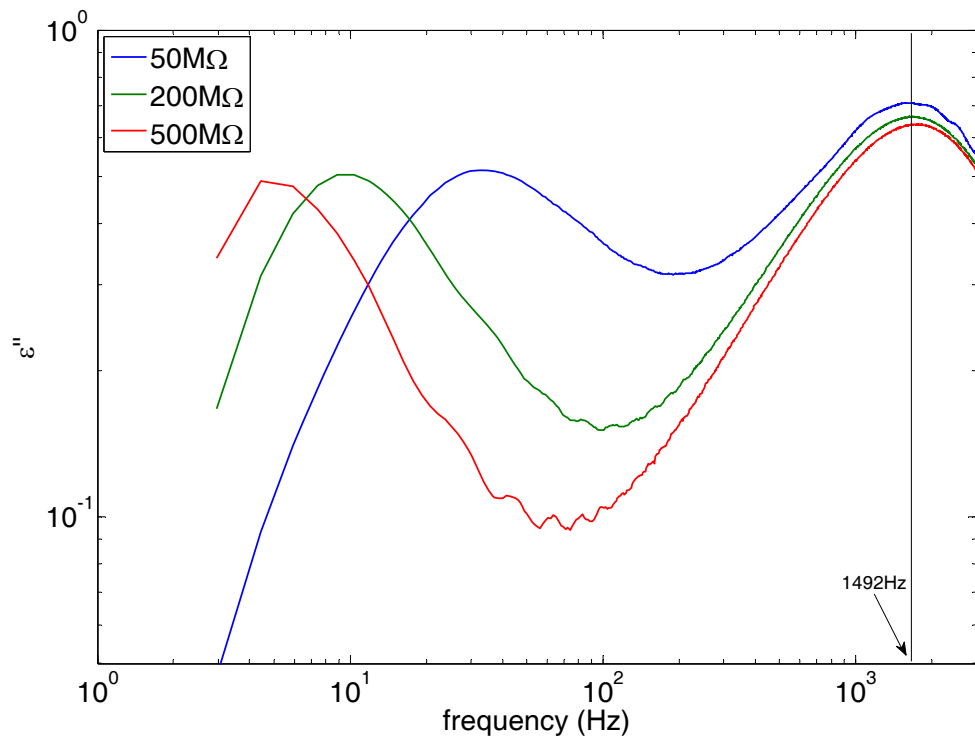


Figure 3.37 Frequency spectra (imaginary permittivity) of the discharging currents measured on the system equivalent circuits with  $100\text{k}\Omega$  protection

### **3.2.3.4 Experiment system specifications**

The novel charging/discharging experiment system was used to measure various types of model cables in the time duration from 1ms to 10s. Discharging current is measured to study the depolarization of the cable insulation. Charging current is then measured to study the conductivity of different cables. By adding the contribution due to DC conductivity, the dielectric spectra in the frequency range from 1Hz to 250Hz can be finally obtained. During the measurement, the cable sample is put in an oven under a fixed temperature for more than three hours to reach thermal equilibrium and then the battery power supply applies 1kV to the sample for about three minutes, which ensures that the sample is fully charged for discharging current measurement (recommended charging time is at least 10 times longer than discharging time [2] [44]). When the high

voltage switch is switched to earth, the oscilloscope detects this action by the potential divider inside the battery supply and then triggers measurement in the other three channels, with different digitizing resolutions. Data is saved on a floppy disk of the storage oscilloscope and transferred to computer for analysis.

The specifications of the charging/discharging current measurement system are:

- applied voltage: 1kV DC
- power supply rising/falling time: 50ms/500 $\mu$ s
- discharging current measurement time: 10s
- oscilloscope sampling rate: 500 sample/second
- frequency range: from 1Hz to 250Hz
- $\tan\delta$  range:  $>10^{-6}$
- temperature range: from 20°C to 120°C (from 293K to 393K)

### 3.3 Experimental procedures

#### 3.3.1 Degassing and ageing of the model cables

All model cables in Table 3.1 were produced and sent from Borealis in Sweden in sealed bags to prevent the cables from degassing. These “fresh” cables were cut into 5m lengths for different experiments.

In order to study the degassing effects on the conductivity of different types of the model cables, fresh cables were degassed in the air and in a vacuum oven. The fresh model cables with volatile by-products still inside the insulation were firstly measured with the battery power supply. Then, the cable samples were put in a normal oven under 80°C for five days. After this air degassing procedure, the cable samples were measured again. Afterwards, the vacuum oven was used for further degassing for another five days under 80°C. Measurement was taken on the same cable sample for comparison with previous results.

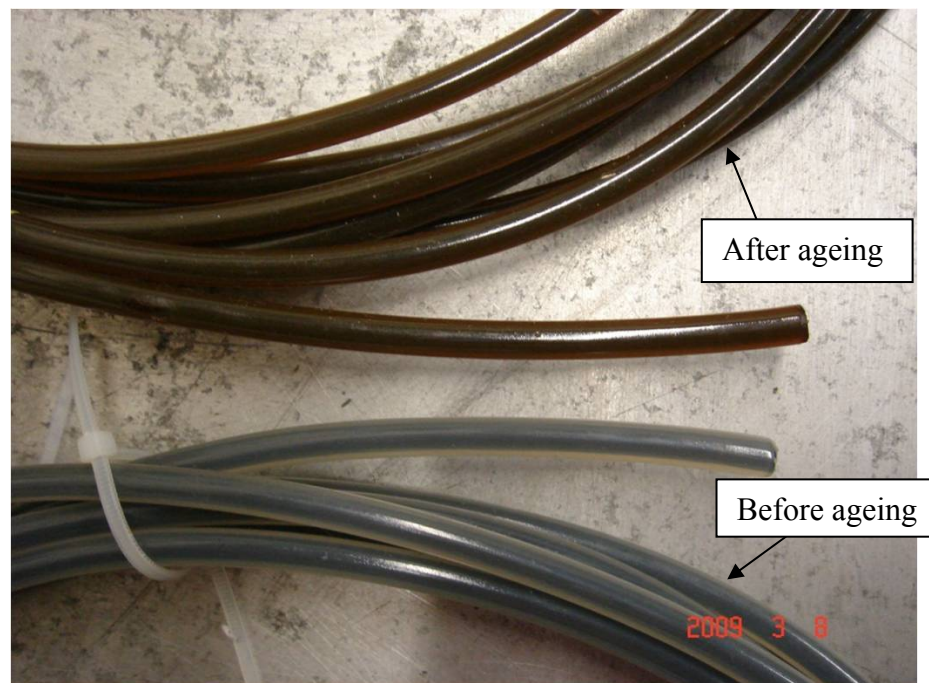


Figure 3.38 Comparison of aged and non-aged model power cables

In order to study the ageing effects, different types of degassed cable samples were thermally aged under the temperature of 135°C, which was suggested by Borealis. The thermal ageing is an accelerated ageing process, and imitates the long term actual thermal ageing condition of power cables. In Figure 3.38, the effect of ageing on cables without outer semicon layer can be observed. The colour of the XLPE insulation layer

changed from grey to dark brown, which indicated chemical reactions happened inside the insulation material. Similarly, all the other cables with outer semicon have extra dark brown colour after the thermal ageing process.

### 3.3.2 Experimental plan on different XLPE model cables

With the three dielectric spectroscopy experiment systems developed, the dielectric response over a wide frequency range, all temperatures and voltages can be studied. Different aspects of the model power cables have been studied with five kinds of experiments.

1. ***Dielectric spectroscopy measurement of different model cables.*** As the most important aim of this research project, the dielectric response of model cables with different insulation and semicon shields was studied. Measurements on different model cables with all three dielectric spectroscopy techniques were carried out to examine the electrical properties and loss mechanisms. This wide range of frequencies and temperatures will help to understand the origins of dielectric loss in cable insulation.
2. ***Degassing effects study.*** Since degassing can practically enhance the insulation performance and is the most popularly used method to make the fresh cables ready for use, degassing effects on different cables were studied by conductivity measurement, which is an effective way to study the influence of by-products.
3. ***Ageing effects study.*** The electrical properties after ageing determine the reliability of power cables in operation. Based on the apparent difference between degassed and aged cables, as shown above in Figure 3.38, the

conductivity and discharging current were measured on different cables to study the thermal ageing effects.

4. ***Semicon material measurement as a complementary study.*** The dielectric loss of cables is dependent on the semicon shields, as some studies in recent year have found [118] [119] [120]. As an essential part of the power cable insulation, both standard and super-smooth semicon materials were measured as complementary experiments to study the origin of dielectric loss in the model power cables.
5. ***High electric field measurement at power frequency 50Hz.*** Using Schering Bridge, the field dependence of the dielectric loss of model power cables were studied at different voltages.
6. ***Morphologic study with scanning electron microscopy (SEM).*** The microscopic morphology of the model cables was studied using SEM. The test results can provide some basic information of the model cables and useful reference for data analysis.

The temperature dependence was studied for all kinds of experiment, because temperature is a critical parameter for the electrical properties of power cables. According to the test results in Figure 3.39, at least three hours are needed for the cable sample to reach thermal equilibrium. Hence, for all experiment, three hours were left before starting the measurement. In order to compare various cables and different kinds of experiment, four temperatures have been studied: 20°C, 40°C, 60°C and 80°C. These temperatures can maximally cover the operating temperature of power cables without melting the cable samples.

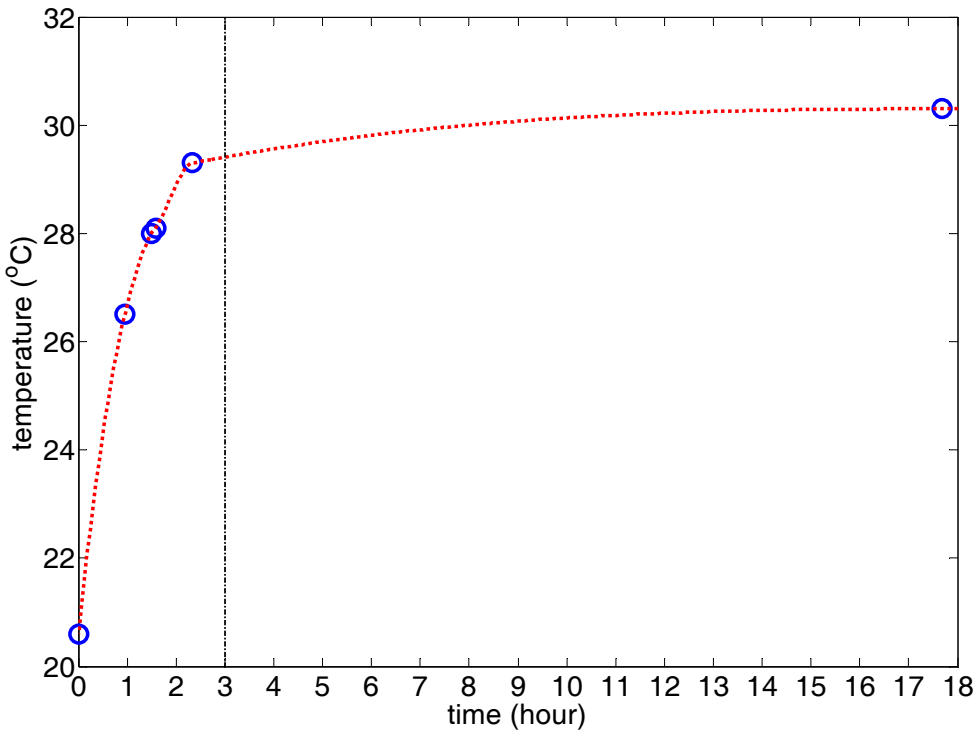


Figure 3.39 Thermal equilibrium time for model cable experiment. Measurement was made on a homo-polymer cable sample in an oven from 20°C to 30°C.

Besides the experimental work, computer simulations for analyzing the measurement data with equivalent circuit method have been used. Based on the measurement results, the thermal breakdown of the model power cables was also studied.

### 3.4 Conclusions

The sample preparation method and experimental systems are studied in this chapter:

1. A new sample preparation method for the power cable samples is proposed using the conductive adhesive copper tapes in order to keep good contact with the measuring electrode and avoid extra influence due to the outer semicon layer.

2. The FRA experimental system has a sensitivity of  $10^{-3}$  for loss tangent measurement in the frequency range  $10^4$ Hz to 1Hz. Normal mode should be used for low loss measurement.
3. A transformer ratio bridge system was developed for measuring the model cables at higher frequencies from  $10^2$ Hz to  $10^4$ Hz. Tuned amplifier was designed to extend the frequency range. Battery is used to drive the bridge with higher sensitivity.
4. TDDS system was developed to measure the frequencies from  $10^{-1}$ Hz to  $10^2$ Hz. A noise-free high voltage supply was made with batteries. The high voltage switch, protective resistor and bandwidth of current-voltage converter have been found to be critical for accurate measurement their parameters were determined experimentally for the low los measurement on the model power cables.

## 4 Dielectric response analysis of model power cables

This chapter presents the measurement data of various model power cables with the dielectric spectroscopy experimental systems developed in chapter 3. Section 4.1 analyzes the data measured using the FRA technique. DC conductivity loss in the power cables dominates the dielectric loss at low frequencies. Section 4.2 analyzes the data measured with transformer ratio bridge system. The contribution due to semicon layers has been studied with equivalent circuit modelling in MATLAB. Section 4.3 studies the discharging current measurement results and the frequency spectra found using Fourier transforms. Combination of all the data in section 4.4 provides a wide frequency range dielectric spectra that help understand the mechanisms of dielectric loss in polymer power cables. In section 4.5, the measurement results on fresh, air degassed and vacuum degassed cable samples are compared in order to find the degassing effects.

### 4.1 Dielectric response at low frequencies of from $10^{-4}\text{Hz}$ to $1\text{Hz}$

#### 4.1.1 Thermal expansion calibration

The degassed model cables of AAA, ABA, ACA, and BAB have been measured using the FRA system. Thermal expansion of the model power cables needs be considered because the cable insulation swells when the temperature increases. Complex capacitance of the test sample  $C^*$  is calculated from measured complex impedance  $Z^*$

$$C^* = \frac{1}{j\omega Z^*} \quad \text{Equation 4-1}$$

where  $j$  is imaginary unit and  $\omega$  is angular frequency. The complex permittivity  $\varepsilon^*$  can be calculated with the geometric capacitance  $C_0$

$$\varepsilon^* = \frac{C^*}{C_0} \quad \text{Equation 4-2}$$

The thermal expansion coefficient for copper is  $1.7 \times 10^{-5}/^\circ\text{C}$  and it is much smaller than the coefficient for polyethylene in Table 4.1. The length of the cable sample does not change because the inner copper conductor holds the polymer layers from expanding its length. Therefore, the assumptions have been made that the radius of the inner copper conductor and the length of the cable sample are constant during thermal expansion, the outer radius  $r_o$  is the only variable to influence the geometric capacitance  $C_0$  in the equation:

$$C_0 = \frac{2\pi\varepsilon_0 L}{\ln(r_o / r_i)} \quad \text{Equation 4-3}$$

From Equation 4-3, the empty cell capacitance  $C_0$  will be smaller when  $r_o$  increases due to thermal expansion.

Thermal expansion was corrected based on the coefficient table for polyethylene in Table 4.1. Figure 4.1 shows the real permittivity measurement results (solid lines) on a homo-polymer cable in comparison with the results after corrections for thermal expansion (dashed line). An increment of about 0.1 can be seen from  $20^\circ\text{C}$  to  $80^\circ\text{C}$ . After thermal calibration, the results have been corrected with smaller gaps between different temperatures. The gaps that are still present are due to the actual permittivity change of the material at different temperatures. The decreasing real relative

permittivity  $\epsilon'$  of polyethylene at higher temperatures was also observed and published [133], as shown in Figure 4.2. The temperature dependence of the relative permittivity  $\epsilon'$  for 12  $\mu\text{m}$  thick PE film sample was measured at the frequency of 100 Hz (result of calorimetric measurements is shown for comparison).  $T_g$  and  $T_m$  are glass transition temperature and melting point respectively. In the temperature region from 20°C to 80°C, it can be seen that the permittivity of polyethylene decreases at higher temperatures. In this study, all the measurement results were calibrated before analysis.

Table 4.1 Thermal expansion coefficient for polyethylene [132]

Celsius	Linear coefficient. ( $\times 10^{-5}/^\circ\text{C}$ )	Volumetric coefficient ( $\times 10^{-5}/^\circ\text{C}$ )
20	23.7	71
25	24.8	74
40	29	87
60	33.7	101
80	40.3	121

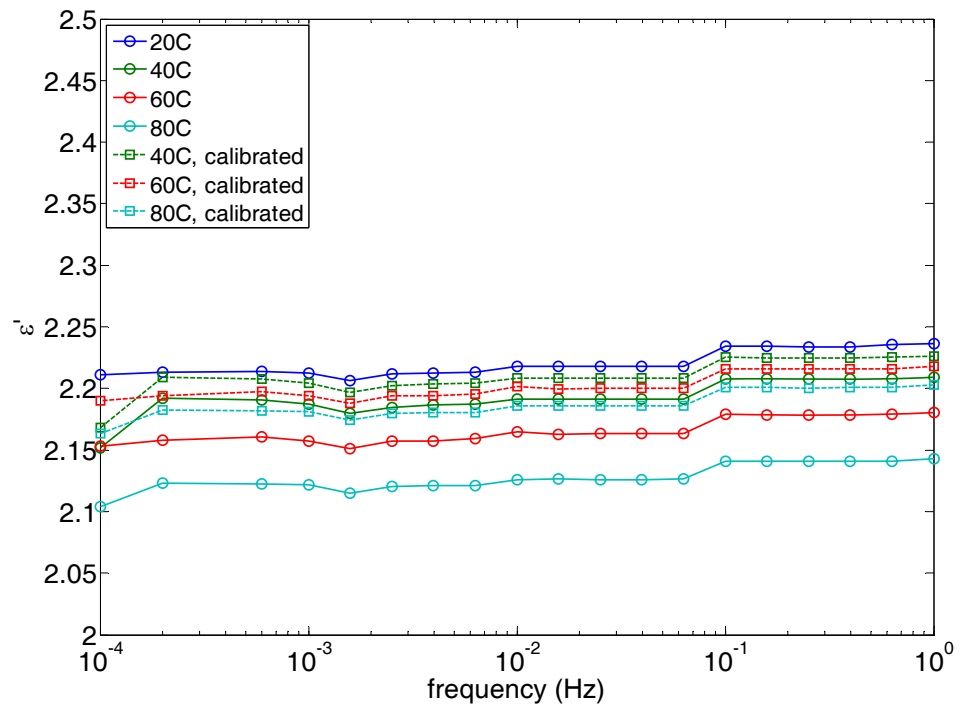


Figure 4.1 Thermal expansion calibration on  $\epsilon'$  of cable AAA

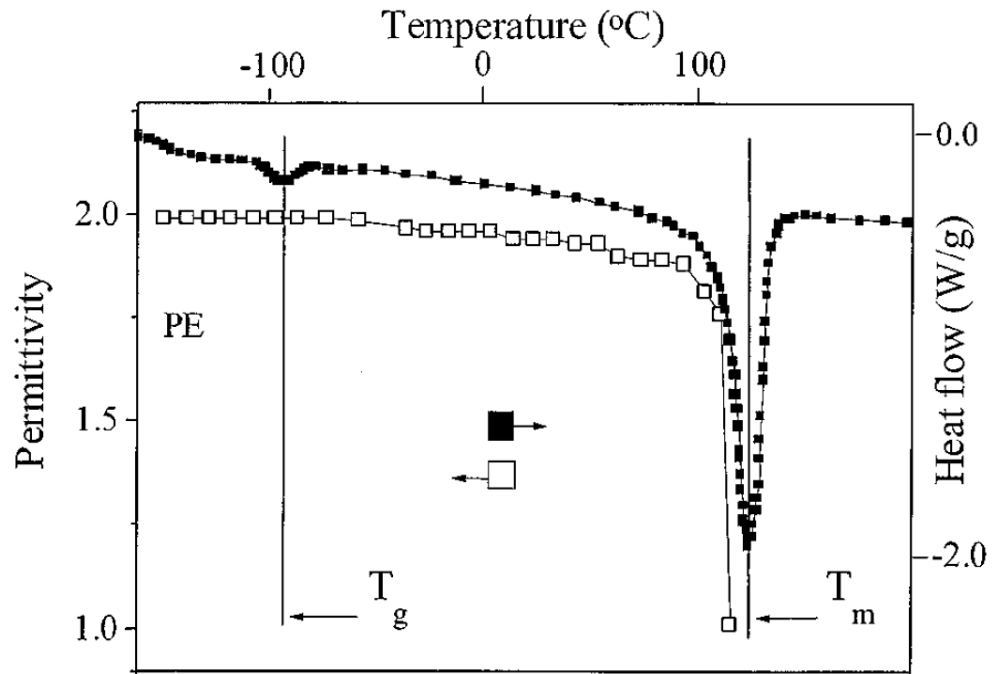


Figure 4.2 Temperature dependence measurements of the real permittivity on polyethylene [133]

#### 4.1.2 Temperature dependent dielectric loss

The FRA measurement results of real and imaginary permittivity on model cables with different insulation materials and same semicon shields are shown in Figure 4.3, Figure 4.4 and Figure 4.5. In these figures, imaginary permittivity at different temperatures is shown in solid lines with left y-axis, while real permittivity is shown in dashed lines with right y-axis. The results for cable AAA are shown in Figure 4.3. It can be seen that this homo-polymer XLPE cable has the best insulation material with the lowest dielectric loss. The imaginary permittivity below 80°C is below the noise floor of about  $10^{-3}$ . Only at 80°C,  $\epsilon''$  shows an increasing slope of -1 towards lower frequencies with the value of 0.14 at  $10^4$ Hz. The real permittivity  $\epsilon'$  does not change in this frequency range under these four temperatures, which indicates that the dielectric loss in  $\epsilon''$  is likely to be due to DC conductivity loss of the cable insulation. The “ripples” in  $\epsilon''$  are due to instrumental errors when measuring such low loss samples, as the equipment switches in different reference components.

Figure 4.4 shows the measurement results on the other homo-polymer model cable ABA which has different low density polyethylene (LDPE) base resin. The imaginary permittivity  $\epsilon''$  is bigger than that of cable AAA. At  $10^4$ Hz,  $\epsilon''$  is  $2.54 \times 10^{-2}$  at 60°C and  $4 \times 10^{-1}$  at 80°C. It has parallel slopes of -1 for these two temperatures. Since the real permittivity stays unchanged, the dielectric loss of this homo-polymer cable is also due to DC conductivity.

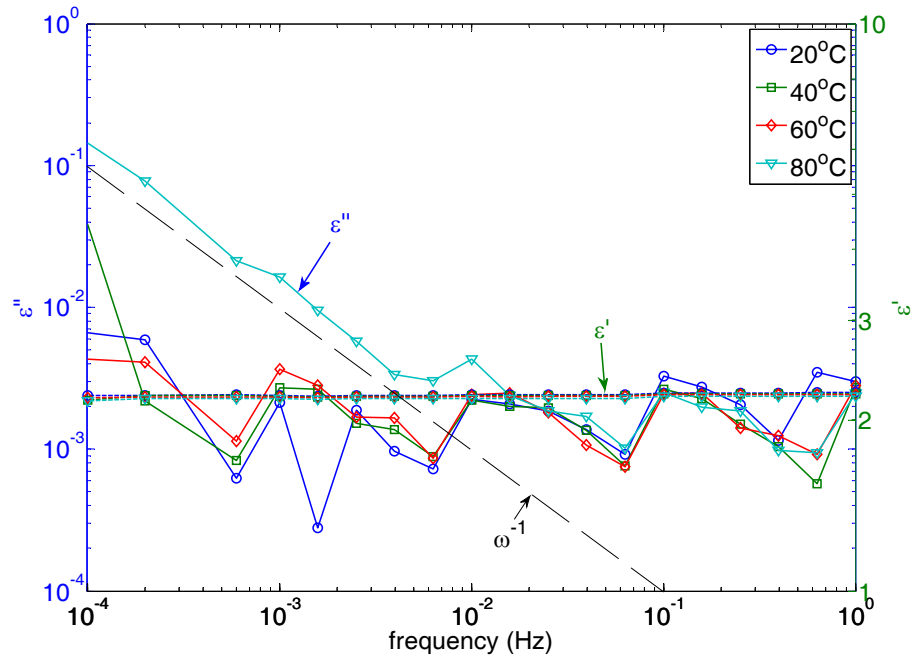


Figure 4.3 Permittivity of cable AAA (solid lines for  $\epsilon''$  with left axis, dashed lines for  $\epsilon'$  with right axis)

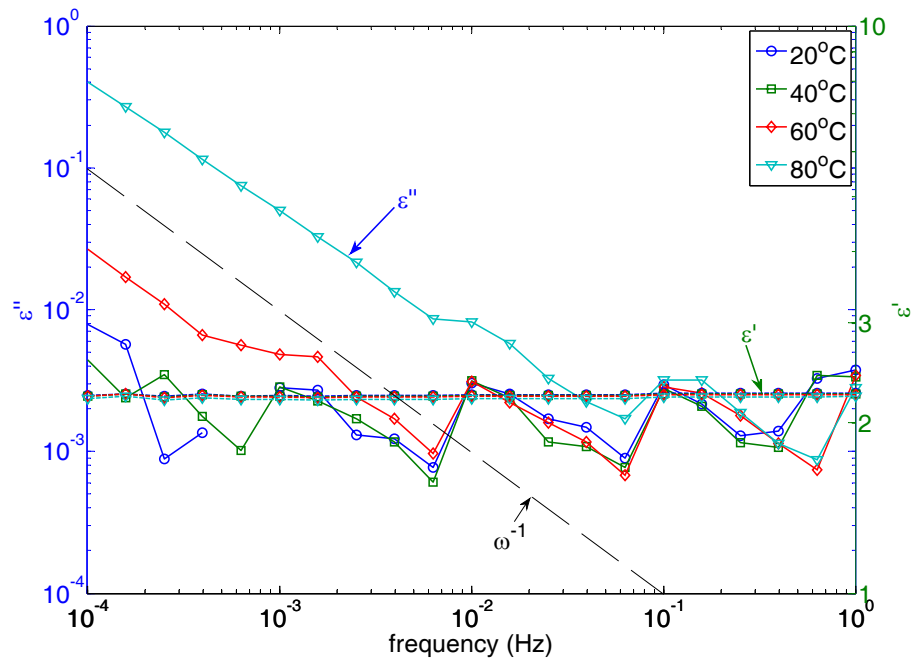


Figure 4.4 Permittivity of cable ABA (solid lines for  $\epsilon''$  with left axis, dashed lines for  $\epsilon'$  with right axis)

Unlike the homo-polymer cables, the measurement results of cable ACA (Figure 4.5) with co-polymer insulation have a different dielectric response. The imaginary permittivity  $\epsilon''$  is bigger than those of homo-polymer cables and can be identified for all the temperatures.  $\epsilon''$  has almost parallel lines for different temperatures and similar intervals between adjacent measurement temperatures. However,  $\epsilon''$  does not have straight slopes of -1 at higher temperatures of 60°C and 80°C. A loss peak adds to  $\epsilon''$  at lower frequencies. This can be confirmed by the increment in real permittivity  $\epsilon'$  at these two temperatures. Therefore, the dielectric loss of the co-polymer cable has multiple loss origins when the temperature becomes higher than 40°C – conduction and low frequency polarization. The low frequency loss peak shifts to higher frequency at higher temperatures. This implies that similar mechanism may be found at lower temperatures at frequencies below  $10^{-4}$ Hz.

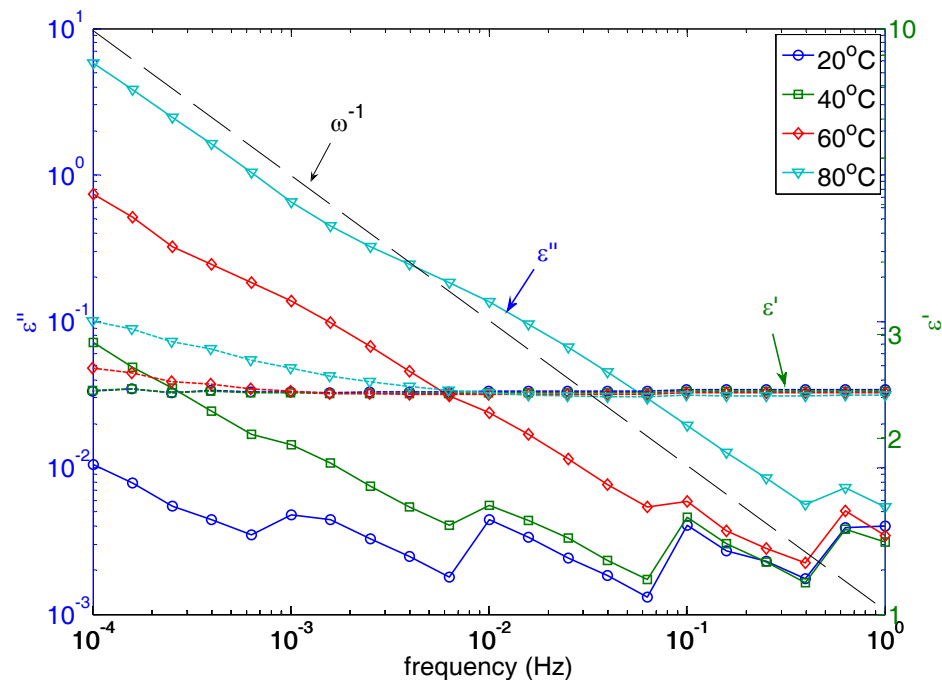


Figure 4.5 Permittivity of cable ACA (solid lines for  $\epsilon''$  with left axis, dashed lines for  $\epsilon'$  with right axis)

#### 4.1.3 Comparison of different model cables

The measurement results on all model cables at 80°C are shown in Figure 4.6 for imaginary permittivity and Figure 4.7 for real permittivity. Besides the cables of different insulation materials – AAA, ABA and ACA, measurement results on the cables with the same homo-polymer insulation but different semicon layers are also shown together.

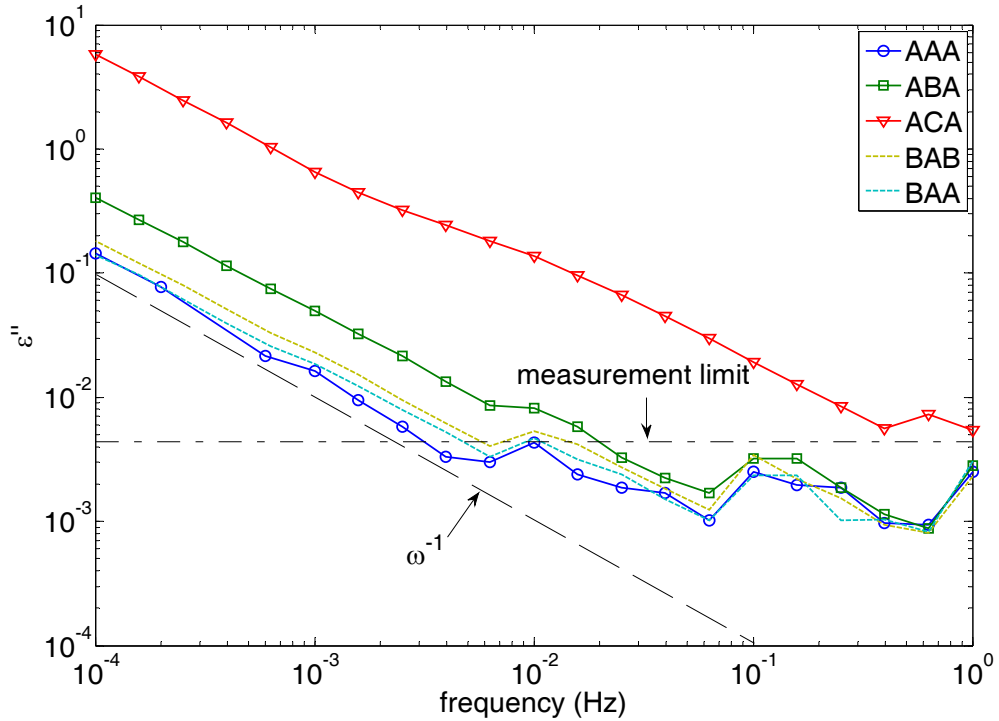


Figure 4.6 Comparison of  $\epsilon''$  for different cables at 80°C

In Figure 4.6, cable AAA has the lowest  $\epsilon''$ . However, all the cables with insulation A are quite similar. This suggests that the low frequency response of these cables is largely controlled by the insulation rather than the semicon layers. Cable ABA has higher  $\epsilon''$  values and the response is similar to that of cable AAA. The measurement limit is at about  $5 \times 10^{-3}$ , and instrumental fluctuation due to the loss of measurement

accuracy brings some influence to the measurement results. The slope of  $\omega^{-1}$  is plotted in Figure 4.6 to compare the measurement results. It can be seen that all the cables except ACA have slopes of -1 in  $\epsilon''$  at lower frequencies where the best measurement accuracy is maintained. Considering the constant real permittivity  $\epsilon'$  in Figure 4.7, the dielectric loss of these homo-polymer cables is due to DC conductivity. With super-smooth semicon shields, the model cables have slightly increased  $\epsilon''$ . When comparing with the slope of -1, it can be seen that there is another overlapping loss peak for cable ACA in this frequency range.

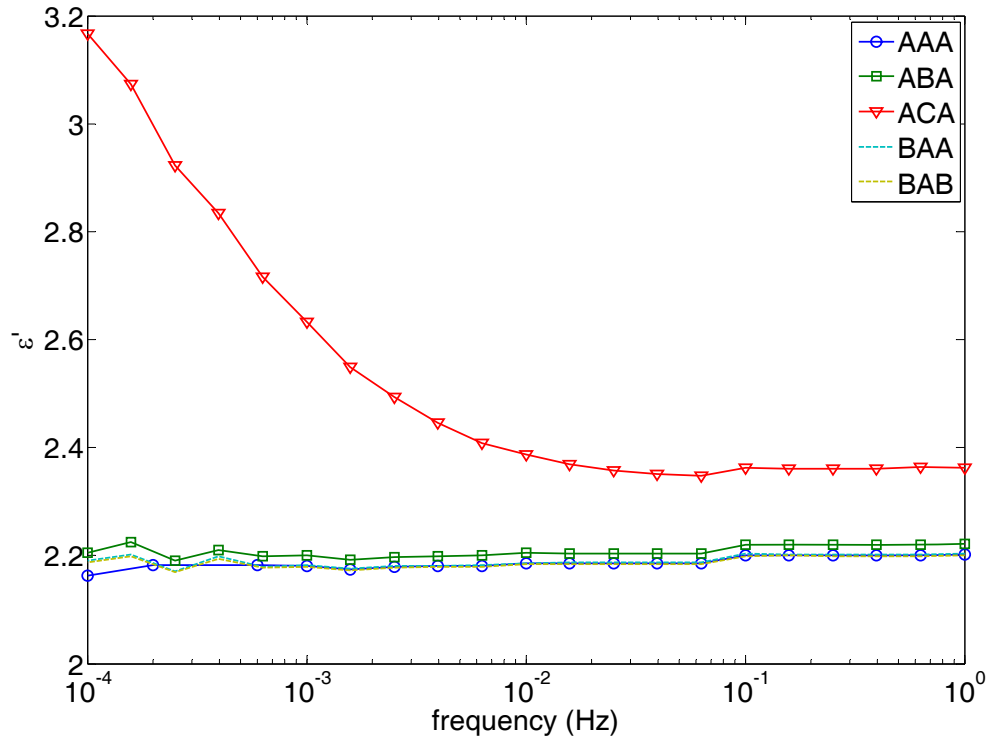


Figure 4.7 Comparison of  $\epsilon'$  for different cables at 80°C

Comparison of the real permittivity in Figure 4.7 shows that  $\epsilon'$  is about 2.2 for all homo-polymer cables, and the semicon shields do not make much difference. This value is very close to reported measurement results in literature [134]. However, cable ACA has

higher  $\epsilon'$  of 2.36 at 1Hz, and it is increasing when the frequency decreases. At  $10^4$ Hz,  $\epsilon'$  of cable ACA is 3.17 (an increment of about 0.8). This substantial increment represents a loss peak which may be due to  $\mu\text{m}$ -size EBA (ethylene-butyl-acrylate) islands added into the XLPE insulation.

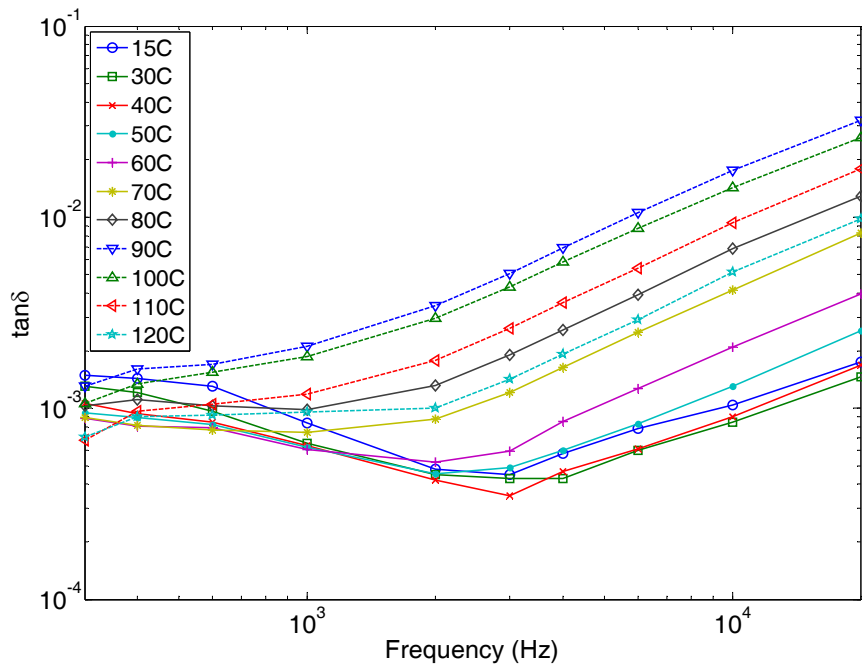
## 4.2 Dielectric loss in the higher frequency range of from 300Hz to 10kHz

### 4.2.1 Loss tangent measurement results on different model cables

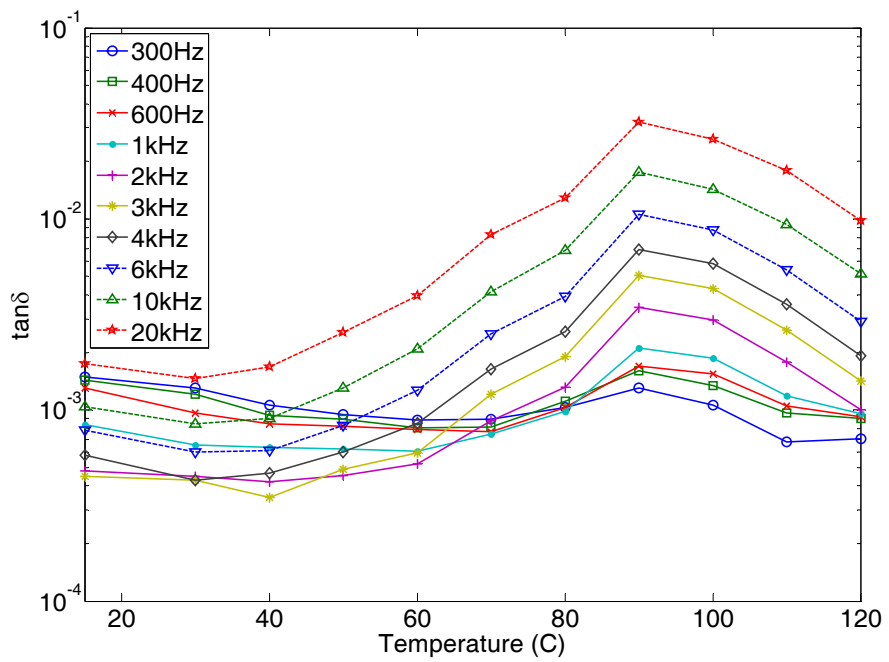
Using the transformer ratio bridge, the dielectric response of the model power cables has been measured in the frequency range 300Hz to 10kHz. The loss tangent values can be calculated from the measured capacitance and conductance

$$\tan \delta = \frac{G}{\omega C} \quad \text{Equation 4-4}$$

This section mainly shows the test results with the effect of outer semicon axial resistance, in contrast to the results of copper taped cable samples in section 4.4. The dielectric spectra of cable AAA and its temperature spectra are shown in Figure 4.8. From Figure 4.8 (a), it can be seen that at lower temperatures from 15°C to 60°C the loss tangent decreases from  $10^{-3}$  to  $3.5 \times 10^{-4}$  at lower frequencies and increases above 300Hz. At higher temperatures above 70°C the loss tangent rises monotonically. No loss peak is present in the frequency range for all types of cables. The ambient temperature during the study was at 20°C at the beginning measuring point.



(a) loss tangent vs. frequency



(b) loss tangent vs. temperature

Figure 4.8 Loss tangent measurement results for cable AAA by transformer ratio bridge

Generally, the dielectric loss decreases when the temperature increases at lower temperatures for each frequency, as shown in Figure 4.8 (b), and this lowest temperature is generally between 30°C and 50°C according to different frequencies. There is not much difference in the loss tangent values under lower frequencies, e.g. at 300Hz the loss tangent is between  $7 \times 10^{-4}$  and  $1 \times 10^{-3}$ . For higher temperatures, the loss tangent for all cables has the same increasing spectra. It is also noticeable in Figure 4.8 (b) that, at 90°C, there is a loss peak for all frequencies. This asymmetric loss peak is more obvious at higher frequencies.

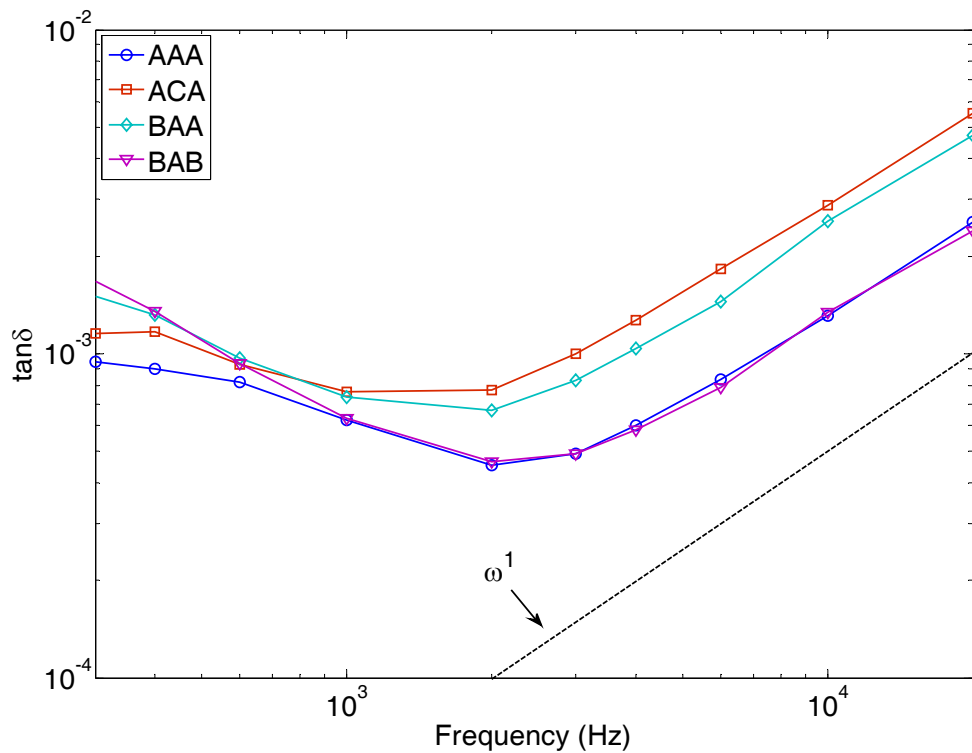


Figure 4.9 Loss tangent spectra of different model power cables at 50°C

All the other cables with both semicon layers have similar measurement results with increasing loss tangent at higher frequencies as shown in Figure 4.9. Cable AAA, ABA, ACA, BAA and BAB have been measured using the transformer bridge system. The

loss tangent has a decreasing slope for all the cables. Above the frequency of about 2kHz, all cables have the same increasing slope of 1. This suggests that there is dominant loss behaviour at higher frequencies for all the cables. From the temperature spectra of different cables, they all have loss tangent peaks at higher temperatures between 90°C and 100°C. There is no reported loss peak at these temperatures for PE and XLPE. Therefore, further study is required to find the origins of this loss in the power cables. Complementary experiments on the semicon materials and equivalent circuit modelling are studied in the next sections in order to find the origins of the dielectric loss at higher frequencies.

#### 4.2.2 The loss origins due to semicon shields

In order to investigate the origins of the loss peak at higher temperatures, the resistivity measurement of semicon materials of the cable AAA and BAB was done by measuring the conductivity of the outer semicon layers. As shown in Figure 4.10, a 1 meter length cable sample was used to make the measurement more accurate. Conductive copper tape was fixed to the outer semicon at the ends of the cable samples. While both ends were fixed with conductive tapes as electrodes, insulation tape was used to prevent contact of different loops when it was hung in the oven.

The resistances of the two different semicon materials on two different cable samples were measured with a multi-meter under temperatures from 30°C to 120°C. According to the basic equation for calculating resistance  $R$

$$R = \frac{\rho L}{A} \quad \text{Equation 4-5}$$

where  $\rho$  is the resistivity,  $A$  is the cross sectional area for the resistive material and  $L$  is the length of the resistor.



Figure 4.10 Test sample for conductivity measurement of semicon layers

Together with the cable's dimension (outer radius  $r_o$ , inner radius  $r_i$  and sample length  $L$ ) shown in Figure 3.1 in chapter 3, the resistivity can be calculated by

$$\rho = \frac{RA}{L} = \frac{R(\pi r_o^2 - \pi r_i^2)}{L} = R\pi(0.00305^2 - 0.0029^2) \quad \text{Equation 4-6}$$

From the measurement results in Figure 4.11, the resistivity of both semicons is about  $1 \Omega \text{ m}$  at  $30^\circ\text{C}$ . At higher temperatures, they have peaks at  $90^\circ\text{C}$  and  $100^\circ\text{C}$  respectively, which is the same as the loss tangent results of cables from the measurement of transformer ratio bridge.

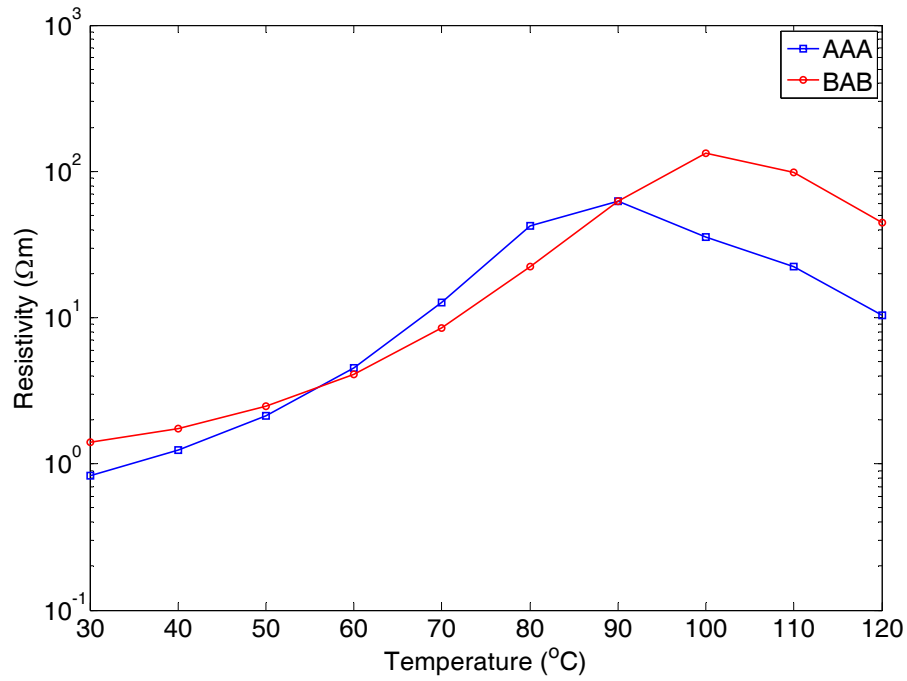


Figure 4.11 Resistivity of different semicon materials: standard (cable AAA) and super-smooth (cable BAB) semicons

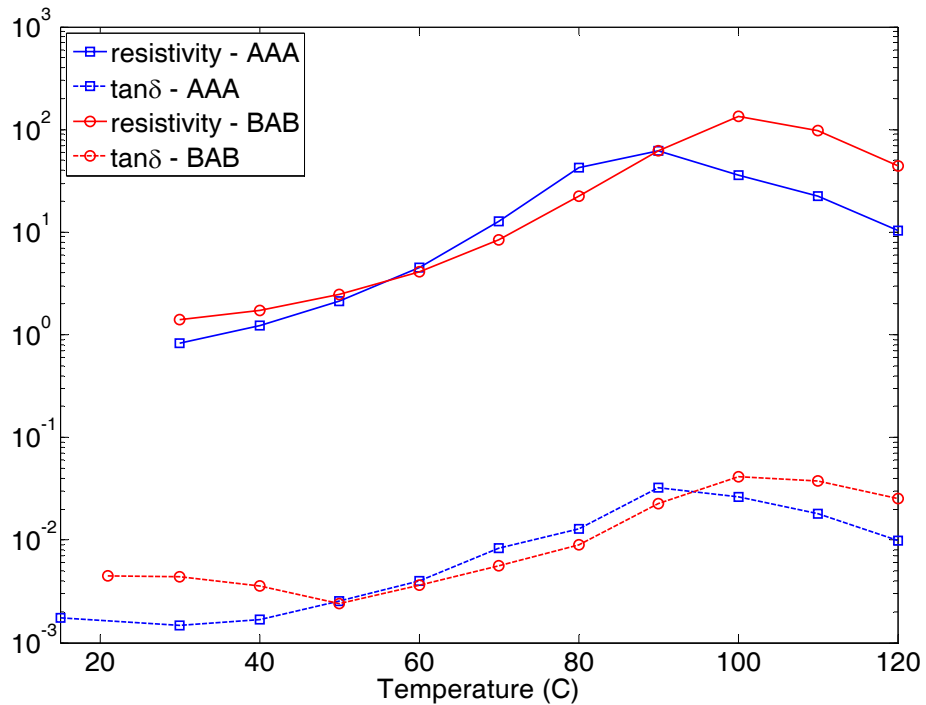


Figure 4.12 Comparison of loss tangent and semicon resistivity ( $\Omega \cdot m$ )

The comparison of loss tangent for different cables (cable AAA with standard semicon and cable BAB with super-smooth semicon) at 10kHz and resistivity of different semicon materials is shown in Figure 4.12. Although the loss tangent and resistivity are on different scales, their temperature spectra have the same shapes for both cables. For cable AAA, the dielectric loss tangent increases when temperature increases and reaches maximum at 90°C. The resistivity of semicon A also has a peak value at 90°C. For cable BAB, the peak value temperature for loss tangent and resistivity of semicon B is 100°C. This similarity indicates that the semicon layers of power cables may play an important role in the dielectric loss of the cable insulation, and the dielectric loss is greatly dependent on the resistivity of semicon layers.

#### 4.2.3 MATLAB modelling of dielectric response of the power cables

MATLAB modelling has been used to simulate the dielectric response of power cables. The simplified equivalent circuit of an ideal cable with both semicon layers is shown in Figure 4.13 (a). If there is no outer semicon layer, the equivalent circuit changes to Figure 4.13 (b). Without any semicon layers as shown in Figure 4.13 (c), the complex impedance of the equivalent circuit  $Z^*$  can be calculated

$$Z^* = \frac{R_p}{1 + \omega^2 C_p^2 R_p^2} - j \frac{\omega C_p R_p^2}{1 + \omega^2 C_p^2 R_p^2} = Z' + jZ'' \quad \text{Equation 4-7}$$

and the complex capacitance  $C^*$  is then

$$C^* = \frac{1}{j\omega Z^*} = C_p - j \frac{1}{\omega R_p} = C' - jC'' \quad \text{Equation 4-8}$$

The loss tangent has a brief expression

$$\tan \delta = \frac{C''}{C'} = \frac{1}{\omega C_p R_p} \quad \text{Equation 4-9}$$

When there are semicon layers, the circuit can be seen as a resistor in series with the former circuit. The impedance, complex capacitance and loss tangent become more complicated as below where  $R_0$  represents the total resistance in series with the parallel circuit:

$$Z^* = \frac{R_p + R_0(1 + \omega^2 C_p^2 R_p^2)}{1 + \omega^2 C_p^2 R_p^2} - j \frac{\omega C_p R_p^2}{1 + \omega^2 C_p^2 R_p^2} = Z' + jZ'' \quad \text{Equation 4-10}$$

$$C^* = \frac{C_p R_p^2}{\omega^2 C_p^2 R_p^2 R_0^2 + (R_p + R_0)^2} - j \frac{R_p + R_0 + \omega^2 C_p^2 R_p^2 R_0}{\omega [\omega^2 C_p^2 R_p^2 R_0^2 + (R_p + R_0)^2]} = C' - jC'' \quad \text{Equation 4-11}$$

$$\tan \delta = \frac{C''}{C'} = \frac{R_p + R_0(1 + \omega^2 C_p^2 R_p^2)}{\omega C_p R_p^2} \quad \text{Equation 4-12}$$

A MATLAB program was built to calculate the loss tangent spectra for the equivalent circuit in Figure 4.13. The function in the program needs three parameters – the insulation geometric capacitance  $C_0$ , conductance  $G$ , and the total resistance of semicon layers  $R_0$ . These parameters can be calculated by

$$C_0 = \frac{2\pi\epsilon_0 L}{\ln(r_o/r_i)} \text{ and } G = \frac{2\pi\sigma L}{\ln(r_o/r_i)} \quad \text{Equation 4-13}$$

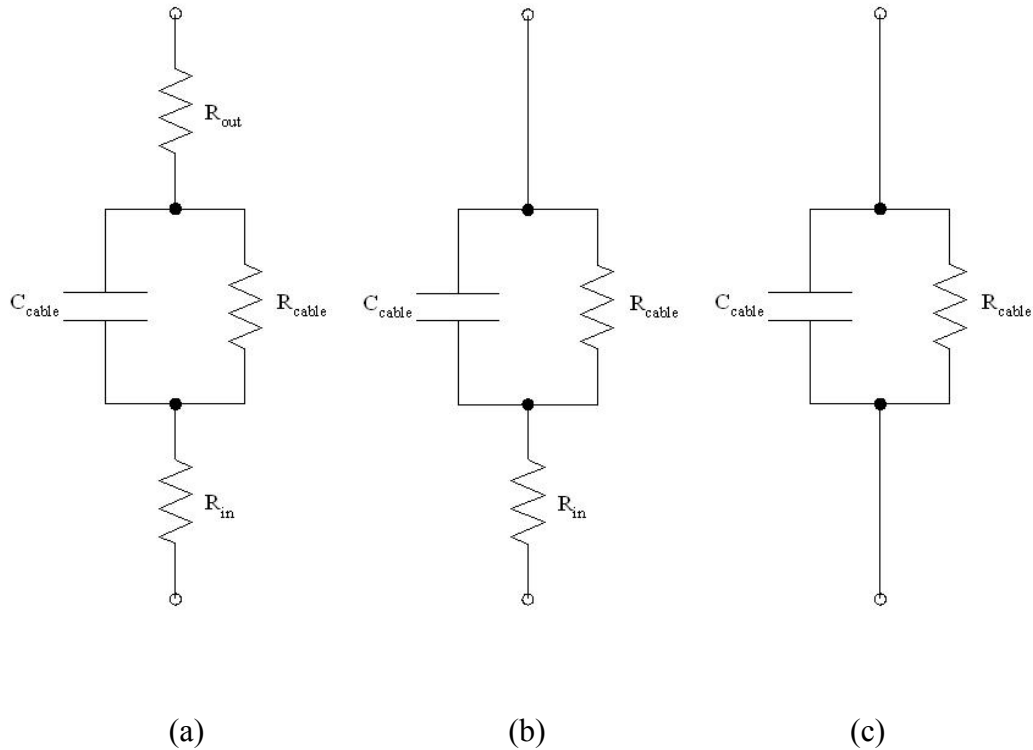


Figure 4.13 Equivalent circuit of cables (a) with both semicon layers; (b) with inner semicon layer only; (c) without semicon layer. ( $C_{cable}$  and  $R_{cable}$  equal  $C_p$  and  $R_p$  in Equation 4-12; the sum of  $R_{out}$  and  $R_{in}$  equal  $R_0$  in Equation 4-12)

The value of  $G$  used in this calculation is the DC conductance; contribution from other dielectric losses is ignored. In order to compare with the results obtained using the transformer bridge measurement, the loss tangent has been calculated and the modelling result is shown in Figure 4.14. In the modelling result graph, the frequency range is from 1Hz to 10kHz and the loss tangent covers 11 decades from  $10^{-9}$  to  $10^2$ . The decreasing curve (blue) with slope of -1 represents the loss tangent spectra of the equivalent circuit for only insulation layer. The situations with only inner semicon layer and with both semicon layers are modelled in green and red curves. The pure conduction loss of the insulation layer without any semicon layers has monotonic decreasing slope of -1. This conduction loss can be measured at lower frequencies but it is not measurable at higher frequencies as it decreases linearly. The radial resistance of

both semicon layers can cause the dielectric loss to increase at 200Hz, but it is beyond the measurement limit. There is not much difference when the outer semicon is removed. However, the loss tangent becomes much higher if there is series resistance due to the contribution of the axial resistance of outer semicon layer. Because the axial resistance is much bigger than the radial resistance for the outer semicon layer, the dielectric loss contribution of the axial resistance is bigger and detectable at lower frequencies as shown in Figure 4.14.

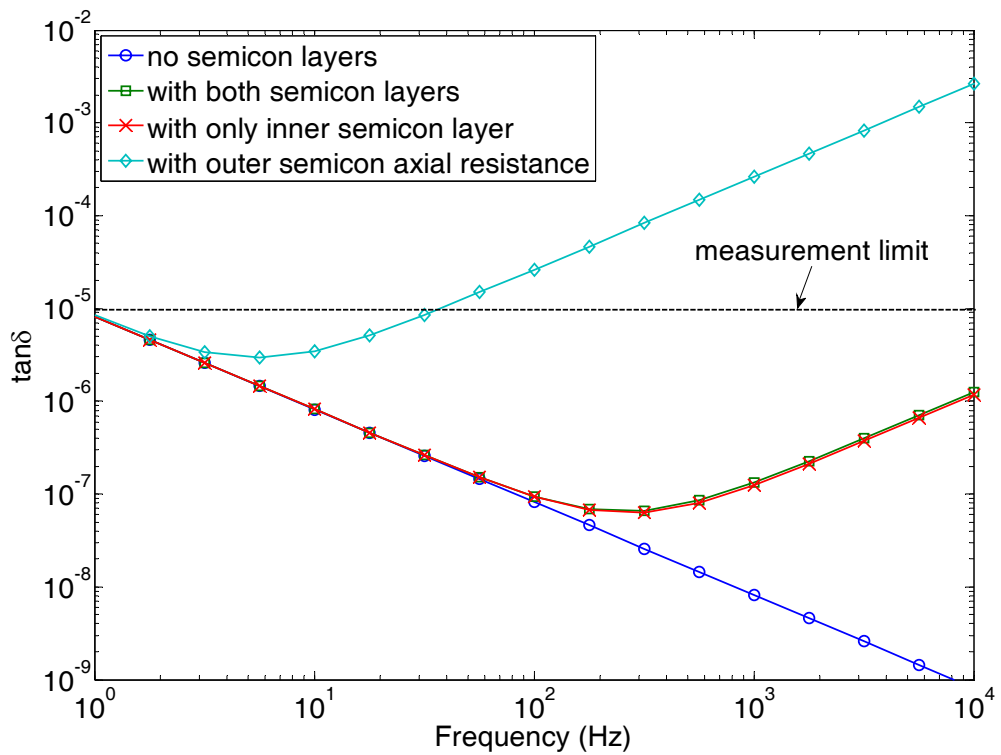


Figure 4.14 Loss tangent simulation on cables with/without semicon

Compared with the modelling results, the rising loss tangent frequency spectra can be explained as the contribution of semicon layers. After examining the measurement setup, the outer semicon's axial resistance was found to be the cause of the increasing loss tangent at higher frequencies. The radial resistance of the outer semicon layer is

calculated as  $0.016\Omega$  for a 5m length cable with the resistivity of  $10\Omega\text{m}$ . This resistance is too small to account for a contribution to the dielectric loss in this frequency range. There is a peak related to this small resistance but at very high frequencies that are out of the measurement frequency range in this study. But if the outer semicon layer is treated as an electrode, most of the current signal flowing into the measurement equipment will have to cross the surface resistance, except at the point where the signal is picked up on the cable sample. This surface resistance is in the range from  $\text{k}\Omega$  to  $\text{M}\Omega$ , which is big enough to make the loss peak occur at low frequency range below kHz. The underlying mechanism from the equivalent circuit explanation is that the outer semicon's surface resistance will take more voltage drop on it as a mainly resistive component while the insulation layer is mainly capacitive whose impedance becomes smaller at higher frequencies. Therefore, the outer semicon layer can contribute and dominate the loss part when the outer semicon is treated as measuring electrode.

The cable insulation, PE or XLPE, has been widely studied with extracted film samples from XLPE cables, but the loss of a whole cable is difficult to measure because of the reasons mentioned in chapter 2. In the a publication of audio-frequency dielectric spectroscopy on 15kV XLPE cables, Das-Gupta [71] observed increasing dielectric loss behaviour at room temperature, as shown in Figure 4.15. As the 40cm cable sample was put into a tap water filled tank as measuring electrode, the resistance of water played the role as the outer semicon axial resistance in this research study. The author also realized that this potential high frequency peak is due to the water electrode [71]. In this research study, the model power cables produced by Borealis were measured with the transformer ratio bridge system. Similarly, the dielectric loss at  $30^\circ\text{C}$  and  $80^\circ\text{C}$  has an increasing loss tangent, which is dependent on the resistivity of the semicon materials.

The loss tangent spectra are slightly higher than that of Das-Gupta, which was made under room temperature.

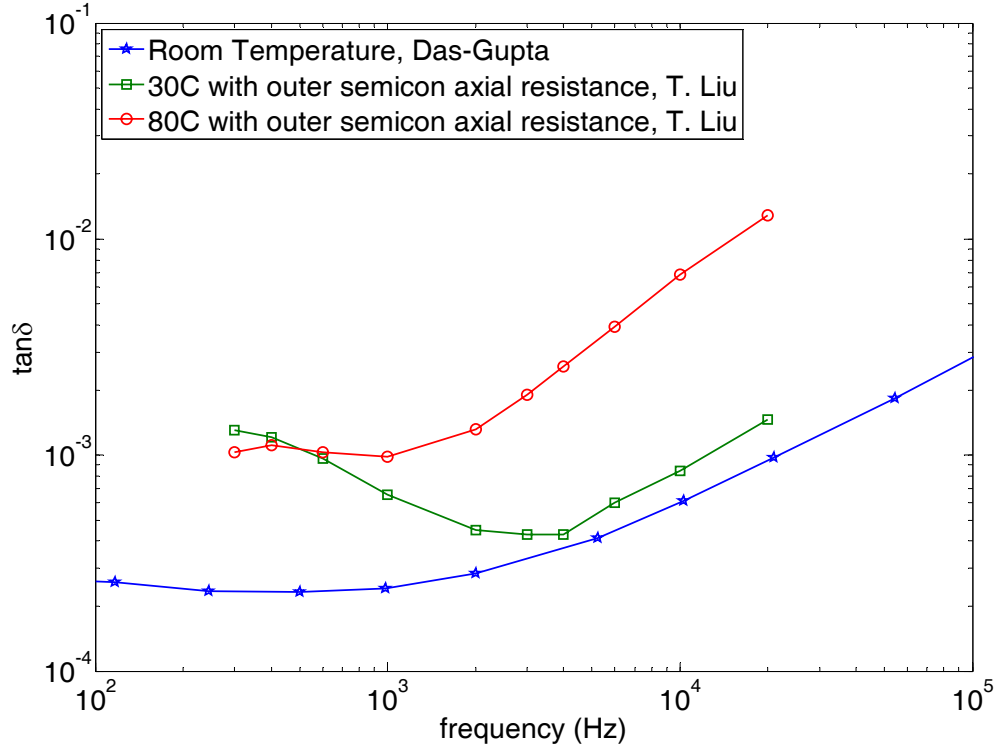


Figure 4.15 Comparison of loss tangent spectra with the results of Das-Gupta

With the cable samples fully wrapped with conductive adhesive tapes, measurements were taken on all cables again to avoid the influence of axial resistance of the outer semicon layer. A comparison using the homo-polymer cable AAA can be seen in Figure 4.16. Two temperatures are chosen for the comparison. It can be seen that the loss tangent is smaller with copper tape electrode. There is a loss peak in the lower frequency range, and this might be due to relaxation process or brought by instrumental effect. At higher frequencies, cable sample with copper electrode has decreasing loss tangent at 40°C. This sharp contrast to the previous results further proves that the increasing loss originates from the axial resistance of the outer semicon

layer. However, at higher temperatures when the resistivity of semicon material becomes bigger, the radial resistance of both semicon layers will still give rise to the dielectric loss and finally dominate the loss tangent with a slope of 1 while the conduction loss contribution is relatively much smaller with a slope of -1. In conclusion, the axial resistance of power cable outer semicon shield is a source of dielectric loss and brings increasing loss at higher frequencies. Good contact using conductive copper tape to wrap the cable samples can prevent the influence of axial resistance of outer semicon layer, as implied in equivalent circuit modelling results as well. This outcome suggests that metallic shielding outside the outer semicon layer is important in reducing the dielectric loss in power cable manufacturing.

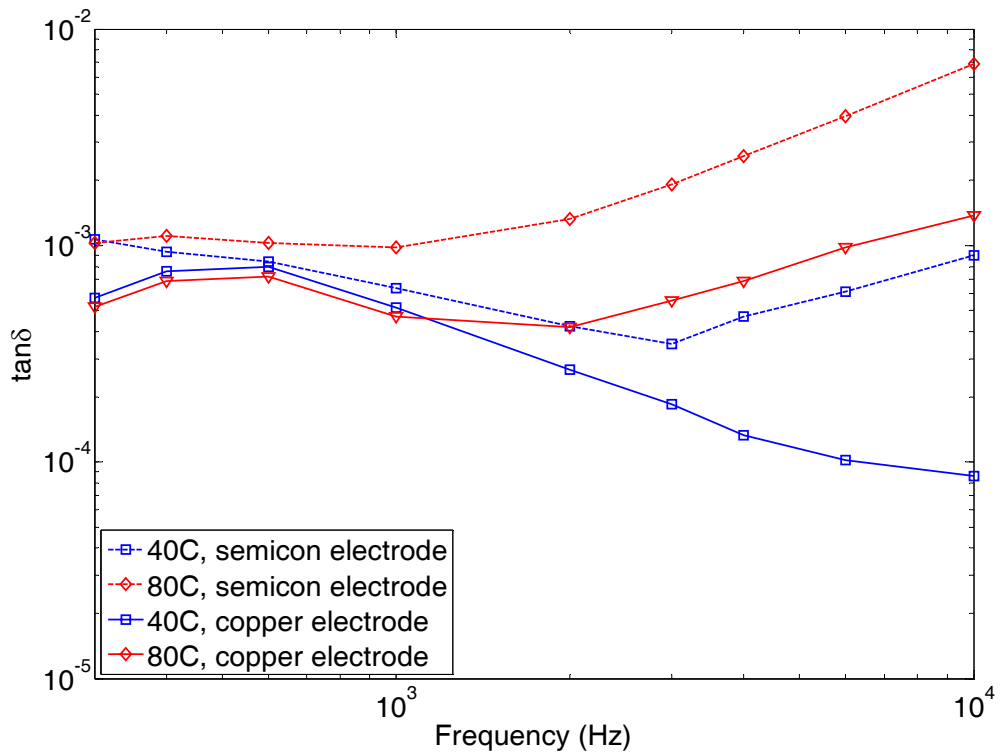


Figure 4.16 Comparison of the results from different sample preparation methods.  
(copper electrode: solid lines, semicon electrodes: dotted lines)

## 4.3 Dielectric response with discharging current measurement

### 4.3.1 Temperature dependent discharging current of different cables

The discharging current of cable AAA, ABA and ACA was measured with the experimental system developed in chapter 3. Before measuring the cable samples, the “air” cable was measured in comparison with cable AAA in order to check that the system background does not influence the measurement results on the model cables. The results are shown in Figure 4.17. During the measuring time of 50ms, cable AAA has more than 10 times the current than that of the “air” cable. The discharging current of the “air” cable decayed very quickly in several ms, and it is always negligible compared to the discharging current of cable AAA. This result further confirmed that the discharging current experimental system can correctly measure the discharging current of these low loss model power cables. Because the purpose of this measurement was to study the influence of measurement system on the cable sample measurement in the short time, a higher range of the electrometer was used. This can reduce the sensitivity of the system. As it can be seen in Figure 4.17, the noise floor is  $10^{-8}\text{A}$  with the range of  $10^{-5}\text{A/V}$  on the current voltage converter. For the measurement on the model power cables, different ranges were used for different time periods, since the discharging current decays for more than five decades in only 10 seconds time. The results of different ranges were merged together for better accuracy.

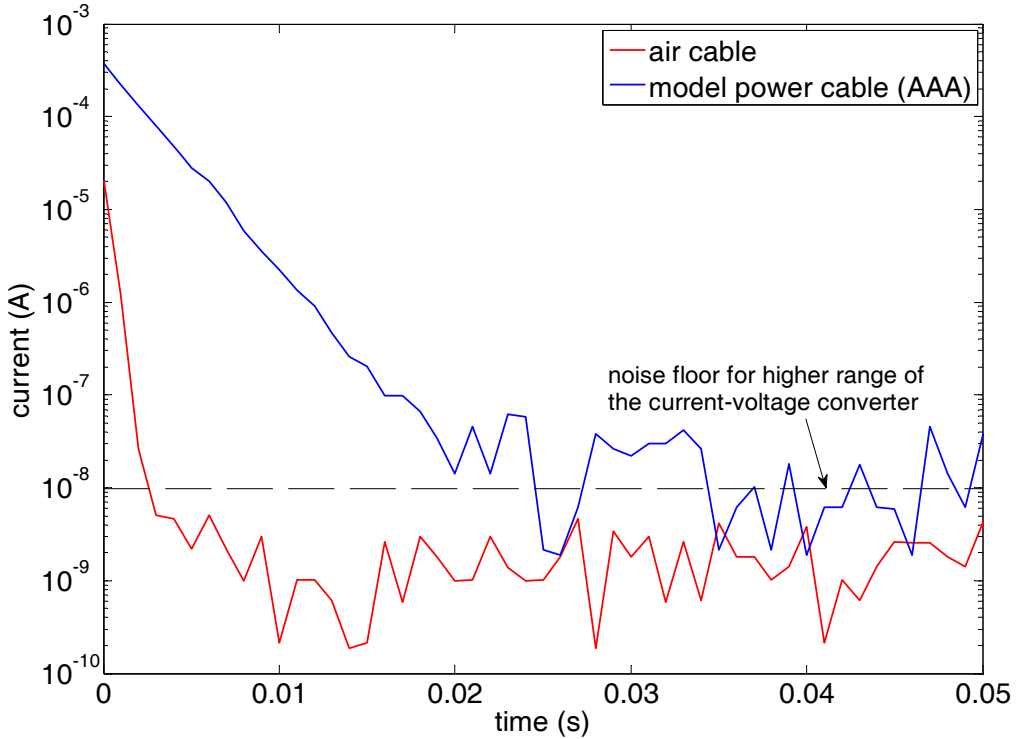


Figure 4.17 Comparison of discharging current between the “air” cable and cable AAA

The discharging current of cable AAA under different temperatures is shown in Figure 4.18. The measurement duration is 13.5s with sampling rate of 1000 sample/second. The discharging current of homo-polymer cables decayed very quickly. The noisy current  $I(t)$  at longer time was fitted with a power law or Curie-Von-Schweidler law,

$$I(t) = At^{-n} \quad \text{Equation 4-14}$$

which was proved to be able to represent the multi-relaxation processes of polymer materials [135] [136] [137].  $A$  and  $n$  in Equation 4-14 are fitting parameters. In the beginning at 20°C, the discharging current was more than  $1.62 \times 10^{-6}$  A. The current decayed linearly in log-log coordinates until several milli-seconds, when there is a small turning point with another linear decay. The current becomes noisy when it decayed below  $10^{-11}$  A. Under higher temperatures, the discharging currents are parallel to that of

20°C. The lowest discharging current occurred at 60°C and it increases at 80°C. When the time is longer than about 1s, the discharging currents drop below  $10^{-10}$ A. There is a trend that in the beginning the discharging current drops faster at higher temperatures but at longer time the current at higher temperatures drops slower with a smaller slope.

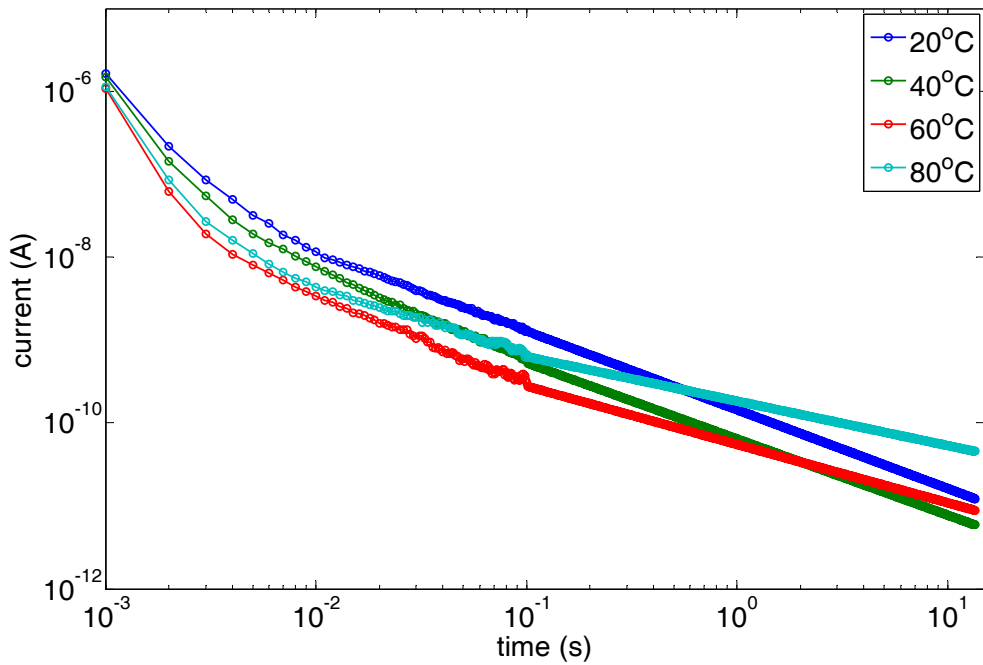


Figure 4.18 Discharging current of cable AAA

Another homo-polymer cable ABA has almost the same discharging current as cable AAA. In comparison with the homo-polymer cables of AAA and ABA, the co-polymer cable ACA has overall higher discharging currents at all temperatures, as shown in Figure 4.19. The discharging current is about  $4 \times 10^{-11}$ A, above the noise floor without data smoothing. The current at 20°C is still the highest within the first 10ms. During this time the temperature dependence is the same as the homo-polymer cables with the lowest discharging current at 60°C. However, the discharging current increases at longer

times at higher temperatures. It is noticeable that at 80°C, the discharging current became almost flat in the last 8s.

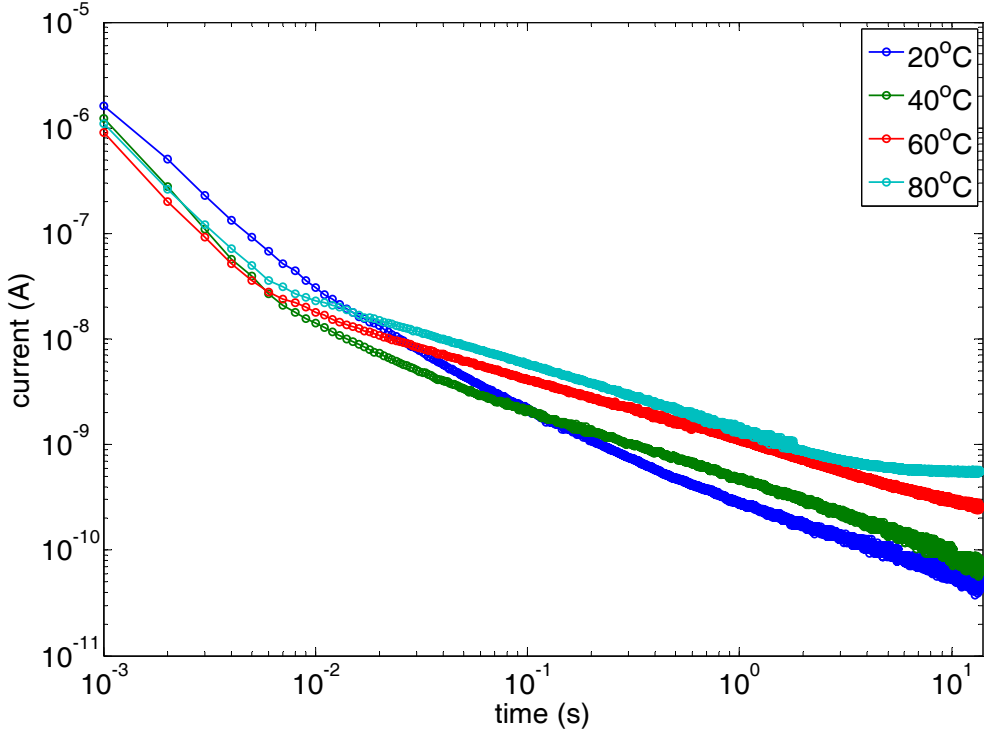


Figure 4.19 Discharging current of cable ACA

In summary, the discharging current decays from about  $10^{-6}$ A at 1ms to about  $10^{-12}$ A for homo-polymer cables and above  $10^{-11}$ A for co-polymer cables. All homo-polymer cables, AAA and ABA, and co-polymer cable ACA have the highest discharging currents at 20°C in the beginning several milli-second. At longer time, the discharging currents of all cables basically follows the power law (Curie-von Schweidler law) decay, which is typical for solid dielectrics [70] [137] [138] [139]. However, different processes can be found especially from the temperature dependence. While the discharging current has a minimum magnitude at 60°C in the beginning 10ms, it has longer decaying trend at higher temperatures at longer time. Higher discharging current for cable ACA indicates that the co-polymer insulation has higher dielectric loss than

that of homo-polymer XLPE insulation. More charge can be stored inside the cable insulation system, and it takes longer time to discharge when being earthed. This result is in accordance with the other two frequency domain dielectric spectroscopy techniques and will be further studied after Fourier transform.

#### 4.3.2 Transformation of discharging current into frequency spectra

Fourier transform is needed to transfer the time domain discharging current data into frequency domain so that the spectra can be merged together with the results by other frequency domain techniques. The complex permittivity  $\varepsilon^*$  can be calculated with the following equation [75]

$$\varepsilon^* = \varepsilon_\infty + \frac{1}{C_0 U} \int_0^\infty I(t) e^{-j\omega t} dt - j \frac{G}{\omega C_0} \quad \text{Equation 4-15}$$

where  $\varepsilon_\infty$  is the high frequency permittivity,  $C_0$  is the geometric capacitance of the measured sample and  $U$  is the applied step voltage.  $\int_0^\infty I(t) e^{-j\omega t} dt$  is the Fourier transform for the measured time dependent current  $I(t)$ . It is necessary to include  $\varepsilon_\infty$  as the Fourier transform only results in the dielectric increment. The term  $j \frac{G}{\omega C_0}$  represents any conduction loss contribution in frequency domain. As there is no conduction in the discharging process, the equation should be rewritten as

$$\varepsilon^* = \varepsilon_\infty + \frac{1}{C_0 U} \int_0^\infty I(t) e^{-j\omega t} dt \quad \text{Equation 4-16}$$

This continuous transform is impractical in real applications while the data is digitized as discrete signal. Discrete Fourier transform (DFT) should be used for the transform. In order to restore correctly the complex permittivity, the discrete Fourier transform algorithm is studied in MATLAB environment [140]. When the equation for forward DFT is

$$X(k) = \sum_{n=0}^{N-1} x(n) e^{\frac{-2\pi j}{N} nk} \quad k = 0, 1, 2, \dots, N-1 \quad \text{Equation 4-17}$$

where  $x(n)$  is the time domain series,  $X(k)$  is the frequency domain series,  $X(k)$  should be divided by  $N$  (number of DFT points) to give the correct real and imaginary permittivity values. The final equation under discharging condition for calculating discrete frequency domain complex permittivity is

$$\varepsilon^*(k) = \varepsilon_\infty + \frac{1}{NC_0U} \sum_{n=1}^N x(n) e^{\frac{-2\pi j}{N} nk} = \varepsilon_\infty + \Delta\varepsilon - j\varepsilon'' \quad k = 1, 2, 3, \dots, N \quad \text{Equation 4-18}$$

Using the DFT algorithm, the complex permittivity for the discharging current data on the model power cables can be calculated and their loss tangent were obtained by

$$\tan \delta = \frac{\varepsilon''(k)}{\varepsilon'(k)} \quad \text{Equation 4-19}$$

Using Equation 4-18, the imaginary permittivity  $\varepsilon''$  and the real permittivity increment  $\Delta\varepsilon'$  have been calculated. Excluding the data that has the influence truncation error, the frequency spectra from 1Hz to 100Hz for the model power cables were obtained. The  $\varepsilon''$  of cable AAA is shown in Figure 4.20, with  $f^1$  and  $f^{-1}$  to help determine the types of relaxation. The  $\varepsilon''$  of all temperatures ranges from  $10^{-6}$  to  $10^{-4}$ . Such low loss cannot be measured by the frequency domain techniques – FRA and bridges. The  $\varepsilon''$  at 20°C is the

biggest in this whole frequency range with its maximum value of  $4.80 \times 10^{-5}$  at 100Hz. The  $\epsilon''$  decreases at higher temperatures until 60°C, which has the minimum value of  $8.96 \times 10^{-6}$  at 2Hz. The  $\epsilon''$  increases again at 80°C with the values between those of 20°C and 60°C. This temperature dependence, which has a minimum dielectric loss at 60°C, has been found in the depolarization current for all the XLPE model power cables. There is no loss peak in this frequency range at all temperatures. Compared with the slope of -1 and 1, the dielectric loss of cable AAA does not have a Debye type loss and it has a very flat dielectric loss especially at lower temperatures, which suggests multiple relaxations typical for solid polymers. It is also noticeable that there is a slope at higher temperatures of 60°C and 80°C at lower frequencies. Although the slope is still smaller than -1, this may indicate an extra broad relaxation process is shifting towards higher frequencies at higher temperature.

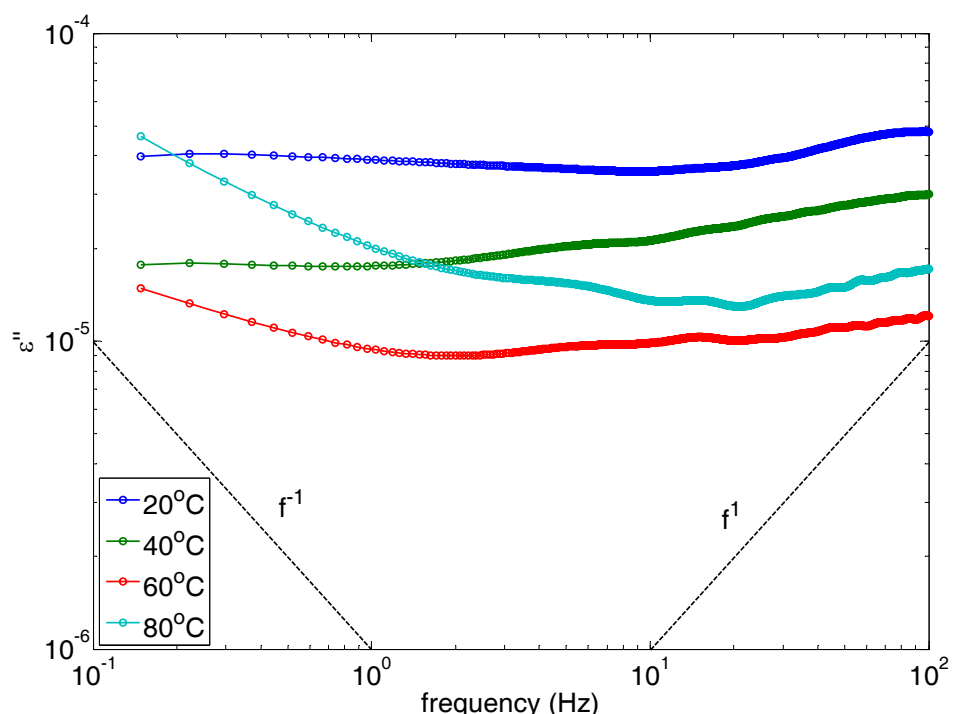


Figure 4.20  $\epsilon''$  of cable AAA under different temperatures,  
transformed from the discharging current

The real permittivity increment  $\Delta\epsilon'$  of cable AAA is shown in Figure 4.21. The increment represents the deviation from the high frequency real permittivity  $\epsilon_\infty$ , i.e. the frequencies above those that are being observed by this technique. Similar to the  $\epsilon''$  results, the biggest increment happens at 20°C with maximum  $\Delta\epsilon'=5.27\times10^{-4}$  at the lowest frequency end 0.15Hz and the smallest at 60°C with maximum  $\Delta\epsilon'=2.67\times10^{-4}$ . For all temperatures, the  $\Delta\epsilon'$  decreases smoothly at higher frequencies. It is noticeable that the  $\Delta\epsilon'$  is negligible with the values at the order of  $10^{-4}$ , comparing the value of  $2.18\pm0.04$  measured using the transformer ratio bridge for the  $\epsilon_\infty$  of polyethylene. However, the  $\Delta\epsilon'$  has the advantage of analyzing the relaxation behaviour more clearly. With the pure permittivity increment at 20°C, it can be seen that the increment of  $\Delta\epsilon'$  in this frequency range is  $2.67\times10^{-4}$ . This very small real permittivity increment indicates there is a very broad loss peak.

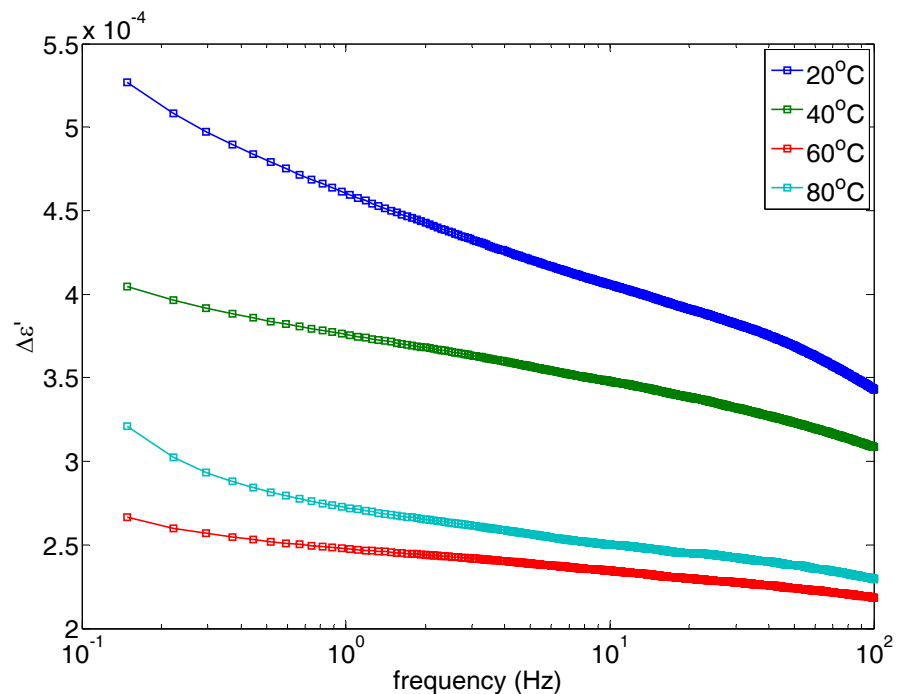


Figure 4.21  $\Delta\epsilon'$  of cable AAA under different temperatures,  
transformed from the discharging current

Considering the average value for high frequency permittivity  $\varepsilon_\infty = 2.18$  for cable AAA, the real permittivity has been calculated

$$\varepsilon' = \varepsilon_\infty + \Delta\varepsilon' = 2.18 + \Delta\varepsilon'(\omega) \quad \text{Equation 4-20}$$

The loss tangent was then calculated with Equation 4-19, and it is shown in Figure 4.22. The shapes of the  $\tan\delta$  at higher frequencies with all temperatures are the same as the  $\varepsilon''$  in Figure 4.20, because the  $\Delta\varepsilon'$  is so small that it does not bring too much increment to the  $\varepsilon'$ . The loss tangent of this homo-polymer cable has very low polarization loss, ranging from  $2.2 \times 10^{-6}$  to  $4.0 \times 10^{-5}$  in general. Practical importance can be considered at 50Hz. At this mains frequency, the loss tangent due to pure polarization for the cables has the lowest value at  $60^\circ\text{C}$ .

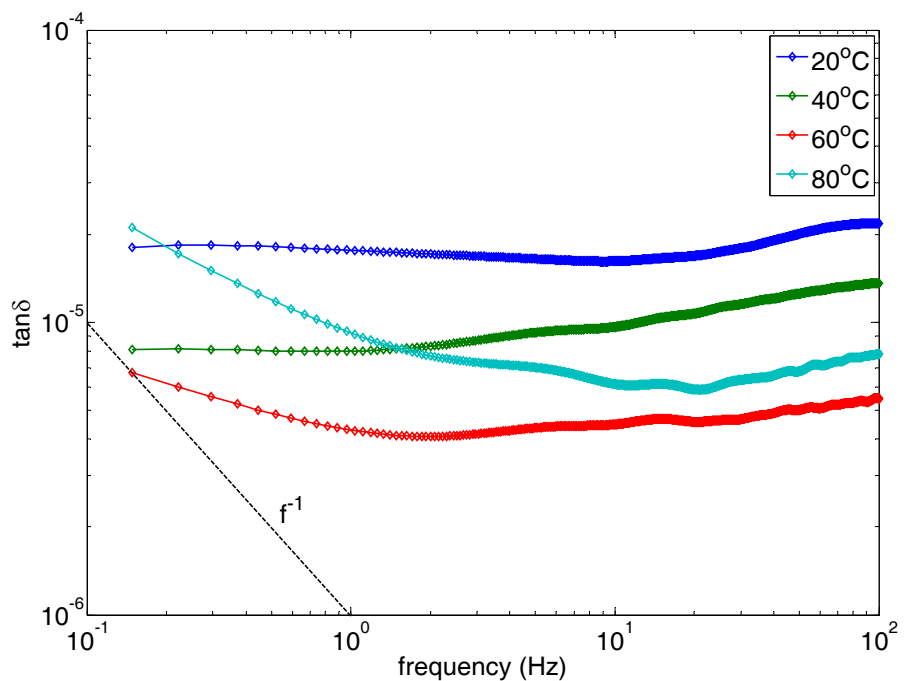


Figure 4.22 Loss tangent of cable AAA under different temperatures, transformed from the discharging current

The 50Hz loss tangent of the model power cables can be obtained from the frequency spectra of the discharging current measurement results, because this time domain technique can accurately cover the frequency range from 1Hz to 100Hz. The 50Hz loss tangent values for cable AAA, ABA and ACA under different temperatures are shown in Table 4.2. All the model cables have a loss tangent of the order of  $10^{-5}$  and  $10^{-6}$  with the lowest dielectric loss tangent at 60°C. The dielectric loss of cable ABA is very close to that of cable AAA, probably because they are both homo-polymer XLPE cables. Different base resin makes the loss tangent of cable ABA slightly higher. The co-polymer cable ACA has the same temperature dependence. Comparing the loss tangent magnitude of different types of cables, cable ACA has the biggest loss tangent for all temperatures than the other two homo-polymer cables.

Table 4.2 Loss tangent ( $\times 10^{-6}$ ) of model power cables at 50Hz under different temperatures

Cable	AAA	ABA	ACA
20°C	20.09	21.2	48.59
40°C	12.55	16.0	23.01
60°C	5.02	6.19	18.80
80°C	6.80	8.89	24.78

A comparison between the time domain transformed spectra and measurement results by Borealis is shown in Figure 4.23. The test sample in Borealis measurement is the same model power cable AAA but with Schering bridge at 50Hz. The applied electric

field is 25kV/mm with the temperatures of 25°C, 60°C, 90°C and 100°C. It can be seen that the 50Hz loss tangent by both techniques have the same trend at different temperatures. The highest loss tangent occurred at lower temperatures and the lowest at 60°C for both techniques. The reason for higher loss tangent values in Borealis measurement results is due to higher applied electric field. The high field dependence has also been studied in this research work and will be introduced in chapter 5. Another reason is that the loss tangent spectra in this study were transformed data from discharging currents without the contribution of conduction loss.

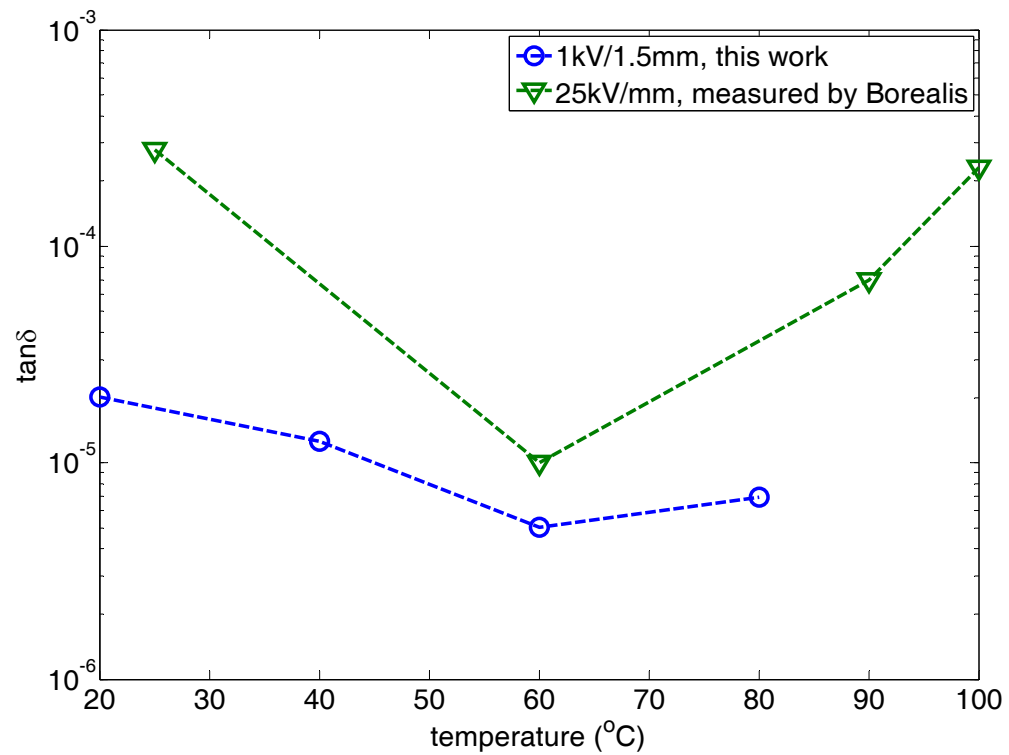


Figure 4.23 Loss tangent of cable AAA at 50Hz, compared with measurement results by Borealis

## 4.4 Master curve in the frequency range from $10^{-4}$ Hz to $10^4$ Hz

### 4.4.1 Data combination of different techniques

The measurement results of the three techniques are in different frequency ranges that makes it possible to show a broader loss tangent spectrum from  $10^{-4}$ Hz to  $10^4$ Hz. With the measurement results of real and imaginary permittivity, the loss tangent for FRA can be calculated by Equation 4-19. The results for cable ABA is shown in Figure 4.24. The results of different temperatures are shown in the same graph but the loss tangent is too small and in the noise floor at lower temperatures and higher frequencies. Because  $\epsilon'$  does not change for cables AAA and ABA, the shapes of  $\tan\delta$  is the same as that of  $\epsilon''$ , shown in Figure 4.4. The magnitudes are decreased by the factor of the  $\epsilon'$ . Valid  $\tan\delta$  values at  $10^4$ Hz can be found for  $60^\circ\text{C}$  and  $80^\circ\text{C}$  as  $1.20 \times 10^{-2}$  and  $1.83 \times 10^{-1}$  respectively. This very low frequency loss can well represent the DC conductivity loss and it mainly originates from the conduction current.

Figure 4.25 shows the loss tangent spectrum for cable ACA. The results have slightly different shapes from  $\epsilon''$  because  $\epsilon'$  has substantial increment, e.g.,  $\epsilon'$  increased 0.8 from 2.36 at 1Hz to 3.16 at  $10^4$ Hz under  $80^\circ\text{C}$  as shown in Figure 4.5. Apart from the DC conductivity loss with slope of -1, the additional loss peaks at  $60^\circ\text{C}$  and  $80^\circ\text{C}$  that relate to  $\epsilon'$  increment are more obvious. The  $\tan\delta$  of cable ACA is the biggest, compared with cables AAA and ABA. At the frequency of  $10^4$ Hz,  $\tan\delta$  is  $1.55 \times 10^{-1}$  at  $60^\circ\text{C}$  and  $7.08 \times 10^{-1}$  at  $80^\circ\text{C}$ , which are 13 times and 4 times bigger than those for cable ABA. Smaller difference at  $80^\circ\text{C}$  implies that the dielectric loss increases faster with increasing temperature and higher thermally activated conduction for homo-polymer cable ABA.

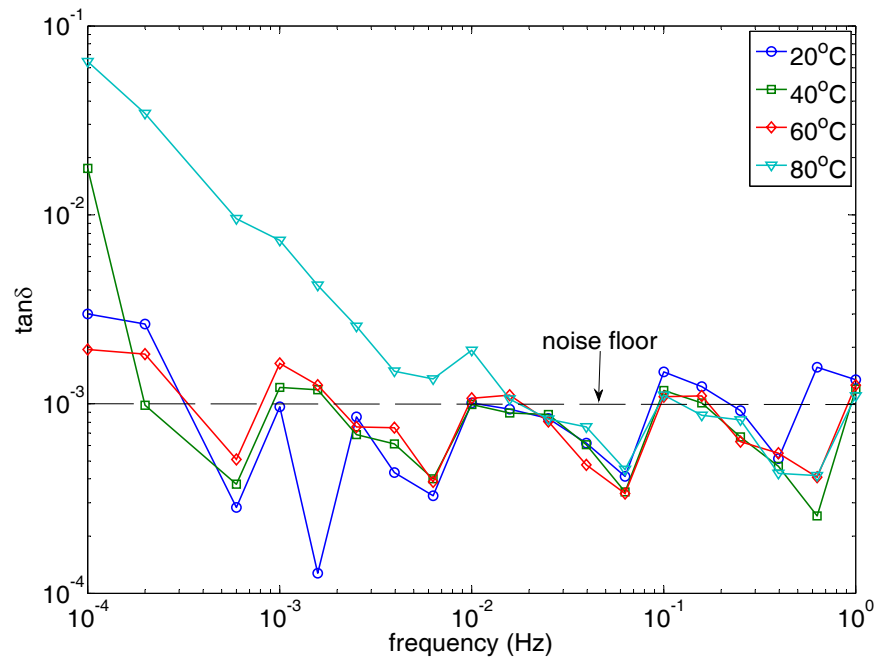


Figure 4.24 Loss tangent of cable ABA,  
calculated from  $\epsilon'$  and  $\epsilon''$  measurement results by FRA technique

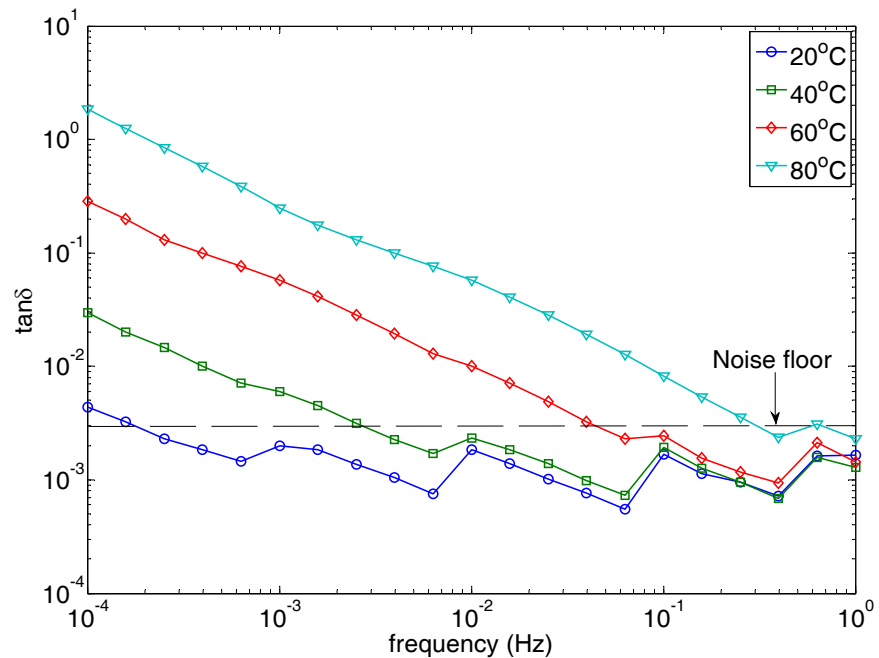


Figure 4.25 Loss tangent of cable ACA,  
calculated from  $\epsilon'$  and  $\epsilon''$  measurement results by FRA technique

In the middle frequency range, the frequency spectra from discharging current can cover the range from 0.1Hz to 100Hz. The transformation from time domain into frequency domain has been introduced in Section 4.3.2 with Equation 4-18. The loss tangent in Figure 4.22 shows the dielectric loss of cable AAA without conduction loss contribution, because the discharging current only includes depolarization of the insulation. In order to conform to the other two frequency domain techniques that measure the dielectric loss including the conduction loss contribution, the conduction loss should be added based on the conductivity measurement results. The conduction loss contribution to the  $\epsilon''$  was calculated with the measurement data on air degassed model power cables in Section 4.5 by

$$\epsilon'' = \frac{\sigma}{2\pi f \epsilon_0} \quad \text{Equation 4-21}$$

Figure 4.26 shows  $\epsilon''$  of cable ACA. The straight lines with slope of -1 represent the DC conductivity loss measured from steady state current during charging process. The line of 20°C is outside of the graph scales. After adding the conduction contribution, the depolarization loss from discharging current was greatly increased at lower frequencies and higher temperatures. The total dielectric loss has been plotted with solid marker lines. Compared with the depolarization loss, there is no observable difference at 20°C because the conduction loss contribution is so small. As the temperature increases, the conduction loss starts to dominate the dielectric loss, and determines the shape of the lower frequency  $\tan\delta$  spectra.

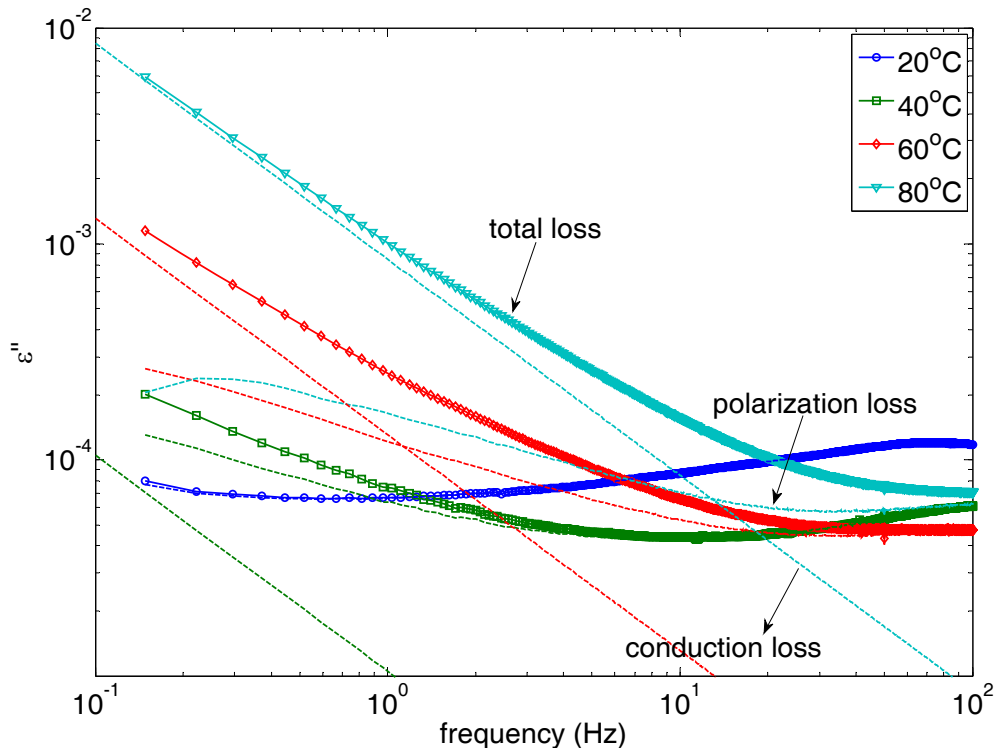


Figure 4.26 The  $\varepsilon''$  of cable ACA showing the addition of conduction loss to the depolarization loss

With the measured higher frequency real permittivity  $\varepsilon_\infty$  of about 2.2 for homo-polymer cables and 2.4 for co-polymer cable,  $\varepsilon'$  can be calculated and finally the total dielectric loss tangent spectra of the model power cables have been obtained. The  $\tan\delta$  of cable ACA is shown in Figure 4.27. Because the real permittivity increment  $\Delta\varepsilon'$  is very small (at the order of  $10^{-5}$ ), the  $\varepsilon'$  remains constant and  $\tan\delta$  has the same shapes as  $\varepsilon''$  for all temperatures. At lower frequencies, where the DC conductivity loss is dominant, the dielectric loss increases as the temperatures increases. At higher frequencies, where the depolarization loss takes part in the main role of the total loss, 20°C has the highest loss and 60°C has the lowest, e.g., at 50Hz with practical importance, the loss tangent value of cable ACA ranges from  $1.99 \times 10^{-5}$  at 60°C to  $4.86 \times 10^{-5}$  at 80°C.

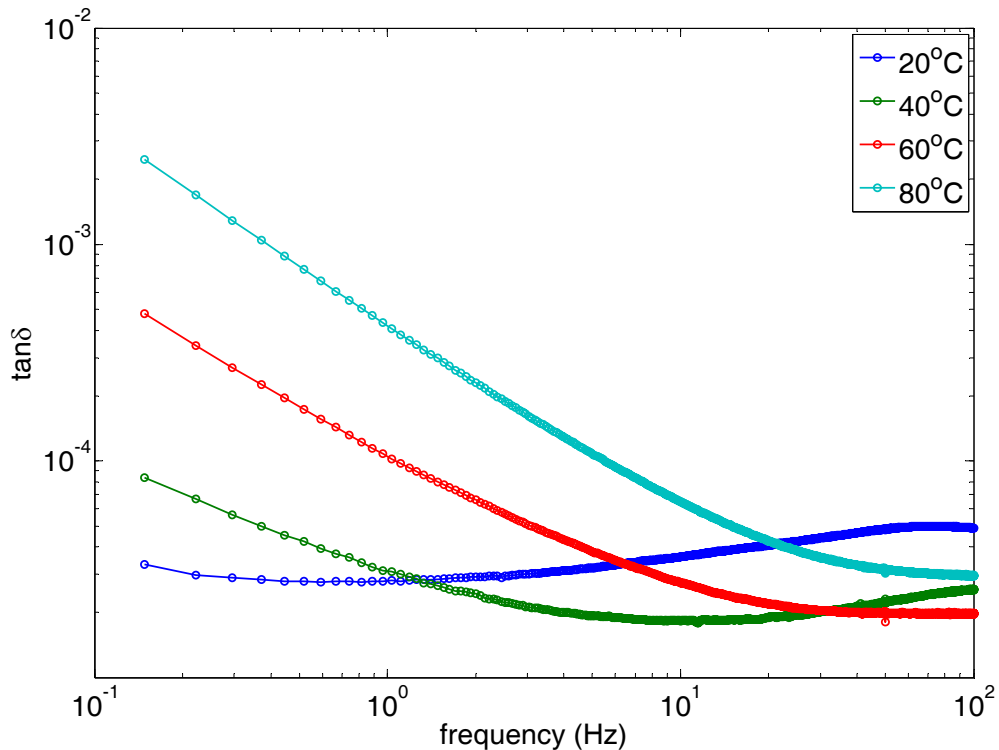


Figure 4.27 Loss tangent spectra of cable ACA at different temperatures

The transformer ratio bridge measurement results cover the frequency range from 300Hz to 10kHz. With the measured capacitance and conductance, Equation 4-4 was used for the loss tangent calculated of all the tested model power cables. After using the conductive adhesive copper tapes to wrap the whole length of the cable samples, the extra loss brought by axial resistance of the outer semicon layer has been largely eliminated. The loss tangent spectra of cable AAA under four temperatures are shown in Figure 4.28. The  $\tan\delta$  ranges from  $10^{-5}$  to  $10^{-2}$ . In the lower frequency range, there is a loss peak at 200Hz. Because this loss peak is independent of temperatures, it might be due to instrument errors. The loss tangent can be distinguished at higher frequencies. It increases at higher temperatures. Increasing loss with slope of 1 can be seen at 60°C and 80°C. The loss tangent at 10kHz is  $4.06 \times 10^{-4}$  at 60°C and  $1.37 \times 10^{-3}$  at 80°C. At 20°C,

the loss tangent is  $2.83 \times 10^{-5}$  on decreasing slope of the first loss peak. At 40°C, the second process starts to increase the dielectric loss tangent to  $8.58 \times 10^{-5}$ .

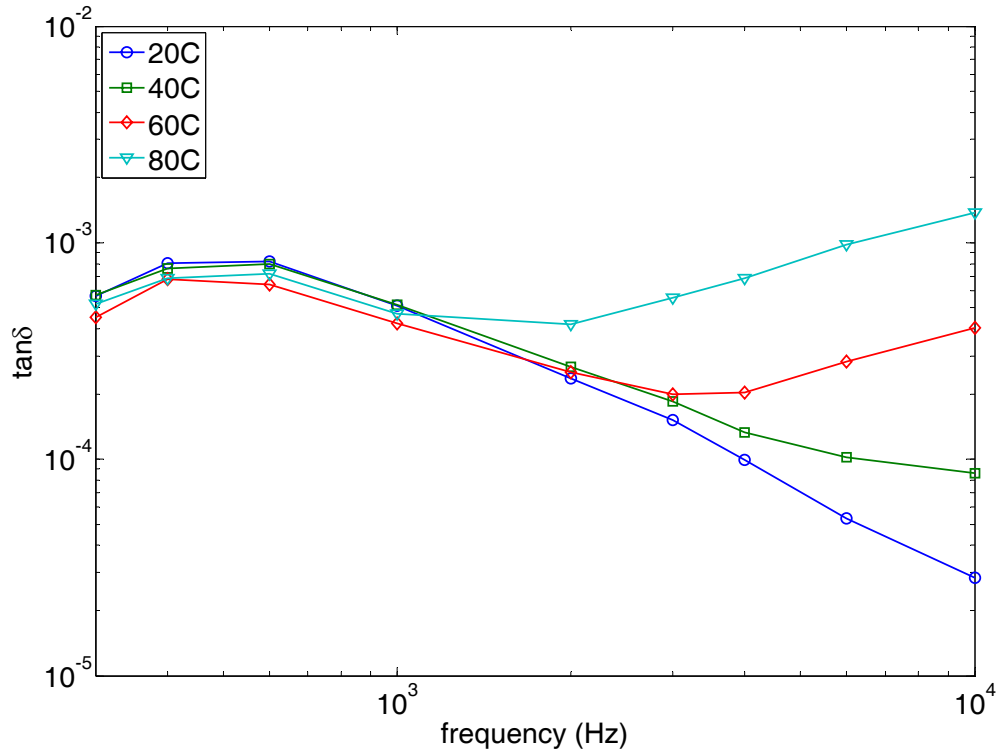


Figure 4.28 Loss tangent of cable AAA by transformer ratio bridge technique

The results of cable ACA can be seen in Figure 4.29. Similar temperature independent loss peak can be found at lower frequencies and the peak frequency slightly shifts to lower frequency. At higher frequencies the increasing slopes are present for three temperatures – 40°C, 60°C and 80°C. These increasing loss tangents at higher frequencies are parallel to each other. Higher dielectric loss can be observed for cable ACA, compared with the results on cable AAA. At 10kHz, the  $\tan\delta$  is  $6.11 \times 10^{-4}$  at 60°C and  $2.12 \times 10^{-3}$  at 80°C. The increasing dielectric loss with slope of 1 originates from the semicon layers. Although the axial resistance of the outer semicon layer had been eliminated by the copper tapes, the radial resistance of inner and outer the semicon

layers will give increase to the loss tangent at higher frequencies. In the equivalent circuit, even a very small series resistance will cause the loss tangent to increase at high frequencies. Because the conductivity of semicon materials decreases with increasing temperatures in the range from 20°C to 90°C, making the semicon layers more resistive, the values of the increasing loss tangent become bigger at higher temperatures. The reason for cable ACA to have higher dielectric loss is that additional dielectric loss origins, e.g. the polarization of the micron-size ethylene-butyl-acrylate islands for this co-polymer cable, have higher contribution to the total dielectric loss than the homo-polymer cables.

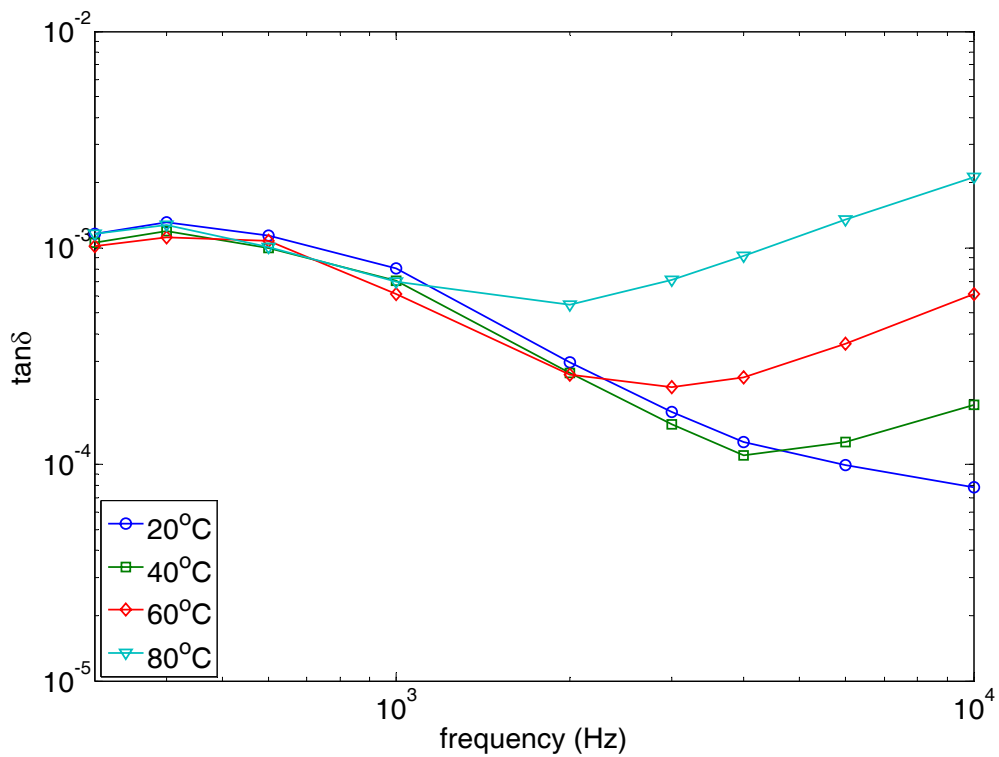


Figure 4.29 Loss tangent of cable ACA by transformer ratio bridge technique

The results of cable BAB are shown in Figure 4.30, in order to compare the effects of different semicon materials. with semicon B – super-smooth semicon, the overall loss

tangent spectra are similar with the cables with semicon A – standard semicon. The lower frequency loss peak has the same magnitude of  $10^{-3}$  and is independent of temperature. At higher frequencies, the loss tangent increases with increasing temperatures from  $60^{\circ}\text{C}$  to  $80^{\circ}\text{C}$ . The slopes of the increasing loss at higher frequencies have the same shape as those of all the other cables. This indicates that the increasing slopes are also due to semicon layers. However, the maximum  $\tan\delta$  at 10kHz are smaller. It is  $1.93 \times 10^{-4}$  at  $60^{\circ}\text{C}$  and  $8.11 \times 10^{-4}$  at  $80^{\circ}\text{C}$ .

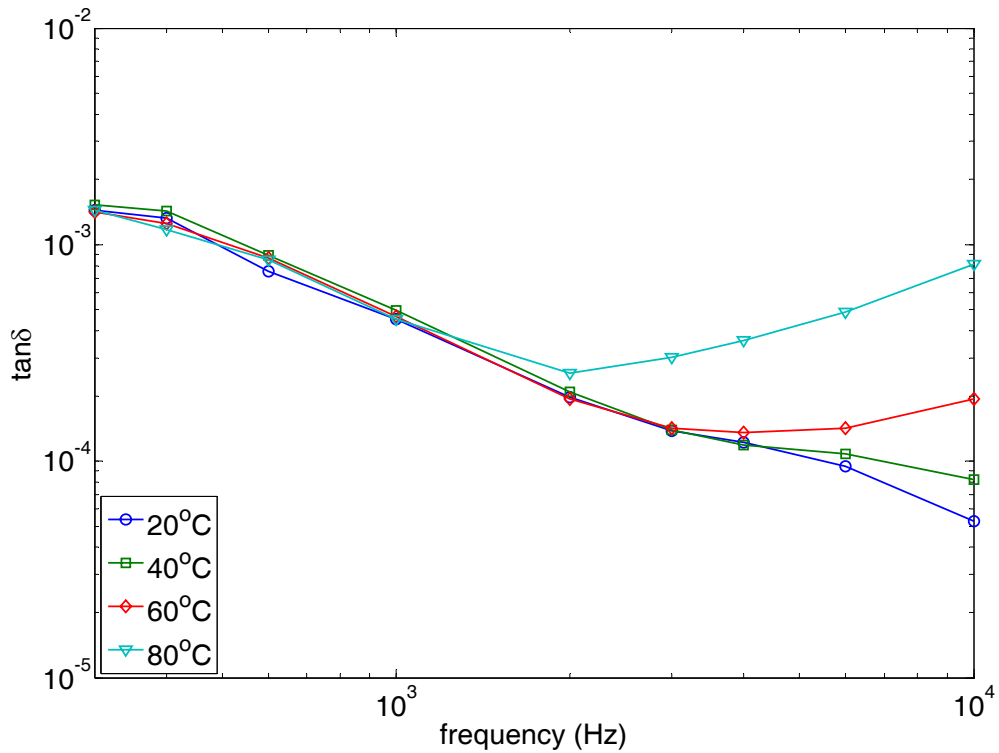


Figure 4.30 Loss tangent of cable BAB by transformer ratio bridge technique

A comparison of the loss tangent at 10kHz for different types of the model power cables is made in Table 4.3. The values in red colour are greatly influenced by the temperature-independent loss peak. Comparing the other  $\tan\delta$  values on the increasing slopes from the semicon layers, there are three main points:

1) Cable AAA has very close dielectric loss to that of cable ABA. This suggests that these two homo-polymer cables with the same semicon material have the dominant loss tangent from semicon layers at higher frequencies, while their dielectric loss from the insulation material – XLPE – is not detectable.

Table 4.3 Loss tangent ( $\times 10^{-5}$ ) of the model power cables at 10kHz under different temperatures, measured with transformer ratio bridge technique (the values in red colour are mainly due to instrument errors rather than due to the semicon resistance)

Cable	AAA	ABA	ACA	BAB
20°C	2.83	3.73	7.87	5.28
40°C	8.58	8.30	18.9	8.20
60°C	40.6	42.1	61.1	1.93
80°C	137	130	212	81.1

- 2) Cable ACA with co-polymer insulation layer has higher dielectric loss than the other homo-polymer cables. The increasing slope can be observed at 40°C. This implies that the co-polymer insulation contribute additional dielectric loss that may be due to the polarization of small polar molecules - the micron-size ethylene-butyl-acrylate.
- 3) Cable BAB with different semicon layers has lower dielectric loss than cable AAA. Since the loss should be mainly from the semicon layers, with the knowledge of the equivalent circuit modelling, this indicates that semicon B has higher conductivity or smaller resistivity in this temperature range, which can be

proved by the measurement results on the conductivity of semicon materials in Section 4.2.

#### 4.4.2 Loss tangent master curves

The loss tangent results by all three dielectric spectroscopy techniques may be merged together. The extrapolated master curves covering a wide frequency range from  $10^{-4}$ Hz to  $10^4$ Hz can be obtained. The extrapolation of master curve for cable AAA is shown in Figure 4.31. The original results of three techniques are plotted separately in different frequency ranges. The data in noise floor and instrumental errors should be excluded from this extrapolation process. The thick dashed black lines show the master curves for 60°C and 80°C. A dashed line with slope of 1 is plotted to help analyze the higher frequency spectra. The loss tangent due to DC conductivity at different temperatures with slope of -1 is also plotted to compare with FRA data and to help explain lower frequency spectra. Because of the measurement accuracy limitations, only at 60°C and 80°C can the master curve be extrapolated for the whole frequency range. At lower frequencies from  $10^{-4}$ Hz to 1Hz, the FRA results can be merged with the TDDS results, assuming a smooth transition in the range from  $10^{-2}$  to  $10^{-1}$ Hz in which there is no valid measurement data. The merging between TDDS results and transformer bridge results should consider the possible instrumental effects that bring a Debye loss peak at the beginning. Therefore, the master curve only connects the second process of the increasing loss in transformer bridge results. From the master curve of cable AAA at 80°C, it can be seen that at lower frequencies, conduction loss with slope of -1 dominates the dielectric loss in the frequency range from  $10^{-4}$ Hz to  $10^{-1}$ Hz. Then, the absolute value of the slope becomes less than 1. In the range  $10^{-1}$ Hz to 100Hz, the dielectric loss is rather “flat” with different temperature dependence as found in

previous sections. This suggests multiple loss behaviour is present. At higher frequencies, the dielectric loss due to semicon layers dominates with slope of 1.

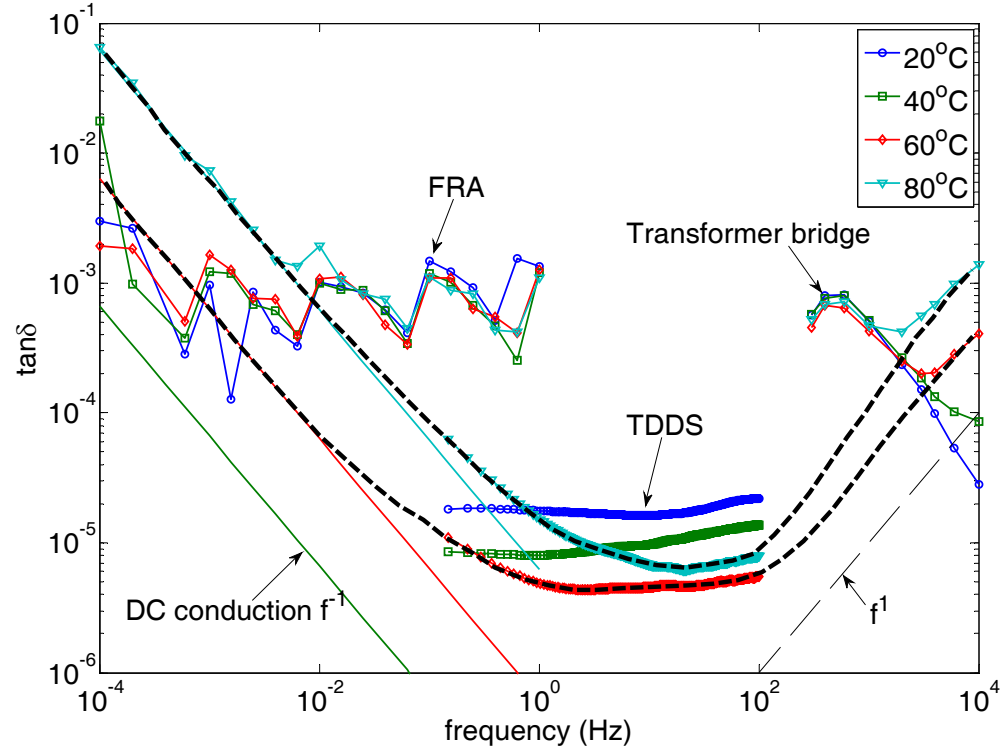


Figure 4.31 Extrapolation of master curve for cable AAA  
from measurement results of three dielectric spectroscopy techniques

In conclusion, cable AAA has multiple loss origins. Its dielectric loss tangent is from  $10^{-6}$  to  $10^{-1}$  in the frequency range from  $10^{-4}$ Hz to  $10^4$ Hz. The most remarkable feature for its dielectric loss spectrum is that conduction loss dominates lower frequencies while semicon layers dominate higher frequencies. The lowest dielectric loss occurs at the middle frequencies from 1Hz to 100Hz. In this frequency range, the intrinsic polarization loss of the XLPE cable insulation can be identified.

Cable ACA with co-polymer insulation has the highest dielectric loss, as found in all three techniques. The master curves for all temperatures have been extrapolated, as

shown in Figure 4.32. At lower frequencies, conduction loss is dominant and its spectra are parallel. The increasing loss with increasing temperatures indicates that the DC conductivity of the model power cables is thermally activated. At 60°C and 80°C, there is an additional loss peak overlapping with the DC conductivity loss. This additional loss is due to polarization because a relevant real permittivity increment was found in FRA measurement as discussed in Section 4.1.2. From 1Hz to 1kHz, the temperature dependence changes, e.g., 20°C has the highest loss tangent. Loss behaviour other than DC conductivity or semicon resistance is dominant, while the DC conductivity loss slope of -1 and semicon loss slope of 1 both attenuate to negligible magnitudes. At higher frequencies, semicon layers produce most of the dielectric loss with increasing loss at higher temperatures.

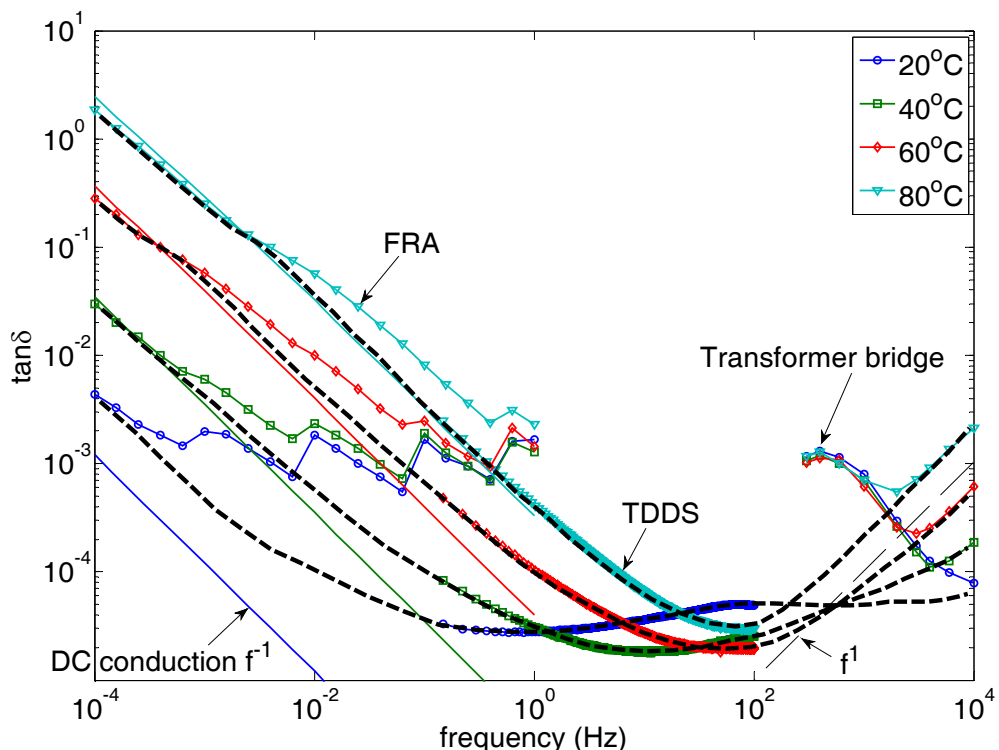


Figure 4.32 Extrapolation of master curve for cable ACA  
from measurement results of three dielectric spectroscopy techniques

## 4.5 Effect of degassing by conduction current measurement

The effects of degassing were studied on the conductivity of the model power cables using DC conduction current measurement. In order to achieve higher accuracy, the “harmonic-free” battery supply was used with Keithley electrometer model 617. Three different types of the model power cables – AAA, ABA and ACA have been tested under non-degassed fresh, air degassed and vacuum degassed conditions. The DC conductivity of those cables under different temperatures will be studied to characterise the degassing effects.

### 4.5.1 Time delay for conduction measurement

Because polymeric insulation materials have long chain molecules and take longer time to be polarized, the pure DC conduction current should be measured with a time delay for the insulation to be charged. With the purpose of finding out the time delay for DC conduction current measurement, the charging current for cable AAA and cable ACA was measured and the results are shown in Figure 4.33. The measurement was taken from  $10^{-3}$  hour to more than 100 hours with irregular time intervals. For cable AAA, the charging current is  $2.71 \times 10^{-10} \text{ A}$  at five seconds and decayed to  $1.56 \times 10^{-12} \text{ A}$  after two hours. After four hours the current was  $4.68 \times 10^{-14} \text{ A}$ , with four decade decay from the beginning. After four hours, very little decrement can be measured. When the voltage was applied for twenty one hours, the current was  $4.25 \times 10^{-14} \text{ A}$ . Only  $4.3 \times 10^{-15} \text{ A}$  decaying was measured from four hours to twenty one hours. Cable ACA has similar decay with a faster charging process. At four hours, the current decayed to  $1.96 \times 10^{-11} \text{ A}$ . From this time point to the last point at one hundred and forty four hours (six days), the

current decayed to  $1.86 \times 10^{-11} \text{ A}$ , with only 1pA decrement. Therefore, four hours time delay was practically chosen for the DC conduction measurement.

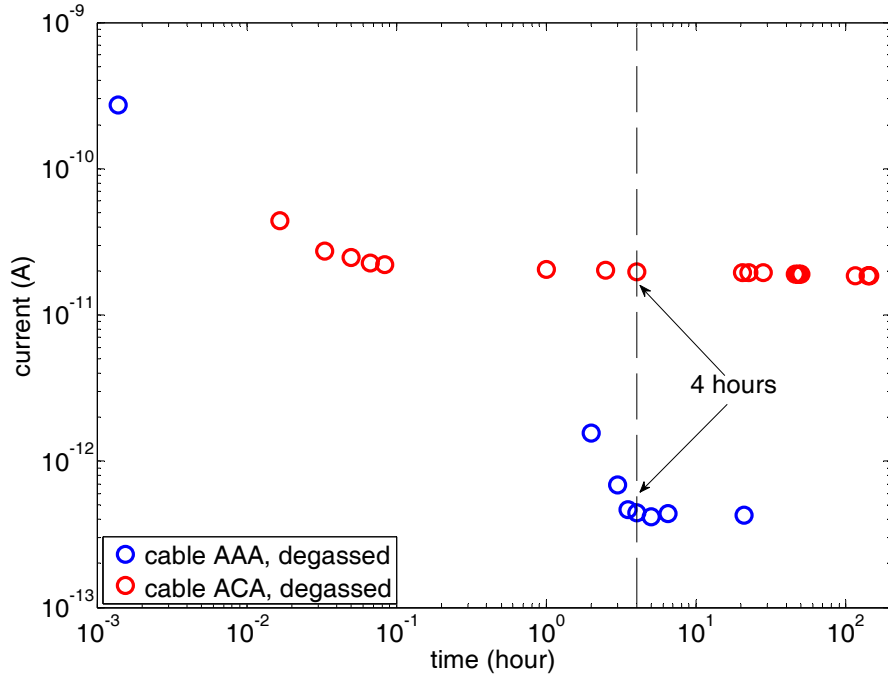


Figure 4.33 Current measurement on cable AAA  
in order to find the time delay for DC conduction measurement

#### 4.5.2 Results of non-degassed, air degassed and vacuum degassed cables

The non-degassed model power cables were firstly tested. Then the cable samples were degassed in air and in vacuum oven for repeated measurements on the same samples. The measurement results on fresh cable samples are shown in Figure 4.34. All three types of cables were measured under four temperatures from 20°C to 80°C. For cable AAA and ABA at 20°C, reliable data cannot be read because the measurement system has current measurement limit at  $10^{-13} \text{ A}$ . All cables have increasing DC conduction current under increasing temperatures. Cable AAA has the lowest DC conduction current with a good linear increasing trend in the semi-log scale axis. Cable ABA has

higher and parallel DC conduction current, compared with cable AAA. Cable ACA has the highest DC current with the biggest of  $7.09 \times 10^{-9}$  A under 80°C for the 5m long sample.

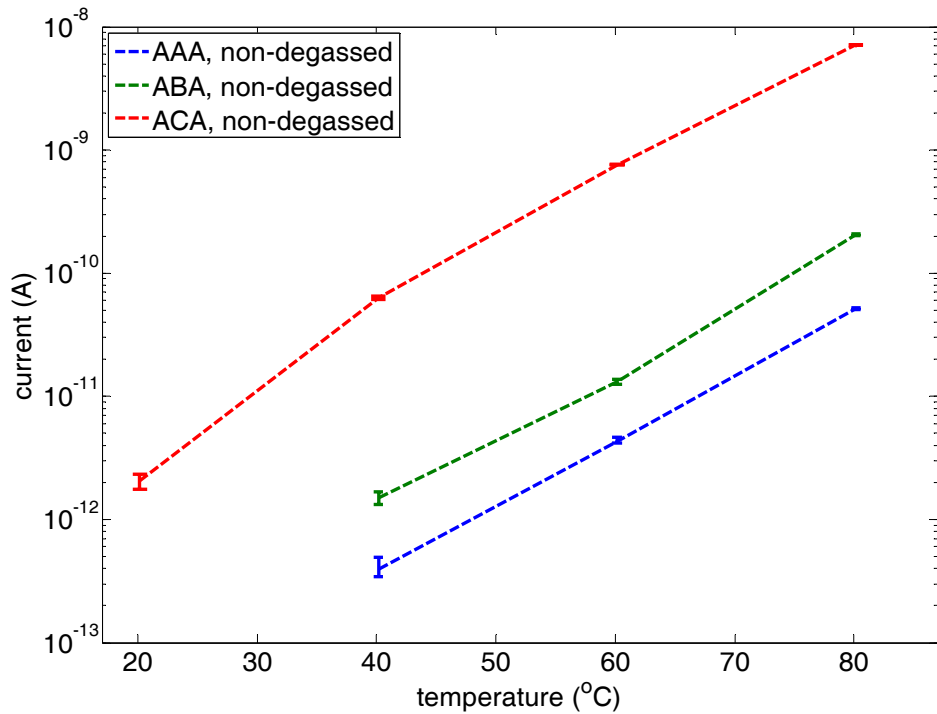


Figure 4.34 DC conduction current measurement results  
for non-degassed cables of AAA, ABA and ACA

Based on the geometric dimensions of the cable samples, the DC conductance is

$$G = \frac{\sigma 2\pi L}{\ln(r_0 / r_i)} \quad \text{Equation 4-22}$$

With Ohm's law  $G = \frac{I}{U}$ , the conductivity of the cable insulation can be calculated

$$\sigma = \frac{\ln(r_0 / r_i) I}{2\pi L U} \quad \text{Equation 4-23}$$

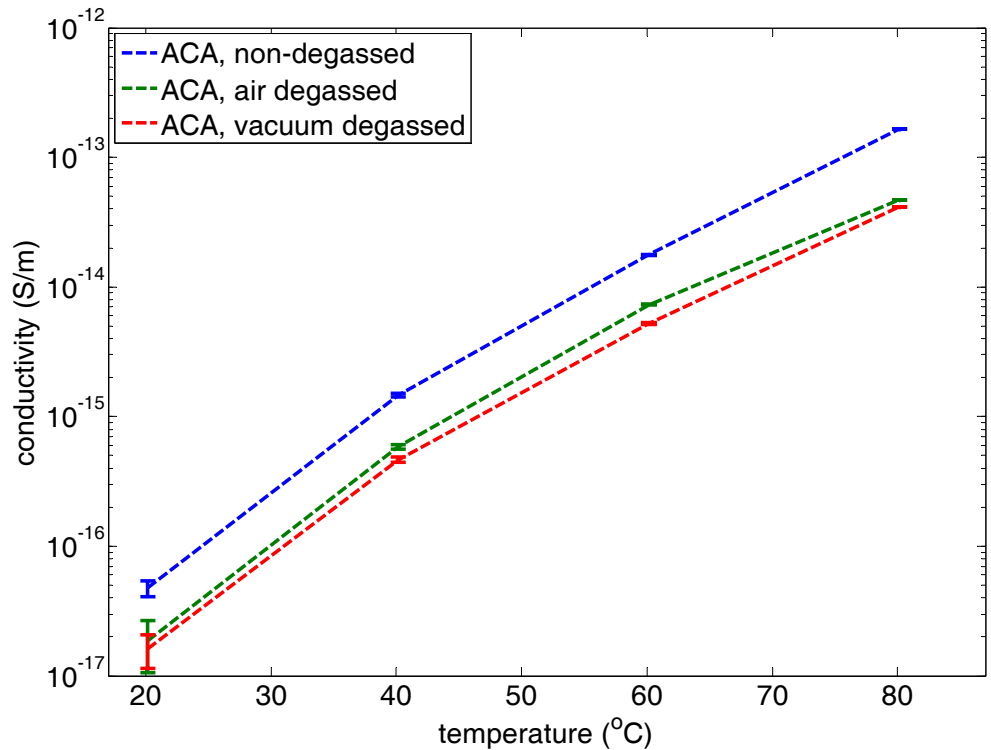


Figure 4.35 Conductivity of cable ACA  
with non-degassed, degassed and vacuum degassed conditions

The conductivity before and after degassing for three model power cables – AAA, ABA and ACA has been calculated from the DC conduction current measurement results. It is an essential electrical property of insulation materials and independent of dimensions. Figure 4.35 shows the conductivity of cable ACA under fresh, air degassed and vacuum degassed conditions. It can be seen from the results that the conductivity decreases after five days degassing in air. For example at 40°C, the conductivity decreases from  $1.47 \times 10^{-15}$  S/m to  $5.85 \times 10^{-16}$  S/m with 60.17% decrement. Further decrement was measured after another five days degassing in vacuum oven with  $10^{-3}$  bar (approximately  $10^{-3}$  atm). At 40°C, the conductivity decreases to  $4.64 \times 10^{-16}$  S/m with 68.35% decrement from the fresh condition and with further 20.55% decrement from the air degassed condition. The conductivity of different conditions is parallel to each other and

increasing at higher temperatures. The other two homo-polymer cables exhibit similar degassing effects with conductivity decrement after air degassing and further decrement after vacuum degassing.

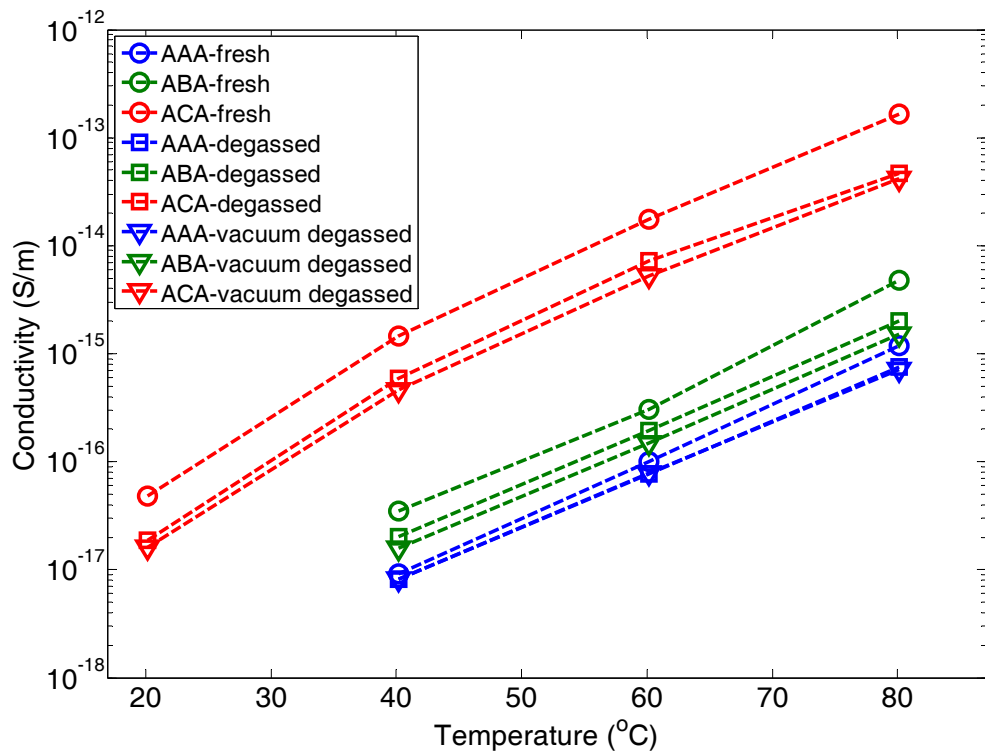


Figure 4.36 Comparison of conductivity on non-degassed fresh, air degassed and vacuum degassed model cables

The conductivity of the three cables under different conditions is shown in Figure 4.36. It ranges from  $10^{-18}\text{S/m}$  to  $10^{-13}\text{S/m}$  over the temperature range  $20^\circ\text{C}$  to  $80^\circ\text{C}$ . The DC conduction current of cable AAA and cable ABA was not measurable at  $20^\circ\text{C}$ . Like the results of cable ACA, all the cables have substantial decreasing of conductivity after air degassing. For example, cable ABA at  $40^\circ\text{C}$  has a conductivity of  $3.50 \times 10^{-17}\text{S/m}$ . It decreases to  $2.01 \times 10^{-17}\text{S/m}$  after air degassing and further decreases to  $1.58 \times 10^{-17}\text{S/m}$  after vacuum degassing. Comparison of different cables indicates that cable AAA has the lowest conductivity of  $8.12 \times 10^{-18}\text{S/m}$  at  $20^\circ\text{C}$  under vacuum degassed condition.

Cable ACA has the highest conductivity. This suggests that homo-polymer cable insulation is better than co-polymer cable insulation because the conductivity of co-polymer cable ACA has much higher conductivity than cable AAA and ABA.

The degassing level in average percentage of temperatures from the non-degassed fresh condition to air and vacuum degassed conditions is shown in Table 4.4. For cable AAA, the degassing in the air can reduce its conductivity for 23.46%. Further degassing in vacuum oven only improved 0.8%. Cable ABA has conductivity decrement of 45.30% after air degassing with 12.76% by further vacuum degassing. Cable ACA has the biggest conductivity decrement of 62.79% after air degassing with 7.15% by further vacuum degassing, compared with the other two homo-polymer cables.

Table 4.4 Average percentage of conductivity decrement  
after air and vacuum degassing for three model power cables

Cable	AAA	ABA	ACA
<b>Fresh→air degassed</b>	23.5%	45.3%	62.8%
<b>Fresh→vacuum degassed</b>	24.3%	58.0%	70.0%

In conclusion, degassing process can decrease the DC conductivity of the model power cables and, therefore, improve the insulation performance by reducing the dielectric loss. All model power cables have large amount of decrement from 23.46% to 62.79% after air degassing. Volatile by-products and impurities in fresh cables can be effectively removed by the degassing process so that the concentration of conductive charge carriers can be reduced. Further improvement can be made by using vacuum oven for the degassing procedure, but air degassing is more practical for mass production.

Comparatively, homo-polymer cables have smaller conductivity decrement after degassing. Cable AAA has the least degassing effect, while cable ABA has the biggest vacuum degassing effect. The further conductivity decrement after vacuum degassing may be also due to longer degassing time after air degassing and depend on the control of peroxide and additives during cable manufacturing.

#### 4.6 Conclusions

Dielectric response of degassed model power cables was measured using FRA, transformer ratio bridge and TDDS systems:

1.  $\epsilon''$  has slope of -1 and  $\epsilon'$  does not change much at lower frequencies from  $10^{-4}$ Hz to 1Hz, indicating that conduction loss is dominant.
2. The  $\tan\delta$  spectra has slope of 1 at higher frequencies from  $10^2$ Hz to  $10^4$ Hz. This is due to semicon layer resistance, according to the cable equivalent circuit modelling results.
3. Fourier transformation is used to convert TDDS data into frequency spectrum. “Flat” loss was found to dominate at the frequency range from  $10^{-1}$ Hz to  $10^2$ Hz.
4. Degassing effects have been studied using stable state current measurement. It was found that the conductivity can be reduced by 24% ~ 63% after degassing process and further reduction may be realized using vacuum degassing.
5. Both the dielectric spectra and DC conductivity of homo-polymer cables is lower than co-polymer cables.

## 5 Thermal ageing effects on model power cables

The model power cables with different insulation were thermally aged in an oven at 135°C for 50 days. This accelerated ageing condition is suggested by the model cable manufacturer. Apart from the obvious change of colour after the ageing process, the dielectric response measurements with FRA and TDDS have been taken to study the cable's electrical property changes. The influence of thermal ageing on the conductivity of the model power cables is also studied. The activation energy of the aged cables, in comparison with new degassed cables, is calculated based on the Arrhenius plots. In order to study the dielectric loss tangent of aged power cables under operating conditions, Schering bridge tests at mains frequency on both new degassed and aged cables are analyzed.

In chapter 3 and chapter 4, it was shown that the transformer ratio bridge measurement was greatly dependent on the contact between measuring electrode and outer semicon layer of the cable samples, so the measurement results are not reported for the aged cables. The conductivity of polymer power cables due to ageing would be expected to change [57] [141] [142]. So, the charging and discharging current measurements are presented in time domain. FRA measurement down to  $10^{-4}$ Hz were presented which showed the change of conductivity in the imaginary part of the capacitance and also a change in the real part of complex permittivity. Spectra from  $10^{-4}$ Hz to  $10^2$ Hz have been merged together and presented to compare aged and unaged cables using all the above information. Finally, the ageing effect with higher electric field has been measured with Schering bridge at 50Hz.

## 5.1 Dielectric response of aged model power cables using FRA

### 5.1.1 Ageing effect on homo-polymer model power cables

Experiments with frequency response analyzer under the same testing conditions as the unaged cables were carried out for different model power cables. Comparison can be made between the results of aged and unaged cable samples. The comparison of FRA measurement results for cable AAA is shown in Figure 5.1.

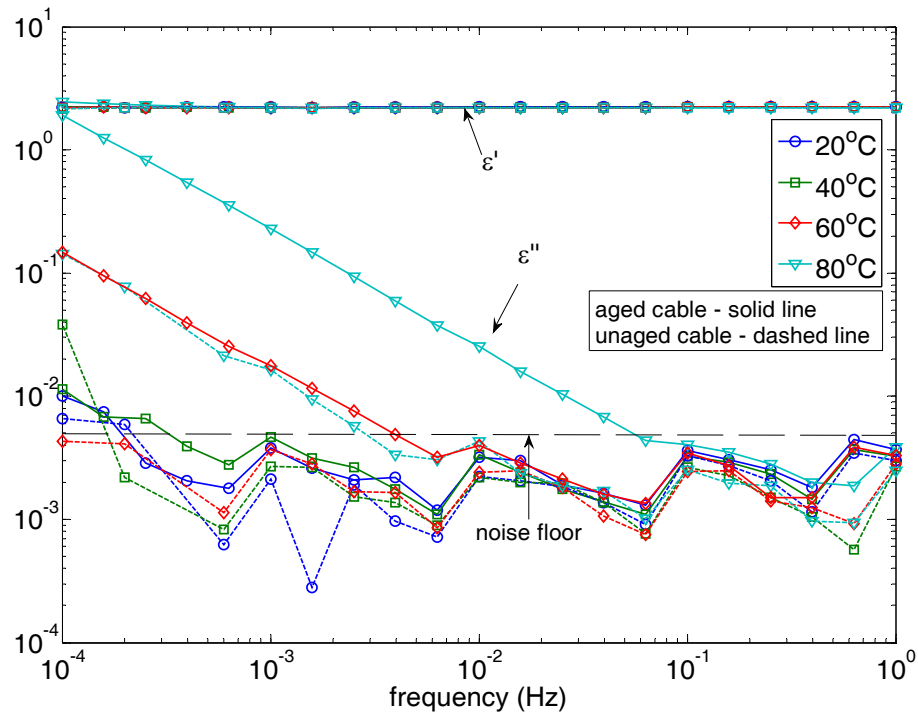


Figure 5.1 Comparison of real permittivity  $\epsilon'$  and imaginary permittivity  $\epsilon''$  between aged and unaged cable AAA, measured with FRA technique at different temperatures

The real permittivity  $\epsilon'$  and imaginary permittivity  $\epsilon''$  are plotted in the same graph in order to judge the types of dielectric loss. All solid lines represent the results of aged cable with different colours for different temperatures, while dashed lines represent the results of unaged cable. As found before, unaged cable AAA has the lowest dielectric

loss. Its  $\epsilon''$  is only measurable at 80°C; it is below the measurement limit for lower temperatures. After cable AAA was aged, its  $\epsilon''$  increased from 0.14 to 4.11 at 10<sup>4</sup>Hz.  $\epsilon''$  at 60°C could be measured and was found to be 0.26 at 10<sup>4</sup>Hz, even higher than that of unaged cable at 80°C ( $\epsilon''=0.14$ ). The  $\epsilon''$  of aged cable AAA at both 60°C and 80°C has a slope of very close to -1. Considering that  $\epsilon'$  does not have a big increment at lower frequencies, e.g., with parallel negative slope to the  $\epsilon''$ , the dielectric loss is mainly due to DC conductivity.

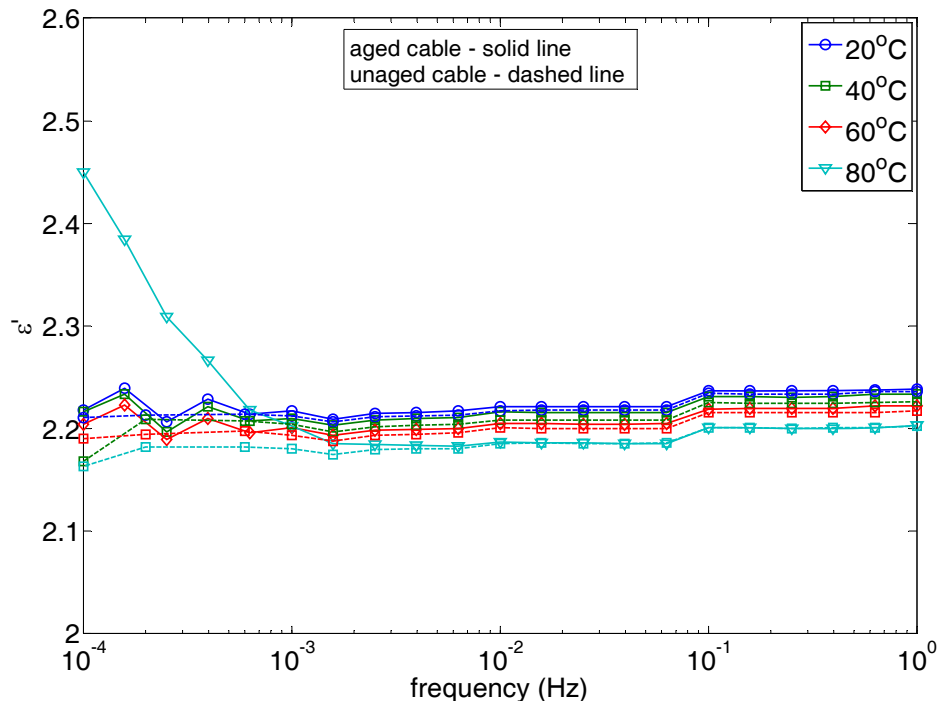


Figure 5.2 Comparison of real permittivity  $\epsilon'$  between aged and unaged cable AAA at different temperatures, showing increment for aged cable at 80°C

Although  $\epsilon'$  seems rather constant for both aged and unaged cables in Figure 5.1,  $\epsilon'$  of aged cable AAA at 80°C in fact has considerable increment at lower frequencies, as shown in Figure 5.2. The comparison of  $\epsilon'$  for aged and unaged cables indicates that the thermal ageing process resulted in its increment at higher temperatures.  $\epsilon'$  at 80°C is

$2.2 \pm 0.03$  before ageing and increases to 2.45 at  $10^4$ Hz after ageing. This increasing trend starts at the frequency of  $2 \times 10^{-3}$ Hz and has an increment  $\Delta\epsilon'$  of 0.25 at  $10^4$ Hz. A relevant loss peak for possible polarization or increasing loss towards lower frequencies for quasi-DC should be in the imaginary permittivity  $\epsilon''$ , though it is not very obvious while conduction loss is dominant.

### 5.1.2 Ageing effect on co-polymer model power cables

The measurement results on co-polymer cable ACA before and after ageing process are also compared to study the ageing effects on the dielectric properties. The comparison of the imaginary permittivity  $\epsilon''$  is shown in Figure 5.3. Because cable ACA has a higher dielectric loss than the homo-polymer cables,  $\epsilon''$  can be measured for all four temperatures.  $\epsilon''$  increased after thermal ageing. The increment becomes bigger at higher temperatures. At  $40^\circ\text{C}$  and  $10^4$ Hz,  $\epsilon''$  increases from  $1.11 \times 10^{-2}$  to  $1.56 \times 10^{-2}$ ; at  $80^\circ\text{C}$ ,  $\epsilon''$  increases from 2.23 to 7.89.  $\epsilon''$  after ageing is not very parallel to slope of -1 indicating similar loss behaviour. Apart from DC conductivity loss, additional loss peak can be seen for  $60^\circ\text{C}$  and  $80^\circ\text{C}$ . These two loss peaks are related to the increment of the real permittivity  $\epsilon'$  at lower frequencies, as shown in Figure 5.4. However, this small polarization loss is overwhelmed by conduction loss.  $\epsilon'$  at  $20^\circ\text{C}$  does not have an apparent increase after the cable is thermally aged. When the temperature increases to  $40^\circ\text{C}$ , a small amount of increment can be seen while  $\epsilon'$  is constant for unaged cable ACA.  $\epsilon''$  is curved at  $40^\circ\text{C}$ , which implies that a polarization peak is present. For higher temperatures of  $60^\circ\text{C}$  and  $80^\circ\text{C}$ ,  $\epsilon'$  increases further after ageing, e.g., from 3.1 to 3.7 at  $80^\circ\text{C}$ .

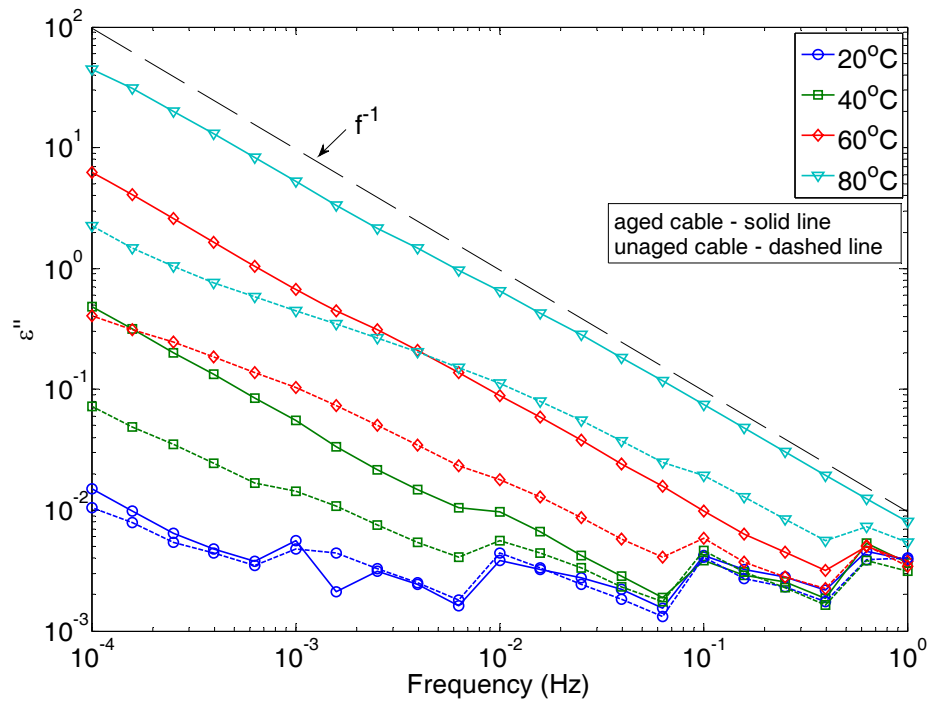


Figure 5.3 Comparison of imaginary permittivity  $\epsilon''$  for aged and unaged cable ACA, measurement with FRA technique

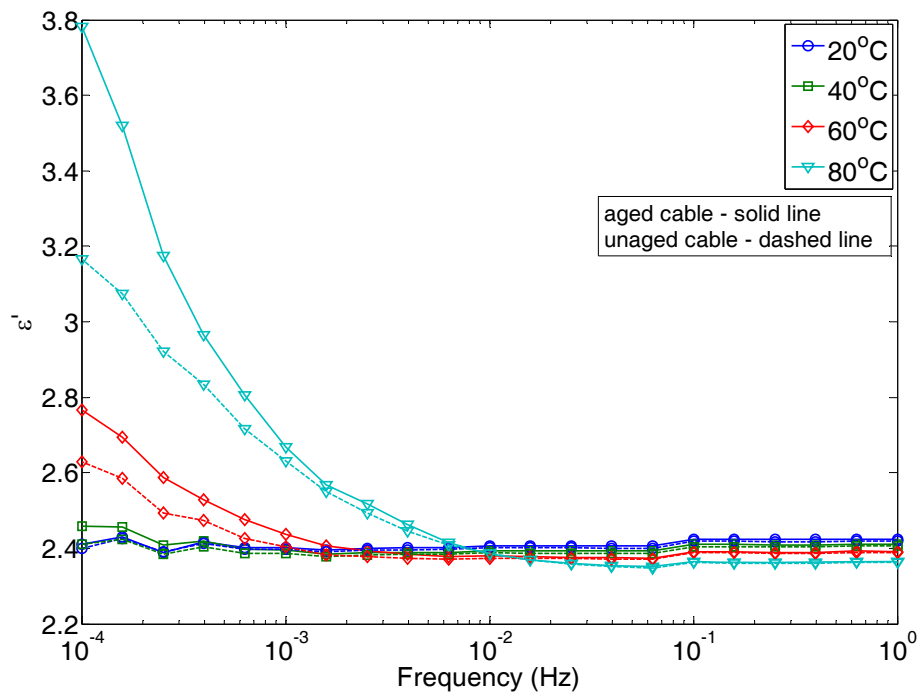


Figure 5.4 Comparison of real permittivity  $\epsilon'$  for aged and unaged cable ACA, measurement with FRA technique

The loss tangent of different model power cables in aged condition were calculated by

$$\tan \delta = \frac{C''}{C'} = \frac{\varepsilon''}{\varepsilon'} \quad \text{Equation 5-1}$$

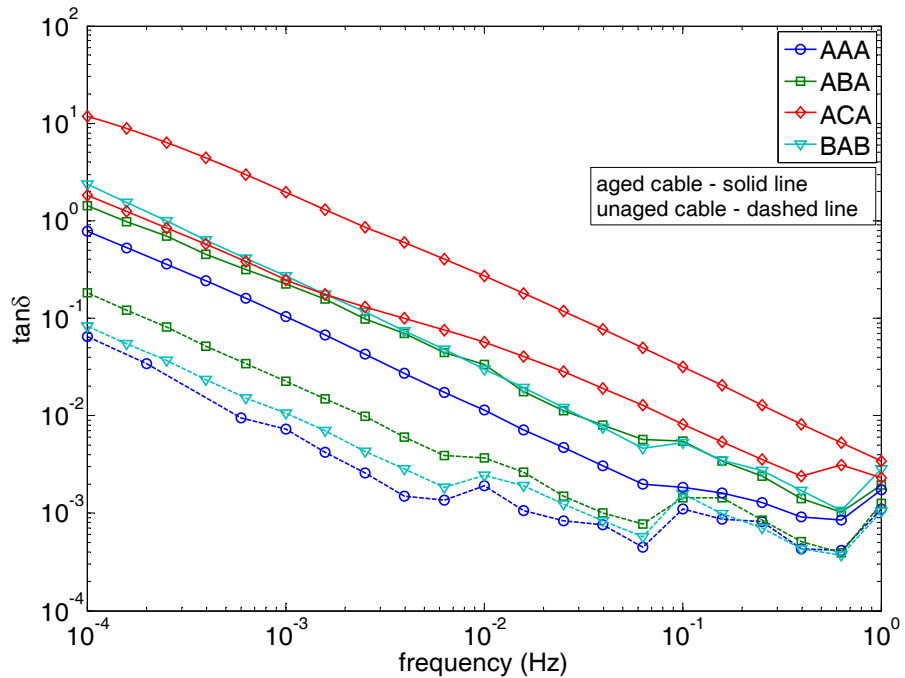


Figure 5.5 Comparison of loss tangent for aged and unaged model power cables, measurement with FRA technique at 80°C

A comparison of the loss tangent between aged and unaged cables at 80°C can be seen in Figure 5.5. It can be seen that the loss tangent increases after the ageing process for all model power cables. The homo-polymer cables have higher increments than the co-polymer cable ACA. This suggests that the thermal ageing process has greater influence on homo-polymer cables than co-polymer cables. Compared with other homo-polymer cables ABA and BAB, cable AAA has the largest increase. This comparison suggests that the homo-polymer cable AAA, which has the lowest dielectric loss under degassed condition, ages more quickly than the other cables. Although the co-polymer cable ACA is the lossiest one under degassed conditions, it may have the best “anti-ageing”

performance. The difference of ageing levels indicates that the thermal ageing has the greatest influence on the homo-polymer cables. With the same proportion of antioxidant, the dielectric loss of the co-polymer cables with EBA additive increases more slowly with better performance against thermal ageing.

## 5.2 Discharging current of aged model power cables

After using the frequency domain technique, frequency response analyzer, to investigate the thermal ageing effects, time domain dielectric spectroscopy technique, discharging current measurement, was used to study the ageing effects of different model power cables. The measurement was made with the same experimental setup as the measurement on unaged cables so that comparison can be easily made to explore the ageing effects.

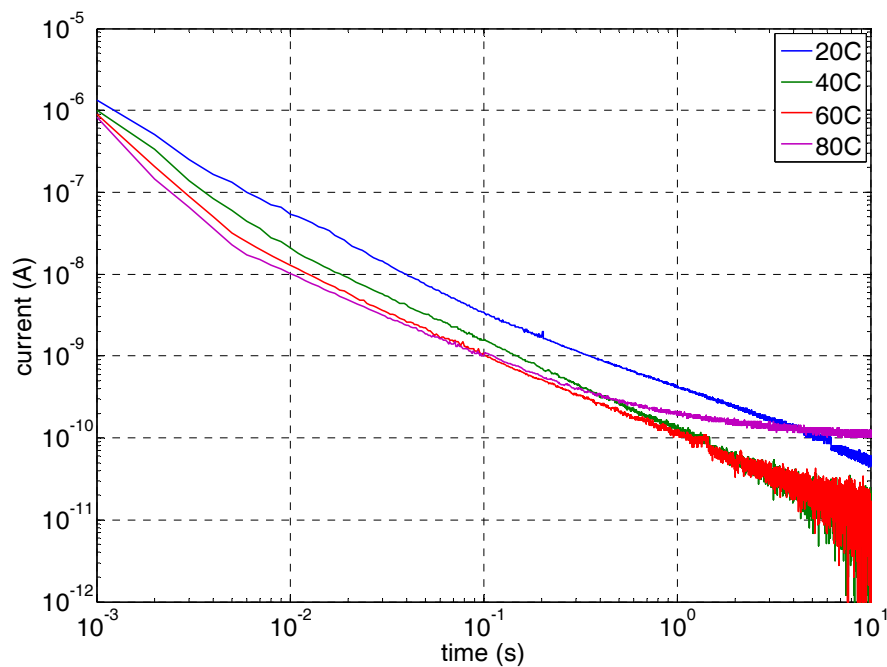


Figure 5.6 Discharging current measurement results on aged cable AAA under different temperatures

The discharging current measurement results on cable AAA is in Figure 5.6. The discharging current starts from  $10^{-6}\text{A}$  for all temperatures in at 1ms and decays 6 decades to  $10^{-12}\text{A}$  at 10s. The biggest discharging current occurred at  $20^\circ\text{C}$ , and this is the same as that of unaged cables. The discharging currents at  $40^\circ\text{C}$  and  $60^\circ\text{C}$  are smaller with the same trend. At  $80^\circ\text{C}$ , the current has the same shape in the first 0.1s and it is smaller than that at  $60^\circ\text{C}$ . However, the discharging current is  $1.18 \times 10^{-10}\text{A}$  at 10s with different trend from the other temperatures. It is even bigger than that of  $20^\circ\text{C}$  –  $4.96 \times 10^{-12}\text{A}$ .

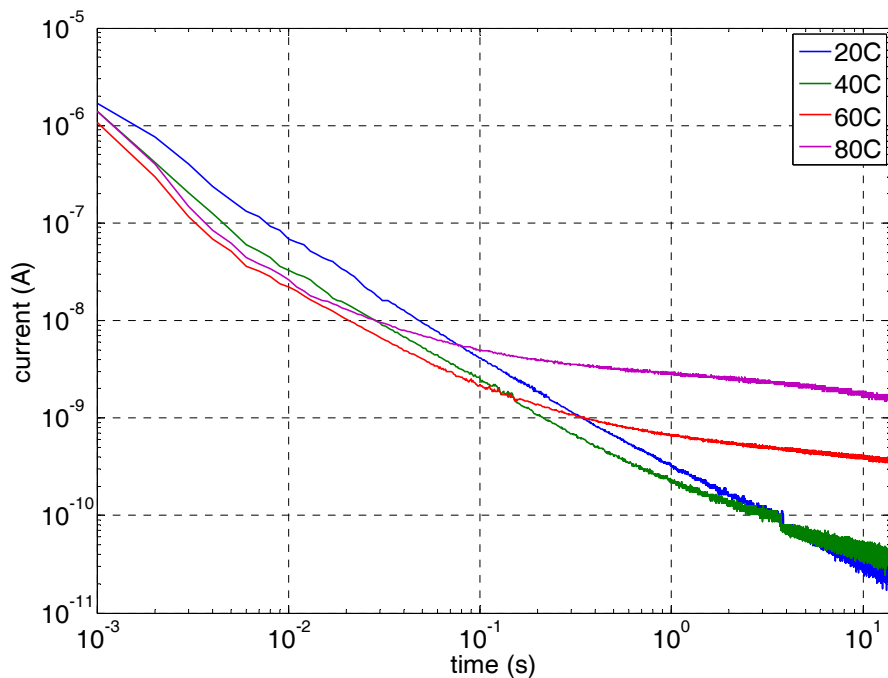


Figure 5.7 Discharging current measurement results on aged cable ACA under different temperatures

Figure 5.7 shows the discharging current measurement results for cable ACA. Better resolution was obtained because the currents are bigger for this lossier co-polymer cable. At  $20^\circ\text{C}$ , the discharging current has the same decaying trend as that of cable AAA. However, at higher temperatures, the currents have slower decaying especially for  $60^\circ\text{C}$ .

and 80°C. The discharging current was  $1.80 \times 10^{-9}$ A at 10s, much bigger than that at 20°C –  $2.86 \times 10^{-11}$ A. This slower decaying phenomenon has been found for all aged cables at higher temperatures, indicating that it takes longer time to discharge/depolarize than unaged cables.

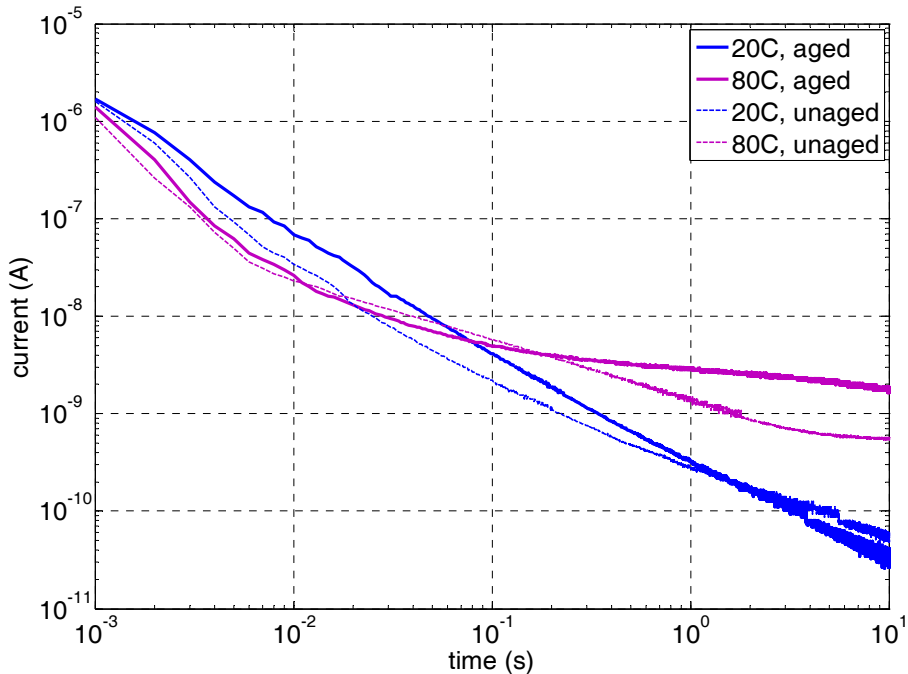


Figure 5.8 Comparison of discharging current for aged and unaged cable ACA at 20°C and 80°C

For all types of tested model power cables, the discharging currents are substantially increased by the thermal ageing process, more apparently at higher temperatures and longer times. Comparison with unaged cable ACA at 20°C and 80°C can be seen in Figure 5.8. The solid lines are the discharging currents of aged cable sample and the dashed lines are for unaged cable sample. It can be seen that both aged and unaged cables have the similar discharging current value of  $(1.5 \pm 0.5) \times 10^{-6}$ A at the beginning of the test. The discharging current at 20°C decayed to  $10^{-11}$ A for both aged and unaged

cables with a similar decaying trend. When the temperature was at 80°C, the discharging current had faster decaying in the first 70ms than that at 20°C for aged cable ACA but it was bigger afterwards. Unaged cable ACA has the same temperature dependence, with an earlier turning point at 20ms. Compared with the unaged cable ACA at 80°C, the aged cable had very close discharging current in the first 200ms. After this point the discharging current of aged cable was bigger and it was  $1.80 \times 10^{-9}$  A at 10s while it was  $5.66 \times 10^{-10}$  A for the unaged cable.

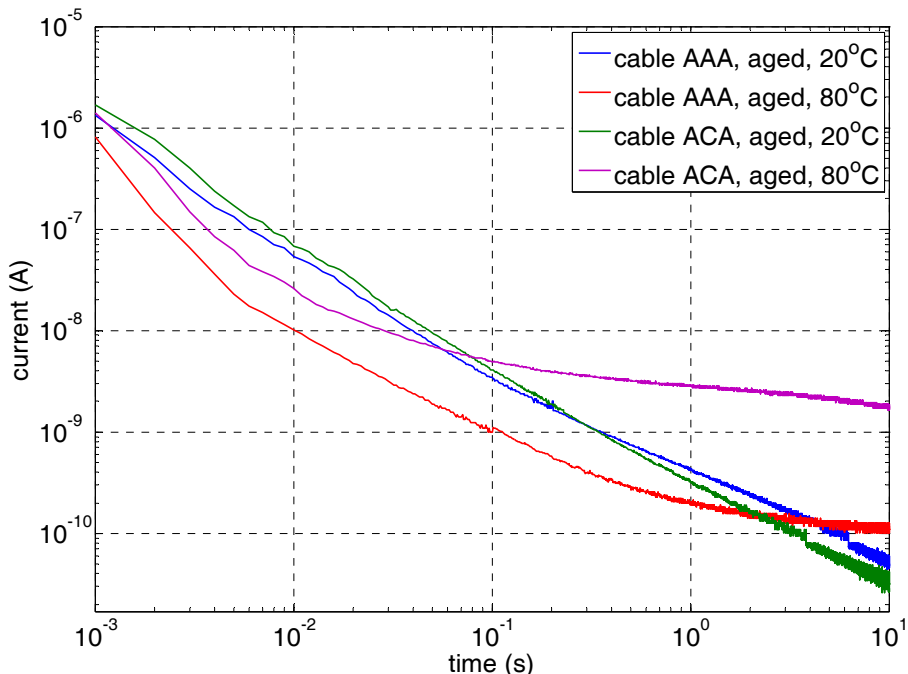


Figure 5.9 Comparison of discharging current for aged cable AAA and ACA at 20°C and 80°C

Comparison between aged homo-polymer and aged co-polymer cables can be made in Figure 5.9. The discharging currents of aged cable AAA and ACA at 20°C and 80°C are plotted together. At 20°C, there is very small difference between the homo-polymer cable and the co-polymer cable, compared with the results at 80°C. The discharging

currents for both aged cables decayed from  $10^{-6}\text{A}$  at 1ms to  $10^{-11}\text{A}$  at 10s. Their decaying trends are almost straight in the log scale graph, which suggests power law decaying (linear decaying in the log-log scale) for both types of cables. Very differently at  $80^\circ\text{C}$ , the difference becomes obvious between homo-polymer and co-polymer cables. The gap at the first 10ms is small and becomes more than 1 decade after 100ms. The bigger discharging current of the aged cable ACA suggests that the aged co-polymer cables can store more charges than the homo-polymer cables at  $80^\circ\text{C}$ .

### 5.3 The loss tangent spectra from $10^{-4}\text{Hz}$ to $10^2\text{Hz}$

After calculating the loss tangent from FRA measurement results and from time domain current, the loss tangent spectra from  $10^{-4}\text{Hz}$  to  $10^2\text{Hz}$  for both homo-polymer and co-polymer XLPE model cables are shown in Figure 5.10 and Figure 5.11 respectively. DC conduction measurement results are also shown in the graphs to help compare with FRA measurement results. In Figure 5.10, the master curves of aged cable AAA show similar conduction loss at lower frequencies with slope of -1. The FRA measurement results have good coherence with the DC conduction measurement results. At  $80^\circ\text{C}$ , FRA results are curved at very low frequency end, because of the real permittivity increment as one of the ageing effects. This means that the actual conduction loss by FRA measurement should be lower than that of charging current measurement, due to the lower applied electric field. A small relaxation process is present at the lower frequencies. At higher frequencies from 1Hz to 100Hz, the loss tangent has the same temeprature dependence as the unaged cables, with the lowest loss at  $60^\circ\text{C}$ . The dielectric loss is flat in this frequency range. Figure 5.11 shows the master curves at different temperatures. This aged co-polymer cable ACA has 10 times bigger dielectric loss tangent than the aged homo-polymer cable AAA.

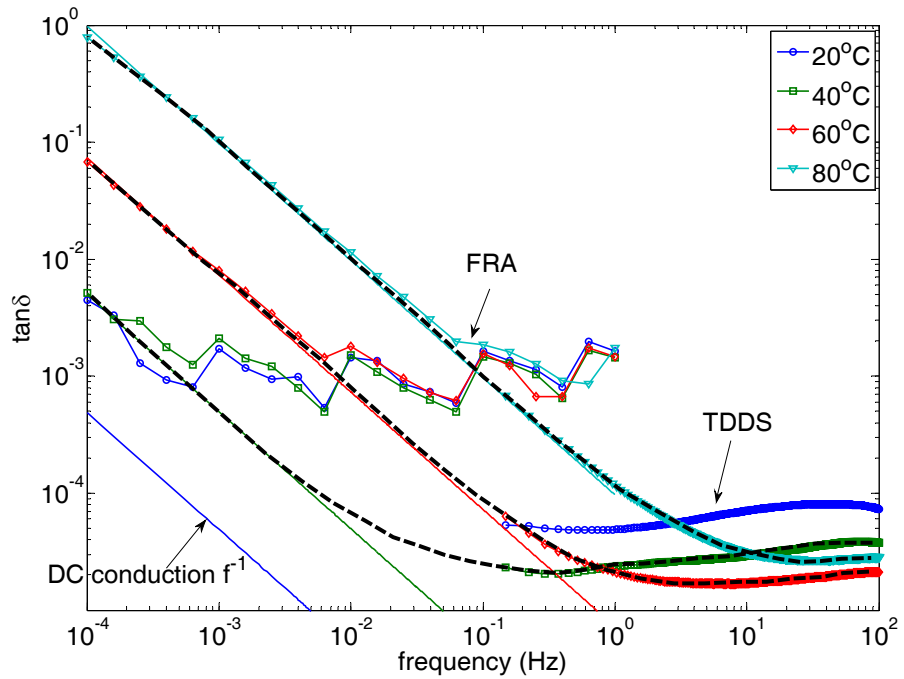


Figure 5.10 Master curve of aged cable AAA, colour lines are measurement data, black dashed lines are extrapolated master curves at different temperatures

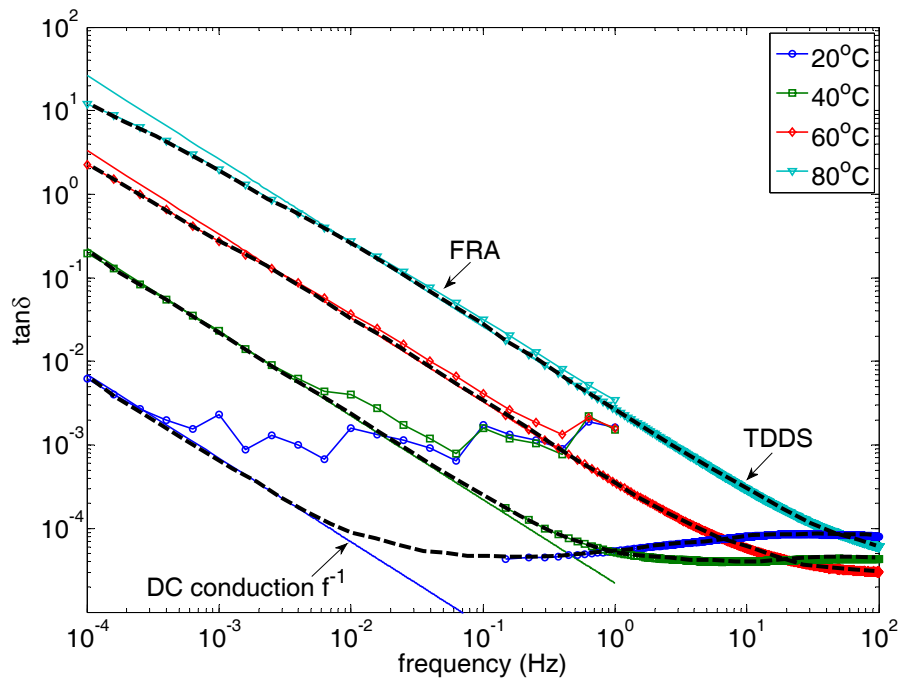


Figure 5.11 Master curve of aged cable ACA, colour lines are measurement data, black dashed lines are extrapolated master curves at different temperatures

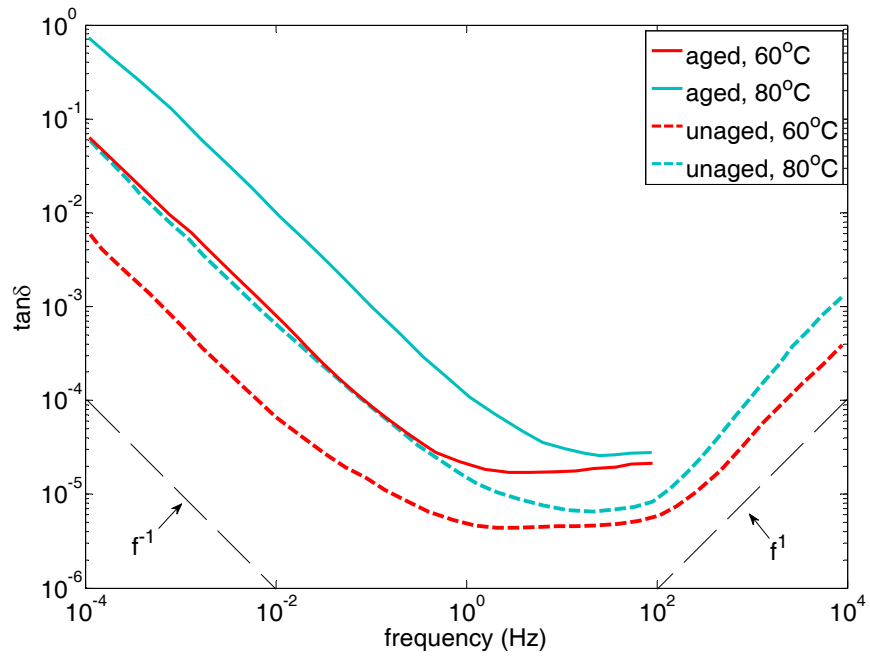


Figure 5.12 Master curves of cable AAA before and after ageing at different temperatures

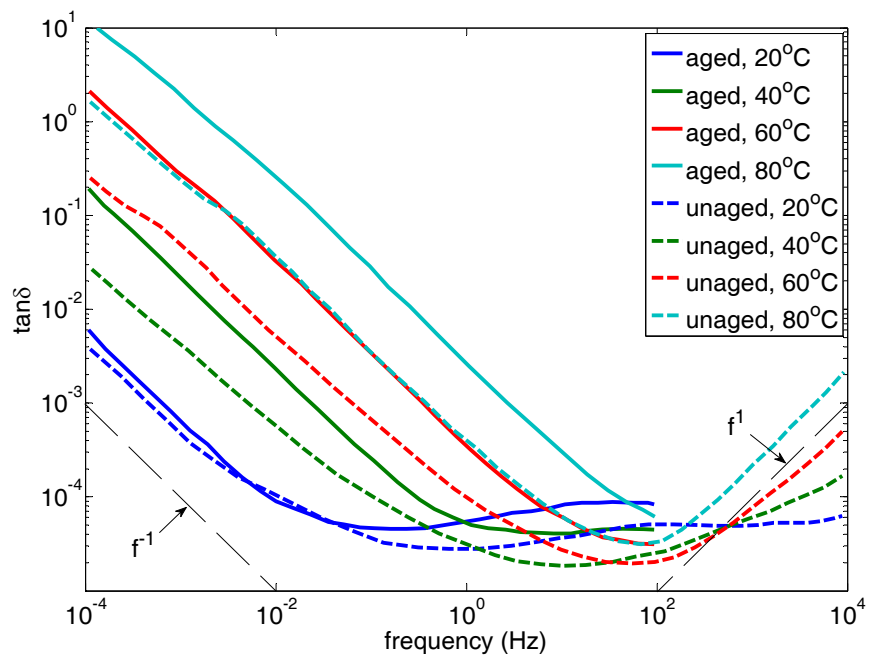


Figure 5.13 Master curves of cable ACA before and after ageing at different temperatures

Comparisons can be made with the master curves of unaged model cables. Figure 5.12 shows the comparison for cable AAA at the temperatures of 60°C and 80°C. For cable ACA, the comparison is shown in Figure 5.13. It can be seen that for both homo- and co-polymer cables, the loss tangent has about 10 times increase for all the temperatures, while the shapes of the loss spectra keep the same.

## 5.4 Ageing effects on conductivity of model power cables

### 5.4.1 Influence of thermal ageing on conductivity of model power cables

The conductivity of the aged model power cables has been measured with the 1kV battery voltage supply and Keithley 617 electrometer. The measurement setup and conditions were the same as for the unaged cables. The thermally aged cable samples, AAA, ABA and ACA, were tested after four hours charging time under four temperatures: 20°C, 40°C, 60°C and 80°C. The DC conduction currents for the aged cable AAA, in comparison with the unaged cable, are shown in Figure 5.14. The DC conduction current increases at higher temperatures. In the temperature range from 20°C to 80°C, the DC conduction current is from  $2.57 \times 10^{-13}$  A to  $5.13 \times 10^{-10}$  A. A linear increasing trend can be seen in the semi-log scale. The trend is parallel to that of the unaged cable AAA, for which the current at 20°C is absent in the plot because of measurement limitations. The measurement results suggest the aged homo-polymer cable AAA still has an increasing conductivity at higher temperatures. It becomes more conductive after thermal ageing, e.g. the DC conduction current at 80°C is 16 times bigger than that of unaged cable sample,  $3.25 \times 10^{-11}$  A. Thermal ageing, therefore, has a significant effect on DC conductivity.

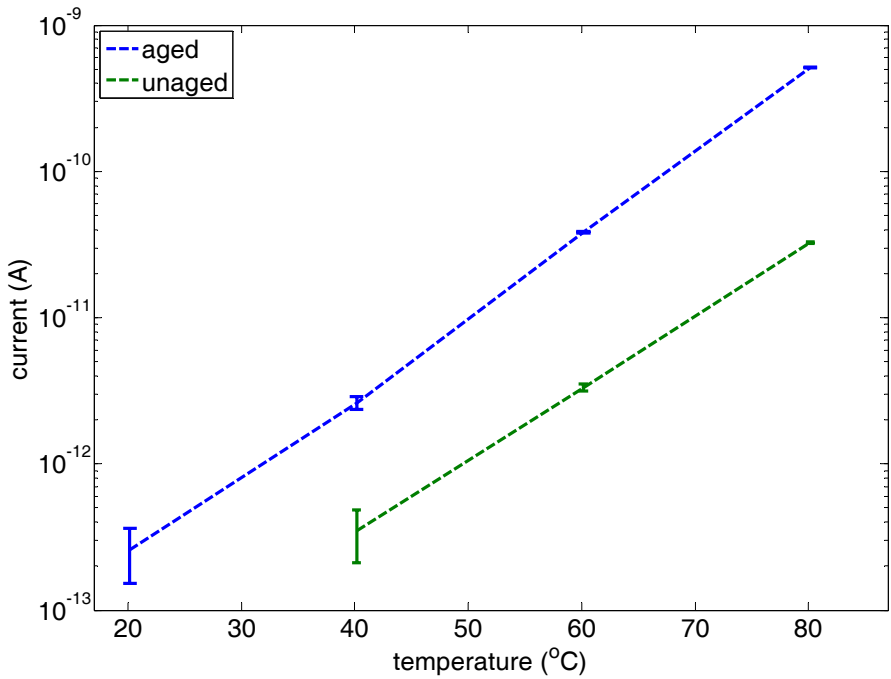


Figure 5.14 DC conduction current of aged and unaged cable AAA at different temperatures

Applying the same equation (introduced in chapter 3),

$$\sigma = \frac{\ln(r_0 / r_i) I}{2\pi L U} \quad \text{Equation 5-2}$$

the conductivity of the aged model cables can be calculated. The calculation results are plotted in Figure 5.15. The conductivity of aged cables is interconnected with solid lines, while the results of unaged cables have dashed lines. It can be seen that the conductivity for all aged cables have increasing temperature dependence. In the semi-log scale graph, the conductivity of cable AAA has a linear relationship with the absolute temperature, indicating a relation of  $\log \sigma \propto T$ . Cable ABA has bigger conductivity than cable AAA. It has the same linear increasing trend until 60°C, but deviation was measured with bigger increment at 80°C. Among the three cables, the co-polymer cable ACA has the biggest conductivity. Its temperature dependence is curved with relatively smaller

increment at higher temperatures, which is different from the homo-polymer cable AAA and ABA. Compared with the unaged cables, the conductivity for all the model cables becomes bigger. The cables still have the same sequence as unaged cables, with cable AAA having the smallest conductivity. With the same thermal ageing condition, it is found that cable ABA has the biggest conductivity increment. Although co-polymer cable ACA has the biggest absolute conductivity, the increment after ageing process is smaller than those of the two homo-polymer cables.

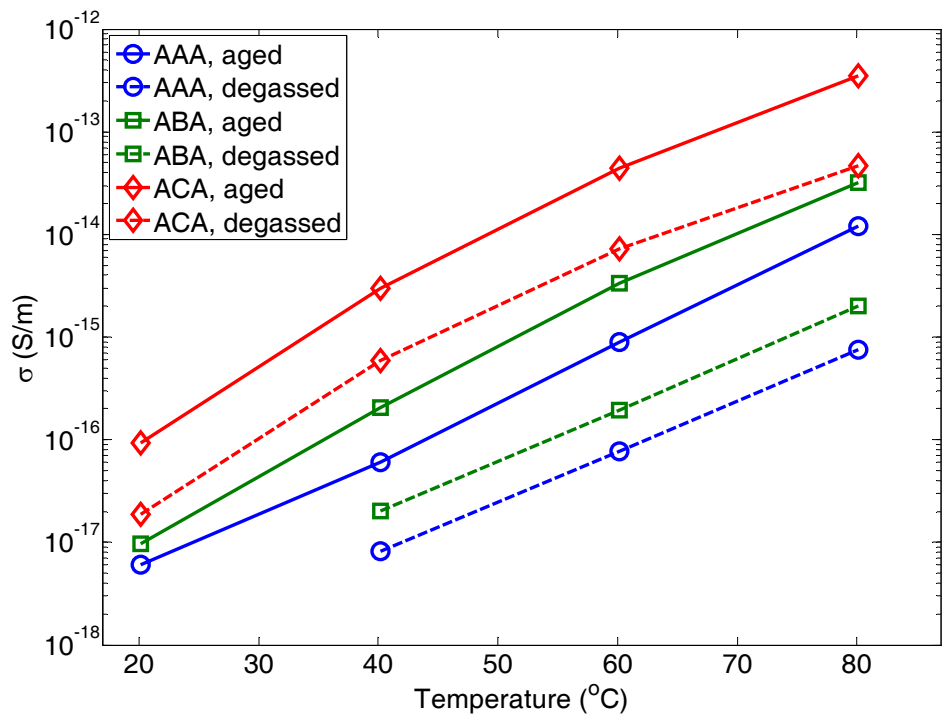


Figure 5.15 Conductivity of aged model power cables, compared with unaged cables

#### 5.4.2 Activation energy change after thermal ageing

The thermal activation energy of the model power cables can be studied through the measurement results of conductivity at different temperatures. According to Arrhenius equation

$$\sigma = \sigma_0 \times e^{-\frac{E_a}{kT}}$$
Equation 5-3

which can also be written as

$$\ln \sigma = \ln \sigma_0 - \frac{E_a}{kT}$$
Equation 5-4

the logarithmic conductivity should have linear relationship with the reciprocal of temperature

$$\ln \sigma \propto \frac{1}{T}$$
Equation 5-5

The thermal activation energy  $E_a$  can be obtained from the gradient of the straight line.

In the Arrhenius equation, the value of the "y-intercept" corresponds to a pre-exponential factor  $\ln \sigma_0$ .  $k$  is the Boltzmann's constant that is  $1.38 \times 10^{-23}$  J/K or  $8.617 \times 10^{-5}$  eV/K.

The Arrhenius plots for different aged model power cables are shown in Figure 5.16. Linear fitting lines are also plotted for the calculation of thermal activation energy. The linear relationship of the fitting lines and the activation energies calculated from the gradients are in separate boxes with relevant colours. From the measurement results, it can be seen that aged cables AAA and ACA have good fitting. The measurement results are closely scattered around the fitted lines. It can also be seen that the results of AAA have opposite curvature to that of ACA. This suggests that the homo-polymer cables have bigger thermal activation energy at higher temperatures and the co-polymer cables have decreasing activation energy at higher temperatures. For cable ABA, the fitting is

very good at the temperatures except 80°C; while at higher temperatures above 60°C, the increasing conductivity has a bigger gradient which suggests higher activation energy. The activation energy values for all three cables are very close – 1.13eV for cable AAA and 1.23eV for cable ACA.

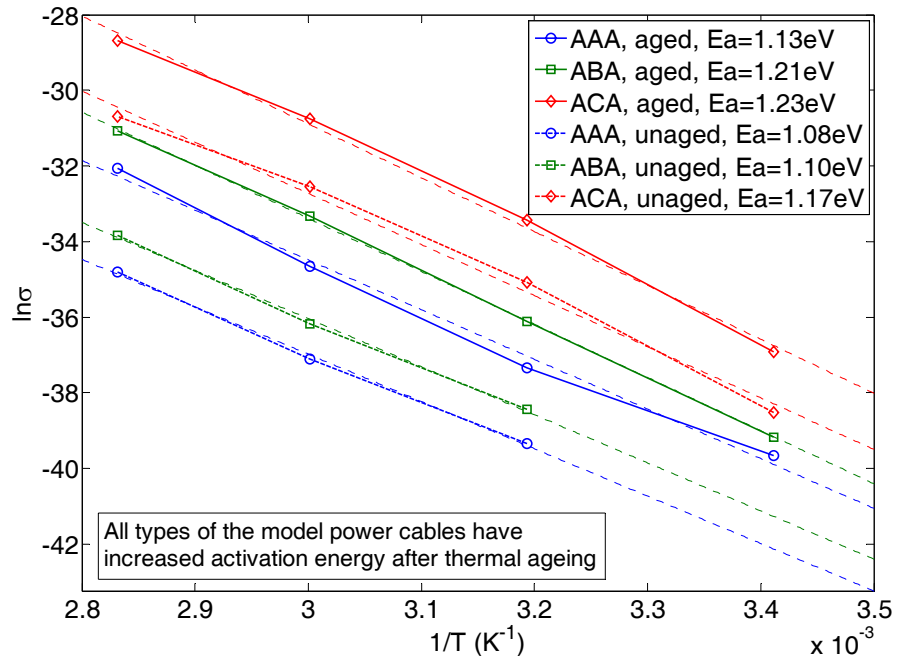


Figure 5.16 Arrhenius plot for aged cables with linear fittings, thermal activation energies calculated from the gradients of the linear fitting lines

The effects of ageing can be studied by the calculated thermal activation energy in Figure 5.16. The most noticeable ageing effect is that the activation energy for all cables has increased, e.g. cable ABA has the biggest increment from 1.10eV to 1.23eV. There is a small increment of activation energy but found for both homo-polymer and co-polymer cables. This increment of thermal activation energy can be characteristic for the ageing evaluation of power cables. Compared with cables having different insulation materials, homo-polymer cables have lower activation energy than the co-polymer cables before and after the ageing. After the ageing process, the co-polymer

cable ACA still has the biggest activation energy. Similar experiments of the same kind on XLPE material [143] can be compared with the results in this study. The activation energy was found to be 0.89eV for unaged XLPE and 1.06eV for aged sample.

## 5.5 Dielectric loss measurement using Schering bridge

### 5.5.1 Measurement system and sample preparation

In order to study the ageing effects with higher electric fields at mains frequency and field dependence of the dielectric response of the model power cables, a Schering bridge was used. The experiment was carried out using the Schering bridge at Areva T&D. The measurement system is shown in Figure 5.17. The high voltage part inside an interlocked safety cage is in the left photo. A sample oven, a potential divider and a 100pF standard high voltage capacitor (the Bushing Company Ltd, UK) are included in the high voltage cage. The low voltage control part is in the right photo that contains the control panel of the Schering bridge (Hartmann & Braun, Western Germany), null detector (Tettex Instrument, Switzerland), control panel for the potential divider and power transformer controller for high voltage delivery.



Figure 5.17 Schering bridge system setup. High voltage part in the left photo and low voltage control part in the right photo.

Before measuring the cable samples, an auxiliary bridge was balanced to exclude the influence of stray capacitance. Measurements were taken at 20°C for aged and unaged cables. The applied voltages were from 1.5kV to 22.5kV. Cables ABA and ACA were also tested at different temperatures up to 80°C. During the measurement, the loss tangent value can be read directly from the Schering bridge adjusting panel. Capacitance of the cable samples  $C_x$  can be calculated from

$$C_x = \frac{C_N \cdot R_4}{R_3} \quad \text{Equation 5-6}$$

where  $C_N$  is 100pF standard high voltage capacitor;  $R_3$  and  $R_4$  correspond to the resistance in the other arms of the Schering bridge. For measuring currents less than 80mA in this study,  $R_4 = \frac{1000}{\pi} \Omega$  and  $R_3$  can be measured together with loss tangent.

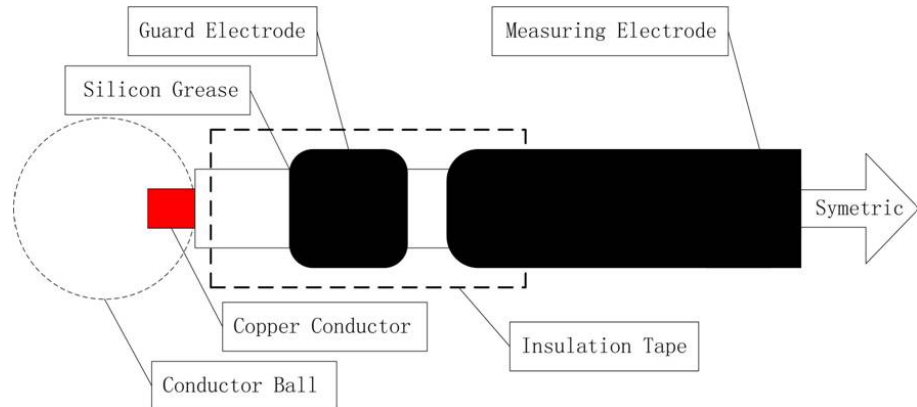


Figure 5.18 Cable sample termination preparation on one end (symmetric for the other)

Terminals of the cable samples were specially prepared to prevent leakage current and flashover under the high electric field. The diagram for preparing the cable terminals is shown in Figure 5.18. There is a 6cm distance without outer semicon layer between the conductor and the guard electrode. At the triple junction of the insulation, guard

electrode and air, discharging tends to occur at this point. Silicone grease is used for this problem around the cable to reduce the electric field enhancement. Between guard electrode and measuring electrode, there is a gap of 5mm. This small gap can help prevent any distortion of electric field lines. Because there is low potential difference across this gap, it is enough to avoid the leakage current flowing into measuring electrode. All field enhancement points were smoothed. Conductor balls are fixed on both conductor ends with same purpose of avoiding discharges.



Figure 5.19 Cable sample in the oven for Schering bridge measurement

The actual connections of the cable sample in the oven are shown in Figure 5.19. Through the bushing on top of the oven, a high voltage cable is plugged into one of the conductor balls at the ends of the cable sample. Guard electrodes are connected from inside the insulation tape to earth directly. The measuring electrode can be at any point along the cable sample that is wrapped with conductive copper tape. During the experiment, it was found by ultraviolet camera that at higher electric field and higher temperatures, discharging started to grow from the triple junction points despite that special treatment had been done for this problem. 22.5kV can be achieved at room

temperature without discharges, but discharging started above 15kV at high temperatures from 40°C. Therefore, the maximum applied field was determined as 15kV for higher temperatures. The maximum applied electric field is also restricted by the radius of the model cables.

### 5.5.2 Measurement results

Figure 5.20 shows the loss tangent measurement results on different aged and unaged model power cables at room temperature: 20°C. It can be seen that the loss tangent increased after ageing, e.g. the loss tangent of cable AAA under 15kV increased from  $7.11 \times 10^{-4}$  to  $1.08 \times 10^{-3}$ . Comparing different cables, homo-polymer cable AAA has the lowest loss tangent while co-polymer cable ACA has highest loss for both aged and unaged samples.

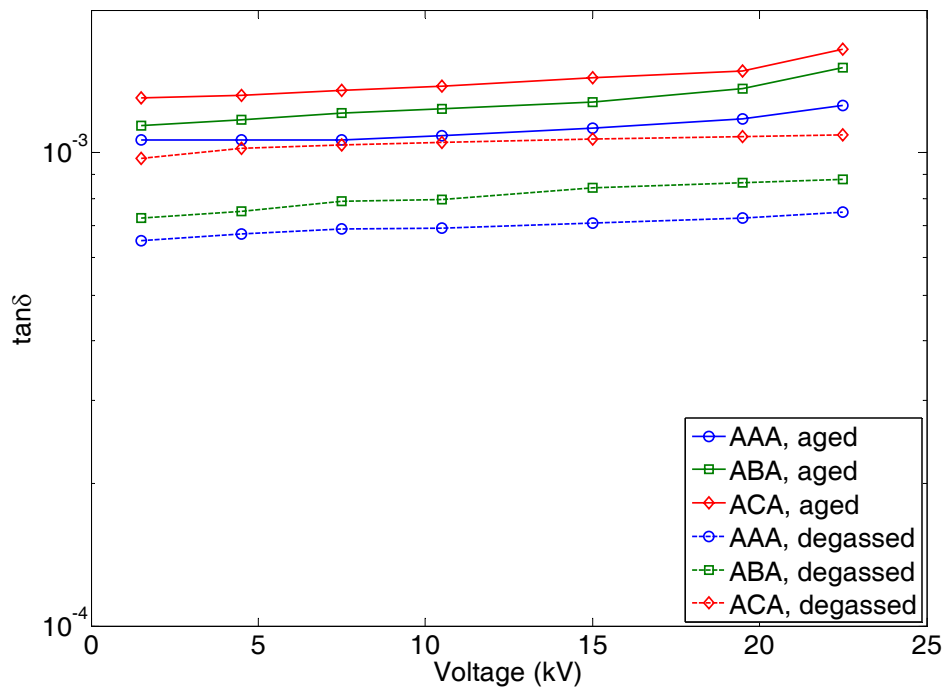


Figure 5.20 Loss tangent of aged and unaged cable samples at 20°C

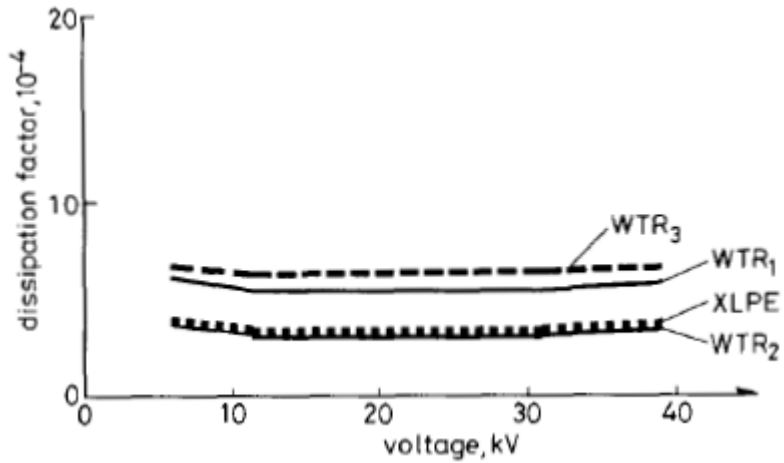


Figure 5.21 Field dependence of loss tangent for different 12kV power cables [145]

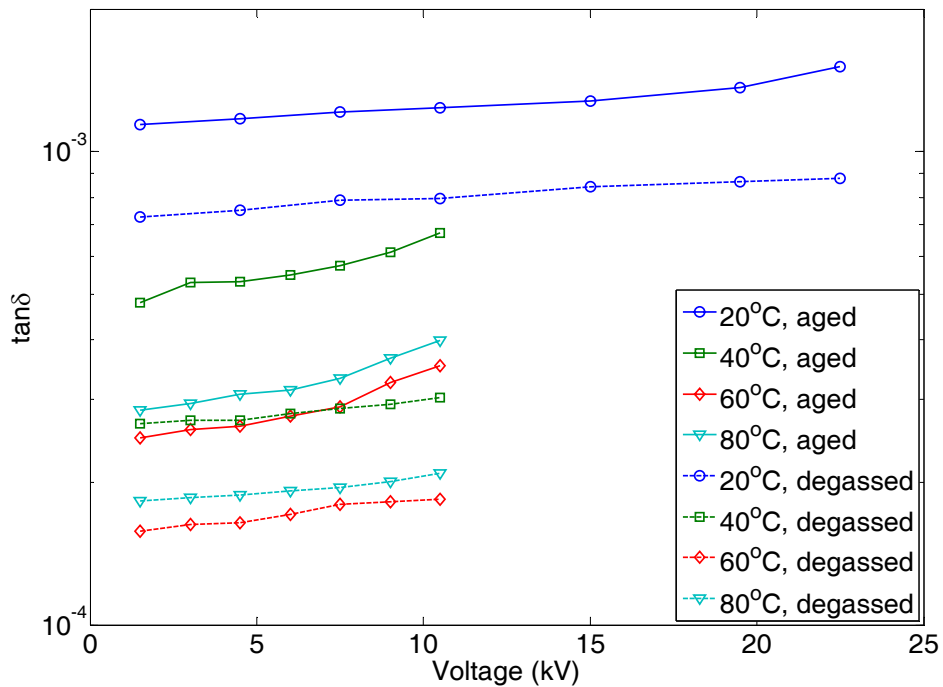


Figure 5.22 Loss tangent of aged and unaged homo-polymer cable ABA at different temperatures

There is a general law of electric field dependent conductivity with exponential increase in higher field range [144]. For all types of model power cables in this study, the electric field dependence in this field range does not vary a lot. This stable electric field

dependence for XLPE materials has also been found by Faremo and Ildstad, who published their Schering bridge measurement results on 12kV XLPE and WTR power cables up to 96kV [145]. Their measurement results in Figure 5.21 include the loss tangent measurement results on XLPE and three water tree retardant cables. It can be seen that all three WTR cables and the XLPE cable have very stable dielectric loss in this field range. It can also be seen that the loss tangent values are at  $10^{-4}$  that is the same as the results of unaged degassed cable AAA in this thesis.

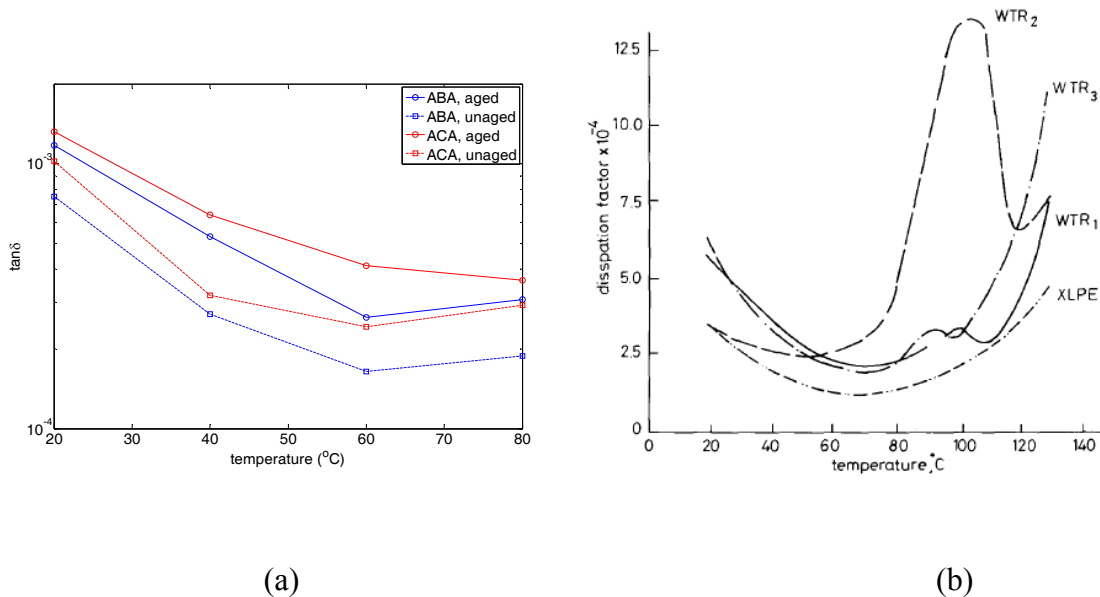


Figure 5.23 Temperature dependence of loss tangent on different polymer power cables.  
 (a) aged and unaged cable ABA, ACA; (b) XLPE and three WTR cables [145]

Figure 5.22 shows the field dependent loss tangent of homo-polymer cable ABA at different temperatures. The results of aged cable samples are shown with solid lines while the dashed lines show the results of unaged ABA. At higher temperatures, there are fewer points because of discharge influence at triple junctions as explained before. It can be seen that at different temperatures, the aged cable ABA always has bigger loss tangent. The lowest loss is at 60°C for both aged and unaged samples. In comparison

with the experimental results by Faremo and Ildstad, the same temperature dependence can be found in Figure 5.23. For the 12kV XLPE cables in (b), it has a decreasing loss tangent from 20°C to 60°C. After this lowest point, the loss tangent increases again towards higher temperatures. WTR-XLPE cables also have this temperature dependence. The results in (a) have the same temperature dependence for cable ABA and ACA, both aged and unaged. Homo-polymer cable ABA has the closest trend as in (b). The bigger magnitudes in this study may be due to the different XLPE materials, thickness of the insulation, additives and crystallinity.

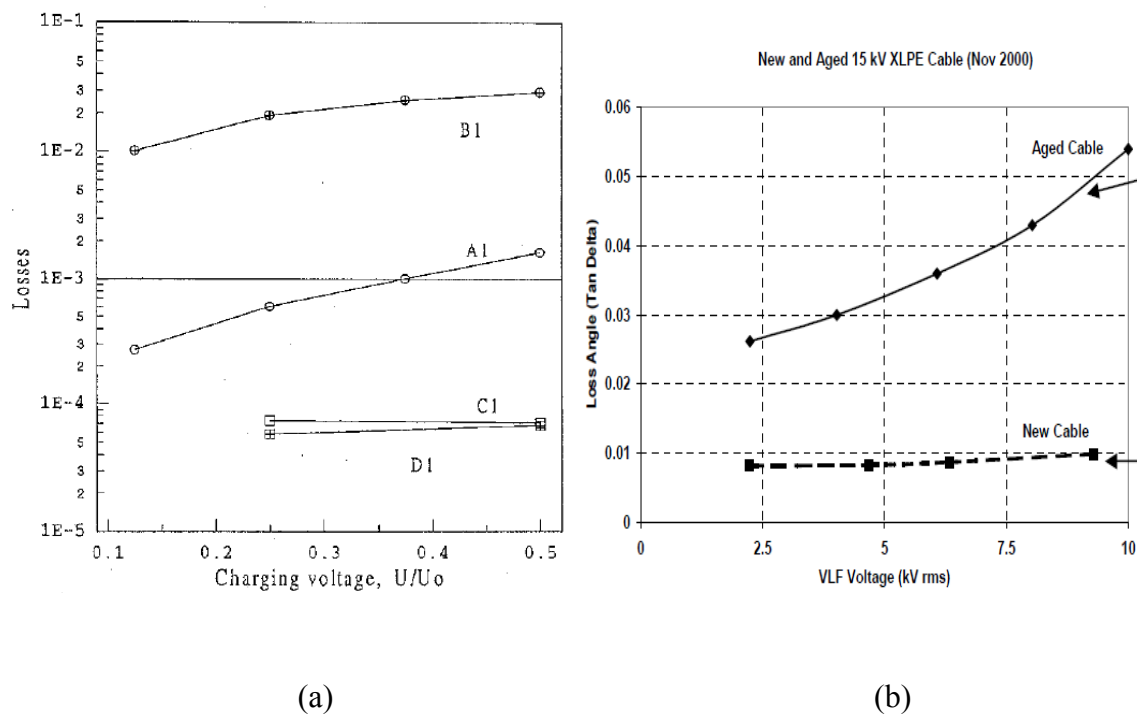


Figure 5.24 Field dependent ageing effect of XLPE power cables at 0.1Hz. (a) increasing loss tangent for aged cable A1 and B1, in comparison with less aged cable C1 and D1 [146]; (b) Ageing effect with higher applied voltages on new and aged 15kV XLPE cable [147]

Another noticeable ageing effect for homo-polymer cable ABA (Figure 5.22) is that the field dependence becomes bigger. For example at 60°C, the loss tangent increases from

$1.58 \times 10^{-4}$  under 1.5kV to  $1.85 \times 10^{-4}$  under 22.5kV for unaged cable, while it increases from  $2.48 \times 10^{-4}$  under 1.5kV to  $3.53 \times 10^{-4}$  under 22.5kV for aged cable. As shown in Figure 5.23 (a), this ageing effects have also been found by Sverre Hvidsten, Erling Ildstad, Bjorn Holmgren and Peter Werelius [146] and cable testing company [147]. Their study at lower frequency of 0.1Hz has the same results that increasing loss tangent was measured with increasing electric field for aged XLPE cables while the loss was unchanged for unaged cables. The same field dependence ageing effects are found in this thesis at high frequency of 50Hz. This suggests that this ageing effect is always present regardless of frequency.

## 5.6 Conclusions

Thermal ageing effects have been experimentally studied on the model power cables:

1. The dielectric loss spectra have increased magnitudes after the accelerated thermal ageing process.
2. Thermal ageing can increase the dielectric loss and conductivity of both homo-polymer and co-polymer power cables. Oxidation may create extra polar groups in the insulation.
3. Schering bridge tests indicates that the electric field has bigger influence on the thermally aged cables than new cables

## 6 Thermal breakdown simulation on model power cables

### 6.1 Introduction

The breakdown of dielectrics is closely related to the thermal instability under electric field. This problem has been studied for a long time with a large amount of literature, e.g. Whitehead has investigated this type of breakdown in great detail in his dedicated works [148]. With the realization of its importance, the thermal breakdown for DC power cables has been intensively studied by Fallou and Eoll [149] [150]. Experimental evidence on polyethylene and oil impregnated paper cables has shown a reduction in breakdown strength with temperature difference across the insulation [150] [151]. Their theoretical study for thermal breakdown has suggested some mathematical methods for the estimation of maximum electric field based on the nonlinear conductivity of the cable insulation. Analytical methods for the computation of temperature-related breakdown in both thick and thin specimens with parallel plane electrodes have already been covered by Dissado, Fothergill and O'Dwyer [152] [12].

As far as high voltage power cables are concerned, the complexity of thermal breakdown study comes not only from the heat transfer due to its special geometry but also due to multifactor conductivity that is dependent on both temperature and electric field. This thermo-electric breakdown in cable insulation is a consequence of the temperature rise in the insulation mainly due to the Ohmic losses in the conductor and to the dielectric loss in the cable insulation. The latter component is due to conduction loss for DC application and also includes polarization loss for AC cables. It is a strong function of the applied field and temperature. If the heat generated by the energy loss

cannot be dissipated efficiently, it will give rise to the heating of the insulation and eventual thermal breakdown. Any microscopic differential volume element inside the insulation can initiate this thermal breakdown process. The heat dissipation across the cable's outer boundary is directly dependent on the thermal conductivity of the insulation material and the boundary conditions of the surrounding environment. For one dimensional consideration on power cables, the high voltage electrode is practically thermally insulated. Any differential element in the bulk insulation close to this electrode only allows heat flow into the element and not out of it. Therefore, the thermal breakdown is greatly related to the boundary conditions, which are usually impossible to compute exact solutions for complex boundary geometries. There exists a steady state thermal breakdown voltage or maximum thermal voltage for every unique power cable. No thermal breakdown should take place below this voltage. In a real application, the time to reach this thermo-electric equilibrium in HVDC cables depends on the thermal and electrical time constants of the cable insulation which are typically less than 24 hours [153]. The time to breakdown can be much less than 24 hours for voltages much greater than the maximum thermal voltage. A small incremental voltage above the maximum thermal voltage could result in a runaway in a very short time due to a positive thermal feedback effect that is basically caused by the temperature and field dependent electrical conductivity [154] [155]. The mathematical complexity for the multifactor conductivity precludes an analytical solution of thermal breakdown study on power cables.

The estimated theoretical calculation of maximum thermal voltage for thermal breakdown phenomenon has been suggested in the literature mentioned above. However, the distributions of the critical parameters such as electric field and temperature had not been easily obtained until the computer aided programs emerged in recent years. In this

chapter, the thermal breakdown simulation with finite element method is studied. Based on the partial differential equations for this multi-physics phenomenon, the thermal-electrical behaviour of the model power cables under DC field can be simulated. The experimental results in previous chapters are used to determine the parameters. The distributions of different parameters can be visualized in FEMLab program.

## 6.2 Mathematical model of thermal-electric behaviour for power cables

The mathematical prototype for the thermal-electric behaviour is based on the partial differential equation (PDE) for heat transfer

$$\rho C_p \frac{\partial T}{\partial t} - \nabla \bullet (k \nabla T) = Q \quad \text{Equation 6-1}$$

where  $\rho$  is density of the thermally conductive material;  $C_H$  is heat capacity;  $k$  is thermal conductivity and  $Q$  is heat source [156]. In this equation, temperature  $T$  is the variable. The first term on the left side represents the time dependence and the second term represents spatial distribution. In this study, the heat source  $Q$  is from resistive heating

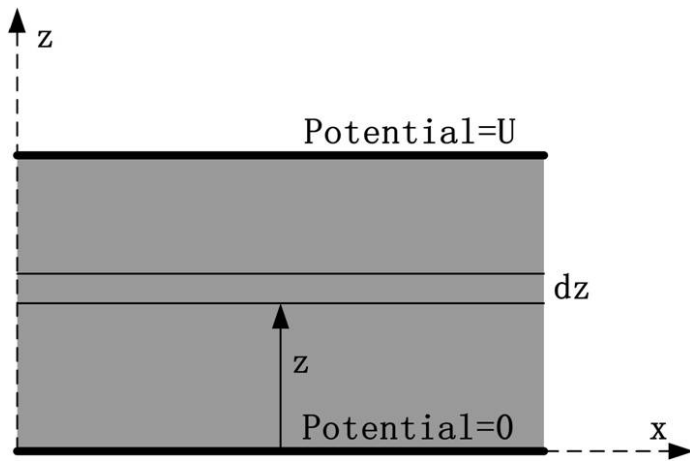
$$Q = JE = \sigma(T, E)E^2 \quad \text{Equation 6-2}$$

where  $J$  is current density;  $\sigma$  is conductivity;  $E$  is electric field. The conductivity may be either DC conductivity with DC electric field or AC conductivity at 50Hz frequency of the alternating electric field.

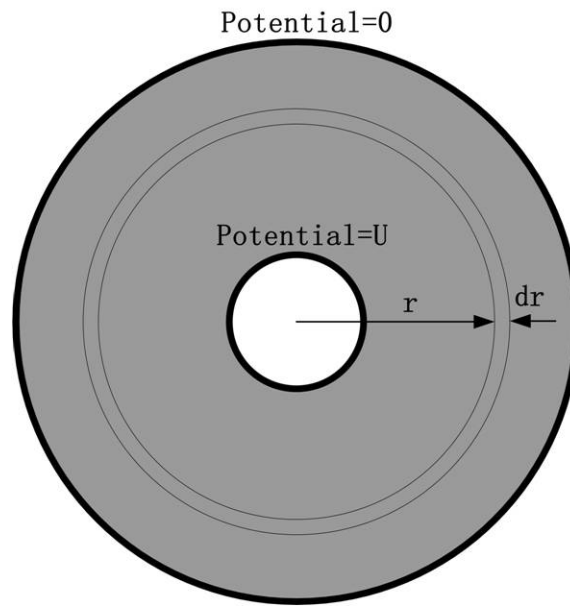
Combining Equation 6-1 and Equation 6-2, the PDE of thermal continuity under steady state for a one-dimensional heat flow is

$$\frac{d}{dz} \left( k \frac{dT(z)}{dz} \right) + \sigma \left( \frac{dU(z)}{dz} \right)^2 = 0 \quad \text{Equation 6-3}$$

where  $U(z)$  is electrical potential function in  $z$  coordinate as shown in Figure 6.1 (a).



(a) parallel geometry



(b) cylindrical geometry

Figure 6.1 Sectional views of one dimensional heat flow

For cylindrical geometry as for cables (Figure 6.1 (b)), the steady state PDE changes to

$$\frac{1}{r} \frac{d}{dr} (rk \frac{dT(r)}{dr}) + \sigma \left( \frac{dU(r)}{dr} \right)^2 = 0 \quad \text{Equation 6-4}$$

where  $r$  is radial distance from the origin;  $T(r)$  and  $U(r)$  are temperature and potential at the radial position  $r$  [153]. In both Equation 6-3 and Equation 6-4, the first term in the above equation represents the divergence of heat and the second term is the amount of heat generated in a differential volume element in insulation due to the dielectric loss.

For a power cable under operation, the heat flow model can be built as in Figure 6.2. In the inner conductor, the energy loss in form of heat is due to Joule heating of the load current and it is injected into the insulation layer that is the only way of dissipating the heat. Together with the dielectric loss inside the insulation layer, the heat due to the conductor loss flows through the insulation and all the energy loss is dissipated into the ambient environment. The highest temperature occurs at the conductor-insulation boundary. As a very big heat capacitor, the environment has a constant temperature in this model. This may be a reasonable assumption for a sub-sea cable which has the ambient temperature of approximately 4°C. Other solutions would be possible e.g. the cable was buried in a trench. In order to solve the PDE, boundary conditions are needed. There are some assumptions for the boundary conditions and environment domain:

1. the inner conductor injects heat, due to load current joule heating of over a unit length of cable  $I_L^2 R_{\text{con}}$ , into bulk insulation; the inner boundary of the insulation cannot dissipate heat into the conductor.

2. the heat only dissipates from the outer boundary of the insulation.
3. the medium outside the insulation has constant temperature (infinite thermal conductivity)

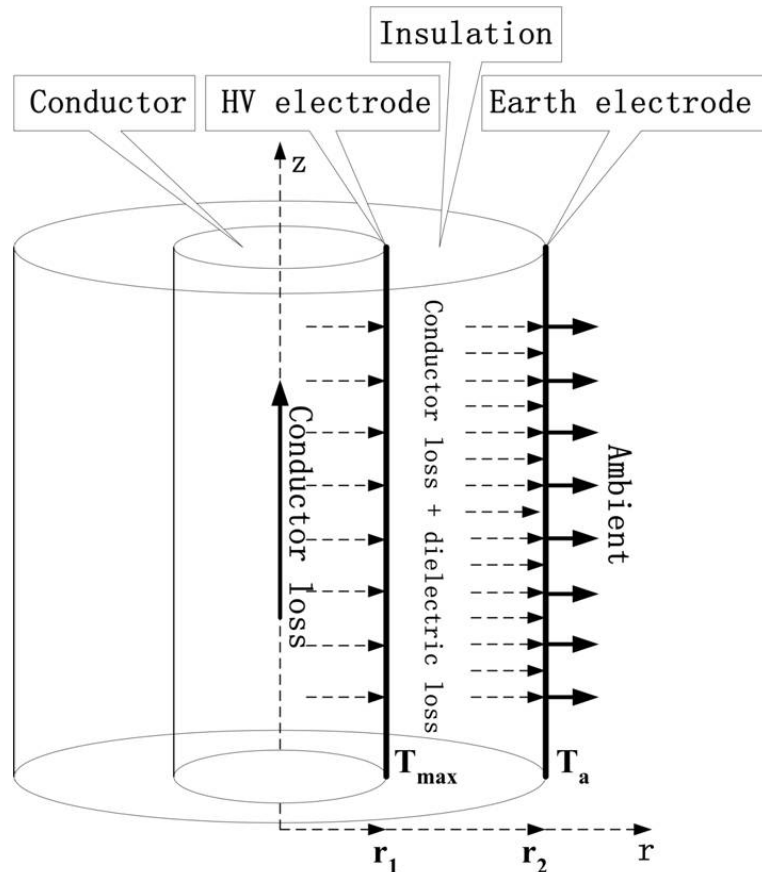


Figure 6.2 Heat flow of a DC power cable

These assumptions for the cable's heat flow model can be mathematically translated as:

1. At the inner conductor-insulation boundary,

$$2\pi r_1 k \frac{dT(r)}{dr} \Big|_{r=r_1^+} = -I_L^2 R_{con} \quad \text{Equation 6-5}$$

where  $I_L$  is the load current;  $R_{con}$  is the conductor resistance per unit length.

2. At insulation outer boundary,

$$2\pi r_2 k \frac{dT(r)}{dr} \Big|_{r=r_2^-} = -I_L^2 R_{con} - UI \quad \text{Equation 6-6}$$

where  $UI$  represents the power of all the dielectric loss in the cable insulation.

3. Outside the insulation,

$$T(r_2) = T_a \quad \text{Equation 6-7}$$

With the above assumptions of boundary conditions, Equation 6-4 for cable geometry can be transformed with rewriting and integration as

$$-\frac{U^2}{2} = \int_{T(r_1)}^{T(r_2)} \frac{k}{\sigma} dT + \frac{I_L^2 R_{con}}{2\pi} \int_{r_1}^{r_2} \frac{1}{r\sigma} dr \quad \text{Equation 6-8}$$

With the upper bound on maximum insulation temperature  $T_{max}$ , the maximum thermal voltage of a loaded cable  $U_{mc}$  can be calculated as

$$U_{mc}^2 = \int_{T_a}^{T_{max}} \frac{2k}{\sigma} dT - \frac{I_L^2 R_{con}}{\pi} \int_{r_1}^{r_2} \frac{1}{r\sigma} dr \quad \text{Equation 6-9}$$

This is the general expression of the solution. The first term in the right hand side determines the maximum thermal voltage without heat injection from conductor, while the second term is due to external heat, which reduces the maximum thermal voltage.

The integration on the right side of Equation 6-9 is a function of conductivity, which is field and temperature dependent. There is no general theoretical model for the electrical conductivity applicable to all kinds of solid dielectrics. There are some semi-empirical

formulations all of which appear formally similar. A commonly used expression as applied to cable insulation is

$$\sigma = Ae^{(a|E| - \frac{b}{T})} \quad \text{Equation 6-10}$$

where  $A$  is material specific constant with unit of S/m;  $a$  is known as the stress coefficient;  $b$  is Boltzmann constant [157] [158]. It has been shown to be applicable over a wide range of temperature and electric field for many types of dielectrics including XLPE. This may be compared with another suggested equation with similar expression and a physical basis of field assisted hopping conduction [154] [155]

$$\sigma = A'e^{(-\frac{b}{T})} \cdot \frac{\sinh(B|E|)}{|E|} \quad \text{Equation 6-11}$$

where  $A'$  is just a coefficient with unit of V/ $\Omega m^2$  and  $B$  is the other coefficient for electric field dependence with unit of m/V. Practically  $B|E|$  is a large positive value. Therefore when the hyperbolic function term is written with exponential function form, the approximation of Equation 6-11 will be the same as Equation 6-10

$$\begin{aligned} \sigma &= A'e^{(-\frac{b}{T})} \cdot \frac{\sinh(B|E|)}{|E|} \\ &= A'e^{(-\frac{b}{T})} \cdot \left[ \frac{1}{2|E|} (e^{B|E|} - e^{-B|E|}) \right] \\ &\approx \frac{A'}{2|E|} e^{(-\frac{b}{T})} \cdot e^{B|E|} \\ &= Ae^{(B|E| - \frac{b}{T})} \end{aligned} \quad \text{Equation 6-12}$$

The simpler Equation 6-10 is a more widely used empirical function of conductivity over a range of several decades. Therefore, Equation 6-10 is used in this study. Because

the conductivity is dependent on electric field, which is dependent on the radius  $r$ , the heat source term for one-dimensional case in the continuity equation becomes very complex to solve

$$\sigma \left( \frac{dU(r)}{dr} \right)^2 = \sigma(T(r), E(r)) \cdot \left( \frac{dU(r)}{dr} \right)^2 = \sigma(T(r), \frac{dU(r)}{dr}) \cdot \left( \frac{dU(r)}{dr} \right)^2 \quad \text{Equation 6-13}$$

To overcome this difficulty, mean value theorems can be used to simplify the field dependent electrical conductivity which is an averaged value of field for the whole insulation [153] [159]

$$\sigma(T(r), E(r)) = \sigma(T(r), \eta \frac{U}{d}) = \sigma(T(r), \eta E_0) = \sigma_0 \sigma(T(r)) \quad \text{Equation 6-14}$$

where  $\eta$  is an empirical constant to adjust the averaged electric field  $E_0$  and produce a conductivity that is dependent on temperature and applied voltage. A more conservative assumption is applied in this study with the highest conductivity value at the inner boundary

$$\sigma(T(r), E(r)) = \sigma(T(r), \frac{dU(r)}{dr} \Big|_{r=r_i}) \quad \text{Equation 6-15}$$

With the basic mathematical model, relevant equations and parameters, the simulation can thus be done numerically. The distributions of electric field and temperature in both transient and steady state are simulated with FEMLAB, which is an interactive environment for modelling and solving scientific and engineering problems based on partial differential equations. When solving the PDEs, FEMLAB uses the proven finite

element method (FEM) that has a prominent position among the most famous three methods – finite element method (FEM), finite volume methods (FVM) and finite difference methods (FDM) [160].

### 6.3 Thermal breakdown simulation setup in FEMLAB

Thermal breakdown occurs when thermal equilibrium cannot be achieved. Figure 6.3 shows the thermal breakdown process when the applied voltage exceeds the maximum thermal voltage (MTV) at the hottest point inside the cable insulation. If the voltage is less than MTV, thermal equilibrium can be reached after some settling time. If the voltage equals MTV, the power cable can operate stably under the highest electric field. When the voltage is higher than MTV, the heat due to dielectric loss and conductor loss cannot be efficiently dissipated and thermal breakdown will occur. Therefore, in the simulation, MTV is the most concerned parameter to find out.

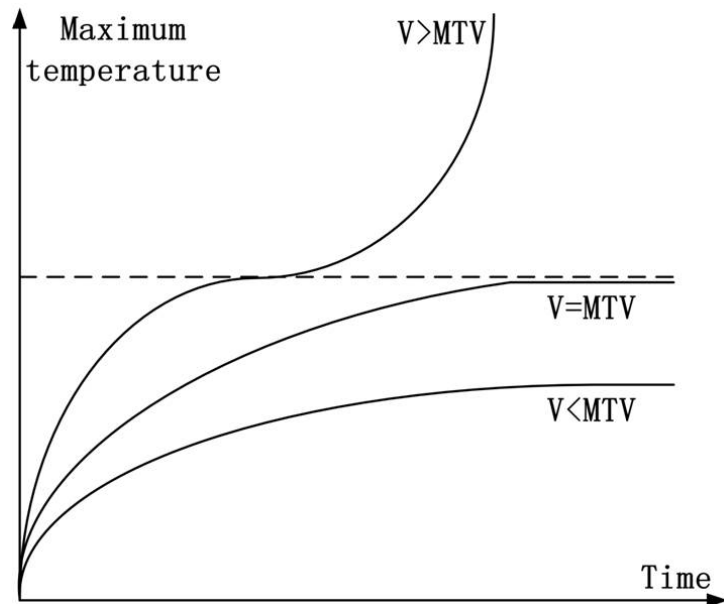
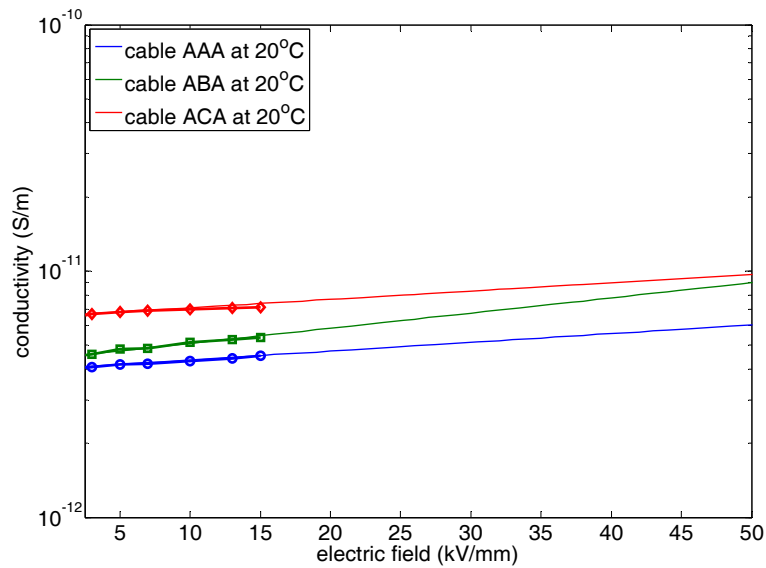
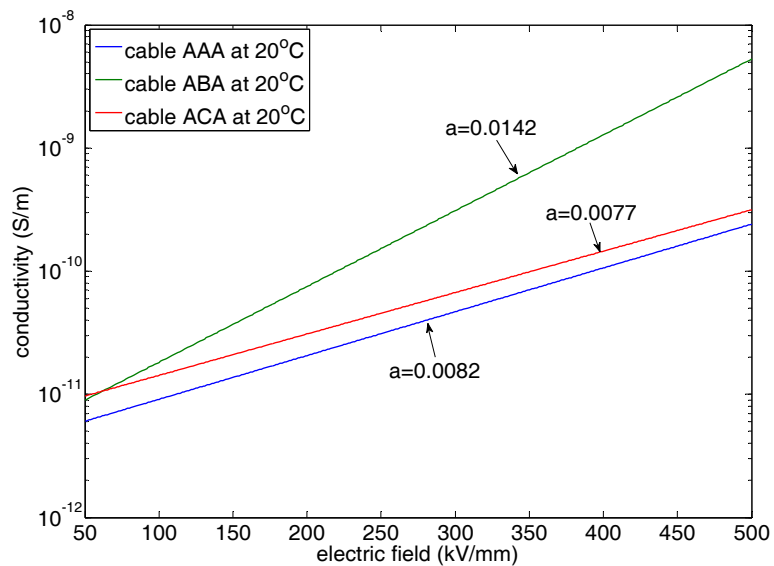


Figure 6.3 Time dependent thermal breakdown process at the maximum temperature with relationship to maximum thermal voltage

Based on the measurement results in previous chapters, the model power cables can be simulated using Equation 6-10 to determine the field and temperature dependent conductivity. The field dependent conductivity exponentially fitted from Schering bridge measurement results is shown in Figure 6.4 (a) and it is extrapolated to 500kV/mm mean field in Figure 6.4 (b).



(a) exponential fitting of conductivity from experiment results



(b) extrapolation of conductivity to higher electric field

Figure 6.4 Field dependence of model power cables, fitted from experimental data

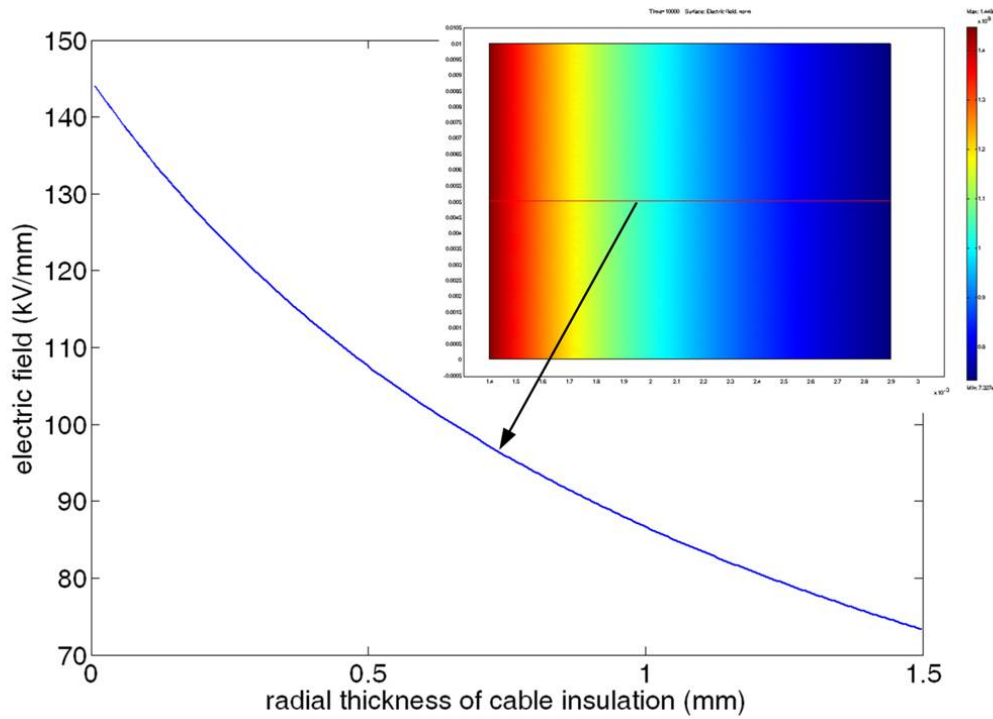


Figure 6.5 Electric field distribution in the model cable insulation with 150kV

When 150kV is applied on 1.5mm insulation, the electric field distribution is shown on Figure 6.5. The average electric field should be 100kV/mm, but the distribution for cable geometry has the highest field near the conductor core with 140kV/mm. The lowest electric field is 70kV/mm near the outside. This electric field distribution at a constant temperature can also be found in literature with [162]

$$E = U \frac{1}{r \ln \frac{r_o}{r_i}} \quad \text{Equation 6-16}$$

where E is the electric field, U is the applied voltage, r is the radius from the cable geometry centre,  $r_o$  and  $r_i$  are the outer and inner radius of the cable insulation layer. Because the maximum field is 1.4 times as the averaged mean field, a multiplying factor of 1.4 is used in this study to conservatively simplify the field dependence in Equation

6-16. It should be noticed that this electric field distribution is different in practice with varying temperature distribution and may be even reversed in certain situations.

With the thermal activation energy  $E_a$ , the temperature dependence can be integrated into the final expression. For the homo-polymer cable AAA ( $E_a = 1.08\text{eV}$ ), the expression for conductivity is

$$\begin{aligned}\sigma(U, T) &= Ae^{(a \left| \frac{1.4U}{d} \right| - \frac{b}{T})} \\ &= 15.168 \times 10^6 \times e^{\frac{0.0082 \times 1.4U}{1.5}} \times e^{-\frac{12533}{T}}\end{aligned}\quad \text{Equation 6-17}$$

Here, U should have the unit of kV and d should have the unit of mm, because E is in the unit of kV/mm.  $\sigma$  is S/m and T is in Kelvin. This is used throughout the following.

Similarly, the conductivity for homo-polymer cable ABA ( $E_a = 1.10\text{eV}$ ) is

$$\sigma(U, T) = 36.816 \times 10^6 \times e^{\frac{0.0142 \times 1.4U}{1.5}} \times e^{-\frac{12765}{T}} \quad \text{Equation 6-18}$$

and for co-polymer cable ACA ( $E_a = 1.17\text{eV}$ ) is

$$\sigma(U, T) = 877.213 \times 10^6 \times e^{\frac{0.0077 \times 1.4U}{1.5}} \times e^{-\frac{13578}{T}} \quad \text{Equation 6-19}$$

A symmetric 2D model is used with 2528 mesh points in FEMLAB, as shown in Figure 6.6. This model represents the cross section along a radius through the insulation (see Figure 6.2). The horizontal direction is the radial thickness, while the vertical axis is the axial direction of the cable with both end thermally and electrically insulated so that the electrical current and heat can only flow through the insulation in radial direction. This is really a 1-D model, so only changes in the radial direction are expected. This

Multiphysics modelling requires boundary definition and sub-domain definition for both electrical heating process and thermal conduction process.

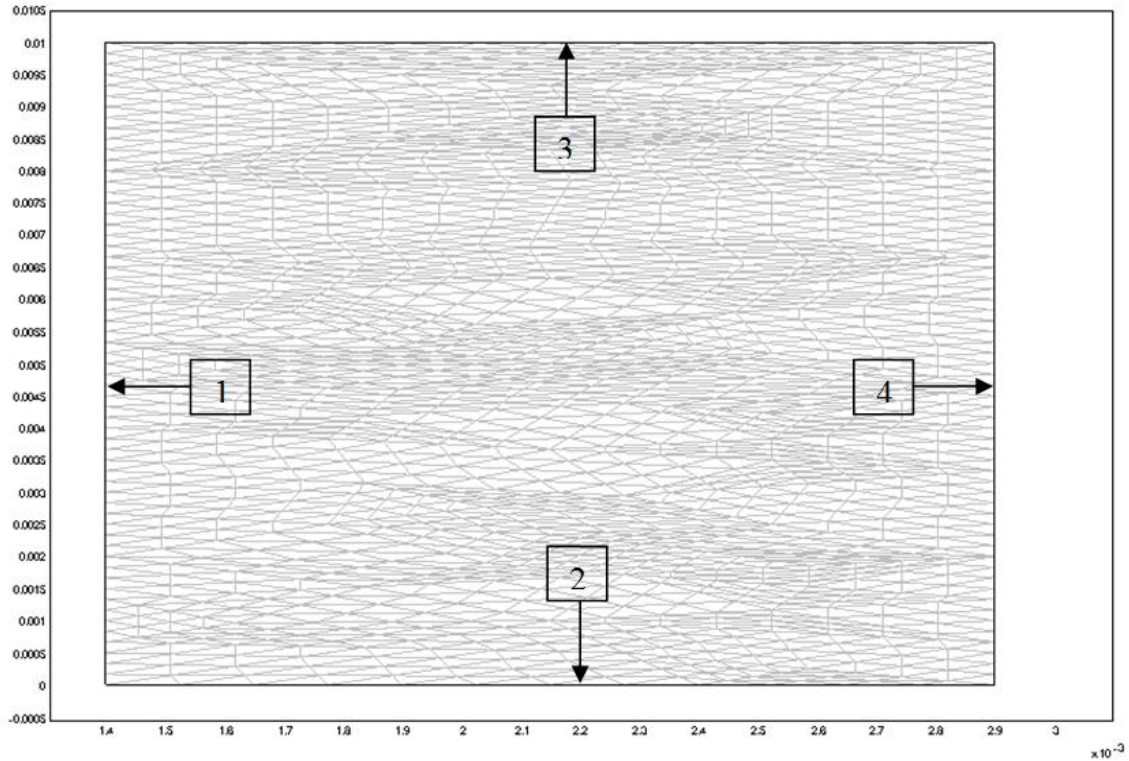


Figure 6.6 The geometry of axial symmetry 2D definition for the model power cables, with 2528 mesh points in the area of  $1.5\text{mm} \times 10\text{mm}$

The modelling parameters for electrical heating are

- Boundary 1: electrical potential/applied voltage;
- Boundary 2: electrical insulation;
- Boundary 3: electrical insulation;
- Boundary 4: ground;

- Sub-domain:
  - conductivity expression for model power cable:  $\sigma(U, T)$
  - initial value:  $U(t_0) = 0$

The modelling parameters for thermal conduction are

- Boundary 1: thermal insulation without heat flux or heat flux due to conductor loss; the simulation without conductor loss is firstly carried out; when there is heat flux crossing boundary 1, it can be calculated with

$$\text{heat flux } k\nabla T = \frac{I^2 RL}{2\pi rL} = \frac{I^2 \rho \frac{L}{\pi r^2}}{2\pi rL} = \frac{I^2 \rho}{2\pi^2 r^3} \quad \text{Equation 6-20}$$

where  $I$  is load current;  $\rho = 1.72 \times 10^{-8} \Omega m$  is the resistivity of copper;  $r$  is the radius of the conductor core.

- Boundary 2: thermal insulation;
- Boundary 3: thermal insulation;
- Boundary 4: ambient temperature  $T_0$ ;
- Sub-domain:
  - Thermal conductivity: 0.45 W/mK

- Density:  $1100 \text{ kg/m}^3$
- Specific heat capacity:  $2000 \text{ J/kg}$
- Heat source:  $Q = \sigma(U, T)E^2(r)$
- Initial value:  $T(t_0) = T_0$ , the insulation sub-domain has the same temperature as ambient.

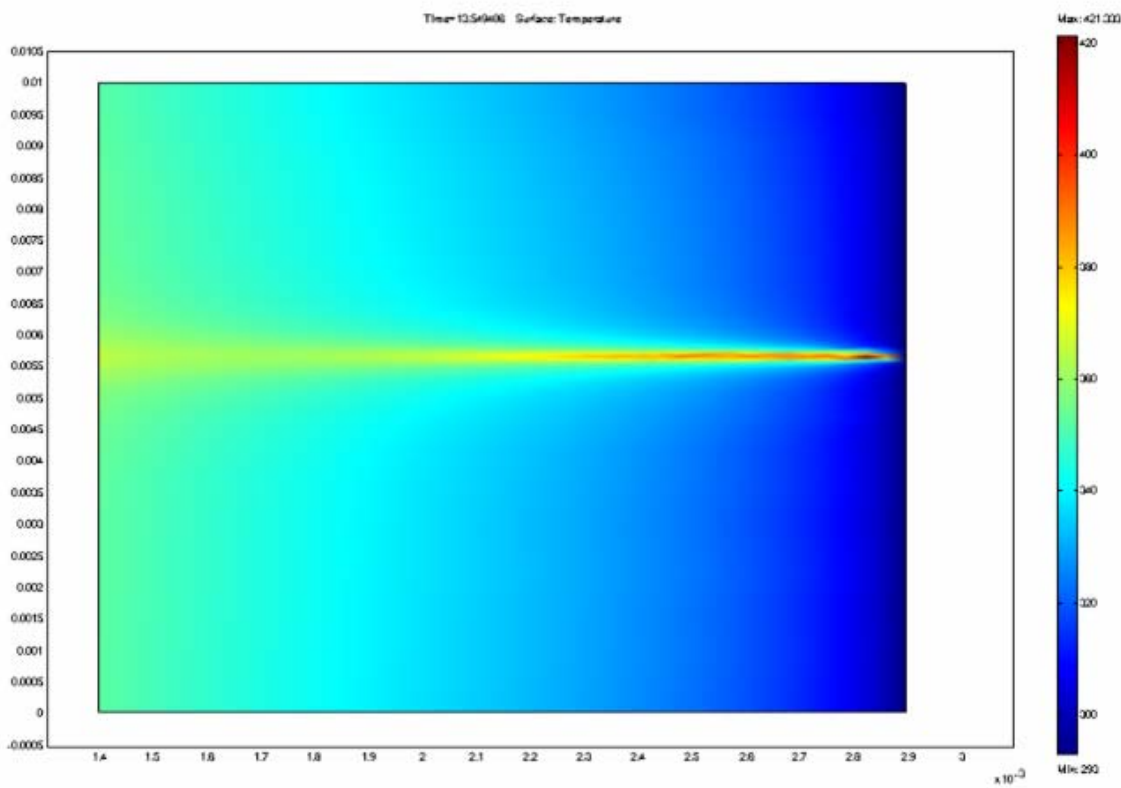


Figure 6.7 Temperature distribution when thermal breakdown occurs, with the highest temperature of 421K in the breakdown channel

Thermal breakdown voltage can be found when the mathematical solution in FEMLAB is not convergent. If the applied voltage exceeds the MTV in a specific situation, the software cannot solve the PDE, and it will give out error message with parameter

distributions after thermal breakdown, as shown in Figure 6.7. Horizontal axis is the thickness of insulation layer from 1.4mm to 2.9mm; vertical axis is 10cm length of cable for this simulation study. All the following simulation results have the same geometry. It can be seen that when the initial temperature is 298K (20°C), the highest temperature after breakdown inside the breakdown channel can be 420K (127°C) that will totally damage the insulation material.

## 6.4 Simulation results of model power cables

### 6.4.1 MTV without load current at different ambient temperatures

The MTV for the model power cables at different temperatures are plotted in Figure 6.8. The temperature ranges from 293K (20°C) to 343K (70°C). Higher temperatures were not simulated because XLPE starts to melt from 353K (80°C). It can be seen that the MTV decreases when temperature increases for all three cables. With homo-polymer insulation, cable AAA at 293K has the highest MTV of 340kV, which is 226kV/mm with its 1.5mm insulation. When the temperature increases to 343K, its MTV drops to 52kV (35kV/mm). At lower temperatures, homo-polymer cable ABA has lower MTV than co-polymer cable ACA. This may be due to the higher conductivity that makes electric field distribution smoother and, therefore, slows down the temperature increase.

Similar simulation on the thermal breakdown of HVDC cables has been done by Ch. Chakradhar Reddy and T. S. Ramu [153]. With bigger conductor radius of 22mm and insulation thickness of 22mm, the maximum breakdown voltage (MTV) calculation results are plotted in Figure 6.9 (a). Using MATLAB estimated calculation on MTV, it has a linear decrease at higher temperatures. The breakdown electric field is about 55kV/mm with 1000A load current as heat injection source through the inner boundary.

Another recently published paper [161] has simulated the thermal breakdown of MgO filled XLPE cables. Higher breakdown field was found for different filler contents, as shown in Figure 6.9 (b).

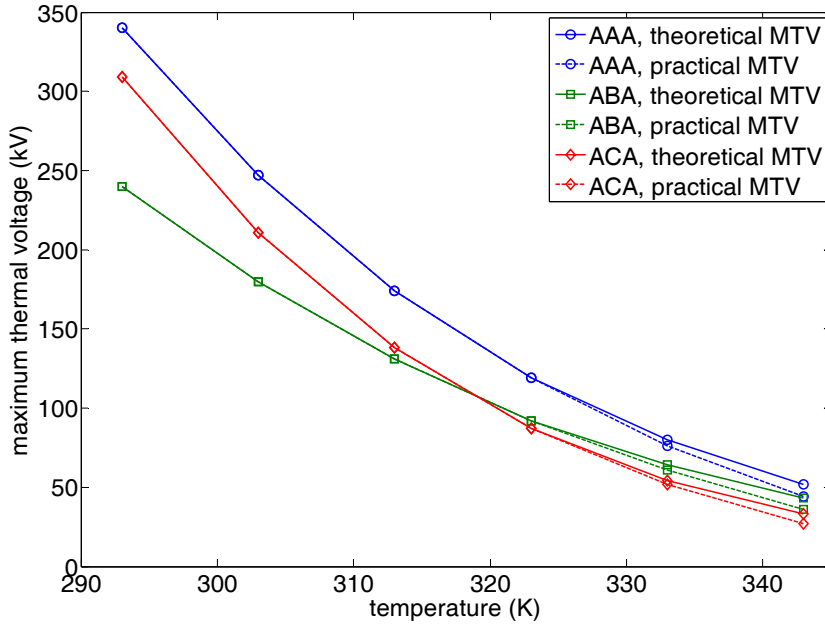


Figure 6.8 MTV for degassed homo-polymer and co-polymer model power cables

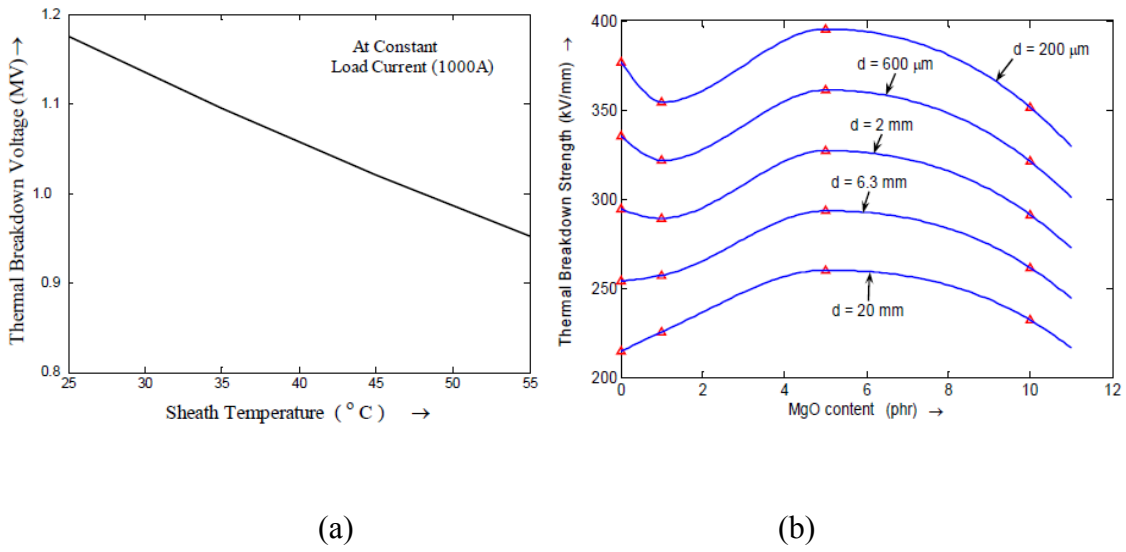


Figure 6.9 MTV simulation results by (a) Chakradhar Reddy [153] and (b) T. S. Ramu [161]

Practical consideration on the melting temperature of XLPE material was included during the simulation process. After reaching steady state, there is a temperature increase inside the cable insulation. The hottest point is the boundary to central conductor. If the maximum temperature of this boundary reaches 353K, melting of XLPE insulation will start, and breakdown will occur from this position. In this simulation, the original temperature everywhere in the cable insulation is assumed to be the same as ambient temperature.

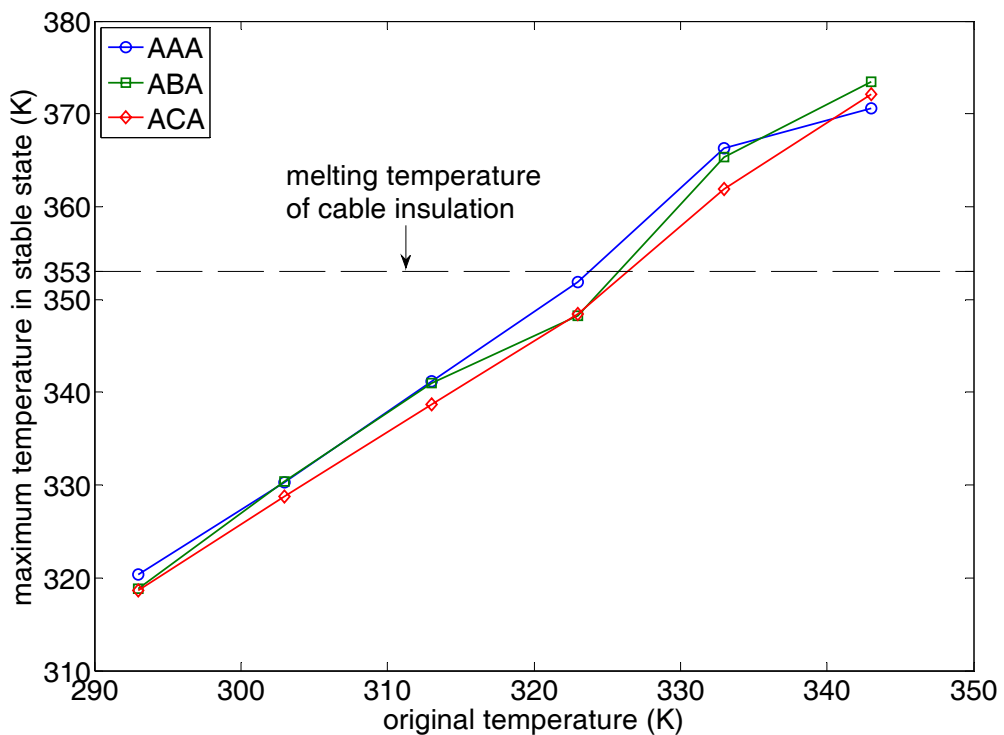


Figure 6.10 Maximum temperature at the inner boundary under MTV

The maximum temperature can be calculated in FEMLAB, as shown in Figure 6.10. It can be seen that the maximum temperature in stable state exceeds 353K when the original temperature is above 323K (50°C). Therefore, the MTV should be recalculated to ensure that the maximum temperature does not exceed 353K. The recalculated

practical MTV are also plotted in Figure 6.8 in comparison with theoretical MTV. There is certain amount of MTV decrease after restricting the maximum temperature, e.g. the MTV of cable AAA with 343K ambient drops from 52kV to 44kV.

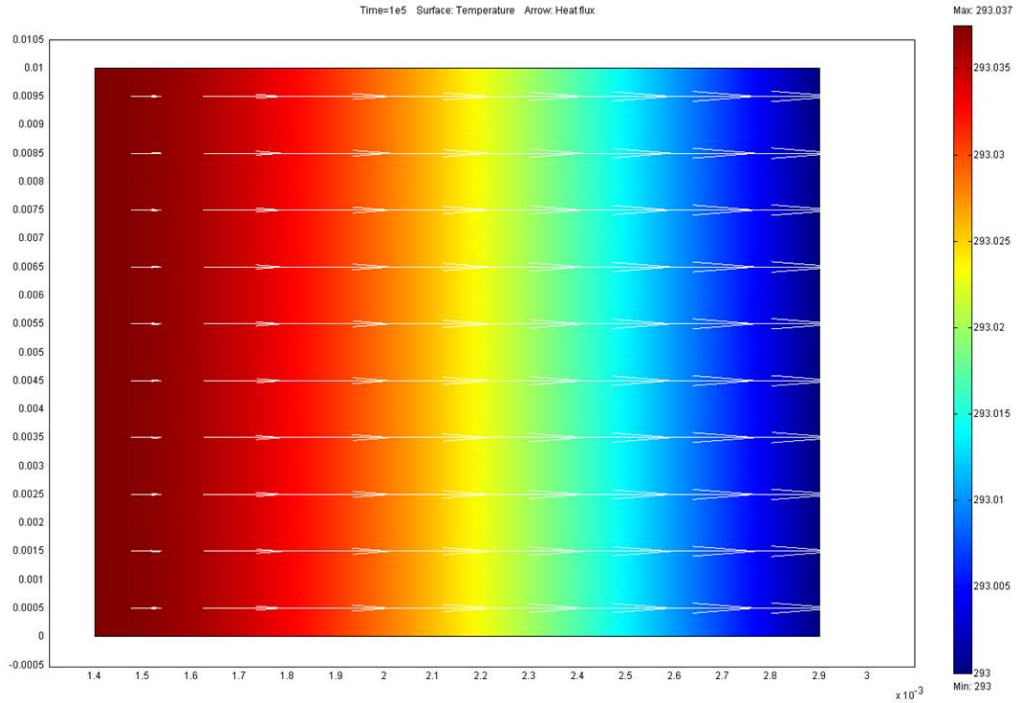


Figure 6.11 Temperature and heat flux distribution in the insulation of cable AAA in FEMLAB, at 70kV under stable state ( $t=10^5$ s)

Because of the cylindrical cable geometry, the temperature in the cable insulation does not have a uniform distribution. Its stable state distribution is dependent on the dimensions of the cable, load current value, ambient temperature and applied voltage. Figure 6.11 shows the FEMLAB simulation results of temperature distribution with heat flux (white arrows). Blue colour area represents the lower temperature and red area for higher temperature, as shown in the colour bar on the right side of the graphs. The radius along the insulation increases from left to right. After reaching stable state at 70kV, it can be seen that the highest temperature is at inner boundary and gradually decreases along the radial thickness of the cable insulation. There is very little

difference for the temperature distribution for voltages except at MTV, which can cause big temperature variation but still keep the same distribution trend. Heat flux becomes bigger near the outer boundary because more accumulated heat due to dielectric loss is dissipated to the environment.

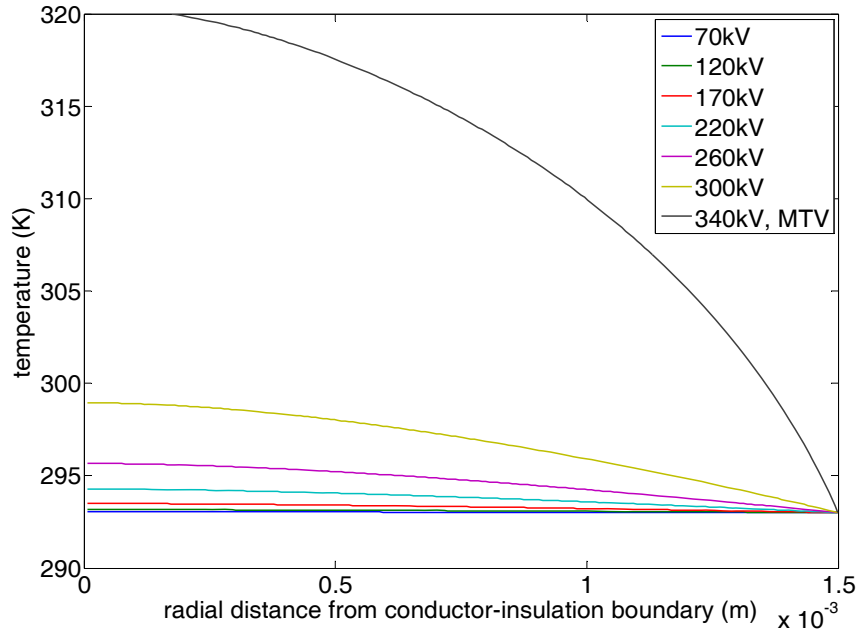
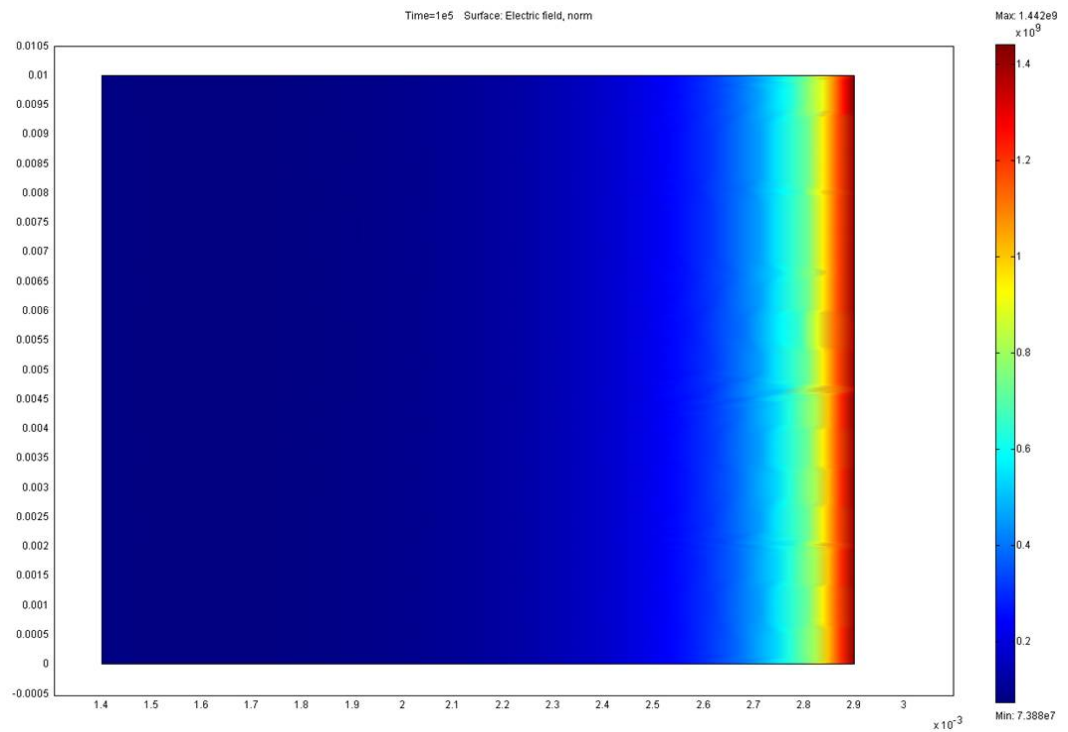


Figure 6.12 Temperature distribution in cable insulation under different voltages, when ambient temperature is 293K

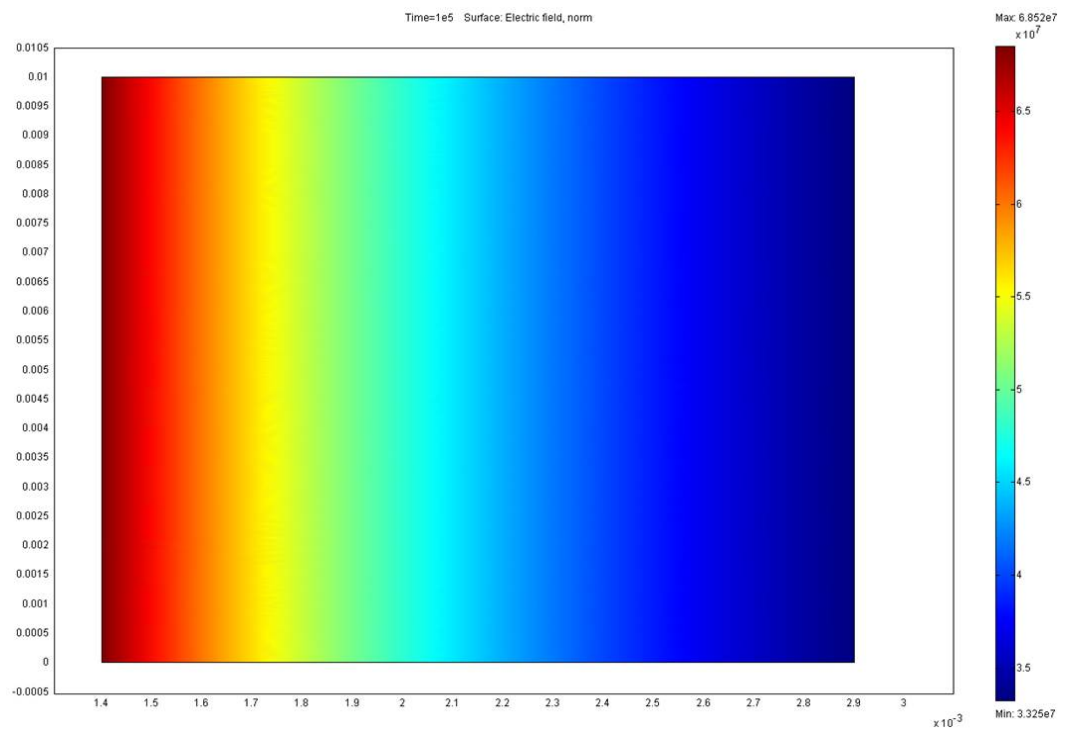
The temperature distribution in the radial direction can be compared for different voltages. Figure 6.12 shows the temperature distribution in stable state inside the cable insulation. The original temperature for cable AAA is 293K. All curves are plotted after the cable insulation reaches stable state. When the applied voltage is much lower than MTV, there is very little increase of 0.037K. Higher voltage increases the stable state temperature inside the insulation, e.g. 2.7K is the increase at the inner boundary when the voltage is 260kV. Under MTV of 340kV, the maximum temperature is 320.4K with 27.4K increase on the original ambient temperature 293K. The comparison of

temperature distribution under different voltages indicates that an increase of voltage that is much lower than MTV does not induce big temperature gradient from the inner boundary to the outer boundary. The maximum temperature is well below 295K with 100kV increase from 70kV to 170kV. However, the maximum temperature increases much faster from 260kV to 340kV. 40kV increase from 300kV to 340kV increases the maximum temperature from 299K to 320.4K. This implies that it will be dangerous for power cables to operate even under the voltages of 100kV below its MTV.

Like the temperature distribution, the electric field distribution is also voltage dependent. The FEMLAB simulation results of electric field distribution for cable AAA with ambient temperature 293K is shown in Figure 6.13. Graph (a) shows the field distribution under 340kV and graph (b) under 70kV. The distribution under a higher voltage in (a) has the maximum electric field at outer boundary. Compared with graph (a), graph (b) has opposite distribution with maximum field at inner boundary. Graph (b) under lower voltage of 70kV in stable state has a similar electric field distribution to that of the original distribution, with the highest field at the inner boundary due to the cylindrical cable geometry. The maximum field at the inner boundary is 68.52kV/mm, about twice of that at the outer boundary, 33.25kV/mm, while the mean field is 46.67kV/mm. Graph (a) under MTV with a reverse field distribution has increasing magnitudes from inner boundary to outer boundary. The maximum field at the outer boundary is 1442kV/mm, about twice of that at the inner boundary, 73.88kV/mm. With practical consideration of the intrinsic electrical breakdown strength of 800kV/mm, the insulation material near the outer boundary will breakdown due to electric field enhancement. Therefore the actual breakdown should be lower than this maximum thermal voltage.



(a) 340kV, MTV



(b) 70kV

Figure 6.13 Electric field distribution in the insulation of cable AAA in FEMLAB

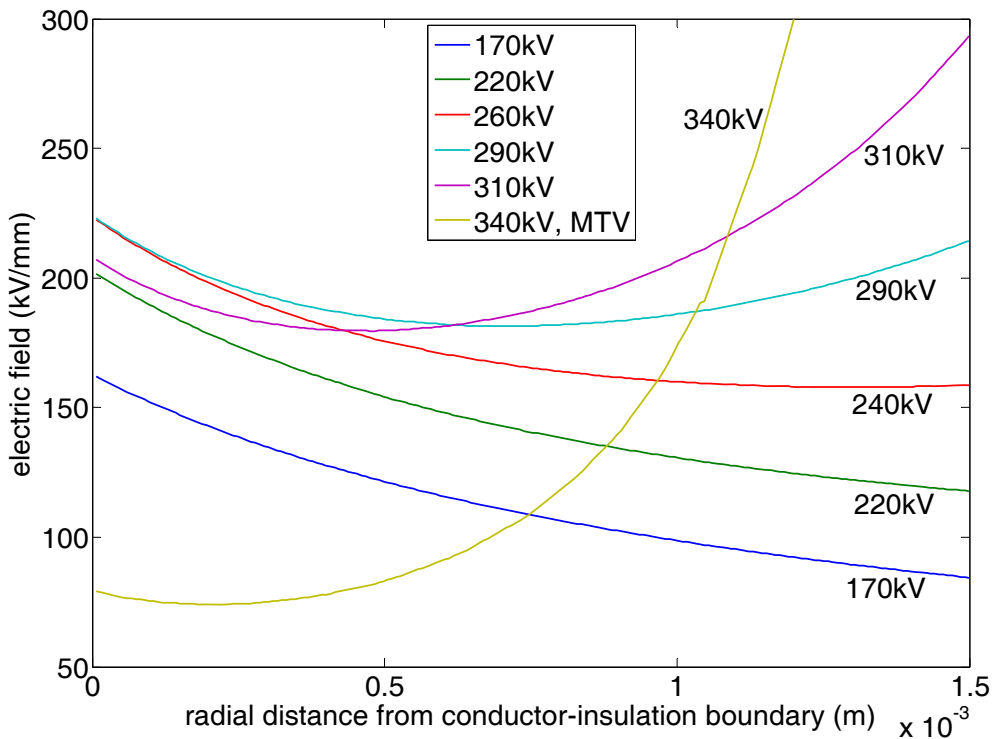
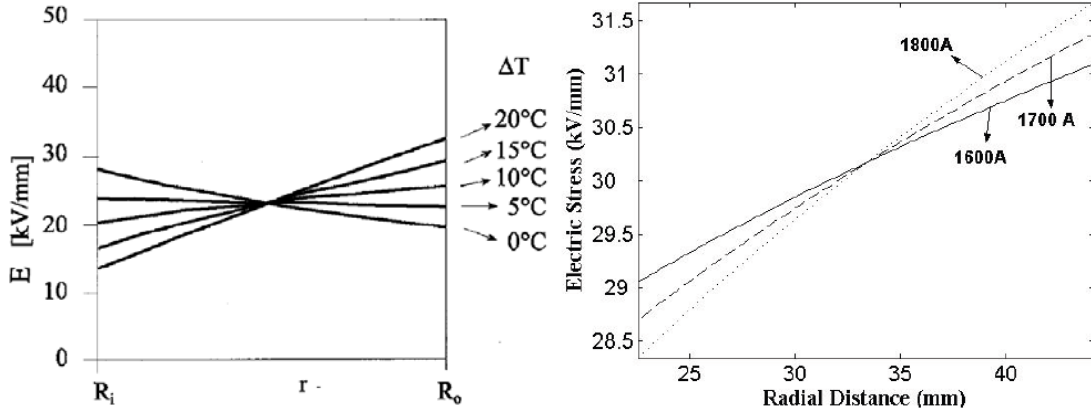


Figure 6.14 Electric field distribution in the insulation of cable AAA under different voltages, when the ambient temperature is 293K

The reversing process of electric field distribution can be obtained from plots in Figure 6.14. Under different applied voltages from 170kV to MTV, the field distribution in the cable insulation undergoes a significant change. The distribution has the same shapes with lower voltages from 170kV to 260kV. The highest electric field is at the inner boundary, and there is small change along the insulation thickness. At 290kV, there is field enhancement at both inner and outer boundaries, and the minimum field is in the middle insulation. At 310kV, the electric field at the outer boundary is much higher than that at the inner boundary. The field at inner boundary becomes smaller than that at 290kV. This distorted reverse distribution is maximized at the MTV, when the electric field at the inner boundary is smaller than all the other voltages and the electric field at the outer boundary is much higher than the originally applied electric field.



(a) by Jeroense [162]

(b) by Reddy [159]

Figure 6.15 Electric field distribution of cable insulation with heat injection due to conductor load current

This reversing field distribution is due to the temperature change of the area near the inner boundary. At higher voltages, the electric field dependent conductivity is higher near the inner boundary at the beginning. There is more resistive heating that is more difficult to dissipate than the situation near the outer boundary. This resistive heating increases the temperature near the inner boundary and therefore increases the temperature dependent conductivity further. According to the temperature distribution in Figure 6.12, the conductivity near the inner boundary can be much higher. This increasing conductivity makes the insulation more conductive and the electric field smaller. Same calculation results on the electric field distribution of cable insulation have also been found by Jeroense [162] and Reddy [159], whose data are shown in Figure 6.15. In Figure 6.15 (a) Jeroense found that the electric field distribution with different temperatures drops between the inner and outer boundaries. It can be seen that if there is no temperature drop, the electric field is higher at the inner boundary. This distribution is the same as the original state in this study when the temperature inside the cable insulation sub-domain is the same as the ambient everywhere. The electric

field becomes bigger at outer boundary when there is bigger temperature drop of more than 10°C. In this study, after reaching stable state, bigger temperature drop with higher applied voltage results in the same calculation. Reddy's calculation was in stable state with heat injection for thicker cable insulation. It can be seen that the electric field at near the inner boundary is higher than that at the outer boundary. Its distribution becomes more distorted with bigger heat injection that brings bigger temperature gradient.

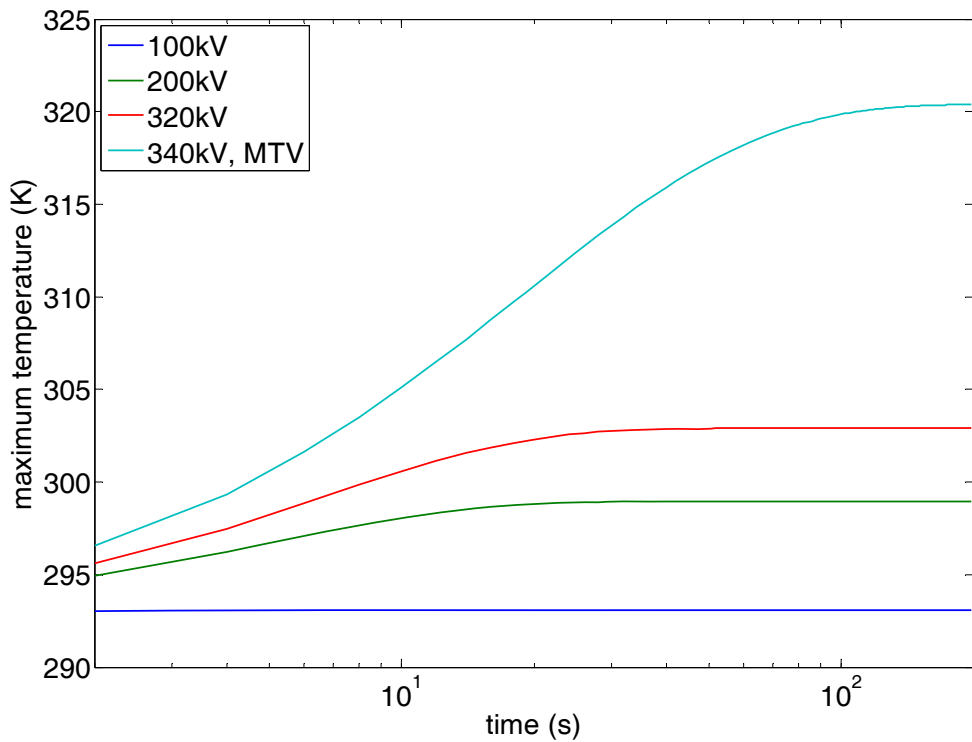


Figure 6.16 Thermal equilibrium time for maximum temperature at the inner boundary under different voltages, with ambient temperature of 293K

A transient simulation was carried out to find out the time required for thermal-electric equilibrium. Comparison can be made under different voltages in Figure 6.16. The simulation time is from 2s to 200s, in order to cover the transition period. It can be seen that the transition time is shorter to for lower voltages. The transition time is less than

40s for the voltages from 100kV to 320kV, but it is 200s under MTV. The reason is that bigger temperature change under MTV makes the process longer. This transient modelling result also support the suggestion that the operating voltage for real applications should be much smaller than its maximum thermal voltage.

#### 6.4.2 MTV with heat injection due to load current

Thermal breakdown simulation with heat injection due to conductor load current has been done in FEMLAB. The inner boundary condition should be changed with heat influx. According to Equation 6-20, the heat flux can be calculated as linear to the square of load current, assuming that the receptivity of copper conductor is constant. Figure 6.17 shows the heat flux of different conductor currents from 1A to 400A. The heat flux increases rapidly from  $2.54\text{J/m}^2$  to  $2.65\times 10^5\text{J/m}^2$ .

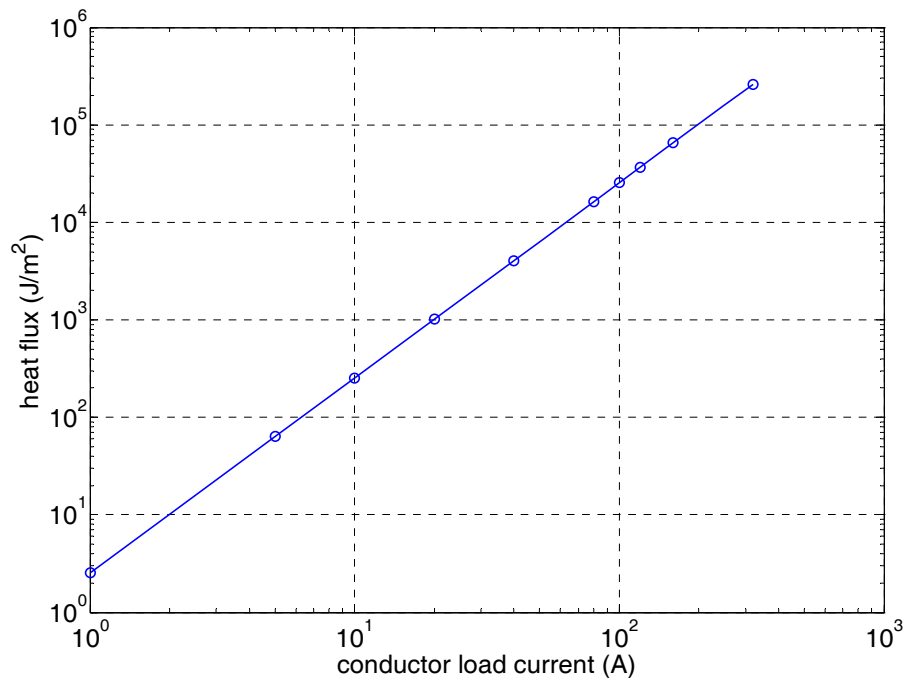
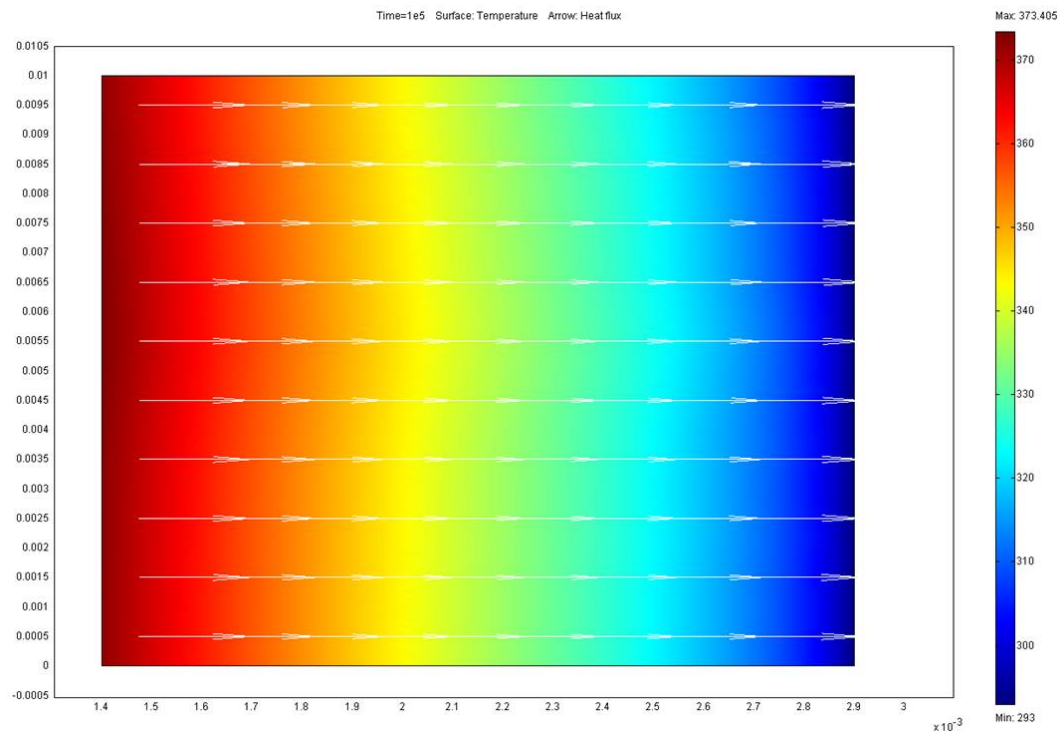
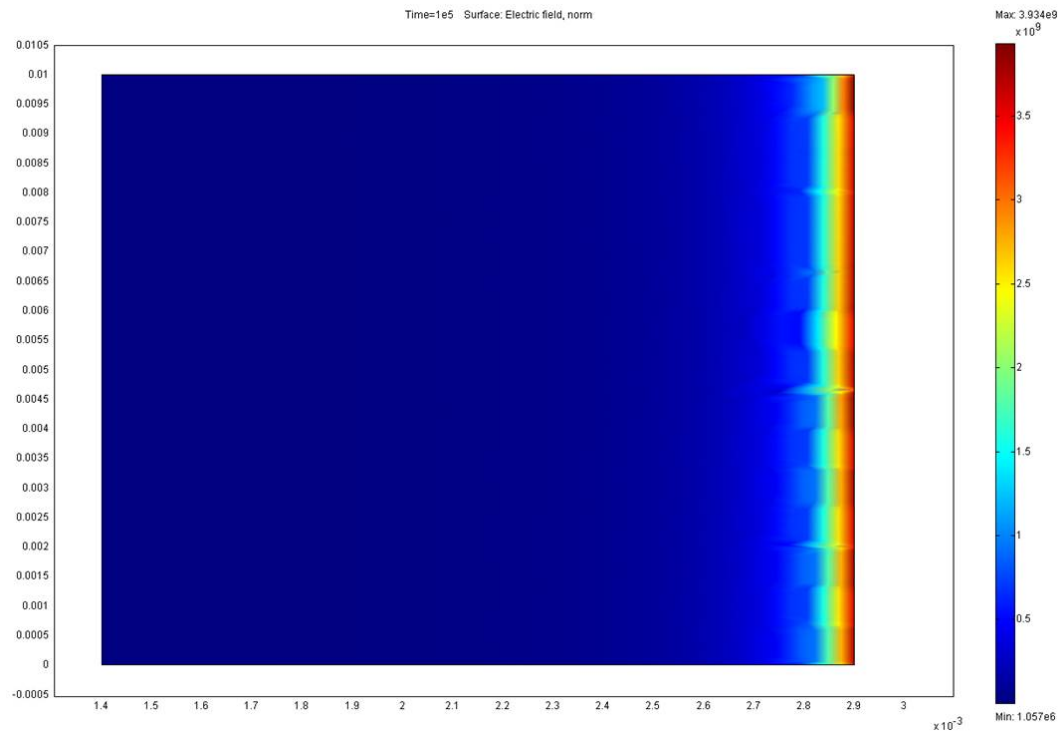


Figure 6.17 Heat flux injected into the cable insulation with different conductor load current



(a) temperature and heat flux



(b) electric field

Figure 6.18 Temperature, heat flux and electric field distribution in the insulation of cable AAA in FEMLAB, under MTV of 318kV with 120A load current

Figure 6.18 shows the FEMLAB simulation results on temperature, heat flux and electric field distribution in stable state with ambient temperature of 293K. With 120A conductor current as heat flux source, the MTV becomes smaller as 318kV, in comparison with 340kV without heat flux. The temperature distribution has much bigger gradient from 373K at the inner boundary to 293K at the outer boundary, in comparison with 320K at the inner boundary without heat flux. The electric field distribution has the same reversed stable state map with field enhancement at outer boundary. This temperature distribution also indicates that the 120A conductor current is too much for the material to reach equilibrium. Considering the melting of the semi-crystalline XLPE insulation starts from 353K, this simulation result is a theoretical situation.

Practically, 100A is found to be the maximum conductor load current for the homo-polymer model power cable at ambient temperature of 293K, as shown in Figure 6.19. The blue curve shows the theoretical MTV without checking the maximum temperature in its distribution. The green curve is the result that keeps the maximum temperature below 353K. It can be seen that with heat injection from the conductor, increasing conductor load current relates to a decreasing MTV. When the load current is less than 5A, the MTV is 340kV, the same as that without load current. From 10A to 20A, the MTV is 339kV. Big decrease of MTV can be seen when the load current is bigger than 40A. The MTV drops to 225kV when the load current is 160A. Practically, the load current has a maximum value of 100A. Any bigger current will overheat the cable insulation near the inner boundary, even without voltage application. There is more than 100kV difference between the theoretical MTV and practical MTV with 100A load current. This simulation results imply that the maximum load current is 100A.

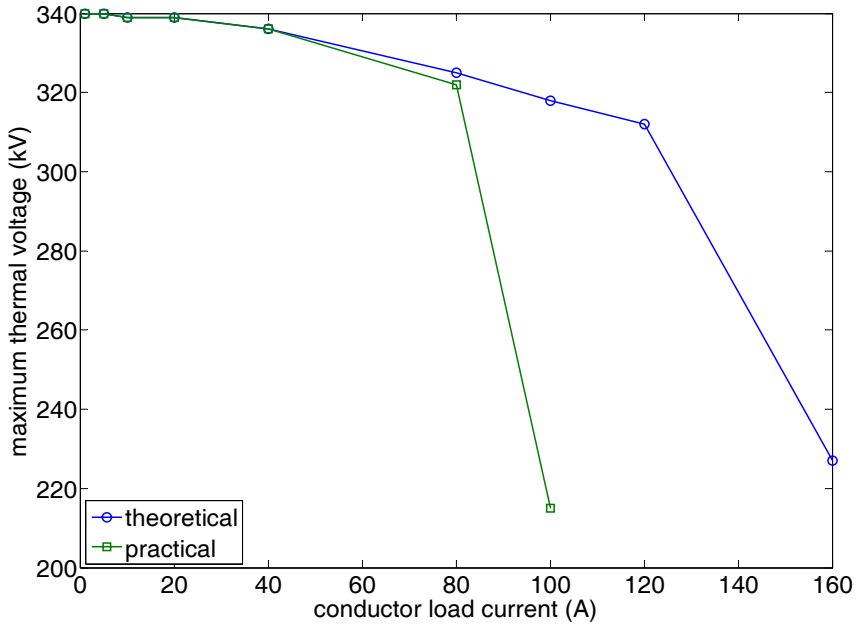


Figure 6.19 MTV with conductor load current for cable AAA at ambient temperature of 293K

It should be noticed that the simulation of thermal breakdown is based on the thermal-electric partial differential equations. The material is treated as homogeneous without polar impurity, protrusion near the boundaries and void containing volatiles, where the actual thermal breakdown can happen with the biggest probability. MTV in the complex real application environment may be smaller than the simulation results. The MTV is 165kV/mm for homo-polymer model cable with 30°C ambient temperature. However, the XLPE insulation for the model power cables in this study can definitely withstand 160kV/mm [163].

## 6.5 Conclusions

The thermal-electric behaviour of the model power cables is investigated in this chapter. FEMLAB is used for the multi-physics simulation based on finite element method:

1. The thermal breakdown voltage decreases at higher temperatures. The breakdown strength of the model power cables due to thermal instability is estimated to be  $\sim 100\text{kV/mm}$ . In practice, a cable would breakdown due to other mechanisms before reaching this calculated field.
2. The temperature distribution has substantial changes especially near the maximum thermal voltages.
3. The position of maximum field changes from inner boundary to outer boundary under higher applied voltages.

## 7 Discussion

Based on the dielectric spectroscopy study on the model power cables, three loss origins of XLPE power cables can be identified – conduction loss of XLPE insulation, intrinsic polarization loss of XLPE insulation, and series resistance loss of semicon layers. Due to the complexity of the XLPE materials and cable insulation systems, there is lack of theoretical basis concerning the dielectric loss in polymers. In this chapter, efforts are made to search the underlying loss mechanisms of the XLPE power cables. Finally, a dielectric loss model of XLPE power cables is proposed in this work, with the aim of further understanding electrical properties of the power cables.

### 7.1 Summary of experimental results on the model power cables

Figure 7.1 shows the experimental results of homo-polymer model cables at 60°C and 80°C (symbol lines), compared with the equivalent circuit simulation results (solid colour lines) over the frequency from  $10^{-4}$ Hz to  $10^4$ Hz. The equivalent circuit is introduced in chapter 4, and the simulation is based on the geometry of the model cables with five meter sample length.

Without any semicon layer, the XLPE cable insulation has the ideal loss due to pure DC conductivity with the slope of -1 all through the frequency range. The loss tangent at 50Hz due to conductivity of the XLPE can be as small as  $10^{-7}$ . The magnitude of conduction loss is determined by the conductivity of the cable insulation layer. The conductivity of the power cables is dependent on the material and temperature. As found in this study, the co-polymer cables have higher DC conductivity than homo-polymer XLPE cables. All the model power cables have Arrhenius type temperature

dependence. Degassing was found to be able to decrease the conductivity, while thermal ageing greatly increased the conductivity by almost ten times. In Figure 7.1, the experimental results of dielectric loss at the lower frequencies are mainly DC conduction response with slope of -1. At higher temperatures the magnitude of dielectric loss tangent increases to be dominant over a wider frequency range towards higher frequencies.

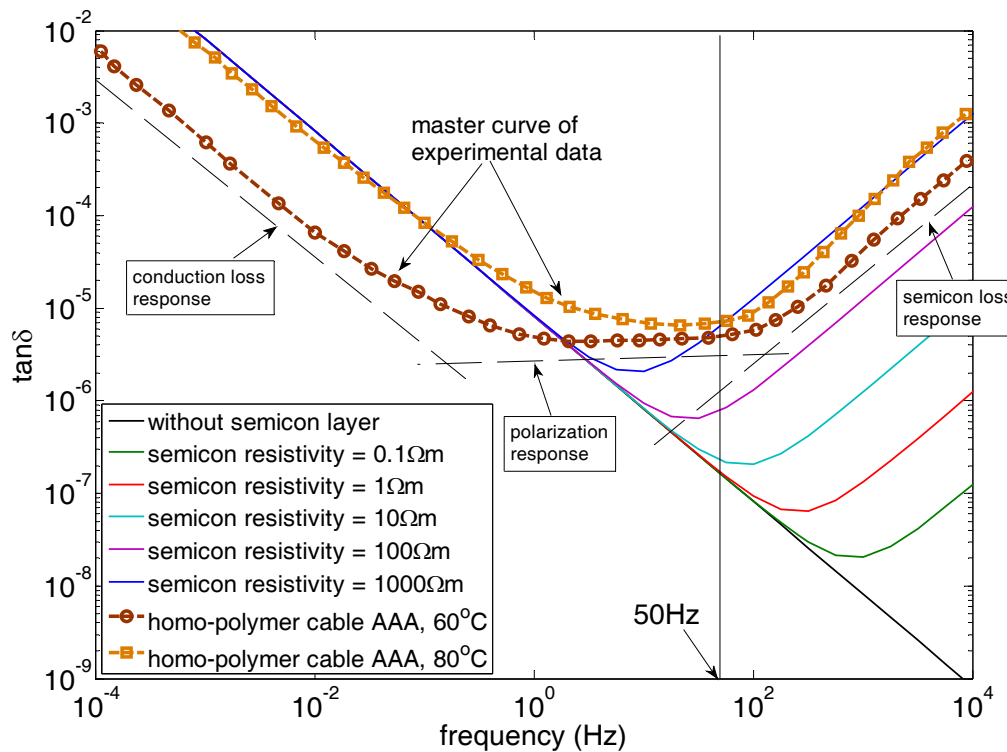


Figure 7.1 Comparison of loss tangent spectra between experimental results and simulation results.

When there is a resistance due to semicon layers, the loss tangent of power cable has a positive increasing slope of 1 at higher frequencies. It can be seen from Figure 7.1 that there is little contribution when the semicon resistivity is below  $1\Omega\text{m}$ , when the total resistance of both semicon layers is as small as  $0.237\Omega$ . The magnitude of the loss tangent due to semicon layers becomes higher with increasing semicon resistivity. It

may become significant at 50Hz, e.g. the loss tangent at 50Hz is dominated by semicon loss if the semicon resistivity is bigger than  $10\Omega\text{m}$ . In this study, the experimental results of loss tangent at higher frequencies have already been proved to be due to semicon layers in chapter 4. The magnitude is also dependent on material of semicon layers and temperature. At temperatures below  $80^\circ\text{C}$ , the semicon resistivity was found to increase. The standard and super-smooth semicon have similar conductivity. The conductivity of super-smooth semicon had smaller increase after thermal ageing.

Besides the slope of -1 at lower frequencies and slope of 1 at higher frequencies, the experimental results have deviations from the equivalent circuit modelling results in the mid-frequency range, especially at lower temperatures as shown in Figure 7.1. This should be due to the intrinsic polarization response of XLPE insulation. As found in chapter 4 and chapter 5, the dielectric loss response, which was transformed from time domain discharging current without DC conductivity contribution in the mid-frequency range, is very “flat”. Typical Debye loss peak does not exist in this semi-crystalline XLPE insulation. This intrinsic dielectric loss was found to have different temperature dependence with minimum loss tangent at  $60^\circ\text{C}$ .

The dashed black lines in Figure 7.1 classifies the three different types of dielectric loss response as DC loss at lower frequencies, polarization loss at mid-frequencies and semicon loss at higher frequencies. The mechanisms of these three loss origins will be studied in the next three sections.

## 7.2 Conduction loss of cable insulation

The DC conductivity of power cables is mainly from the XLPE insulation layer that has considerably larger resistance (approximately 15 orders of magnitude) than semicon

layers. The chemical and physical complexity of XLPE insulation implies that there are different conduction and insulation mechanisms, which cooperate and interfere. However, the measurement results can give some clues on the determination of possible electrical conduction mechanisms in XLPE.

In crystalline regions of semi-crystalline XLPE, simple band theory for covalently-bound crystal materials is usually used to explain the conduction of polymeric insulators. This simple conduction mechanism along the crystal lattice through the bulk insulation is not likely to happen for XLPE material because of the imperfect arrangement of the carbonic main chains of crystalline regions that surrounded by interrupting amorphous regions. Figure 7.2 shows the band gap of a charge carrier between valence band and conduction [98] [164], with the vacuum level of polyethylene. Firstly, the electrons of the saturated  $\sigma$  carbon bonds in the valence band needs 8.8eV to reach conduction band [165] [166]. This wide band gap makes it unlikely for an electron to have adequate thermal energy for direct transition to the conduction band. Extra energy may also be needed for the electron to escape the current molecule to the adjacent one. While the experimental apparent thermal activation energy in this study is between 1eV and 1.2eV for both homo- and co- polymer model power cables, the probability for an electron to obtain 8eV is extremely small. The probability of an electron occupying the lowest level in the conduction band due to thermal excitation at 100°C is about  $3.7 \times 10^{-60}$ , and is negligible [12]. Secondly, the vacuum level of XLPE is below the conduction band. This indicates that an electron would be ejected from the crystalline region before reaching conduction state. The electron cannot move in the crystalline region as a conducting particle. Thus, it can be concluded that charge carrier transport in the crystalline region is too small and inappropriate to be responsible for the conduction loss mechanism in XLPE.

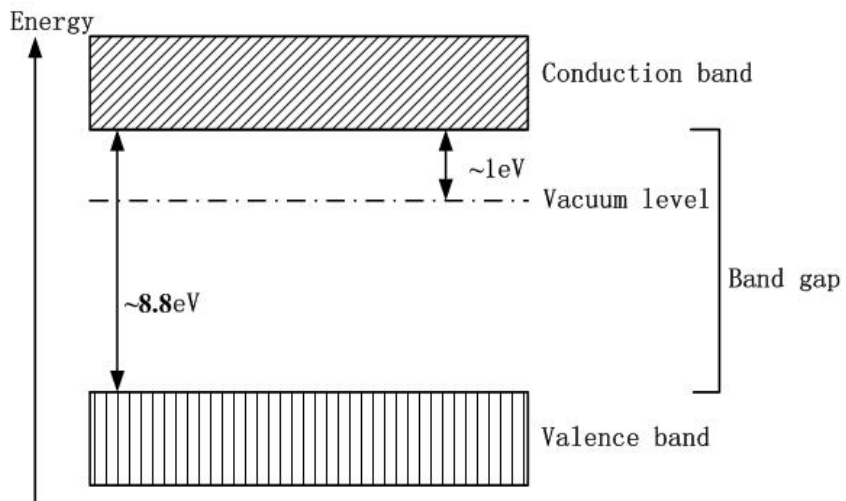


Figure 7.2 Electron energy scheme based on band theory, with negative electron affinity [98]

In amorphous regions, temporal and spatial inhomogeneities cause more localized energy states in the non-crystalline parts inside XLPE, as shown Figure 7.3. Instead of acquiring large amount of activation energy to be “conducting”, the electrons may have more chance of hopping to other localized states under the influence of local electric field. Further from the centre of the band gap, the localized states are in much closer proximity, and it may be possible for electrons to tunnel or hop between sites which are close to each other. Charge carriers, hence, may move even in the absence of band conduction towards the opposite electrode. With flexible interconnecting polymer chains and other impurities or additives, the amorphous regions are more likely to be responsible for electrical conduction in XLPE. The inter-state distance is very critical for the occurrence of this form of conduction and the probability of hopping or tunnelling increases rapidly as the distance decreases below a few nanometres. While the electrons hop through the insulation under electric field, hole conduction would also occur at the same time. Besides, the waxy or semi-liquid environment of amorphous regions provides easier paths for charge carrier transportation.

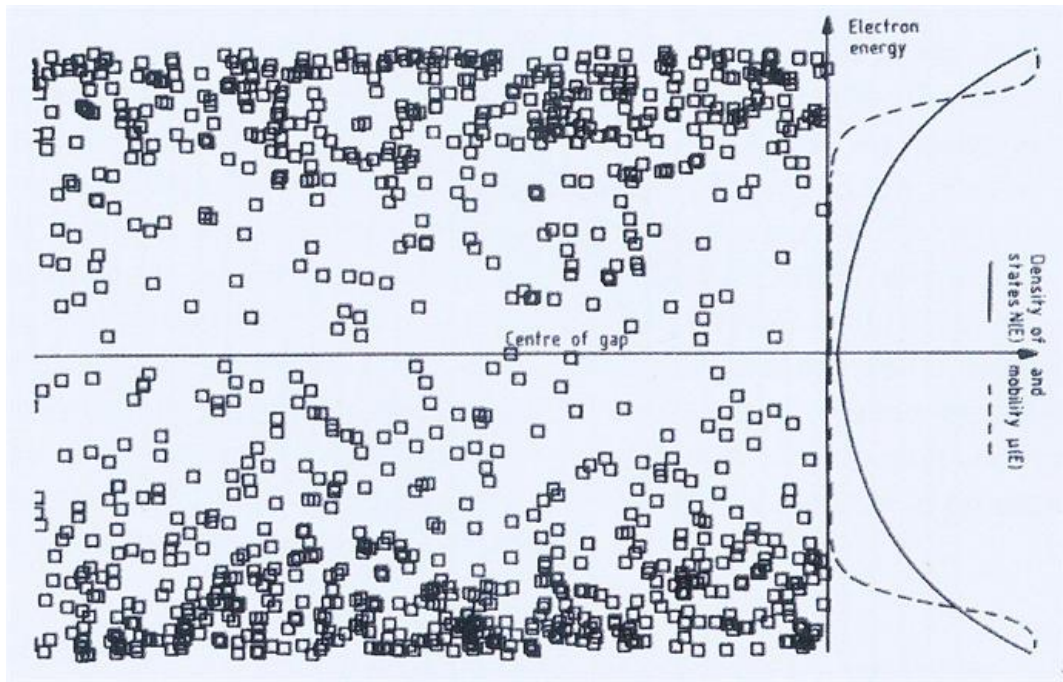


Figure 7.3 Localized states (indicated by squares) in amorphous regions of semi-crystalline XLPE material as a function of electron energy; the density of states and mobility are shown on the right side curves [12]

A diagram of electrical conduction is shown in Figure 7.4. In this semi-crystalline XLPE, the amorphous region provides a path for charge transport. Only the conducting path of an electron is demonstrated for simplification, as hole conduction has similar process with opposite direction, though hole conduction may be more difficult than electron transport in the bulk insulation. The electron near the cathode hops to the direction of anode in distributed energy states. Except electronic hopping, it may be recombined with another molecule to become ionic conduction perhaps under high electric field. Trapping and de-trapping may also occur in the amorphous region as well as the surface of crystalline regions. Dissociation of ionic species when the electron acquires enough energy could result in the electron finally reaching the anode. A hole has a similar transporting process through amorphous region. Neutralization with the electron may occur in the bulk insulation but with a very small probability in the XLPE

of extremely low charge concentration. Temperature increase can provide external thermal energy to the charge carriers and expand the volume of amorphous region. This is a very likely reason for the model power cables to have Arrhenius-type DC conductivity increase, as found in the experimental results of this study. Therefore, this trap-limited transport by electrons (holes) through amorphous regions is the most likely conduction loss origin.

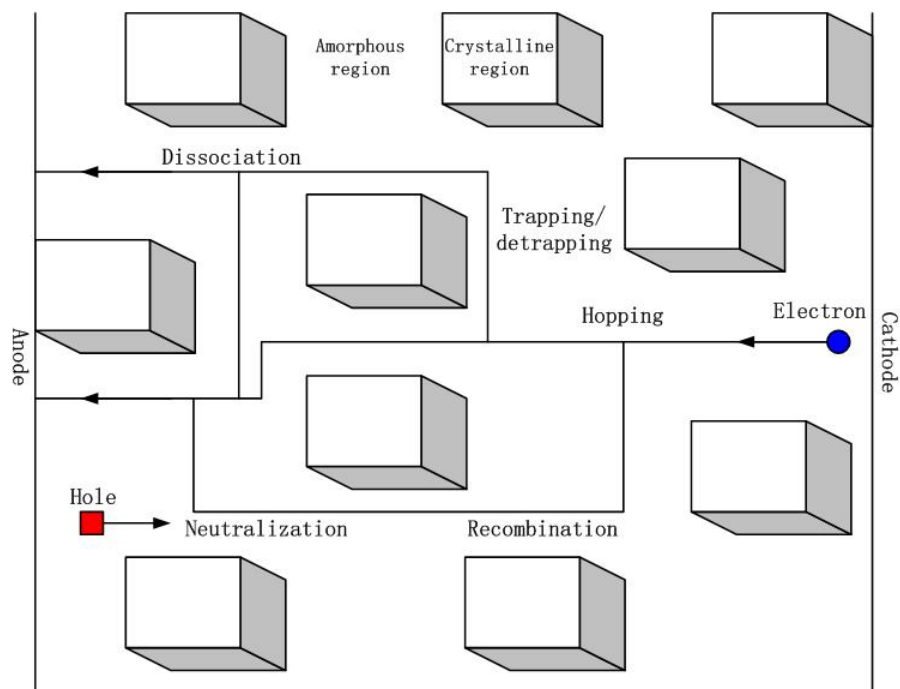


Figure 7.4 Diagram of electrical conduction mechanism in semi-crystalline XLPE

The electrical conduction mechanism for homo-polymer XLPE cables (AAA and ABA) in this study can be further extended for explaining the higher conduction loss of the co-polymer (ACA) model cable. The co-polymer insulation is a cross-linked product of low density polyethylene and co-polymer ethylene-butyl-acrylate (EBA), as shown in Figure 7.5 in comparison with the homo-polymer insulation [167]. The two-phase structure, with LDPE as a matrix phase and with the copolymer as dispersed phase, can bring considerable difference to electrical properties. Firstly, the micron-size EBA

islands greatly disturb the crystalline XLPE network and, therefore, expand the proportion of amorphous region, which account for the increasing DC conductivity in comparison with homo-polymer cables, as experimentally found in this study that the addition of co-polymer structure brought up the DC conductivity more than ten times higher than the homo-polymer cables. Secondly, the EBA main chain does not provide extra charge carriers because there is no conjugated C=C bond, but the C=O bond on its branch may be ionized for extra conductivity increase.

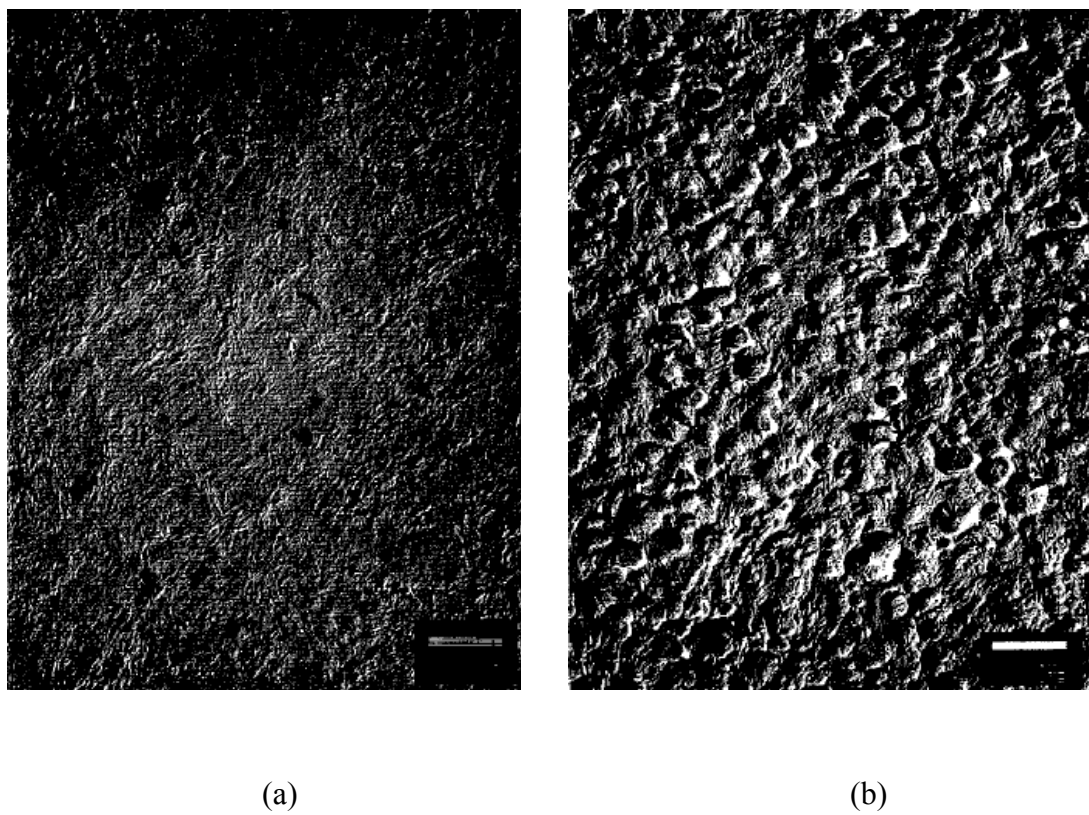


Figure 7.5 Comparison of homo-polymer insulation (a) and composite insulation (b) added with EBA co-polymer, both cross-linked with dicumyl-peroxide and antioxidant

### 7.3 Resistive loss of semicon layers

As introduced in chapter 2, semicon layers of power cables are used to avoid electric field enhancement due to protrusions and voids [168] at insulation boundaries with

uneven interface, as shown in Figure 7.6 (a). It can also reduce electron injection from the inner copper conductor and outer metal sheath. The semicon layers are generally carbon black filled polymer, such as the carbon black filled ethylene-butyl acrylate in this study. The morphology of XLPE layer and semicon layer in the model cables can be compared in Figure 7.6. However, these semi-conductive layers become a source of dielectric loss for power cables because its radial resistance is in series with the XLPE insulation layer which is basically capacitive, as shown in Figure 7.6. Equivalent circuit analysis is helpful for explaining this loss mechanism. The semicon layers form a typical series equivalent circuit with increasing dielectric loss at higher frequencies as the measurement results have shown. As already been proved in chapter 4, higher semicon resistivity can increase the dielectric loss of power cables at higher frequencies.

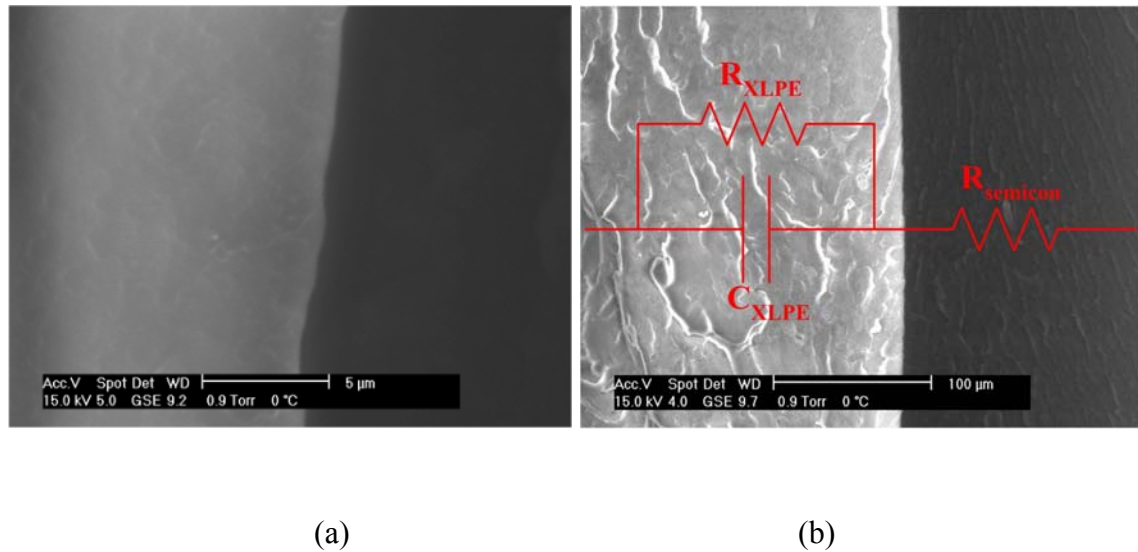


Figure 7.6 SEM photos of interface between XLPE layer and semicon layer. (a): 5 $\mu\text{m}$  bar magnification; (b) 100 $\mu\text{m}$  bar magnification with cable equivalent circuit

With much smaller contribution of conduction loss at higher frequencies, the resistivity of semicon is critical to this type of loss origin. The loss mechanism can be investigated based on the properties of semicon materials. Figure 7.7 shows the measurement results

of temperature dependent resistivity of two different semicon materials before and after thermal ageing in this study. The standard semicon is furnace carbon black filled EBA, while super-smooth semicon is acetylene carbon black filled EBA. There are two main factors to be responsible for increasing resistivity of semicon layer resistance:

1. Temperature increase will increase the resistivity as shown in Figure 7.7. As found in chapter 4, the loss tangent is proportional to the resistivity of semicon materials at higher frequencies.

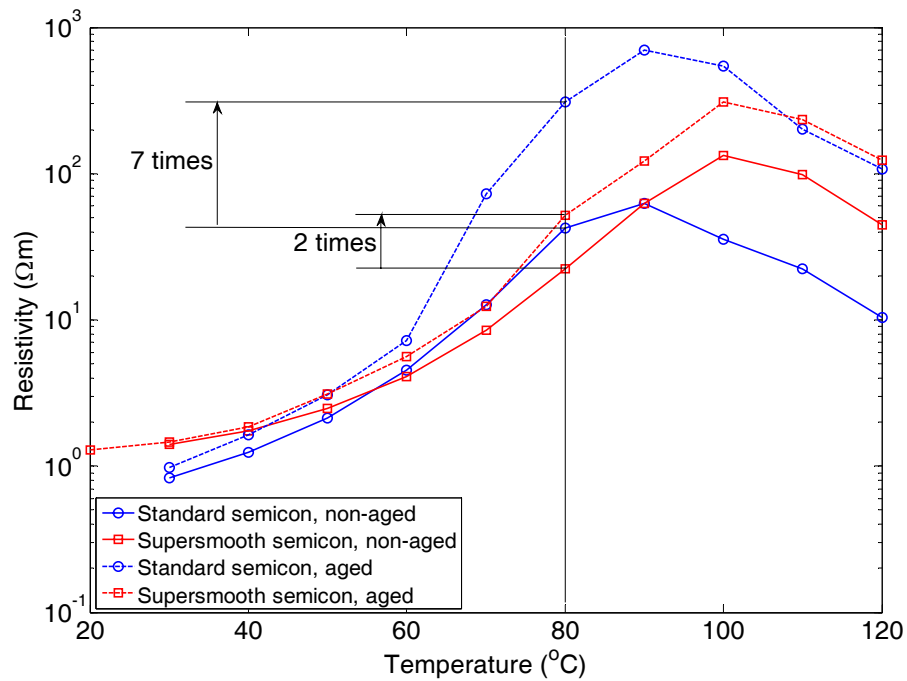


Figure 7.7 Resistivity of semicon materials in this study, standard semicon and super-smooth semicon before and after thermal ageing were measured in comparison

All the measurement samples have increasing resistivity at higher temperatures below 90°C, regardless of carbon fillers and ageing conditions. The decrease of semicon resistivity should be due to the phase change above 90°C that is beyond the temperature range of this study, though indicating the different melting

temperature for the two semicon materials. Therefore, a power cable would have higher dielectric loss due to semicon layer resistance at higher operating temperatures, as observed in this study (also shown in Figure 7.1).

2. The ageing of the semicon layer also increases the semicon resistivity as shown in Figure 7.7. Both semicon materials have increased resistivity after thermal ageing. At lower temperatures, there is not much increase for either of the semicon materials. The increment becomes more marked at higher temperatures. At 80°C, the resistivity of standard semicon increased 7 times while the super-smooth semicon only increased 2 times after ageing.
3. Comparing the two semicon materials in Figure 7.7, the super-smooth semicon, which is filled with a special type of carbon black formed by an exothermic decomposition of acetylene, has a more stable electrical property during ageing, probably because the acetylene carbon black filler has the highest degree of aggregation and crystalline orientation when compared with all types of carbon black [169]. Therefore, super-smooth semicon is better for reducing the dielectric loss due to semicon layers at higher frequencies.

Besides the above factors, some other aspects should be considered, e.g. concentration of carbon black fillers. Diffusion of carbon black fillers from the semicon layer into the insulation layer may also increase the actual semicon resistance. The interfacial diffusion during the cable extrusion process [170] occurs when flexible long polymer chains diffuse into each other in a melt state during the co-extrusion. The molecular entanglements at the interface, as shown in Figure 7.8, may increase the effective

semicon layers resistance and the effective XLPE layer capacitance. The minimum frequency  $f_{\min}$  would shift to lower frequency according to

$$f_{\min} = \frac{1}{2\pi\tau} = \frac{1}{2\pi R_{\text{semicon}} C_{\text{XLPE}}} \quad \text{Equation 7-1}$$

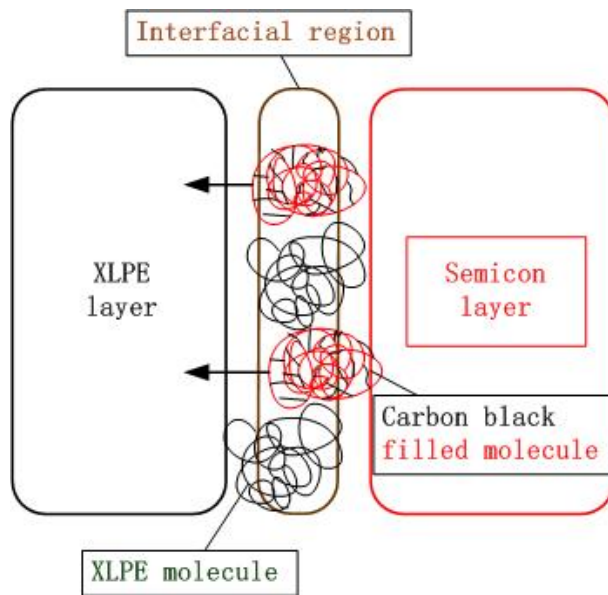


Figure 7.8 Schematic diagram showing interfacial diffusion of semicon molecules

The loss origin from the semicon layers imply that power cable manufacture should include importance of semicon materials. There should be criteria for the resistivity of semicon shield, which should not become dominant in loss tangent. For example, the resistivity should be kept below  $10\Omega\text{m}$ , above which the dielectric loss at 50Hz is mainly due to the semicon resistance rather than the XLPE insulation. The super-smooth semicon with acetylene carbon black fillers has been found to have better performance during thermal ageing. It is also indicated that the cable outer semicon layer should be perfectly sheathed or earthed. Since the axial resistance of the semicon layer is much larger than its radial resistance, the loss tangent increases very quickly with a small non-earthed area of outer semicon shield.

## 7.4 Polarization loss of XLPE insulation

As shown in chapter 4 (for degassed cables) and chapter 5 (for aged cables), the master curves of all the model power cables have shown that the middle frequency range spectra are due to the polarization behaviour of XLPE insulation rather than DC conductivity or semicon layers. The comparisons shown in Figure 7.1 indicate the differences between typical experimental loss tangent spectra and the modelling results that only incorporate DC conductivity and semicon resistance. Apart from the conduction loss at lower frequencies and semicon loss at higher frequencies, a broad polarization loss peak can be identified in the frequency range from  $10^{-1}\text{Hz}$  to  $10^2\text{Hz}$ .

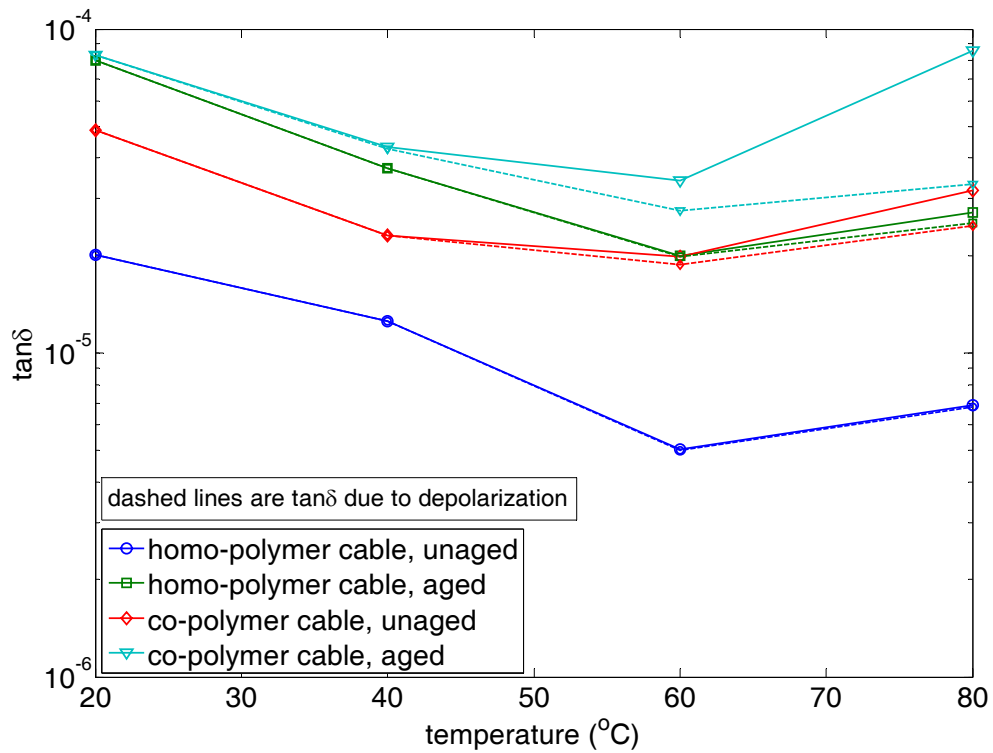


Figure 7.9 Loss tangent of unaged and aged homo-polymer and co-polymer XLPE cables at 50Hz

As found in this work, the temperature dependence of the dielectric loss is different from the other two loss origins. Figure 7.9 summarizes the temperature dependent loss tangents observed for both homo- and co- polymer cables at 50Hz. All the cables have minimum values at 60°C, in accordance with other researchers [145] as introduced in chapter 5. Since the depolarization current was measured, the loss tangent without conduction contribution can be obtained as shown with dashed lines, which have the same temperature dependence.

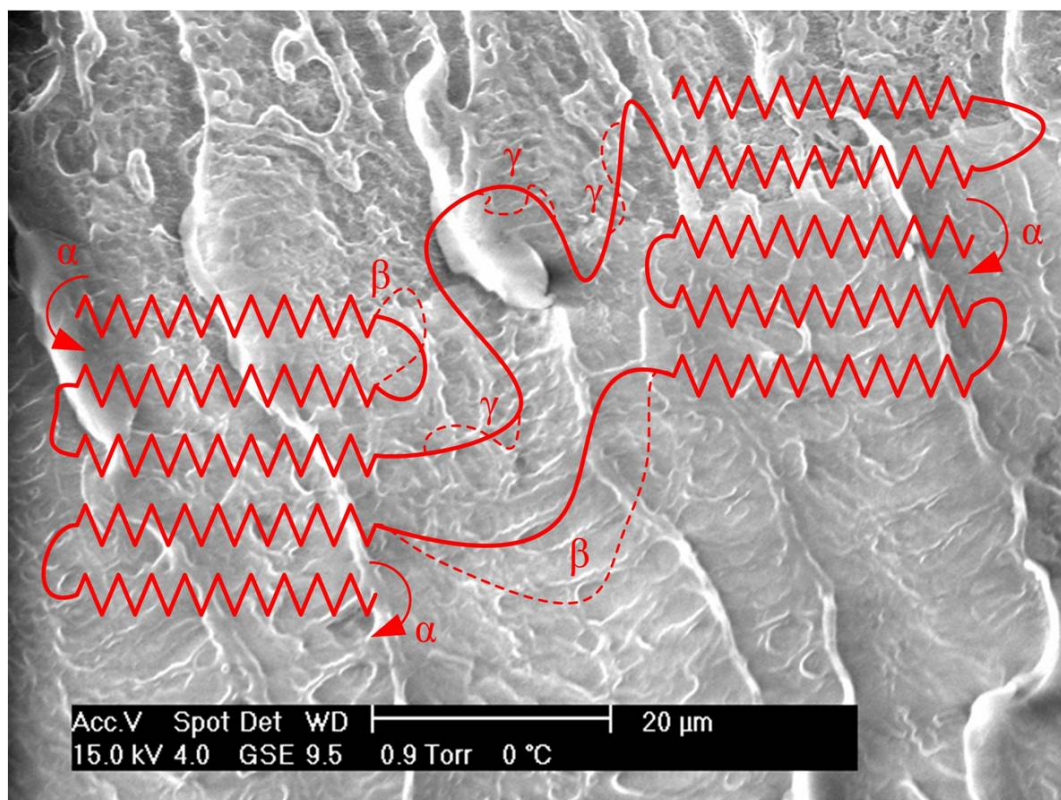


Figure 7.10 SEM photo (20μm magnification) of XLPE cable insulation with polarization mechanisms

This mid-frequency range loss mechanism could be explained from a molecular view point. The polarizability of XLPE is small because of its symmetric main chain molecular structure with saturated C-C bonds. A molecule may be non-polar either because there is (almost) no polarity in the bonds or because of the symmetric

arrangement of polar bonds. XLPE molecules have the C-H bonds arranged symmetrically around the carbon atom main chain. Although each C-H bond has a small polarity, the bonds are arranged symmetrically so there is no overall dipole in the molecules of crystalline region. The amorphous region and impurities can contribute greatly to the total polarization of the XLPE insulation in power cables. For the low loss XLPE model cables in this study, intrinsic polarization may dominate the dielectric loss in the middle frequency range where the conduction and semicon resistance have much smaller contribution to the total loss.

The basic molecular polarization mechanisms are explained in chapter 2. Furthermore, more specific and recent theories are needed to explain the polarization behaviour in XLPE. Based on a previous theoretical study on the molecular polarization of the semi-crystalline XLPE material and experimental work by other researchers and in this study [171] [172] [173] [113], an intrinsic polarization model is proposed in order to help explain the temperature dependence of the dielectric loss in the middle frequency range in this study. On top of the SEM photo of XLPE layer in the power model cables in Figure 7.10, the three types of polarization in the semi-crystalline polymer can be seen.  $\alpha$  polarization that occurs in the crystalline region represents the main chain polarization in the lamella sheets. The spinning rotation of the whole chain is difficult to occur for the XLPE lamella. Only partial reorientation may be possible in the middle frequency range (from  $10^{-1}$  to  $10^2$ ) in this study. The  $\alpha$  polarization in cable insulation is thus relatively negligible, compared to  $\beta$  and  $\gamma$  polarizations. Because the melting temperature for the crystalline region starts from  $80^\circ\text{C}$ ,  $\alpha$  polarization has very weak temperature dependence from  $20^\circ\text{C}$  to  $80^\circ\text{C}$  in this study.  $\beta$  polarization may occur in the waxy amorphous regions, which interconnect crystalline regions with loose disordered carbon chains and some chemical impurities that are rejected as the

crystalline lamellar forms. It is relatively easy for the electric field to polarize the molecules in the amorphous regions, because there is much more room for any polar group to reorientate. In the waxy state, the segmental loose chains and other polar groups overcome viscous force for the  $\beta$  type polarization. Larger amount of dielectric loss can be induced during this process, especially at low temperatures with higher viscous amorphous regions. With increasing temperature, the amorphous region would become more liquid with lower viscosity, making the polarization easier to be done with less energy loss. Continuing temperature increase will result in thermal expansion of the XLPE material. The proportion of amorphous region becomes larger and more segmental polar groups can be released to contribute to the polarization. Above 60°C, the expansion effect of amorphous region may overtake the effect of decreasing viscosity. Therefore, the dielectric loss increases again at 80°C.  $\gamma$  polarization is the crank type movement of segmental molecular chains. This type of polarization is mainly in amorphous regions where more crank shape segments are available. It is characterized by weak relaxation strength that is insensitive to morphology and degree of crystallinity, and by extremely broad relaxation in both frequency and time domain. Another characteristic of the XLPE cables in the middle frequency range is the “flat” dielectric loss spectra, as shown in chapter 4 and chapter 5. The main reason for the non-Debye loss is the diversity of polarizable groups in the semi-crystalline XLPE. Besides the various shapes and states of the segmental chains in the amorphous regions, other additives and impurities also play important part in the total polarization. The multiple polarizable groups give a distribution of adjacent loss peaks over a wide frequency range. Hence, the measured dielectric loss spectrum is an overlapping result of the multiple polarizations.

In conclusion, the intrinsic polarization is dominant in the middle frequency range from  $10^{-1}\text{Hz}$  to  $10^2\text{Hz}$ . While  $\alpha$  polarization has very little temperature dependence from  $20^\circ\text{C}$  to  $80^\circ\text{C}$  and  $\gamma$  polarization is too weak to contribute greatly to the total dielectric loss,  $\beta$  polarization has the strongest contribution. At lower temperatures, it has an inverse relationship to temperature in the waxy state of the amorphous regions with decreasing viscosity. When the amorphous regions become totally liquid above  $60^\circ\text{C}$  for the XLPE insulation, the expansion of amorphous regions give rise to the  $\beta$  polarization. Multiple relaxations are characteristic for the bulk XLPE insulation with no Debye peak present [9] [122].

## 7.5 Dielectric loss model for XLPE power cables

The black dashed lines in Figure 7.1 have shown that there are three dielectric loss origins in XLPE power cables, based on experimental results. In order to gain a better understanding of the cable insulation system, the mechanisms of these loss origins have been studied in previous sections of this chapter. For practical importance, a mathematical expression may be suggested based on the three types of dielectric loss with a basic form of

$$\tan \delta_{cable} = \tan \delta_{DC} + \tan \delta_{polarization} + \tan \delta_{semicon} \quad \text{Equation 7-2}$$

where the total dielectric loss of power cables  $\tan \delta_{cable}$  consists of DC conductivity loss  $\tan \delta_{DC}$ , intrinsic polarization loss  $\tan \delta_{polarization}$  and loss due to semicon layers  $\tan \delta_{semicon}$ . The loss tangent considering DC and semicon loss can be calculated based on the equation derived in chapter 4

$$\tan \delta = \frac{R_p + R_0(1 + \omega^2 C_p^2 R_p^2)}{\omega C_p R_p^2} \quad \text{Equation 7-3}$$

where  $C_p$  and  $R_p$  are the equivalent capacitance and resistance of the insulation layer;

$R_0$  is the total resistance of both semicon layers. Equation 7-3 equals

$$\tan \delta = \frac{1}{\omega C_p R_p} + \frac{1}{\omega C_p R_p} \cdot \frac{R_0}{R_p} + \omega C_p R_0 \quad \text{Equation 7-4}$$

If practically assuming  $R_p \gg R_0$ ,

$$\tan \delta \approx \frac{1}{\omega C_p R_p} + \omega C_p R_0 \quad \text{Equation 7-5}$$

whree DC conductivity loss and semicon loss can be therefore separated into

$$\tan \delta_{DC} = \frac{1}{\omega C_p R_p} \text{ and } \tan \delta_{semicon} = \omega C_p R_0 \quad \text{Equation 7-6}$$

As observed by TDDS, the intrinsic polarization loss is “flat” due to the distributed relaxation times of XLPE insulation. This loss contribution can be practically assumed to be constant as the 50Hz loss tangent. Thus, the mathematical expression of the XLPE cable should be

$$\tan \delta_{cable} = \frac{1}{\omega C_p R_p} + \tan \delta_{50Hz} + \omega C_p R_0 \quad \text{Equation 7-7}$$

For a given geometry of power cable, the loss tangent can be calculated using Equation 7-7. The capacitance and resistance of cylindrical cable dimension can be calculated by

$$C_p = \frac{2\pi\epsilon_0\epsilon'L}{\ln(r_o/r_i)} \text{ and } R = \frac{\ln(r_o/r_i)}{2\pi\sigma L} \quad \text{Equation 7-8}$$

where the outer and inner radius are different for calculating  $R_p$  and  $R_0$ . As found in this study, the conductivity/resistivity of XLPE and semicon are both dependent on temperature, while the capacitance has negligible change. Arrhenius temperature dependence was found for insulation layer of all model cables. The temperature dependence of semicon materials and the intrinsic polarization of XLPE insulation can be found in Figure 7.7 and Figure 7.9 separately.

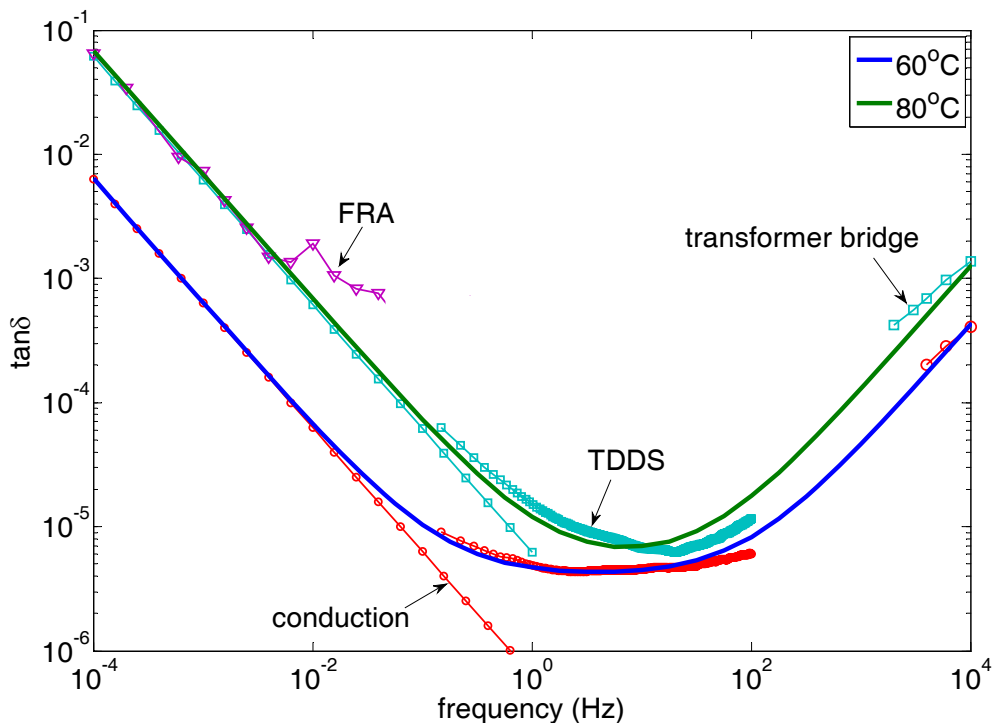


Figure 7.11 Mathematical fitting of experimental data for homo-polymer model power cables using Equation 7-7

As an example, Figure 7.11 shows the fitting of experimental results using Equation 7-7 for homo-polymer cables at 60°C and 80°C. The conductivity measurement results of

homo-polymer cable AAA are used to calculate the DC conductivity loss spectra  $\tan \delta_{DC}$ . FRA result at 80°C is also shown in comparison with a noise floor at  $10^{-3}$ . The measured semicon resistivity was used to calculate the semicon loss spectra  $\tan \delta_{semicon}$ . The intrinsic polarization loss of XLPE insulation is practically assumed as the 50Hz value in the calculation of  $\tan \delta_{polarization}$ . The total dielectric loss is shown in blue and green solid curves, which are composed of the three loss origins. The semicon loss contribution includes the calculated radial resistance and anomalous axial resistance due to imperfect contact. While the blue curve can fit well the 60°C experimental results, the deviation of the green curve for 80°C may be due to the assumption of constant intrinsic loss that may actually have variation.

In summary of the three types of dielectric loss discussed in previous sections, a dielectric loss model is proposed in Figure 7.12:

1. At lower frequencies below  $10^1$ Hz, conduction loss dominates the dielectric loss of homo-polymer cables. With slope of -1, it rises very quickly towards lower frequencies. Electron hopping conduction under thermal-electric driving force and ionic conduction due to impurities in amorphous regions are the underlying mechanism. Temperature dependence of the conduction loss follows Arrhenius behaviour with activation energy of about 1eV for all the model power cables. There is a small distortion to the -1 slope for co-polymer cables due to slow strong polarization of EBA islands, but conduction loss still has the biggest contribution.
2. In the middle frequency range from  $10^1$ Hz to  $10^2$ Hz, intrinsic polarization loss has been measured with TDDS system. The intrinsic polarization is dominant in

the middle frequency range from  $10^{-1}\text{Hz}$  to  $10^2\text{Hz}$  with “flat” dielectric loss.

Since  $\alpha$  polarization has very little temperature dependence below XLPE melting temperature and  $\gamma$  polarization is too weak to contribute greatly to the total dielectric loss,  $\beta$  polarization has been postulated to have the biggest contribution. The temperature dependence of dielectric loss can be explained based on the molecular polarization model of semi-crystalline XLPE material.

At 50Hz, the XLPE cables have the lowest loss tangent at  $60^\circ\text{C}$ .

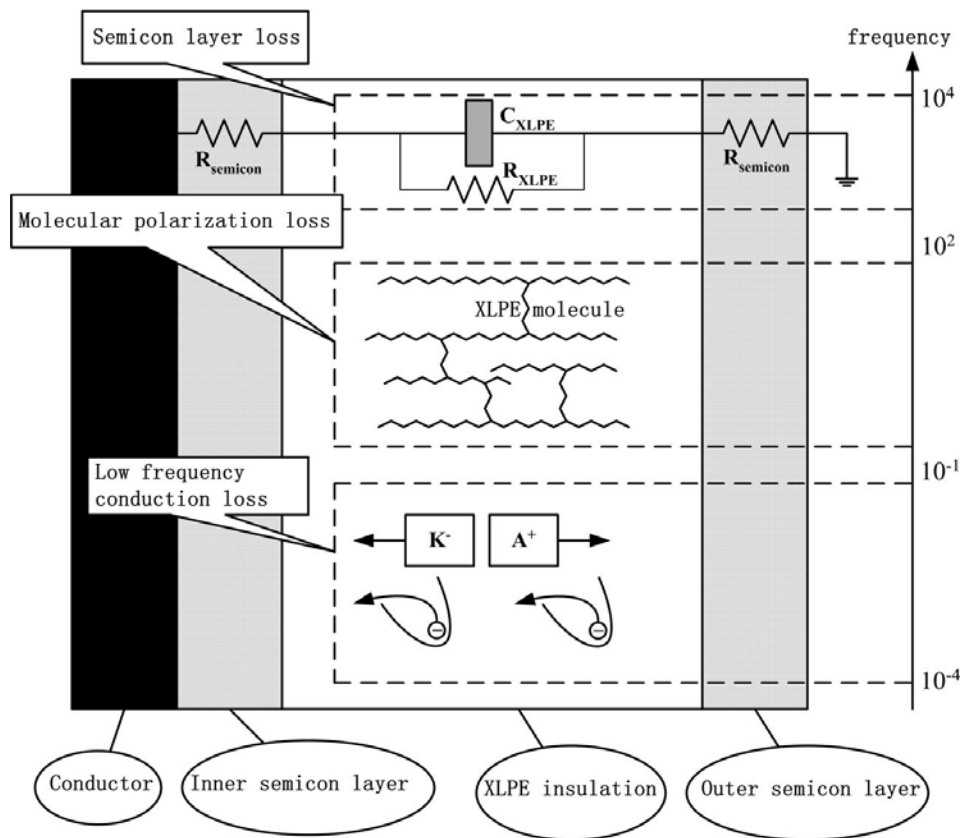


Figure 7.12 Dielectric loss origins of power cables, with different mechanisms dominating different frequency ranges

3. At higher frequencies above  $10^2\text{Hz}$ , dielectric loss from semicon layers is dominant. According to the cable equivalent circuit, small amount of semicon resistance can bring up the dielectric loss at higher frequencies with slope of 1.

Temperature increase, ageing and interfacial diffusion between semicon and XLPE layers would increase the semicon layers' radial resistance, and results in the emergence of the positive slope at lower frequencies. Imperfect earthing of the outer semicon layer is another important factor to increase the dielectric loss due to semicon layers.

## 8 Conclusions and Further Work

This research study focused on the dielectric response of XLPE model power cables that have combinations of homo-polymer insulation, co-polymer insulation, furnace carbon black semicon layers and acetylene carbon black semicon layers. Three dielectric spectroscopy techniques for the low loss XLPE cables were studied and jointly used to measure the frequency range from  $10^{-4}$ Hz to  $10^4$ Hz. Based on the measured dielectric spectra, three loss origins of the XLPE cables have been identified with different loss mechanisms. Degassing effects and thermal ageing effects have also been studied. The conductivity of different types of the model cables under different temperatures, before and after degassing and ageing and under different applied electric field has been measured. Based on the measurement results, thermal-electric behaviour has been simulated and the maximum voltages for thermal breakdown have been investigated theoretically for the XLPE cables. Finally, a loss mechanism model was proposed to explain the total dielectric loss of polymer power cables.

The primary conclusions of this work are:

1. The frequency response analyzer (FRA) technique can be used to measure the conduction loss of the XLPE cables at lower frequencies from  $10^{-4}$ Hz to 1Hz. The FRA has a  $\tan\delta$  noise floor of  $10^{-3}$  in this frequency range for imaginary permittivity measurement. DC conductivity measured in this way agrees with that of charging current measurement using the “noise-free” HV battery supply. This comparison between frequency domain and time domain has not been seen previously in the literature for XLPE.

2. A transformer ratio bridge system was developed. It can be used to detect higher frequency dielectric response of the XLPE cables in the frequency range from 1kHz to 10kHz. The dielectric loss due to semicon layer resistance of the power cables can be measured with this technique. It was found to be of importance to ensure that the whole surface of the outer semicon is in good contact with the metal electrode. Anomalous measurement results due to the poor contact have been reported in the literature before [71].
3. Time domain dielectric spectroscopy technique – charging/discharging current system – was developed to measure the dielectric loss tangent down to  $10^{-6}$  in the frequency range of  $10^{-1}\text{Hz}$  to  $10^2\text{Hz}$  that is transferred by Fourier transform from time domain. A high voltage battery supply with very stable output was made to increase sensitivity. The speed of switch, bandwidth of the current-voltage converter and protective resistor has been found to be critical for the measurement accuracy. This novel system has allowed more sensitive measurement of very low loss insulation materials.
4. Degassing effects have been investigated on the XLPE cables by conductivity measurement using time domain charging current system designed in this work. The conductivity can be greatly reduced by 24% ~ 63% after degassing process (chapter 4). Further reduction of conductivity may be realized using vacuum degassing.
5. Thermal ageing can increase the dielectric loss and conductivity. Oxidation may create extra more polar groups in the insulation. The increase of conductivity may be due to more amorphous regions after ageing process.

6. Computer simulation of the thermal-electric behaviour has shown that the thermal breakdown voltage decreases at higher temperatures. The temperature distribution has big change near the thermal breakdown voltage. The position of maximum field changes from inner boundary to outer boundary under higher applied voltages. The breakdown strength of the model power cables due to thermal instability is estimated to be  $\sim 100\text{kV/mm}$ . In practice, a cable would breakdown due to other mechanisms before reaching this calculated field.
7. Three dielectric loss origins of the XLPE cables have been identified to dominate in different frequency ranges:
  - a. The bulk DC conductivity loss is dominant at lower frequencies with slope of -1 in dielectric spectrum. Conduction through amorphous regions due to electrons moving between traps is found to be the most likely charge transport mechanism. Ionic impurities may also contribute to the DC conductivity, suggested by the degassing study (chapter 4).
  - b. The radial and/or axial resistance of semicon layers increases the dielectric loss at higher frequencies with slope of 1 in dielectric spectrum. An equivalent circuit has been used to reveal the loss origin due to semicon layers as a resistance in series with the cable insulation layer.
  - c. Polarization loss is observed in the mid-frequency range with a reasonably “flat” dielectric spectrum.  $\beta$  polarization in the amorphous regions of the semi-crystalline XLPE may be responsible for this intrinsic loss mechanism. This is the primary loss mechanism at 50Hz.

8. Comparing different types of the model power cables in this study, homo-polymer insulation A has the lowest dielectric loss and DC conductivity, super-smooth semicon B has lower resistivity and smaller increase after thermal ageing. The homo-polymer cable BAB, therefore, has the best thermal-electrical properties for real application.
9. The model power cable specimens are very useful for measuring the properties of cable materials and for studying the behaviours of full-size cables.

Further work may include:

1. High field ( $>60\text{kV/mm}$ ) cable measurement for new generation HVDC application may be realized by using the charging/discharging measurement system. A noise-free high voltage power supply may be designed to measure the conductivity and loss spectrum of full-size cables. The electric field dependence of polymer power cable insulation system and the loss mechanisms can be then further understood and make the research closer to high voltage application.
2. It is worthwhile to investigate the difficulty of high voltage FRA experiment system (explained in chapter 3), especially for high-voltage-high-frequency-low-loss dielectric spectroscopy.
3. The difficulty to measure the frequency range from 100Hz to 1000Hz using transformer ratio bridge should be studied. Either improving the measurement sensitivity of the current experimental system or extending the TDDS frequency range to cover the spectrum gap is suggested.

4. The combined use of different spectroscopy techniques in this work can extend the measurement bandwidth, and may be applied to developing new materials e.g. nano-filled composites.

## 9 References

- [1] R. M. Black, *The History of Electric Wires and Cables*, Peter Peregrinus, London 1983
- [2] Walter S. Zaengl, "Applications of Dielectric Spectroscopy in Time and Frequency Domain for HV Power Equipment", IEEE Electrical Insulation Magazine, Vol. 19, No. 6, pp. 9-22, 2003
- [3] Vahdat Vahedy, "Polymer Insulated High Voltage Cables", IEEE Electrical Insulation Magazine, Vol. 22, No. 3, pp. 13-18, 2006
- [4] T. Kubota, Y. Takahashi, S. Sakuma, M. Watanabe, M. Kanaoka and H. Yamanouchi, "Development of 500 kV XLPE Cables and Accessories for Long Distance Underground Transmission Line - Part I: Insulation Design of Cables –", IEEE Trans. on Power Delivery, Vol. 9, No. 4, pp. 1741-1749, October, 1994
- [5] T. Kubota, Y. Takahashi, T. Hasegawa, H. Noda, M. Yamaguchi and M. Tan, "Development of 500 kV XLPE Cables and Accessories for Long Distance Underground Transmission Line - Part 11: Jointing Techniques –", IEEE Trans. on Power Delivery, Vol. 9, No. 4, pp.1750-1756, October, 1994.
- [6] J. Daintith, *Biographical Encyclopedia of Scientists*, page 943, CRC Press, 1994.
- [7] H Fröhlich, *Theory of Dielectrics*, Oxford University Press, London, 1958
- [8] A. K. Jonscher, *Dielectric Relaxation in Solids*, Chelsea Dielectrics Press, London 1983
- [9] A. K. Jonscher, *Universal Relaxation Law*, Chelsea Dielectrics Press, London, 1996
- [10] V. Daniel, *Dielectric Relaxation*, Academic Press, London, 1967
- [11] Nora E. Hill, Worth E. Vaughan, A. H. Price, and Mansel Davies, *Dielectric Properties and Molecular Behaviour*, Van Nostrand Reinhold Company, London, 1969
- [12] L. A. Dissado and J. C. Fothergill, *Electrical Degradation and Breakdown in Polymers*, Peter Peregrinus, Londond, 1992
- [13] John Densley, "Ageing mechanisms and diagnostics for power cables-an overview", IEEE Electrical Insulation Magazine, Vol. 17, No. 1, pp. 14-22, 2001

- [14] J. C. Fothergill, G. C. Montanari, G. C. Stevens et al., "Electrical, Microstructural, Physical and Chemical Characterization of HV XLPE Cable Peelings for an Electrical Aging Diagnostic Data Base", IEEE Transactions on Dielectrics and Electrical Insulation, Vol. 10, No. 3, pp. 514-527, 2003
- [15] Fabiani, D. Montanari, G.C. Laurent, C. et al., "Polymeric HVDC Cable Design and Space Charge Accumulation. Part 1: Insulation/Semicon Interface", IEEE Electrical Insulation Magazine, Vol. 23, No. 6, pp. 11-19, 2007
- [16] Delpino, S. Fabiani, D. Montanari, G.C. et al., "Polymeric HVDC Cable Design and Space Charge Accumulation. Part 2: Insulation Interfacec", IEEE Electrical Insulation Magazine, Vol. 24, No. 1, pp. 14-24, 2008
- [17] Fabiani, D. Montanari, G.C. Laurent, C. et al., "Polymeric HVDC Cable Design and Space Charge Accumulation. Part 3: Effect of Temperature Gradient", IEEE Electrical Insulation Magazine, Vol. 24, No. 2, pp. 5-14, 2008
- [18] F. N. Lim, R. J. Fleming, and R. D. Naybour, "Space charge accumulation in power cable XLPE insulation", IEEE Transactions on Dielectrics and Electrical Insulation, Vol. 6, No. 3, pp. 273-281, 1999
- [19] Hozumi, N. Takeda, T. Suzuki, H. Okamoto, T., "Space charge behavior in XLPE cable insulation under 0.2-1.2 MV/cmdc fields", IEEE Transactions on Dielectrics and Electrical Insulation, Vol. 5, No. 1, pp. 82-90, 1998
- [20] Fu, M., Chen, G. and Fothergill, J. C., "“Mirror Image Effect” Space Charge Distribution in XLPE Power Cable under Opposite Stressing Voltage Polarity", 15th International Symposium on High Voltage Engineering (ISH), Beijing, China, August 25-29, 2005
- [21] Choo, W. Chen, G., "Electric field determination in DC polymeric power cable in the presence of space charge and temperature gradient under dc conditions", International Conference on Condition Monitoring and Diagnosis, Beijing, China, April 21-24, 2008
- [22] Dissado, L.A. Zadeh, S. Fothergill, J.C. See, A., "Temperature dependence of charge packet velocity in XLPE cable peelings", Annual Report - Conference on Electrical Insulation and Dielectric Phenomena, CEIDP, pp. 425-428, 2007
- [23] W. R. Kegerise, "Feature article - Manufacturing and Performance Criteria for Medium Voltage Power Cable Semiconducting Shields", IEEE Electrical Insulation Magazine, Vol. 24, No. 2, pp. 15-21, 2008
- [24] T.J. Person, P.J. Caronia, S.J. Han, "The Influence of the Semicon on Cable Dielectric Losses", The Dow Chemical Company, 2006
- [25] S. S. Bamji, A. T. Bulinski, R. J. Densley et al., "Degradation Mechanism at. XLPE/Semicon. Interface Subjected to. High Electrical Stress", IEEE Transactions on Dielectrics and Electrical Insulation, Vol. 26, No. 2, pp. 278-284, 1991

- [26] Tanaka, T. Okamoto, T. Hozumi, N. Suzuki, K., "Interfacial improvement of XLPE cable insulation at reduced thickness", IEEE Transactions on Dielectrics and Electrical Insulation, Vol. 3, No. 3, pp. 345-350, 1996
- [27] Andrews, T. Hampton, R.N. Smedberg, A. et al., "The role of degassing in XLPE power cable manufacture", IEEE Electrical Insulation Magazine, Vol. 22, No. 6, pp. 5-16, 2006
- [28] Tamon Ozaki, Noriyuki Ito, Jiro Kawai, and Shuhei Nakamura, "Relative permittivity and conductivity of water treed region in XLPE estimated by an equivalent circuit", Electrical Engineering in Japan, Vol. 148, No. 3, pp. 7-14, 2004
- [29] BOUBAKEUR A.; MECHERI Y.; BOUMERZOUG M., "Influence of continuous thermal ageing on the properties of XLPE used in medium voltage cables", IEE Conference on High Voltage Engineering Symposium, 4.236.P2, 1999
- [30] S. S. Bamji, A. T. Bulinski, "Thermoluminescence in XLPE cable insulation", IEEE Transactions on Dielectrics and Electrical Insulation, Vol. 3, No. 2, pp. 316-319, 1996
- [31] Xiaoguang Qi and Steven Boggs, "Thermal and Mechanical Properties of EPR and XLPE Cable Compounds", IEEE Electrical Insulation Magazine, Vol. 22, No. 3, pp. 19-24, 2006
- [32] Ewen Kellar, Graham Williams, Valeri Krongauz et al., "Dielectric relaxation spectroscopy and molecular dynamics of a liquid-crystalline polyacrylate containing spiropyran groups", Journal of Materials Chemistry, Vol. 1, No. 3, pp. 331-337, 1991
- [33] M. Ehsani, G. R. Bakhshandeh, J. Morshedian et al., "The dielectric behavior of outdoor high-voltage polymeric insulation due to environmental aging", European Transactions on Electrical Power, Vol. 17, No. 1, pp. 47-59, 2006
- [34] M. Farahani, H. Borsi and E. Gockenbach, "Dielectric response studies on insulating system of high voltage rotating machines", IEEE Transactions on Dielectrics and Electrical Insulation, Vol. 13, No. 1; pp. 383-393, 2006
- [35] C.D. Paraskevas, P. Vassiliou and C.T. Dervos, "Temperature dependent dielectric spectroscopy in frequency domain of high-voltage transformer oils compared to physicochemical results", IEEE Transactions on Dielectrics and Electrical Insulation, Vol. 13, No. 3; pp. 539-546, 2006
- [36] CIGRÉ Task Force, "Dielectric response methods for diagnostics of power transformers", IEEE Electrical Insulation Magazine, Vol. 19, No. 3, pp. 12-18, 2003
- [37] G C Montanari, G Mazzanti, F Palmieri et al., "Space-charge trapping and conduction in LDPE, HDPE and XLPE", Journal of Physics D: Applied Physics, Vol. 34, pp. 2902–2911, 2001

- [38] Montanari, G.C., "The electrical degradation threshold of polyethylene investigated by space charge and conduction current measurements", IEEE Transactions on Dielectrics and Electrical Insulation, Vol. 7, No. 3, pp. 309-315, 2000
- [39] Murakami, Y. Nagao, M. Sekiguchi, Y. et al., "Assessment of diffusion coefficient of acetophenone in insulating polymer by using conduction current measurement", Annual Report Conference on Electrical Insulation and Dielectric Phenomena, pp. 776-779, 2007
- [40] Griseri, V. Dissado, L.A. Fothergill, J.C et al., "Electroluminescence excitation mechanisms in an epoxy resin under divergent and uniform field", IEEE transactions on dielectrics and electrical insulation, Vol. 9, No. 1, pp. 150-160, 2002
- [41] Riaz Shaikh, Saeed Ul Haq, Gorur Govinda Raju, "Electrical conduction processes in polyimide-teflon FEP films", IEEE Transactions on Dielectrics and Electrical Insulation, Vol. 15, No. 3, pp. 671-677, 2008
- [42] E. R. Neagu, R. M. Neagu, "Analysis of charging and discharging currents in polyethyleneterephthalate", Physica status solidi. A. Applied research, Vol. 144, No. 2, pp. 429-440, 1994
- [43] T. Wiktorczyk, K. Nitsch, "Dielectric properties of holmium oxide films", IEEE Transactions on Dielectrics and Electrical Insulation, Vol. 8 No. 3, pp. 447-453, 2001
- [44] W. S. Zaengl, "Dielectric spectroscopy in time and frequency domain for HV power equipment. I. Theoretical considerations", IEEE Electrical Insulation Magazine, Vol. 19, No. 5, pp. 5–19, 2003
- [45] D Hayward, M Gawayne, B Mahboubian-Jones et al., "Low-frequency dielectric measurements ( $10^4$  to  $6 \times 10^4$  Hz): a new computer-controlled method", Journal of Physics E: Scientific Instruments, Vol. 17, No. 8, pp. 683–690, 1984
- [46] Tetsuroh Tokoro, Masayuki Nagao, Masamitsu Kosaki, "Development of new method for measuring AC dissipation current in dielectric materials", Electrical Engineering in Japan, Vol. 111, No. 3, pp. 1–9, 2007
- [47] Kwaaitaal, T. van den Eijnden, W.M.M.M., "A ratio transformer bridge for the measurement of low-loss tangents", 7th IEEE Instrumentation and Measurement Technology Conference, pp. 20–26, 1990
- [48] *1255A HF Frequency Response Analyzer Specification*, Solartron Analytical, 2003
- [49] P. Tharning, P. Werelius, B. Holmgren, and U. Gafvert, "High voltage dielectric response analyser for cable diagnostics", IEEE Conference on Electrical Insulation and Dielectric Phenomena, pp. 745–750, 1993

- [50] P. Werelius, P. Thärning, B. Holmgren, and U. Gäfvert, “High Voltage Dielectric Response as a Tool for Diagnostics of XLPE Cables”, Nordic Insulation Symposium, pp. 217–225, 1994
- [51] U. Gäfvert, R. P. Eriksson, P. Werelius, B. Holmgren, and L. Olsson, “XLPE cable diagnosis by measurement of dielectric losses as function of frequency and voltage”, International conference and exhibition on electricity distribution (CIRED), pp. 2.06.1 – 3.06.6, 1995
- [52] B. Holmgren, P. Werelius, R. Eriksson, and U. Gafvert, “Dielectric measurements for diagnosis of XPLE cable insulation”, International conference and exhibition on electricity distribution (CIRED), pp. 3.11.1–3.11.4, 1997
- [53] P. Werelius, B. Holmgren, and U. Gafvert, “Diagnosis of medium voltage XLPE cables by high voltage dielectricspectroscopy”, IEEE 6th International Conference on Conduction and Breakdown in Solid Dielectrics, pp. 79–84, 1998
- [54] P. Werelius, P. Tharning, R. Eriksson, B. Holmgren, and U. Gafvert, “Dielectric spectroscopy for diagnosis of water tree deterioration in XLPE cables”, IEEE Transactions on Dielectrics and Electrical Insulation, Vol. 8, No. 1, pp. 27–42, 2001
- [55] Roberts Neimanis and Sarah Acker, “General condition assessment of XLPE and PILC cables”, GE Energy, pp. 1–5, 2005
- [56] Sverre Hvidsten, Björn Holmgren, Lars Adeen et al., “Condition Assessment of 12- and 24-kV XLPE Cables Installed During the 80s”, IEEE Electrical Insulation Magazine, Vol. 21, No. 6, pp. 17–23, 2005
- [57] KIM Chonung; ZHIJIAN JIN; PINGKAI JIANG et al., “Investigation of dielectric behavior of thermally aged XLPE cable in the high-frequency range, Polymer Testing”, Vol. 25, No. 4, pp. 553–561, 2006
- [58] Jean Pierre Crine, “Influence of high electrical fields on ageing and polarisation properties of polyethylene”, Polymer International, Vol. 51, No. 11, pp. 1159–1163, 2002
- [59] Anders Helgeson and Uno Gafvert, “Dielectric response measurements in time and frequency domain on high voltage insulation with different response”, Proceedings of 1998 International Symposium on Electrical Insulating Materials, pp. 393–398, 1998
- [60] H.M.Li, R.A.Fouracre, B.H.Crichton, “Transient Current Measurement for the Detection of Water Tree Growth in Polymeric Power Cables”, IEEE Transactions on Dielectrics and Electrical Insulation, Vol. 2 No. 5, pp. 866–874, 1995
- [61] D. Malec, R. Essolbi, Hoang The-Giam, “Space charge and anomalous discharge currents in crosslinked polyethylene”, IEEE Transactions on Dielectrics and Electrical Insulation, Vol. 3 No. 1, pp. 64–69, 1996

- [62] M. Abou Dakka, A. Bulinski, and S. Bamiji, “On-site Diagnostic Tests on Polymer Insulated Cables Using Depolarization Current Measurements”, International Conference on Solid Dielectrics , ICSD, pp. 725–728, 2007
- [63] M. Abou-Dakka, A. Bulinski, S.S. Bamji, “Depolarization Current Measurements on Field-Aged XLPE Cable Insulation”, Annual Report Conference on Electrical Insulation and Dielectric Phenomena, CEIDP, pp. 21–24, 2008
- [64] B. Oyegoke, D. Birtwhistle and J. Lyall, “Condition assessment of XLPE cable insulation using short-time polarisation and depolarisation current measurements”, IET Science, Measurement & Technology, Vol. 2 No. 1, pp. 25–31, 2008
- [65] Xu Shuzhen, R. Middleton, F. Fetherston, and D. Pantalone, “A comparison of Return voltage measurement and frequency domain spectroscopy test on high voltage insulation”, 7th International Conference on Properties and Applications of Dielectric Materials, 1, pp. 351–355, 2003
- [66] E. David, A. Sami, R. Soltani et al., “Low-Frequency Dielectric Response of Epoxy-Based Polymer Composites”, Annual Report Conference on Electrical Insulation and Dielectric Phenomena, CEIDP, pp. 505–508, 2008
- [67] A. Setayeshmehr, I. Fofana, C. Eichler, “Dielectric Spectroscopic Measurements on Transformer Oil-paper Insulation under Controlled Laboratory Conditions”, IEEE Transactions on Dielectrics and Electrical Insulation, Vol. 15, No. 4, pp. 1100–1111, 2008
- [68] O. Hassan, A. A. Shyegani, H. Borsi, E. Gockenbach, E. M. Abu-Elzahab, and M. I. Gilany, “Detection of oil-pressboard insulation aging with dielectric spectroscopy in time and frequency domain measurements”, IEEE International Conference on Solid Dielectrics (ICSD), 2, pp. 665–668, 2004
- [69] Tapan K. Saha, R. Middleton, and A. Thomas, “Correlation between Time and Frequency Domain Polarisation Measurements for Transformer Moisture Assessment”, Australasian Universities Power Engineering Conference, 2004
- [70] M. Farahani, H. Borsi, and E. Gockenbach, “Dielectric spectroscopy in time and frequency domain on insulation system of high voltage rotating machines”, IEEE International Conference on Solid Dielectrics (ICSD), 1, pp. 60–63, 2004
- [71] P. C. N. Scarpa, A. Svatík, D. K. Das-Gupta, “Dielectric spectroscopy of polyethylene in the frequency range of  $10^{-5}$  Hz to  $10^6$  Hz”, Polymer Engineering and Science, Vol. 26, No. 8, pp. 1072–1080, 1996
- [72] J. M. Fourmigue, J. L. Parpal, and J. N. Seguin, “Dielectric Spectroscopy of XLPE Cable Insulation: Comparison between Time Domain and Frequency Domain Methods”, Proceedings of the 4th International Conference on Conduction and Breakdown in Solid Dielectrics, pp. 235–240, 1992
- [73] M.Kuschel and W.Kalkner, “Dielectric response measurements in time and frequency domain of different XLPE homo- and copolymer insulated medium

voltage cables”, IEE Proceedings - Science, Measurement and Technology, Vol. 146, No. 5, pp. 243–248, 1999

- [74] Bolarin Oyegoke, Petri Hyvonen, Martti Aro, “Application of dielectric response measurement on power cable systems”, IEEE Transactions on Dielectrics and Electrical Insulation, Vol. 10, No. 5, pp. 862–873, 2003
- [75] Tony Blythe, David Bloor, *Electrical Properties of Polymers*, Cambridge University Press, 2005
- [76] A. von Hippel, Arthur R., *Dielectrics and Waves*, Artech House, 1994
- [77] L. A. Dissado, R. M. Hill, “Non-Exponential decay in Dielectrics and Dynamics of Correlated Systems”, Nature, 279, pp. 685–689, 1979
- [78] L. A. Dissado, R. M. Hill, “Anomalous Low-frequency Dispersion”, J. chemical Society, Faraday Transactions. 80(2), pp. 291–319, 1984
- [79] A. K. Jonscher, R. M. Hill, *Physics of Thin Films*, 8, pp. 169–249, 1975
- [80] Francesco Pizzitutti, Fabio Bruni, “Electrode and interfacial polarization in broadband dielectric spectroscopy measurements”, *Review of Science Instruments*, Vol 72, No. 5, pp. 2502–2504, 2001
- [81] Debye P., *Polar molecules*, The Chemical Catalog Co. Dover Publications, London, 1929
- [82] Debye P., *Polar molecules*, The Chemical Catalog Co. Dover Publications, London, 1945
- [83] Havriliak, Negami S., “A complex plane analysis of dispersion in some polymer systems”, *J.Polym. Sci. C* 14, 99, 1966
- [84] Havriliak, S. and Negami, S., “A complex plane representation of dielectric and mechanical relaxation processes in some polymers”, *Polymer*, 8 (4), pp. 161, 1967
- [85] Cole K. S., Cole R. H., ‘Dispersion and adsorption in dielectrics’, *J. Chem. Rev.* **9** 341–52, 1941
- [86] Davidson D. W., Cole R. H., ‘Dielectric relaxation in Glycerol, Propylene Glycol, and n-Propanol’, *J. Chem. Phys.* **19**, 1484–1490, 1951.
- [87] Egon Peschke, Rainer von Olshausen, *Cable Systems for High and Extra-High Voltage: Development, Manufacture, Testing, Installation and Operation of Cables and their Accessories*, Publicis MCD Verlag, 1999
- [88] F.M.. Precopio and A.R. Gilbert, US. Patent. 3079370, 1955

- [89] Peter Werelius, *Development and Application of High Voltage Dielectric Spectroscopy for Diagnosis of Medium Voltage XLPE Cables*. PhD thesis, Stockholm: KTH, Electrical Engineering, 2001
- [90] A. Smedberg, B. Gustafsson, and T. Hjertberg, “What is crosslinked polyethylene?”, IEEE International Conference on Solid Dielectrics, ICSD 2004
- [91] Henryk Herman, Janet Thomas and Gary Stevens, “Exploring relationships between chemical species and electrical properties in cross-linked polyethylene”, IEEE Annual Report Conference on Electrical Insulation and Dielectric Phenomena, CEIDP, pp 569-572, 2005
- [92] Y.Miyashita, Y.Makishi and H.Kato, “New approach to elucidate the properties of carbon black-filled semiconducting materials for high voltage power cables”, IEEE Annual Report Conference on Electrical Insulation and Dielectric Phenomena, CEIDP, pp 678-687, 1993
- [93] E. J Kim, D. H. Park, H. S. Kim, and G.J. Lee, “An investigation of the influence of semiconductive electrodematerials in the ac breakdown and the charge accumulation in XLPE”, IEEE Annual Report Conference on Electrical Insulation and Dielectric Phenomena, CEIDP, pp 546-549, 1998
- [94] J V Champion and S J Dodd, “The effect of voltage and material age on the electrical tree growth and breakdown characteristics of epoxy resins”, Journal of Physics D: Applied Physics, pp 398-407, 1995
- [95] “Evaluation and Qualification of Electrical Insulation Systems”, IEC Standard 60505, 1999
- [96] J. G. Head, P. S. Gale, D. J. Skipper, and A. W. Stannett, “Ageing of oil-filled cable insulation”, CIGRE, 1982
- [97] Bernasconi J., “Conduction in anisotropic disorder systems: Effective-medium theory”, Physical Review B: Vol 9, No. 10, pp 4575-4579, 1974
- [98] T. J. Lewis, “Polyethylene under Electrical Stress”, IEEE Transactions on Dielectrics and Electrical Insulation vol. 9 No. 5, pp 717-729, 2002
- [99] David Braun, “Electronic Injection and Conduction Processes for Polymer Devices”, Journal of Polymer Science: Part B: Polymer Physics, Vol. 41, pp. 2622–2629, 2003
- [100] P. N. Murgatroyd, “Theory of space-charge-limited current enhanced by Frenkel effect”, J. PHYS. D: APPL. PHYS, VOL. 3, pp 151-156, 1970

- [101] J. Frenkel, "On pre-breakdown phenomena in insulators and electronic semiconductors", Phys. Rev., vol. 54, pp. 647-648, 1938
- [102] Sze, S. M. *Physics of Semiconductor Devices* (Second Edition); Wiley: New York, pp 254–264, 402–404, 1981.
- [103] Maruska H. P., Stevenson D. A., "Mechanism of Light Production in Metal-Insulator-Semiconductor Diodes; GaN:Mg Violet Light-Emitting Diodes", Solid-State Electronics, Vol. 17, pp.1171–1179, 1974
- [104] Lewis T. J., "Electrical Effect at Interfaces and Surfaces", IEEE Transactions on Electrical Insulation., EI-21(3), pp.289–295. 1986
- [105] Schottky, W. (1923). "Über kalte und warme Elektronenentladungen". Zeitschrift fur Physik a Hadrons and Nuclei **14** (63): 63–106
- [106] Fowler, R.H.; Dr. L. Nordheim. "Electron Emission in Intense Electric Fields", Proceedings of the Royal Society of London **119** (781): 173–181, 1928
- [107] I. D. Parker, "Carrier tunneling and device characteristics in polymer light-emitting diodes", J. Appl. Phys. 75, 1656, 1994
- [108] Razavy, Mohsen, *Quantum Theory of tunnelling*. World Scientific. ISBN 981-238-019-1, 2003
- [109] Bjorn Sanden, *XLPE cable insulation subjected to HVDC stress: space charge, conduction and breakdown strength*, PhD thesis, Norwegian Univ. of Sci, 1996
- [110] A. A. Shayegani, H. Borsi, E. Gockenbach and H. Mohseni, "Transformation of Time Domain Spectroscopy Data to Frequency Domain Data for Impregnated Pressboard", Annual Report Conference on Electrical Insulation and Dielectric Phenomena, CEIDP, pp. 162-165, 2004
- [111] A. K. Jonscher. "The "Universal Dielectric Response: Part I", IEEE Electrical Insulation Magazine, Vol. 6, No. 2, pp. 19-24, 1990
- [112] Sławomir Tumański, *Principles of electrical measurement*, pp99~101, CRC Press, 2006
- [113] James P. Runt, John J. Fitzgerald, *Dielectric Spectroscopy of Polymeric Materials: Fundamentals and Applications*, American Chemical Society, 1999

- [114] Ranko Richert, “A simple current-to-voltage interface for dielectric relaxation measurements in the range  $10^{-3}$  to  $10^7$  Hz”, Review of Scientific Instruments, Vol. 67, No. 9, pp. 3217-3221, 1996
- [115] Tong Liu, John Fothergill, Steve Dodd, Ulf Nilsson, “Dielectric Spectroscopy Measurement on very low loss Cross-linked Polyethylene Power Cables”, Journal of Physics: Conference Series, pp. 1-6, 2009
- [116] Ulf Nilsson, “The use of model cables for evaluation of dc electrical properties of polymeric cable materials”, 7th JICABLE Conference, 2007
- [117] Technical documents on XLPE model cables from Borealis AB, Sweden, 2008
- [118] E. Wen Shu and S. Boggs, “Dispersion and PD Detection in Shielded Power Cable, IEEE Electrical Insulation Magazine”, Vol. 24, No. 1, pp. 25-29, 2008
- [119] K. Steinbrich, “Influence of semiconducting layers on the attenuation behaviour of single-core power cables”, IEE Proc.-Gener. Transm. Distrib., Vol. 152, No. 2, pp. 271-276, 2005
- [120] T.J.Person, P.J.Caronia, S.J.Han, “The Influence of the Semicon on Cable Dielectric Losses”, The Dow Chemical Company, 2006
- [121] *Solartron 1296 Dielectric Interface Operating Manual*. Solartron Group Ltd. April 1998
- [122] Graham Williams and Dale K. Thomas, “Phenomenological and Molecular Theories of Dielectric and Electrical Relaxation of Materials”, Novocontrol Application Note, pp. 1-29, 1998
- [123] N. Hirano, T. Tsujimura, N. Shimizu, and K. Horii, “Diagnosis of the aged XLPE cable using frequency and temperature characteristics of tan delta”, Electrical Insulating Materials, pp. 179–182, 1988
- [124] Walter G. Jung, *Basic OpAmp Applications*, ISBN 0-672-20969-1, Analog Devices Inc., US, 2002

- [125] Robert T. Paynter, *Introductory Electronic Devices and Circuits (Sixth Edition)*, Pearson Education Inc., 2008
- [126] *User Manual for Universal Bridge B221*, Wayne Kerr Laboratories Limited, England, 2000
- [127] *Model 6485 Picoammeter Instruction Manual*, Keithley Instruments Inc., November 2001
- [128] Peter A. Blume: *The LabVIEW Style Book*, 2007, Prentice Hall, ISBN 0-13-145835-3
- [129] Jeffrey Travis, Jim Kring: *LabVIEW for Everyone: Graphical Programming Made Easy and Fun, 3rd Edition*, 2006, Prentice Hall. ISBN 0-13-185672-3
- [130] *Low Level Measurements Handbook*, 6<sup>th</sup> edition, Keithley Instruments Inc., 2004
- [131] Tong Liu, John Fothergill, Steve Dodd and Ulf Nilsson, “Dielectric spectroscopy of XLPE cables using discharging current measurement”, International Electrical Insulation Conference (INSUCON), 2009
- [132] Reference: *polymer handbook* (second edition), J. Brandrup, E.H. Immergut, John Wiley & Sons. Inc., 1975
- [133] V. Svorcík, O. Ekrt, V. Rybka, et al., “Permittivity of polyethylene and polyethyleneterephthalate”, Journal of Materials Science Letters, vol. 19, pp. 1843 – 1845, 2000
- [134] Sears, F. W., Zemansky, M. W., Young, H. D., *University Physics* (6th Ed.), Addison-Wesley, 1982
- [135] J. Curie, “The so-called Curie-Schweidler law”, Ann. Chim. Phys. 17, 385, 1889
- [136] von Schweidler E, “Studien ber anomalien im verhalten der dielektrika (Studies on the anomalous behaviour of dielectrics)” *Ann. Phys., Lpz.* 24 711–70 Series 4 (in German), 1907

- [137] T C Guo and W W Guo, “A transient-state theory of dielectric relaxation and the Curie-von Schweidler law”, Journal of Physics C: Solid State Physics, Vol. 16, Issue 10, pp. 1955-1960, 1983
- [138] M. Schumacher and R. Waser, “Curie - Von Schweidler behaviour observed in ferroelectric thin films and comparison to superparaelectric thin film materials”, Integrated Ferroelectrics, Volume 22, Issue 1-4, pp. 109 - 121, 1998
- [139] J. Malecki and B. Hilczer, “Dielectric behaviour of polymers and composites”, Key Engineering Materials, vol. 92-93, pp. 181-215, 1994
- [140] *MATLAB Function Reference on Fourier Transform*, The MathWorks Inc., 2007
- [141] Antonio Moton and Gian Carlo Montanari, “Electrical properties of EPR cable models aged under thermal and electrothermal stresses”, IEEE International Conference on Conduction and Breakdown in Solid Dielectrics, pp. 198-201, 1998
- [142] Shoshi Katakai and Kichinosuke Yahagi, “Effect of Thermal Aging on Breakdown Strength of Polyethylene”, Jpn. J. Appl. Phys. Vol. 24 pp. 441-445, 1985
- [143] John Fothergill, Alex See, N. Ajour and Len Dissado, ““Sub-Hertz” Dielectric Spectroscopy”, IEEE International Symposium on Electrical Insulating Materials (ISEIM), 2005
- [144] R. Bodega, *Space charge accumulation in polymeric high voltage DC cable systems*, PhD thesis, Delft University of Technology, 2006
- [145] Faremo, H., Ildstad, E., “Water treeing and dielectric loss of WTR-XLPE cable insulation”, Science, Measurement and Technology, IEE Proceedings A, Vol. 140, Issue: 5, pp. 393-396, 1993
- [146] Hvidsten, S., Ildstad, E., Holmgren, B. and Werelius, P., “Correlation between AC breakdown strength and low frequency dielectric loss of water tree aged XLPE cables”, IEEE Transactions on Power Delivery, Vol. 13, No. 1, pp. 40-45, 1998

- [147] Tan  $\delta$  (delta) cable testing – overview and answers to frequently asked questions, High Voltage Inc.
- [148] S. Whitehead, *Dielectric Breakdown of Solids*, Oxford University Press, London, 1951.
- [149] M. M. Fallou, “Perforation dielectrique par instabilite thermique des cables a courant continu”, Revue Generale de LElectricite, pp. 693-695, 1959
- [150] C. K. Eoll, “Theory of Stress Distribution in Insulation of High Voltage DC Cables: Part I”, IEEE Trans. Electr. Insul., Vol. 10, pp. 27-35, 1975
- [151] U. Riechert, R. Vogelsang, and J. Kindersberger, “Temperature Effect on DC Breakdown of Polyethelene Cables”, 12th Intern. Sympos. High Voltage Engineering, ISH, pp. 537-540, 2001
- [152] J. J. O’Dwyer, *The Theory of Dielectric Breakdown of Solids*, Oxford University Press, London, UK, 1964
- [153] Ch. Chakradhar Reddy and T. S. Ramu, “Estimation of Thermal Breakdown Voltage of HVDC Cables - A Theoretical Framework”, IEEE Transactions on Dielectrics and Electrical Insulation Vol. 14, No. 2; pp. 400-408, April 2007
- [154] J. Hjerrild, S. Boggs, J. T. Hollboll and M. Henricksen, “DC-field in solid dielectric cables under transient thermal conditions”, IEEE, Intern. Conf. Solid Dielectrics, pp. 58-61, 2001
- [155] X.Qi, Z. Zheng and S. Boggs, “Engineering with Nonlinear Dielectrics”, IEEE Electr. Insul. Mag., Vol. 20, No.6, pp. 27-34, 2004
- [156] Yugnus A Cengel, *Heat transfer-A Practical Approach*, 2nd ed., McGraw Hill Professional, 2003
- [157] J. M. Oudin and H. Thevenon, “DC cables – determination of the gradient actually applied to the insulant and its experimental correlation with breakdown gradient”, CIGRE, paper 208, 1966

- [158] F. H. Buller, "Calculation of Electrical stresses in DC Cable insulation", IEEE, Power App. Syst., Vol. 86, pp. 1169-1178, 1967
- [159] Ch. Chakradhar Reddy and T. S. Ramu, "On the Computation of Electric Field and Temperature Distribution in HVDC Cable Insulation", IEEE Transactions on Dielectrics and Electrical Insulation Vol. 13, No. 6; pp. 1236-1244, December 2006
- [160] Y. Pinchover and J. Rubinstein, *An Introduction to Partial Differential Equations*, Cambridge University Press, Cambridge, 2005
- [161] Ch. Chakradhar Reddy and T. S. Ramu, "Polymer Nanocomposites as Insulation for HV DC Cables - Investigations on the Thermal Breakdown", IEEE Transactions on Dielectrics and Electrical Insulation, Vol. 15, No. 1; pp. 221-227, 2008
- [162] M. J. P. Jeroense and P. H. F. Morshuis, "Electric fields in HVDC paper-insulated cables", IEEE Transactions on Dielectrics and Electrical Insulation Vol. 5 No. 2, pp. 225-236, April 1998
- [163] M.C. Lanc, M. Fu, E. Neagu, L.A. Dissado, "Space charge analysis of electrothermally aged XLPE cable insulation", Journal of Non-Crystalline Solids, pp. 4462–4466, 2007
- [164] M. Tahara, Y. Hayase, M. Honjoh, K. Nagasawa, Y. Tanaka, T. Takada and M. Yoshida, "Charge accumulation properties in saturated and aromatic hydrocarbons by electron beam irradiation", Annual Report Conference on Electrical Insulation Dielectric Phenomena, pp. 165-168, 2008
- [165] M. Ieda, "Electrical Conduction and Carrier Traps in Polymeric Materials", IEEE Transaction on Electrical Insulation, Vol. EI-19, No. 3, pp. 162-178, 1984
- [166] T. Mizutani and M. Ieda, "Electrical Conduction in Solid Dielectrics", IEEE Transactions on Electrical Insulation Vol. EI-21 No.6, pp. 833-839, 1986
- [167] Ulf H. Nilsson, Ruth C. Dammert, Alfred campus, Asko Sneck, Hannele Jakosuo-Jansson, "Morphology of polyethylene for power cable insulation: effects of antioxidant and crosslinking", IEEE International Conference on Conduction and Breakdown in Solid Dielectrics, pp. 365-367, 1998

- [168] John Densley, “Ageing and Diagnostics in Extruded Insulations for Power Cables”, IEEE 5th International Conference on Conduction and Breakdown in Solid Dielectrics, pp. 1-15, 1995
- [169] IUPAC *Compendium of Chemical Terminology* 2nd Edition, 1997
- [170] Suh Joon Han, Alfred M. Mendelsohn, Ram Ramachandran, “Overview of Semiconductive Shield Technology in Power Distribution Cables”, LOES Form Number 310-02201, pp. 1-6, 2004
- [171] Richard H Boyd, “Relaxation Processes in Crystalline Polymers: Molecular Interpretation – a Review”, Polymer Revies, Vol 26, pp. 1123-1133, 1985
- [172] J. P. Jones, J. P. Llewellyn and T. J. Lewis, “The Contribution of Field-Induced Morphological Change to the Electrical Aging and Breakdown of Polyethylene”, IEEE Transactions on Dielectrics and Electrical Insulation, Vol. 12, No. 5, pp. 951-966, 2005.
- [173] Gary C. Stevens and Patrick J. Baird, “Nano- and Meso-measurements Metods in the Study of Dielectrics”, IEEE Transactions on Dielectrics and Electrical Insulation, Vol. 12, No. 5, pp. 979-992, 2005

## **Appendix A: Meetings and publications**

Meetings attended:

1. IEEE 9th International Conference on Solid Dielectrics (ICSD), Winchester, UK, June 2007
2. Institute of Physics (IOP) 75 years of Polyethylene: Past Successes and Future Challenges, London, UK, March, 2008
3. Electrical Ageing Workshop, Autrans, France, June 2008.
4. Project progress report meeting, Borealis AB, Stenungsund, Sweden, November 2008
5. IOP conference of Dielectrics Group, University of Reading, UK, April 2009
6. Oral presentation, IET INSUCON 2009 Conference, Birmingham, UK, May 2009
7. Oral presentation, IOP Conference of Early Career Research in Electrostatics and Dielectrics, London, UK, December 2009
8. Poster presentation, Third UHVNet Colloquium on technologies for future high voltage infrastructure, The University of Manchester, UK, January 2010

Publications:

1. C. D. Green, A. S. Vaughan, G. R. Mitchell, and T. Liu, Structure Property Relationships in Polyethylene/Montmorillonite Nanodielectrics, *IEEE Transactions on Dielectrics and Electrical Insulation*, Vol. 15, No. 1; 2008.
2. Tong Liu, John Fothergill, Steve Dodd, Ulf H Nilsson, Dielectric Spectroscopy of XLPE Cables using Discharging Current Measurement, *IET INSUCON 2009 Conference*, Birmingham, May 2009

3. Tong Liu, John Fothergill, Steve Dodd, Ulf Nilsson, Influence of Semicon Shields on the Dielectric Loss of XLPE Cables, IEEE Conference on Electrical Insulation and Dielectric Phenomena, USA, October 2009
4. Tong Liu, John Fothergill, Stephen Dodd, Ulf Nilsson, Dielectric Spectroscopy Measurement on Very Low Loss Crosslinked Polyethylene Power Cables, Journal of Physics: Conference Series, 183 (2009)
5. Tong Liu, John Fothergill, Steve Dodd, Len Dissado et al., Dielectric spectroscopy study of thermally-aged extruded model power cables, IEEE 10th International Conference on Solid Dielectrics (ICSD), July, Potsdam, Germany (accepted)